NUREG/CR-6440
BMI-2190

The Effects of Cyclic and Dynamic Loading on the Fracture Resistance of Nuclear Piping Steels

Technical Report
October 1992 – April 1996

Manuscript Completed: September 1996
Date Published: December 1996

Prepared by
D. L. Rudland, F. Brust, G. M. Wilkowski

Battelle
505 King Avenue
Columbus, OH 43201

M. E. Mayfield, NRC Project Manager

Prepared for
Division of Engineering Technology
Office of Nuclear Regulatory Research
U.S. Nuclear Regulatory Commission
Washington, DC 20555–0001
NRC Job Code D2060

ABSTRACT

This report presents the results of the material property evaluation efforts performed within Task 3 of the IPIRG-2 Program. Several related investigations were conducted. (1) Quasi-static, cyclic-load compact tension specimen experiments were conducted using parameters similar to those used in IPIRG-1 experiments on 6-inch nominal diameter through-wall-cracked pipes. These experiments were conducted on a TP304 base metal, an A106 Grade B base metal, and their respective submerged-arc welds. The results showed that when using a constant cyclic displacement increment, the compact tension experiments could predict the through-wall-cracked pipe crack initiation toughness, but a different control procedure is needed to reproduce the pipe cyclic crack growth in the compact tension tests. (2) Analyses conducted showed that for 6-inch diameter pipe, the quasi-static, monotonic J-R curve can be used in making cyclic pipe moment predictions; however, sensitivity analyses suggest that the maximum moments decrease slightly from cyclic toughness degradation as the pipe diameter increases. (3) Dynamic stress-strain and compact tension tests were conducted to expand on the existing dynamic database. Results from dynamic moment predictions suggest that the dynamic compact tension J-R and the quasi-static stress-strain curves are the appropriate material properties to use in making dynamic pipe moment predictions.

DISCLAIMER

CONTENTS

CONTENTS

CONTENTS

CONTENTS

Page

LIST OF FIGURES

CONTENTS

CONTENTS

CONTENTS

CONTENTS

Page

CONTENTS

Page

CONTENTS

CONTENTS

Page

LIST OF TABLES

CONTENTS

EXECUTIVE SUMMARY

This report describes the work conducted within Task 3 of the Second International Piping Integrity Research Group (IPIRG-2) Program. The IPIRG-2 program was an international group program coordinated by the U.S. NRC and conducted at Battelle. The main objective of the IPIRG-2 program was to evaluate the mechanical behavior of nuclear piping containing flaws and subjected to seismic/dynamic loadings.

Task 3 was undertaken specifically to study the effects of cyclic and dynamic load histories on the fracture behavior of nuclear pipe steels. In the IPIRG-1 program, a series of monotonically and cyclically loaded 6-inch nominal diameter circumferential through-wall-cracked pipe experiments was conducted using both quasi-static and dynamic loading rates. It was concluded from those experiments that dynamic loading marginally increased the load-carrying capacity of the austenitic steel pipes tested and decreased the load-carrying capacity of the ferritic steel pipes tested as compared to quasi-static loading. Also, it was concluded that fully reversed cyclic loading lowered the apparent fracture toughness of both the ferritic and austenitic steel pipes tested as compared to monotonic loading. Because of these observations, laboratory specimen data were desired to determine if these pipe-test results are predictable.

Materials Examined

The specimens used in this investigation were machined from pipe that was used in the full-scale pipe experiments in both the IPIRG-1 and IPIRG-2 programs. For the cyclic-loading compact tension specimen experiments, the following materials were evaluated: a 6-inch nominal diameter, Schedule 120, TP304 stainless steel pipe; a 6-inch nominal diameter, Schedule 120, A106 Grade B carbon steel pipe; a submerged-arc weld (SAW) in a 16-inch nominal diameter, Schedule 100, TP304 stainless steel pipe; and a submerged-arc weld in an A106 Grade B plate. For the dynamic-loading experiments, the materials evaluated were: a 30-inch nominal diameter, Schedule 80, STS49 carbon steel pipe; a 10-inch nominal diameter, Schedule 100, A333 Grade 6 carbon steel pipe; a 6-inch nominal diameter, Schedule 80, A106 Grade B carbon steel pipe; and a 6-inch nominal diameter, Schedule 120, STS410 carbon steel pipe. Additional dynamic data from the IPIRG-1 program and other tasks in the IPIRG-2 program were also available for assessing the effects of loading rates on strength and toughness.

Observations from Cyclic-Load Fracture Tests

All of the cyclic-load compact tension [C(T)] specimens that were machined from pipe were in the L-C orientation, simulating the circumferential through-wall crack growth direction. The cyclic C(T) specimens that were machined from plate welds were in the L-T orientation, which corresponds to the L-C orientation in a pipe. All cyclic C(T) specimens were tested at 288 C (550 F). The stainless steel base metal C(T) experiments were conducted at quasi-static rates with stress ratios (P_{min}/P_{max}) of 0, -0.3, -0.6, -0.8, and -1 and normalized cyclic displacement increments (the ratio of the displacement per cycle to the displacement at crack initiation in a monotonic experiment, δ_{cyc}/δ_i) of 0.1, 0.2 and 0.025. The cyclic displacement increment is synonymous with ratcheting in uncracked pipe. δ_{cyc}/δ_i is inversely equal to the number of cycles at crack initiation if no cyclic degradation occurs, i.e., δ_{cyc}/δ_i of 0.1 corresponds to 10 cycles to crack initiation. Under cyclic loading, the displacement to crack initiation may decrease and the actual number of cycles to crack initiation would decrease. The carbon steel base metal was tested at the same rate and stress ratios but with only one normalized cyclic displacement increment, 0.1. Cyclic C(T) specimens machined from the submerged-arc welds were tested at stress ratios of -0.6 and -1 with both quasi-static and dynamic loading rates and at $\delta_{cyc}/\delta_i = 0.1$.

In order to conduct experiments that required cyclic loading, a computer was used for real-time control of the experiments. The control program used in these experiments was identical to that used in the IPIRG-1 circumferential through-wall-cracked pipe experiments. This BASIC program performs the cyclic loading by loading the specimen to a prescribed displacement in tension, recording the peak load, and then loading the specimen in compression to the previous peak load value multiplied by the desired stress ratio. These loading/unloading cycles were continued throughout the experiments. In addition to these cyclic experiments, cyclic-loading tests were also conducted on stainless steel and carbon steel base metal C(T) specimens in order to (metallographically) study the damage-formation process. All data from this effort will be included in a future version of the NRC's PIFRAC database.

A number of key findings from the cyclic-loading experiments can be noted:

- Several observations can be made directly from the cyclic C(T) experiments that explain the calculated J-R curve trends. These are:
  - The maximum loads were reduced in the C(T) tests by 20 percent at most when compared with the quasi-static monotonic C(T) tests.
  - Even though the maximum loads did not change dramatically, the load-line displacement decreased by a factor of five in the worst case. This decrease in the load-line displacement depended on the load ratio and δ_{cyc}/δ_i. The more negative the load ratio or the smaller δ_{cyc}/δ_i, the greater the toughness reduction from cyclic loading. These dramatic changes in the load-line displacement were also observed in the IPIRG-1 cyclic through-wall-cracked pipe experiments. Effectively, the pipe has less plasticity under cyclic loading. Hence, inherent margins in elastic pipe stress analyses may not be as large as might be anticipated if the plasticity from monotonic pipe fracture behavior was considered.
  - The A106 Grade B carbon steel pipe material examined was more affected by the cyclic loading than the stainless steel pipe material examined, i.e., at a load ratio of -0.3 there was no effect on the stainless steel material, but the A106 Grade B material examined had a significant lowering of the load-displacement test record.
  - The carbon steel material load-displacement record and hence the J-R curve, appeared to reach a lower bounding level at a load ratio of -0.8, but the stainless steel material did not show signs of reaching a lower bounding level at a load ratio of -1. Perhaps if a more negative load ratio was used for the stainless steel, then a lower bounding level might be reached. Hence, the cyclic degradation appears to be sensitive to material toughness, as well as load ratio and δ_{cyc}/δ_i.
- For the weld metal C(T) experiments, reduction in maximum load due to cyclic loading was small at quasi-static loading rates but somewhat larger for dynamic loading rates. In all of the quasi-static, cyclic-load weld C(T) cases, the greatest reductions in maximum load as compared to the quasi-static, monotonic experiment was 10 percent. For the dynamic, cyclic load weld C(T) cases, the greatest reduction in maximum load, as compared to the dynamic, monotonic experiments was 20 percent. These findings suggest that dynamically load cycling a specimen increases the degradation as compared

to cycling at quasi-static rates. (The interaction between cyclic and dynamic loading effects on toughness are discussed later.)

- Crack-tip sharpening was observed to be one of the main mechanisms in the cyclic degradation process, both for the stainless steel and the carbon steel. This sharpening acts to increase the crack-tip stress intensity and promote crack extension, thus lowering the apparent fracture resistance. Because of the more ductile nature of stainless steel, its tendency toward more-pronounced crack-tip blunting resulted in less-severe crack-tip sharpening than in the carbon steel. Because the carbon steel has a lower toughness and less-pronounced crack-tip blunting than stainless steel, it may take less compressive load to sharpen the crack tip. Therefore, intermediate stress ratios could decrease the load-carrying capacity in the carbon steel, but have little effect on the stainless steel.

- Void sharpening also appeared to be an important mechanism in the degradation process, but only the carbon steel experienced substantial void sharpening. Sharp voids tend to enhance void coalescence and lower apparent fracture toughness. The rationale for this mechanism is similar to the one made for the crack-tip sharpening; the higher the material toughness, the larger the compressive load needed to promote void sharpening. Crack-tip sharpening and void sharpening can work together in degrading a material's fracture resistance under cyclic loading.

Analysis of Cyclic-Load Fracture Tests

In order to determine the extent of toughness degradation resulting from cyclic loading, an estimate for the J-integral was made for the C(T) specimen geometry. For C(T) specimens under monotonic loading, estimations of J have been made and published in ASTM E1152, "Standard Test Method for Determining J-R Curves". In the cyclic-loading analyses, the upper envelope of the load-displacement curve was used in the J formulation. Even though the formal definition of J is violated when unloadings occur, calculating J from the upper envelope of the load-displacement record can provide a useful tool in the determination of cyclic effects on fracture toughness.

A series of finite element analyses was conducted on cyclically-loaded C(T) specimens, aimed at predicting their load-displacement response and verifying the use of the upper envelope approach in calculating J. Two specimens were modeled. The first was a stainless steel base metal specimen tested at a quasi-static rate at a stress ratio of -1, and the second was one of the additional stainless steel specimens that was used in the crack-tip damage studies. Each of the specimens was modeled with both classical isotropic and kinematic hardening laws and assuming plane stress conditions. The first specimen was also modeled assuming generalized plane strain conditions. The ABAQUS finite element code was used for these analyses. The J-integral was calculated using Battelle's T-Post ABAQUS post processor, which calculates integral parameters. The crack-tip-opening angle was also evaluated using the displacements of the corner nodes behind the growing crack tip divided by the distance to the crack tip.

In addition to these finite-element analyses, several moment predictions were made to determine whether it was necessary to use the C(T) specimen cyclic J-R curves to predict the cyclic TWC pipe response. These predictions were made using a variety of analysis methods -- Net Section Collapse, LBB.NRC, LBB.ENG2, and GE/EPRI methods. In addition, a sensitivity analysis was conducted to predict the cyclic behavior of larger-diameter through-wall-cracked pipes. Quasi-static stress-strain curves were used in all cyclic-load predictions.

The key results from the cyclic-load analyses were:

- From the finite element analyses, the kinematic hardening law produced load predictions that closely matched the tensile portion of the experimental cyclic loading history but severely underpredicted the compressive portion. On the other hand, using the isotropic-hardening law (using both a linear fit and Ramberg-Osgood fit of the stress-strain behavior) overpredicted both the tensile and compressive loads. The predicted value of J at crack initiation compared well with the experimental ASTM J predictions for both the kinematic and isotropic analyses. After the first unloading, J became very path dependent in these analyses. After crack growth, the kinematic analysis, which predicted the tensile load accurately, slightly underpredicted the experimental ASTM J values. The isotropic analysis predicted slightly higher J values than the experimental results. When the ASTM procedure for calculating J was used with the upper envelope of the finite-element predicted load-displacement response, the resulting J-R curve agreed well with the far-field J-R curve calculated directly from the finite element analysis. These results demonstrate that the upper-envelope approach to calculating the J-R curve produces an accurate representation of the material's fracture behavior.

- For both base metal materials tested, the C(T) experiments produced J_i values that were in reasonable agreement with the calculated through-wall-cracked pipe J_i values. That is, using the δ_{cyc}/δ_i parameter gave good similitude between the TWC pipe and C(T) specimen J_i values.

- Using the same displacement increment in both the pipe and C(T) experiments produced poor agreement between the crack growth results. As an example, for the stainless steel base metal tested in this study, it was found that doubling the displacement increment in the C(T) tests gave a more reasonable estimate of the crack growth per cycle in the TWC pipe tests. Furthermore, by using a pipe J-estimation scheme, such as the GE/EPRI method, it was determined that the δ_{cyc}/δ_i value needs to be changed after crack initiation to produce the same crack growth per cycle in a C(T) test as in a TWC pipe test.

- The trends suggest that the decrease in resistance due to cyclic loading may be linearly related to the material's yield-to-ultimate strength ratio. Because only limited experimental data are available, this trend will need further validation.

- The TWC cyclic maximum-moment predictions were relatively insensitive to the J-R curve used for the existing 6-inch diameter pipe tests. When the monotonic J-R curve was used, the maximum moment predictions were approximately equal to the maximum-moment predictions made when the cyclic J-R curve was used in the analyses. For the 6-inch nominal diameter TWC pipes investigated, the moments at crack initiation and maximum moment were very close to limit load and, therefore, are not very sensitive to changes in toughness. Because the experimental scatter in maximum load from replicate pipe experiments could be as much as 10 percent, the difference between using a monotonic or cyclic-load J-R curve for predicting maximum moment appears to be insignificant for this pipe size.

- The sensitivity studies showed that, as the pipe diameter was increased, the maximum moment at all stress ratios decreased. Interestingly, for the stainless steel base metal, the decrease in load-carrying capacity was constant for all pipe diameters. The decrease in load-carrying capacity in the carbon steel was greater at large diameters than at small diameters. For the $R = -1$ case, there was a 16 percent decrease in maximum load for a 170 mm (6.7 inches) diameter pipe, while there was a 20 percent decrease in maximum load for a 1,300 mm (51.2 inches) pipe, indicating that the cyclic degradation is greater for larger diameter pipes. These analyses also indicate that a seismic event with a stress ratio of -1 is likely to produce enough crack growth with a typical number of large amplitude cycles in a seismic event to take a TWC pipe beyond its maximum load-carrying capacity for all practical nuclear pipe sizes.

Dynamic-Load Results

In addition to the cyclic-loading investigation, a series of dynamic tensile and fracture toughness tests were conducted on a variety of carbon steel materials at 288 C (550 F). The purpose of these experiments was to expand the database of existing dynamic material properties for carbon steels. A series of moment predictions was also conducted to determine what material properties are appropriate in making dynamic moment predictions. In addition to the through-wall-cracked pipe estimation schemes used above, the following surface-cracked pipe prediction schemes were used: SC.TNP1, SC.TKP1, SC.ENG2, and the R6 Revision 3 Option 1.

Key results from the experimental and analytical dynamic-loading efforts were:

- All of the carbon steel materials tested at 288 C (550 F) showed a decrease in ultimate strength with an increase in strain rate. Yield strength values, on the other hand, increased slightly or were unchanged in all cases.

- Even though the tensile stress-strain response was similar among the carbon steels tested, the effects of dynamic loading on the fracture resistance were inconsistent. While some base metal specimens showed a decrease in fracture resistance with increasing strain rate, others showed no change in resistance with the same increase in rate. The submerged-arc welds tested showed a significant increase in resistance with increasing strain rate. However, the STS410 TIG weld showed no change in resistance with increasing strain rate.

- The variable effect of dynamic loading on fracture resistance may be related to the material's susceptibility to dynamic strain aging. The DSA sensitivity may be correlated with the material's yield-to-ultimate strength, and to the high temperature to room temperature Brinell hardness ratio. The trends presented suggest that dynamically loaded carbon steel materials whose yield-to-ultimate strength ratio is greater than 0.5 will have toughness values that are equal to or higher than those obtained at quasi-static loading rates. This apparent dependency on the yield-to-ultimate strength ratio and the high temperature to room temperature Brinell hardness ratio may aid in the creation of a criterion that would characterize a material's fracture toughness response to dynamic loading. However, there was significant scatter in each of these correlations, and perhaps some combination of these parameters would produce a better correlation.

- The specified rate for the dynamic C(T) experiments (0.2 seconds to crack initiation) was determined in the IPIRG-1 program from a finite element analysis of a pipe test conducted with inertial loading. It is appropriate to use these data in predicting moments for a cracked pipe which has the same time to crack initiation. However, choosing a proper strain rate for the dynamic tensile stress-strain curve was less straightforward. Because the strain rate near the crack tip of a dynamic TWC pipe experiment is difficult to quantify and varies with distance from the crack tip, rates of 1/s and 10/s were chosen arbitrarily; however, calculations based on the STS410 6-inch nominal diameter pipe tests showed that the strain rate in the uncracked pipe was on the order of 10^{-3}/s, which is much closer to the quasi-static rate than the dynamic rate. Note that subsequent to concluding these tests, it was found in Task 1 of the IPIRG-2 program that crack initiation might occur as fast as one quarter of the period of the first natural frequency of a piping system. For a pipe system with a natural frequency of 4 Hz, this corresponds to a time of 0.0625 seconds, or about 3 times faster than the tests conducted. This factor of 3 is not considered highly significant considering that DSA effects are usually plotted on a log scale.

- A comparison between the load-displacement responses of the quasi-static and dynamic monotonic through-wall-cracked pipe and C(T) experiments for an STS410 material showed no differences up to crack initiation. The STS410 material showed no change in toughness properties with increasing strain rate. Hence for that material, it appears appropriate to assume that the strength at the test strain rate is equal to the quasi-static rate strength. In addition, several A106 Grade B steel dynamic and quasi-static C(T) specimen load-displacement records were compared up to crack initiation. No perceptible differences were found, implying similar effective strain-hardening behavior for these materials. Therefore, the quasi-static stress-strain properties were considered to be sufficient for fracture predictions at the rates investigated in this program.

- It was found that using the J_M-R curve, rather than the J_D-R curve, in making crack initiation and maximum moment predictions tended to reduce the scatter between the estimation schemes. When predicting maximum moments, the J-estimation schemes performed better for the case of pure bending then they did for pressure and bending. In general, for the case of pressure-plus-bending the estimation schemes produced experimental-to-predicted maximum longitudinal stress ratios about 20 percent higher than for the case of pure bending. This conclusion was consistent with results from the NRC's Short Cracks in Piping and Piping Welds program.

- The difference in maximum load predictions of the 6-inch nominal diameter pipe tests when using J-R curves from the pipe experiments, the quasi-static C(T) experiments, or the dynamic C(T) experiments was small. This observation is expected in the stainless steel because the maximum moments for the pipes investigated were close to limit load, which would cause an apparent insensitivity to toughness. However, the scatter between the estimation schemes may mask the effect of the different J-R curves. If results from one particular estimation scheme are examined, the effect of varying the J-R curve becomes more apparent. In almost all cases, use of the dynamic C(T) J-R curve produced lower moment predictions than when the quasi-static J-R curve was used.

- The sensitivity studies for a ferritic steel highly sensitive to DSA suggest that the maximum load-carrying capacity of larger diameter pipe will be slightly more affected by dynamic loading than smaller diameter pipes. There was a 16 percent decrease in maximum load for a 6-inch nominal diameter pipe, while there was a 20 percent decrease in maximum load for a 1,300 mm (51.2 inches) diameter pipe.

- The interaction between cyclic and dynamic crack growth was investigated by comparing the J values from a dynamic cyclic (R = -1) C(T) test to the J value from a simple quasi-static monotonic C(T) test multiplied by a dynamic correction factor (F_{dyn}) and a cyclic correction factor (F_{cyc}). F_{dyn} was the ratio of the J values from the dynamic monotonic C(T) test to the quasi-static monotonic C(T) test at the same amount of crack growth ($J_{dyn,mono}/J_{QS,mono}$). F_{cyc} was the ratio of the J values from the quasi-static cyclic C(T) test to the quasi-static monotonic C(T) test also at the same amount of crack growth ($J_{QS,cyc}/J_{QS,mono}$). The results were encouraging in that for four materials covering a wide range in toughness, the J value from $F_{cyc}*F_{dyn}*J_{QS,mono}$ was essentially identical to the J value from the dynamic, cyclic C(T) test for the same amount of crack growth. Hence, these data showed no interaction between dynamic and R = -1 cyclic loading.

In a similar comparison, the cyclic dynamic J value was estimated using trends of F_{dyn} and F_{cyc}, as a function of the material's yield-to-ultimate strength. Due to scatter in these correlations, there was an overprediction of the actual dynamic cyclic toughness, which was more significant in the low toughness region. Some improvement to these correlations is needed, or a safety factor should be applied to them.

Finally, in reviewing the applicability of the results from this program, it was noted that past Battelle/DOE pipe-system nonlinear seismic analyses showed that load ratios were more negative for cracked pipe than uncracked pipe. Lower bounds from pipe stress analysis reports showed that uncracked pipe stress ratios might be as low as -0.6. Hence, using an R-ratio of -1 might be a bounding R-ratio for cracked pipe. One could then account for cyclic effects by using the lower bounding R = -1 results and correlations with yield-to-ultimate strength. Alternatively, a state-of-the-art methodology could be used, where a cracked-pipe, nonlinear, seismic, time-history analysis could be used to determine the load history for a C(T) test that would be consistent with plant piping loads. This alternative method would also account for plasticity effects on the dynamic loads. Hence, the trade-offs of cyclic load degradation on toughness versus the nonlinear reductions of elastically calculated moments could be accounted for in this approach.

ACKNOWLEDGMENTS

The IPIRG Program was an international group program coordinated by the U.S. Nuclear Regulatory Commission's Electrical, Materials, and Mechanical Engineering Branch of the Office of Nuclear Regulatory Research under Contract No. NRC-04-91-063 to Battelle. Mr. Michael Mayfield was the U.S. NRC program manager. Dr. Allen Hopper was the Battelle program manager.

The members of the IPIRG-2 Program and their representatives to the IPIRG Technical Advisory Group (TAG) were:

Bulgaria	
- CUAEPP	Mr. Y. Yanev
Canada	
- AECB(*)	Dr. B. Jarman(**), Mr. J. K. Pereira
- Ontario Hydro	Mr. M. Kozluk
Czech Republic	
- NRI	Dr. J. Zdárek, Dr. M. Brumovsky, Dr. P. Kadečka, Mr. J. Palyza
France	
- EDF(*)	Mr. C. Faidy(**), Mr. P. Le Delliou
- CEA	Ms. F. Gantenbein, Mr. E. Debec-Mathet
- Framatome	Dr. Ph. Gilles
Hungary	
- HAEC	Mr. A. Fehérvári
Italy	
- ANPA-DISP(*)	Dr. C. Maricchiolo(**)
Japan	
- CRIEPI(*)	Dr. K. Kashima(**), Mr. N. Miura
Lithuania	
- VATESI	Mr. P. Vaisnys
Republic of China	
- INER/AEC(*)	Dr. Li-Fu Lin(**)

(*) Contractual organization

(**) TAG representative

Republic of Korea	
- KINS(*)	Dr. J. B. Lee(**), Dr. Y. H. Choi
- SKKU	Dr. Y. J. Kim
Slovak Republic	
- VUJE	Dr. L. Kupca
- NRA	Dr. J. Misak
Sweden	
- SKI(*)	Dr. G. Hedner
- SAQ	Dr. B. Brickstad
Switzerland	
- KKL(*)	Mr. R. Wanner(**)
- HSK	Dr. D. H. Njo
United Kingdom	
- Nuclear Electric(*)	Dr. T. C. Chivers(**), Dr. J. Darlastan
United States	
- U.S. NRC-RES(*)	Mr. M. Mayfield(**)
- U.S. NRC-NRR(*)	Mr. K. Wichman(**)
- EPRI(*)	Mr. S. Gosselin(**), Dr. Y. K. Tang

We would like to express our appreciation for the support and interest of the IPIRG members in this program.

In addition, we would like to thank Mr. Naoki Miura of CRIEPI (Japan) who was a visiting scientist at Battelle during the course of conducting this task. Mr. Miura assisted in the sensitivity calculations and helped to refine the η-factor computer code for calculating J-R curves from pipes.

Finally, we would like to thank others at Battelle who have helped in these efforts. Technicians who have contributed include: Mr. J. Anthony, Mr. E. Blakesley, Mr. R. Gertler, Mr. P. Mincer, Mr. M. Oliver, Mr. D. Shoemaker, Mr. G. Wall, Mr. P. Held, and Mr. D. Roberts. We also would like to recognize Mrs. V. Kreachbaum and Ms. Brenda Fuller for their assistance in preparing this report and Dr. A. Hopper for editorial assistance.

(*) Contractual organization

(**) TAG representative

NOMENCLATURE

1. SYMBOLS

a	Crack depth or length
a_i	Initial crack depth or length
A_p	Area under plastic portion of load-displacement curve
b	Length of uncracked ligament in a fracture specimen
b_i	Initial length of uncracked ligament in a fracture specimen
B	Thickness of C(T) specimen
B_N	Net thickness of side-grooved C(T) specimen
C	A parameter in the power-law to fit J-R curve
da/dN	Crack growth rate
E	Elastic modulus
F_{dyn}	$J_{dyn,mono}/J_{QS,mono}$ at some crack growth
F_{cyc}	$J_{QS,cyc}/J_{QS,mono}$ at some crack growth
J	J-integral fracture parameter
J_D	J based on deformation theory
$J_{dyn,mono}$	J for a dynamic, monotonic experiment
$J_{dyn,cyc}$	J for a dynamic, cyclic experiment
J_D-R	J-resistance based on deformation theory form of J
J_e	Elastic component of J
J_i	J at crack initiation

Nomenclature

J_{Ic}	Plane strain J at crack initiation by ASTM E399
J_M	Modified form of J
J_M-R	J-resistance based on modified form of J
J_p	Plastic component of J
$J_{QS,cyc}$	J for a cyclic-load experiment
$J_{QS,mono}$	J for a quasi-static monotonic experiment
J-R	J-resistance (curve)
K_e	Elastic portion of LEFM stress intensity factor fracture parameter
M	Moment
$M_{MAX.\ PRED.}$	Maximum predicted moment
$M_{INIT.\ PRED.}$	Initiation predicted moment
M_{NSC}^{B}	Net-Section-Collapse moment from a bend pipe experiment
M_{NSC}^{B+T}	Net-Section-Collapse moment from a pressure (axial tension) and bend pipe experiment
M_{Pred}^{B}	Predicted moment from a bend pipe experiment
M_{Pred}^{B+T}	Predicted moment from a pressure (axial tension) and bend pipe experiment
m	A parameter in the power-law fit J-R curve
n	A parameter in the Ramberg-Osgood equation
P_{min}	Minimum load during a cyclic test
P_{max}	Maximum load during a cyclic test
R	Stress ratio (P_{min}/P_{max})
R_M	Mean pipe radius
T*	Fracture mechanics parameter
t	Pipe wall thickness

w	Width of fracture mechanics specimen
α	A parameter in the Ramberg-Osgood equation
δ_{cyc}	Cyclic plastic displacement increment
δ_i	Displacement at crack initiation in a monotonic experiment
Δa	Change in crack length or depth, i.e., crack growth
ΔK	K_e range calculated during a cyclic load history
ΔJ	J-integral range calculated during a cyclic load history
ΔM	Moment reduction factor for adjusting moment-rotation curve
θ	Half crack angle
ϵ_o	A parameter in the equation Ramberg-Osgood
ϵ_y^p	Plastic component of y-direction strain
U	Electric potential
U_o	Electric potential at onset of crack extension
Y	Half of the distance between d-c electric potential leads on a C(T) specimen
ν	Poisson's ratio
γ	$1 + 0.76$ b/w
η	Geometric constant used in general analytical procedure where J_p is calculated using experimental load, displacement, and crack growth data
ϕ	Half-rotation of pipe
σ_f	Flow stress
σ_{max}	Maximum stress
σ_{min}	Minimum stress
σ_o	A parameter in the Ramberg-Osgood equation
σ_{UTS}	Ultimate tensile strength

Nomenclature

σ_{ys}	Yield strength
σ_y	y-axis component of stress
Ω	Angle of through-wall crack from circumferential plane

2. ACRONYMS AND INITIALISMS

AECB	Atomic Energy Control Board, Canada
ANPA-DISP	Agenzia Najionaleperla Protezoin deli Ambiarte, Italy
ASM	American Society for Metals
ASTM	American Society for Testing and Materials
BMI	Battelle Memorial Institute
BHN	Brinell hardness number
CEA	Commissariat A L'Energie Atomique, France
CMOD	Crack-mouth-opening displacement
COD	Crack-opening displacement
CRIEPI	Central Research Institute of Electric Power Industry, Japan
C(T), CT	Compact (Tension)
CTOA	Crack-tip-opening angle
CUAEPP	Commercial Use of Atomic Energy for Peaceful Purposes, Bulgaria
Cyc	Cyclic
d-c EP	Direct-current electric potential
DP2	Degraded Piping Program - Phase II
DPZP	Dimension-Plastic-Zone parameter
DSA	Dynamic strain aging
Dyn	Dynamic

EDF	Electricité de France
EDI	Equivalent domain integral
EPFEAM	Elastic-plastic finite element alternating method
EPRI	Electric Power Research Institute
FEM	Finite element method
GE	General Electric
HAEC	Hungarian Atomic Energy Commission
HSK	Hauptabteilung für die Sicherheit der kernanlagen, Switzerland
INER	Institute of Nuclear Energy Research, Republic of China
IPIRG-1	First International Piping Integrity Research Group
IPIRG-2	Second International Piping Integrity Research Group
KINS	Korea Institute of Nuclear Safety
KKL	Kernkraftwerk Leibstadt AG, Switzerland
LBB	Leak-Before-Break
L-C	Orientation that indicates crack plane is normal to longitudinal axis (L) and crack growth direction is circumferential (C)
LLD	Load-line displacement
L-T	Orientations code that indicates crack plane is normal to longitudinal rolling direction (L) and crack growth direction is transverse (T) to plate rolling directions
LVDT	Linear variable differential transformer
LWR	Light water reactor
MSD	Multi-Site-Damage
MTS	Supplier of servo-hydraulic equipment
N/A	Not applicable

NRA	Nuclear Regulatory Authority, Slovak Republic
NRC	Nuclear Regulatory Commission, U.S.
NRI	Nuclear Research Institute, Czech
NRR	Office of Nuclear Reactor Regulation, U.S. NRC
NSC	Net-Section-Collapse
NUREG/CR	Nuclear Regulatory Contractor's Report
OBE	Operational-basis earthquake
PC	Personal computer
PIFRAC	PIping FRACture mechanics data base
PVP	Pressure Vessel and Piping
PWR	Pressurized Water Reactor
QS	Quasi-static
RES	Office of Nuclear Reactor Research, U.S. NRC
RT	Room temperature
R6	Defect assessment criterion developed by CEGB
SAW	Submerged-arc weld
SKKU	Sung Kyun Kwan University, Korea
SC	Surface crack
SEN(T)	Single edge-notch (tension)
SKI	Statens Kärnkraftinspektion (Swedish Nuclear Power Inspectorate)
SSE	Safe shutdown earthquake
STP	Special Technical Report
TAG	Technical Advisory Group
TIG	Tungesten inert gas

TWC	Through-wall crack
U.S.	United States
U.S. NRC	United States Nuclear Regulatory Commission
UTS	Ultimate tensile strength
VATESI	State Nuclear Energy Safety Inspection of the Republic of Lithuania
VUJE	Vyskumny Ustav Jadravyeh Elektrarni (Nuclear Power Plant Research Institute), Slovak

PREVIOUS REPORTS IN SERIES

Previous Reports from this Program

"Summary of Results from the IPIRG-2 Round-Robin Analyses," NUREG/CR-6337, BMI-2186, February 1996.

"Pipe System Experiments with Circumferential Cracks in Straight Pipe Locations," NUREG/CR-6389, BMI-2187, May 1996.

"The Effect of Cyclic and Dynamic Loads on Carbon Steel Pipe," NUREG/CR-6438, BMI-2188, February 1996.

"Design of the IPIRG-2 Simulated Seismic Forcing Function," NUREG/CR-6439, BMI-2189, February 1996.

"Deterministic and Probabilistic Evaluations for Uncertainty in Pipe Fracture Parameters in Leak-Before-Break and In-Service Flaw Evaluations," NUREG/CR-6443, BMI-2191, June 1996.

"Development of a J-Estimation Scheme for Internal Circumferential and Axial Surface Cracks in Elbows," NUREG/CR-6445, BMI-2193, June 1996.

Reports from the IPIRG-1 Program

"Evaluation and Refinement of Leak-Rate Estimation Models," NUREG/CR-5128, Revision 1, June 1994.

"Loading Rate Effects on Strength and Fracture Toughness of Pipe Steels Used in Task 1 of the IPIRG Program," Topical Report, NUREG/CR-6098, October 1993.

"Stability of Cracked Pipe Under Inertial Stresses," NUREG/CR-6233, Vol. 1, August 1994.

Previous Related Documents from NRC's Short Cracks in Piping and Piping Welds Program

"Short Cracks in Piping and Piping Welds," First Semiannual Report, NUREG/CR-4599, Vol. 1, No. 1, March 1991.

"Short Cracks in Piping and Piping Welds," Second Semiannual Report, NUREG/CR-4599, Vol. 1, No. 2, April 1992.

"Short Cracks in Piping and Piping Welds," Third Semiannual Report, NUREG/CR-4599, Vol. 2, No. 1, September 1992.

"Short Cracks in Piping and Piping Welds," Fourth Semiannual Report, NUREG/CR-4599, Vol. 2, No. 2, February 1993.

"Short Cracks in Piping and Piping Welds," Fifth Semiannual Report, NUREG/CR-4599, Vol. 3, No. 1, October 1993.

"Short Cracks in Piping and Piping Welds," Sixth Semiannual Report, NUREG/CR-4599, Vol. 3, No. 2, March 1994.

"Short Cracks in Piping and Piping Welds," Progress Report, NUREG/CR-4599, BMI-2173, Vol. 4, No. 1, April 1995.

"Fracture Behavior of Short Circumferential Short-Surface-Cracked Pipe," NUREG/CR-6298, November 1995.

"Fracture Evaluations of Fusion Line Cracks in Nuclear Pipe Bimetallic Welds," NUREG/CR-6297, April 1995.

"Effect of Dynamic Strain Aging on the Strength and Toughness of Nuclear Ferritic Piping at LWR Temperatures," NUREG/CR-6226, October 1994.

"Effects of Toughness Anisotropy and Combined Loading on Fracture Behavior of Ferritic Nuclear Pipe," NUREG/CR-6299, April 1995.

"Refinement and Evaluation of Crack-Opening Analyses for Circumferential Through-Wall Cracks in Pipes," NUREG/CR-6300, April 1995.

"Probabilistic Pipe Fracture Evaluations for Leak-Rate Detection Applications," NUREG/CR-6004, April 1995.

"Stainless Steel Submerged Arc Weld Fusion Line Toughness," NUREG/CR-6251, April 1995.

"Validity Limits in J-Resistance Curve Determination: Volume 1: An Assessment of the J_M Parameter," NUREG/CR-6264, Volume 1, February 1995.

"Validity Limits in J-Resistance Curve Determinations: Volume 2: A Computational Approach to Ductile Crack Growth Under Large-Scale Yielding Condition," NUREG/CR-6264, Volume 2, February 1995.

Previous Related Documents from NRC's Degraded Piping Program - Phase I Reports

"The Development of a Plan for the Assessment of Degraded Nuclear Piping by Experimentation and Tearing Instability Fracture Mechanics Analysis," NUREG/CR-3142, Vols. 1 and 2, June 1983.

Previous Related Documents from NRC's Degraded Piping Program - Phase II Reports

"Degraded Piping Program - Phase II," Semiannual Report, NUREG/CR-4082, Vol. 1, Oct. 1984.

"Degraded Piping Program - Phase II," Semiannual Report, NUREG/CR-4082, Vol. 2, June 1985.

"Degraded Piping Program - Phase II," Semiannual Report, NUREG/CR-4082, Vol. 3, March 1986.

"Degraded Piping Program - Phase II," Semiannual Report, NUREG/CR-4082, Vol. 4, July 1986.

"Degraded Piping Program - Phase II," Semiannual Report, NUREG/CR-4082, Vol. 5, Dec. 1986.

"Degraded Piping Program - Phase II," Semiannual Report, NUREG/CR-4082, Vol. 6, April 1988.

"Degraded Piping Program - Phase II," Semiannual Report, NUREG/CR-4082, Vol. 7, March 1989.

"Degraded Piping Program - Phase II," Semiannual Report, NUREG/CR-4082, Vol. 8, March 1989.

"NRC Leak-Before-Break (LBB.NRC) Analysis Method for Circumferentially Through-Wall Cracked Pipes Under Axial Plus Bending Loads," Topical Report, NUREG/CR-4572, March 1986.

"Elastic-Plastic Finite Element Analysis of Crack Growth in Large Compact Tension and Circumferentially Through-Wall-Cracked Pipe Specimen--Results of the First Battelle/NRC Analysis Round Robin," Topical Report, NUREG/CR-4573, September 1986.

"An Experimental and Analytical Assessment of Circumferential Through-Wall Cracked Pipes Under Pure Bending," Topical Report, NUREG/CR-4574, June 1986.

"Predictions of J-R Curves With Large Crack Growth From Small Specimen Data," Topical Report, NUREG/CR-4687, September 1986.

"An Assessment of Circumferentially Complex-Cracked Pipe Subjected to Bending," Topical Report, NUREG/CR-4687, September 1986.

"Analysis of Cracks in Stainless Steel TIG Welds," Topical Report, NUREG/CR-4806, November 1986.

"Approximate Methods for Fracture Analyses of Through-Wall Cracked Pipes," Topical Report, NUREG/CR-4853, January 1987.

"Assessment of Design Basis for Load-Carrying Capacity of Weld-Overlay Repair," Topical Report, NUREG/CR-4877, February 1987.

"Analysis of Experiments on Stainless Steel Flux Welds," Topical Report, NUREG/CR-4878, February 1987.

Previous Reports in Series

"Experimental and Analytical Assessment of Circumferentially Surface-Cracked Pipes Under Bending," Topical Report, NUREG/CR-4872, April 1987.

Other Related Program Reports

"Validation of Analysis Methods for Assessing Flawed Piping Subjected to Dynamic Loading," NUREG/CR-6234, August 1994.

1.0 INTRODUCTION

The IPIRG-2 program was an international group program coordinated by the U.S. NRC and conducted at Battelle-Columbus. The main objective of the IPIRG-2 program was to evaluate the fracture behavior of nuclear piping subjected to seismic/dynamic loadings. The efforts in the IPIRG-2 program consisted of five tasks:

Task 1 Pipe System Experiments with Cracks in Straight Pipe and Welds

Task 2 Fracture of Cracked Fittings

Task 3 Cyclic and Dynamic Load Effects on Fracture

Task 4 Resolution of Issues from IPIRG-1 and Related Programs

Task 5 Information Exchange Seminars and Workshops, and Program Management

This report describes the work conducted within Task 3 of the IPIRG-2 Program. Prior to the discussion of the specific objectives of the Task 3 efforts, background information on the effect of cyclic and dynamic load histories on strength and toughness of nuclear piping steels and analysis methodologies is given.

1.1 Background on Cyclic and Dynamic Loading Effects on Ductile Fracture Resistance

This background section briefly describes:

- the physical aspects associated with of cyclic loading effects during ductile tearing,
- basic analysis approaches that can be used to account for cyclic tearing in predicting pipe fracture behavior,
- early specimen cyclic tearing evaluation results, and
- summary of the relevant results from the IPIRG-1 program.

This background information provides the basis of the specific objectives undertaken in this task.

Seismic events are cyclic and dynamic in nature, yet typically quasi-static monotonically loaded specimen tests are used to determine the fracture toughness. The cyclic and dynamic loads are not considered in current LBB and in-service flaw evaluation procedures. The possible cyclic tearing in a seismic event could be viewed as either low-cycle fatigue or interrupted ductile tearing. Either way, the crack growth mechanism for both fatigue and ductile tearing is by ductile dimple rupture. The cyclic aspects are much more difficult to deal with, and hence they are discussed more than the dynamic effects.

1.1.1 Physics of Cyclic Loading Effects During Ductile Tearing

For cracked structures, the stresses and strains ahead of the crack tip control the mode of failure. For a ductile material, a plastic zone is formed around the crack tip. In some smaller region close to the crack tip, there is a tensile fracture process zone where voids nucleate and grow together. As the crack advances, the plastic zone advances with the crack. When unloading or reverse loading occurs, the stresses and strains at the crack tip are altered. A compressive plasticity zone or damage zone within the original tensile plastic zone is formed. This compressive damage zone is greatest at the crack tip and decays with distance from the crack tip. The damage that occurs dictates the amount of ductile tearing resistance immediately ahead of the crack. Hence, the magnitude of the compressive loading, expressed as the minimum/maximum load ratio (or R-ratio), is one key parameter in evaluating cyclic load effects.

Another parameter that may affect the fracture resistance under cyclic loading is the magnitude of cyclic crack growth. With large amounts of crack growth after a compressive load cycle, the crack would eventually grow out of the damaged region back into virgin material. If the crack growth is small for each cycle, the crack is always growing in highly damaged material. Additionally, the cyclic damage might accumulate differently for a stationary crack than a growing crack. In the IPIRG-1 program, a normalized cyclic plastic displacement increment parameter (the cyclic plastic displacement/displacement to reach crack initiation in monotonic loading) was introduced to investigate the effects of cyclic loading prior to crack growth. Hence, the effect of the cyclic loading on the apparent fracture resistance would depend on the magnitude of the compressive loading, the cyclic plastic displacement prior to crack growth, and how far the crack grows after each cycle of loading.

1.1.2 Basic Analysis Approaches to Account for Cyclic Tearing

Although detailed finite element analyses could be used, such analysis procedures would be computationally too intensive for practical applications. Reference 1.1 gives an example of such an effort. Time and cost constraints dictate that simpler analyses or estimation methods be used. Nevertheless, such relatively simple methods should be validated by more detailed analyses or experimental data.

Two different simple mechanics approaches could be used to predict the effect of cyclic loading during ductile tearing on the load-carrying capacity of cracked pipes. The first one is from the low-cycle fatigue crack growth viewpoint, while the other is from a modification of the J-R curve to account for load-history effects from cyclic and dynamic loads. Each of these are briefly discussed below. They have their advantages and disadvantages, especially in the manner that they could be applied for piping analyses. However, it should be recognized that current LBB and in-service flaw evaluation procedures do not account for low-cycle fatigue crack growth during a seismic event. They typically use the peak dynamic load in an elastic-plastic fracture mechanic analysis with quasi-static monotonic material properties.

1.1.2.1 The Dowling Low Cycle Fatigue Analysis Methodology

The classic analysis of cyclic crack growth involves the use of the linear-elastic stress-intensity factor, K_e. In the presence of plasticity at the crack tip, Dowling (Ref. 1.2) used the J-integral parameter. The cyclic J, ΔJ, is calculated by integrating the load-displacement test record on a cycle by cycle basis, see Figure 1.1.

Such an approach can be applied in a generation mode or predictive mode analysis procedure. In a generation mode analysis procedure, one uses experimental data to calculate the ΔJ values. This is done using an η-factor type of analysis (Ref. 1.3). The structural ΔJ values are then compared to high cycle fatigue crack growth da/dN versus ΔJ (or ΔK) data for validation of the general methodology. This was done in Reference 1.4 for a circumferential through-wall-cracked pipe experiment. Figure 1.2 shows the pipe test ΔK values compared with high cycle fatigue data. The good agreement in Figure 1.2 is a

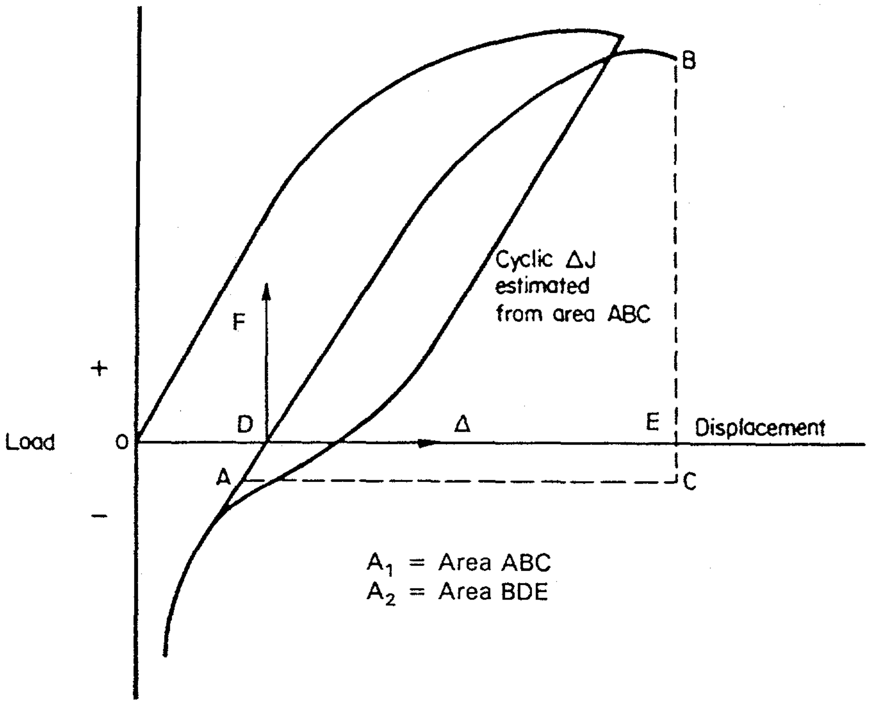

Figure 1.1 Dowling analysis of area used in J calculations for crack growth in the presence of plasticity

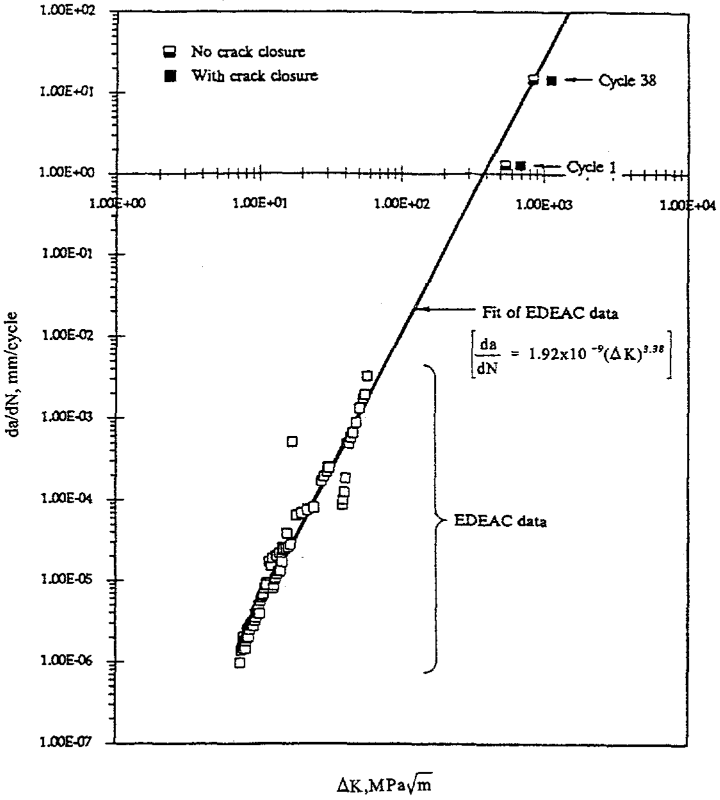

Figure 1.2 Comparison of cyclic crack growth rate from C-pipe experiment to the extrapolation of EDEAC data for TP304 stainless steel at ambient temperature

necessary first step in validating the ΔJ methodology for structural applications, but this procedure by itself is not a predictive methodology.

One of the important features in the Dowling ΔJ methodology is a means to handle reverse loading. With compressive loads, the load-displacement relationship is integrated down to the point where there is crack closure. Fully reversed experimental results on C(T) specimens (Ref. 1.5), and in circumferential through-wall-cracked pipe (Ref. 1.4) have shown that the compressive crack closure load is between 30 to 40 percent of the maximum tensile load. This is helpful information in making predictive analyses.

For predictive analyses, it is important to recognize that the Dowling ΔJ parameter is ***not*** the same as the J_D parameter used in J-estimation schemes when negative loads occur. This is because the Dowling ΔJ is calculated using the compressive crack closure loads which would produce a negative J value in the compressive load region. The Dowling ΔJ is sometimes referred to as an operational J value, i.e., it is a modification of the classical J-integral parameter. Hence, a transformation between the Dowling Operational ΔJ and the J_D parameter needs to be made. Such a methodology was developed in Reference 1.4 for circumferential through-wall-cracked pipe for constant amplitude cyclic load levels. Effectively, this transformation involves the following process: (1) the load-displacement (or moment-rotation) curve for the cracked pipe is calculated using existing J_D-estimation schemes, (2) the absolute value of the area under the load-displacement curve between zero and the closure load is added to the area under the J_D -estimation scheme load-displacement curve, (3) this total area is used with the η-factor method to get the Dowling ΔJ value, and (4) the amount of crack growth is calculated from an extrapolated high cycle fatigue crack growth curve, i.e., see Figure 1.2. The crack length is then increased and Step (1) is performed again for the next cycle. This procedure can get to be a very involved process compared to existing LBB or in-service flaw evaluation procedures. Further simplifying procedures might be needed for practical application.

1.1.2.2 Cyclic J-R Curve Approach

A second approach for evaluating cyclic loading effects is to account for the cyclic effects on the J-R curve of the material. In this manner, the classical J_D-estimation schemes can be used. The disadvantage is knowing how the cyclic loading affects the typical J-R curve developed under quasi-static and monotonic loading. This load history needs to be consistent between the anticipated structural loads and the correction on the monotonic J-R curve. One way to calculate the J-R curve using this approach is to employ the "upper envelope" method. In this method, the J-integral is calculated using an η-factor approach and the upper envelope of the load-displacement record. With this method, the decrease in load-carrying capacity is embedded directly into the J-integral calculations.

1.1.2.3 Advantages and Disadvantages of Detailed FEM, Dowling Operational ΔJ, and Cyclic J-R Curve Methods

Table 1.1 lists some of the main advantages and disadvantages with each method. From this assessment, it was determined that it would be easier to implement the cyclic J-R curve approach for pipe fracture analyses rather than to try to implement the other two methods. The cyclic J-R curve is computationally manageable and it can be integrated into the existing LBB framework with relative ease. Nevertheless, the experimental data were obtained so that the Dowling Operational ΔJ approach could also be evaluated in the future.

Table 1.1 Advantages and disadvantages of several analysis methods for assessing cyclic load effects on load-carrying capacity of cracked pipes

Aspect	**Detailed FEM Analyses**	**Dowling Operational ΔJ Approach**	**Cyclic J-R Curve Approach**
Theoretical validity	Can be assessed by various integral fracture parameters	Empirical modification in compressive load region. Transformation to J_D needed. Application to ΔJ values above J_{Ic} needs verification.	Violates J_D theory. Validation by FEM needed.
Ease of Application	Impractical at this time	Much more complicated than current analysis methods	Consistent with current LBB and in-service flaw evaluation analysis procedures
Material property needs	If a damage mechanism unexplainable by other than continuum mechanics occurs (i.e., void flattening), then load-history specific material property data needed.	Extrapolation of high cycle fatigue crack growth curve. (Fracture toughness not a consideration.)	Trend curve of the effects of cyclic and dynamic loading on J-R curve needed. Similitude from specimen to structural cyclic J-R curves needed to be shown.
Additional requirements	Knowledge of the load history, i.e., global loads and displacements	Knowledge of the load-history , i.e., loads, displacements, and when crack closure occurs.	Knowledge of the load history, i.e., R-ratio, incremental cyclic plastic displacement. These load-history corrections on the toughness may change during the course of a seismic event, so *simplification is required.*
Additional advantages	Can consider each individual cycle in detail		Readily lends itself to dynamic cracked-pipe analysis of the type in Reference 1.6.
More disadvantages	High time and computer costs		

1.1.3 Early Specimen Cyclic Tearing Evaluation

As part of IPIRG-1 Subtask 1.2, a review report entitled the "Effect of Cyclic Loads on Ductile Fracture Resistance" was prepared (Ref. 1.7). The main conclusions from that report are summarized below.

- The effect of cyclic loads on ductile fracture resistance seems to be well documented for tests where the stress ratio ($\sigma_{min}/\sigma_{max}$) is positive. Landes and McCabe (Ref. 1.8) developed a simplistic model to describe the effect. They suggest that a resistance curve from a monotonic test can be shifted to accommodate crack extension from cyclic loading. The cyclic crack extension can be approximated from the material's fatigue-crack-growth characterization. The original idea for this model was based on the assumption that there is no interaction between the monotonic and cyclic components of crack extension. It also does not address any damage done before "initiation" of ductile tearing. If the cyclic component of the crack extension is small, i.e., small unloadings or a few large unloadings, the effect on the fracture resistance is small. The work performed by Clarke, et al. (Ref. 1.9), Kanninen (Ref. 1.10), Sutton (Ref. 1.11), Kaiser (Ref. 1.12), and Joyce (Ref. 1.13) on fracture testing with periodic unloadings to zero load, showed no toughness reductions due to these unloadings.

Tests performed with negative stress ratios, however, have shown fracture degradation that cannot be modeled with simple summation techniques. These findings suggest that damage at the crack tip due to the compressive plasticity is degrading the material's resistance to ductile tearing. Results from Landes and McCabe (Ref. 1.8) and Landes and Liaw (Ref. 1.14) show a significant decrease in toughness for specimens undergoing negative stress ratios. Neither set of authors was successful in bringing the measured crack extension and the calculated extension into agreement when assuming the cyclic loading effects only increased the crack growth due to typical fatigue crack growth analyses.

1.1.4 Summary of the Relevant Results from the IPIRG-1 Program

From the IPIRG-1 program, several efforts were undertaken to determine if cyclic and dynamic loading, typical of seismic load histories, could affect the fracture behavior of cracked pipe. The following conclusions were drawn from the IPIRG-1 program results:

- For pipes with cracks in base metal, monotonic dynamic loading:
    - marginally increased the load-carrying capacity of the *austenitic* steel pipes, and
    - decreased the load-carrying capacity of the *ferritic* steel pipes (Ref. 1.15).

- For cracks in base metals, reversed cyclic loading lowered the apparent fracture toughness of both ferritic and austenitic steel pipes (Ref. 1.15).

- For cracks in weld metals, combined cyclic and dynamic loading:
    - had a negligible detrimental effect on the load-carrying capacity of a pipe with a crack in a low toughness *austenitic* weld, and
    - increased the load-carrying capacity of a pipe with a crack in a low toughness *ferritic* weld (Ref. 1.16).

Because of these observations, it was considered important to determine if the effects observed in the pipe experiments are present in small-scale specimens and whether these pipe test results could be predicted using laboratory-scale specimen results. Task 3 of the IPIRG-2 program was, therefore, undertaken specifically to study the effects of cyclic and dynamic loading histories on the fracture behavior of nuclear piping steels.

1.2 Specific Objectives of IPIRG-2 Task 3 Efforts

The general objective of Task 3 was to investigate the effect of cyclic and dynamic loading on the fracture behavior of nuclear piping. This was accomplished by first examining cyclic loading effects, and then examining dynamic loading effects. Seismic events would involve both cyclic and dynamic loading histories on the material, whereas events like water hammer or pressure relief blowdown loads might involve only dynamic loading history effects on the material properties.

The following steps were followed to investigate the effects of cyclic loading on toughness and cracked-pipe load-carrying capacity:

- The main experimental effort was to develop small-scale cyclically loaded laboratory-specimen fracture toughness data that could be used in a direct comparison with the through-wall-cracked (TWC) pipe fracture data developed in Subtask 1.2 of the IPIRG-1 program. In the IPIRG-1 program, reverse cyclic loading was found to lower the apparent toughness and hence, the load-carrying capacity of through-wall-cracked pipe. Sensitivity studies in the IPIRG-1 program using the cyclic J-R curves from these pipe experiments suggested that for larger diameter pipe under similar cyclic loading, the fracture resistance would be reduced more than for the 6-inch diameter pipe experiments. Therefore, it was important to determine if these effects are present in small-scale specimens and whether these specimens could be used to reasonably predict larger pipe behavior. To accomplish this, a series of cyclic-load C(T) specimen tests were conducted on various materials.

- The specimen tests with cyclic loading were conducted at more R-ratios (minimum/maximum cyclic loads) than the past IPIRG-1 pipe experiments. From trends observed in the C(T) tests, it was subsequently decided to conduct a pipe experiment at an intermediate R-ratio for one specific material.

- To assess the similitude of the C(T) specimens and the pipe experiments, the J-integral parameter was calculated for each experiment and compared to J-values calculated from the TWC pipe experiments.

- A more fundamental investigation involved an assessment of fracture toughness analyses under cyclic loading. In order to verify the procedure for calculating J from a C(T) specimen, and to determine whether the load-displacement response can be predicted, FEM studies were conducted on selected stainless steel C(T) specimens subjected to cyclic loading.

- Using the J-R curves calculated from the cyclic-load C(T) specimens, full-scale pipe moment predictions were made in an attempt to determine whether it is necessary to use cyclic material properties to predict the past IPIRG-1 TWC pipe response.

- A series of sensitivity studies was conducted to predict the effect of cyclic loads on larger diameter pipes.

Another objective of Task 3 was to expand the current database of dynamically-loaded carbon steel toughness and strengths. In the IPIRG-1 program, carbon steels were shown to be strain-rate sensitive. The material's susceptibility to dynamic strain aging (Ref. 1.16) dictates its strain-rate sensitivity. The results in Reference 1.16 showed that for common U.S. carbon steel pipe grades, all were affected by dynamic strain aging at LWR temperatures. In the IPIRG-1 program, it was noticed that the three carbon steels tested responded differently to changes in the displacement rate. A 16-inch diameter A106 Grade B pipe (DP2-F29) showed the greatest loss of toughness and strength at higher loading rates. A 6-inch-diameter A106 Grade B pipe (DP2-F30) showed only moderate loss in toughness, but a significant loss in strength at higher displacement rates. Finally, a carbon steel SAW (DP2-F29W) showed a loss of strength, but an increase in toughness at higher loading rates. Investigations of dynamic strain aging on numerous carbon steels was conducted in the NRC's Short Cracks in Piping and Piping Welds program (Ref. 1.16), but that study did not address the effects of dynamic loading. The investigations in this effort involved the following:

- A series of tensile and C(T) specimens were tested at monotonic dynamic loading rates believed to be typical of seismic loading. This was done for a variety of carbon steel pipe materials to expand the IPIRG-1 nuclear pipe dynamic strength and toughness database.

- As part of a parallel effort for Japanese IPIRG-2 program members, Ref. 1.17, it was found that a specific Japanese carbon steel pipe had the unusual characteristics of having the same toughness in static and monotonic dynamic loading in C(T) tests, but the dynamic stress-strain curve was lower than the quasi-static stress-strain curve. The lowering of the stress-strain curve is typical of dynamic strain aging effects. A key technical issue in predicting pipe fracture behavior under dynamic loading is not only what toughness to use, but what stress-strain curve should be used in the analyses. Consequently, a quasi-static pipe experiment was conducted for relative comparison with an existing Japanese monotonic dynamic pipe experiment.

- TWC pipe predictions and sensitivity studies were conducted to determine what material properties should be used for accurate moment predictions, and to predict how dynamic loading affects larger diameter pipes.

1.3 Structure of Report

Including this introduction, this report is divided into five main sections. Section 2.0 contains details pertaining to the cyclic-load C(T) experiments. This section describes the experimental procedures, the experimental results, the detailed J-R calculation using the ASTM E813/1152 procedure, and the detailed finite element analyses of a cyclic C(T) experiment. The dynamic testing efforts are described in Section

3.0. This section contains a description of the procedure and results for the dynamically tested carbon steel tensile and C(T) specimens. A comparison of the cyclic J-R curves from the C(T) experiments to the cyclic J-R curves from the 6-inch nominal diameter TWC pipe experiments is given in Section 4.0. This section also contains a series of moment predictions aimed at determining if the cyclic J-R curves can be used to predict cyclic TWC pipe response. Also, a series of dynamic moment predictions are discussed in Section 4.0 which are aimed at determining which material properties should be used in making dynamic moment predictions. Finally, a summary of the technical results from this report is given in Section 5.0

1.4 References

1.1 Brust, F. W., McGowan, J. J., and Atluri, S. N., "A Combined Numerical/Experimental Study of Ductile Crack Growth After a Large Unloading Using T*, J, and CTOA Criteria," *Engineering Fracture Mechanics*, Vol. 22, No. 6, pp 1079-1103, 1985.

1.2 Dowling, N. E., and Begley, J. A., "Fatigue Crack Growth during Gross Plasticity and the J-Integral", *Mechanics of Crack Growth*, ASTM STP 590, pp 82-103, 1976.

1.3 Paris, P. C., Ernst, H., and Turner, C. E., "A J-integral Approach to the Development of η-Factors," ASTM STP700, pp 338-351, 1980.

1.4 Wilkowski, G., Rahman, S., and Mohan, R., "Low-Cycle Fatigue Crack Growth Considerations in Pipe Fracture Analyses," ASME PVP Vol. 280, pp 281-298, June 1994.

1.5 Joyce, J. A. and Hackett, E. M., "Elastic-Plastic Characterization of a Cast Stainless Steel Pipe Elbow Material," NUREG/CR-5774, January 1992.

1.6 Olson, R., Wolterman, R., Scott, P., Krishnaswamy, P., and Wilkowski, G., "The Next Generation Methodology for Cracked Pipe System Subjected to Dynamic Loads," ASME PVP Vol. 275-1, pp 159-172, June 1994.

1.7 Marschall, C. W. and Wilkowski, G. M., "Effect of Cyclic Loads on Ductile Fracture Resistance," in ASME Special Technical Publication, Vol. 166, pp 1-14, July 1989.

1.8 Landes, J. D., and McCabe, D. E., "Load History Effects on the J_R-Curve," *Elastic Plastic Fracture: Second Symposium, Volume II-Fracture Resistance Curves and Engineering Applications,* ASTM STP 803, C. F. Shih and J. P. Gudas, Eds., American Society for Testing and Materials, pp II723-II738, 1983.

1.9 Clarke, G. A., Andrews, W. R., Paris, P. C., and Schmidt D. W., "Single Specimen Tests for J_{Ic} Determination," *Mechanics of Crack Growth,* ASTM STP 590, American Society for Testing and Materials, pp 27-42, 1976.

1.10 Kanninen, M. F., Zahoor, A., Wilkowski, G., Abou-Sayed, I., Marschall, C., Broek, D., Sampath, S., Rhee, H., and Ahmad, J., "Instability Predictions for Circumferentially Cracked Type 304 Stainless Steel Pipes Under Dynamic Loading," EPRI Report NP-2347, April 1982.

1.11 Sutton, G. E., and Vassilaros, M. G., "Study of the Effect of Elastic Unloadings on the J-R Curves from Compact Specimens," David W. Taylor Naval Ship R & D Center, NUREG/CR-4283, June 1985.

1.12 Kaiser, S., "On the Relation Between Stable Crack Growth and Fatigue," *Fatigue of Engineering Materials and Structures,* Vol. 6, No. 1, pp 33-49, 1983.

1.13 Joyce, J. A., "Development of a Criterion for the Effect on the J-R Curve of Elastic Unloadings," *Fracture Mechanics: Eighteenth Symposium, ASTM STP 945,* D. T. Read and R. P. Read, Eds., American Society for Testing and Materials, pp 647-662, 1988.

1.14 Landes, J. D., and Liaw, P. K., "Effect of Cyclic Loading on Fracture Toughness of a Modified 4340 Steel," *Effect of Load and Thermal Histories on Mechanical Behavior of Materials,* P. K. Liaw and T. Nicholas, Eds., a publication of the Metallurgical Society, Inc., 1987.

1.15 Wilkowski, G., Kramer, G., Vieth, P., Francini, R., and Scott, P., "The Effect of Cyclic Loading During Ductile Tearing on Circumferentially Cracked Pipe -- Analytical Results," ASME PVP Vol. 280, pp 221-240, June 1994.

1.16 Scott, P., Olson, R., and Wilkowski, G., "The IPIRG-1 Pipe System Fracture Tests -- Analytical Results," ASME PVP Vol. 280, pp 153-165, June 1994.

1.17 Marschall, C. W., Mohan, R., Krishnaswamy, P., and Wilkowski, G. M., "Effect of Dynamic Strain Aging on the Strength and Toughness of Nuclear Ferritic Piping at LWR Temperatures," NUREG/CR-6226, October 1994.

1.18 Rudland, D. L., Scott, P. M., and Wilkowski, G. M., "The Effect of Cyclic and Dynamic Loads on Carbon Steel Pipe," NUREG/CR-6438, February 1996.

2.0 CYCLIC-LOAD C(T) SPECIMEN TESTING AND ANALYSIS PROCEDURE

2.1 Cyclic-Load C(T) Experiments

This section of the report addresses the material selection, the cyclic loading experiments, and discusses the effect of stress ratio and plastic displacement increment on the experimental results.

2.1.1 Material Selection

2.1.1.1 Base Metal

In order to compare the behavior of cyclic-loaded C(T) specimens with that of cyclic-loaded TWC pipe tested in the IPIRG-1 program, the base metal materials selected for the C(T) specimens were the same as those used in the pipe tests, namely, a nominal 6-inch diameter Schedule 120 TP304 stainless steel pipe and a nominal 6-inch diameter Schedule 120 A106 Grade B carbon steel pipe. These pipes have the Battelle designations DP2-A23 (stainless steel) and DP2-F30 (carbon steel), respectively, and both were procured in the Degraded Piping Program (Ref. 2.1). Pipe DP2-A23 came from a canceled nuclear power plant, and Pipe DP2-F30 was purchased from a pipe supply warehouse. Both of these pipe materials were tested extensively in the Degraded Piping and the IPIRG-1 programs.

2.1.1.2 Weld Metal

In addition to the base metal specimens, a series of cyclic-loaded weld-metal specimens was tested. The welds chosen for this study were carbon steel and stainless steel submerged-arc welds that had been characterized in the IPIRG-1 program and in this program. The stainless steel SAW joined two section of TP304 stainless steel 16-inch nominal diameter pipe. The Battelle designation for the pipe was DP2-A8, while the weld was given a designation DP2-A8W. This was an SAW procedure obtained from General Electric. The portion of the weld used for material property evaluation was given the designation A8W4.

The carbon steel SAW was made specifically for this task with a weld procedure identical to that used for the IPIRG-1 and IPIRG-2 (DP2-F29W) pipe weld specimens. This was a Babcock and Wilcox C-Mn-Mo-Ni submerged-arc weld procedure. This carbon steel SAW joined two sections of 25.4-mm (1-inch)-thick A106 Grade B carbon steel plate. The plate has the designation DP2-F40, while the weld is designated DP2-F40W.

2.1.2 Previous Material Characterization

2.1.2.1 Base Metal

The DP2-A23 pipe or other pipes from the same heat were used in the circumferential cracked-pipe experiments at 288 C (550 F) in the Degraded Piping and IPIRG-1 programs shown in Table 2.1.

Table 2.1 Circumferential cracked pipe experiments using Pipe DP2-A23

Experiment No.	Program	Crack Type	Loading
4131-5	Degraded Piping	Through-wall	Four-point bending
4121-1	Degraded Piping	Through-wall	Pressure to failure
4131-1	Degraded Piping	Through-wall	Pressure and four-point bending
4121-3	Degraded Piping	Surface	Four-point bending
4112-3	Degraded Piping	Surface	Pressure to failure
4115-8	Degraded Piping	Surface	Compliant four-point bending
4115-9	Degraded Piping	Surface	Compliant four-point bending
4131-6	Degraded Piping	Surface	Compliant four-point bending
4131-2	Degraded Piping	Surface	Pressure and four-point bending
4113-1	Degraded Piping	Complex	Four-point bending
4113-2	Degraded Piping	Complex	Four-point bending
4114-2	Degraded Piping	Complex	Compliant four-point bending
1.2-3	IPIRG-1	Through-wall	QS Cyc four-point bending $R = 0$
1.2-5	IPIRG-1	Through-wall	QS Cyc four-point bending $R = -1$
1.2-1	IPIRG-1	Through-wall	Dyn four-point bending
1.2-9	IPIRG-1	Through-wall	Dyn Cyc four-point bending $R = -1$

The DP2-F30 pipe, or another pipe from the same heat, was used in the circumferential cracked pipe experiments at 288 C (550 F) in the Degraded Piping and IPIRG-1 programs shown in Table 2.2

Table 2.2 Circumferential cracked pipe experiments using Pipe DP2-F30

Experiment No.	Program	Crack Type	Loading
4112-6	Degraded Piping	Surface	Four-point bending
4113-5	Degraded Piping	Complex	Four-point bending
4113-6	Degraded Piping	Complex	Four-point bending
4114-1	Degraded Piping	Complex	Compliant four-point bending
1.2-7	IPIRG-1	Through-wall	QS four-point bending
1.2-2	IPIRG-1	Through-wall	QS Cyc four-point bending $R = 0$
1.2-4	IPIRG-1	Through-wall	QS Cyc four-point bending $R = -1$
1.2-8	IPIRG-1	Through-wall	Dyn four-point bending
1.2-12	IPIRG-1	Through-wall	Dyn four-point bending
1.2-11	IPIRG-1	Through-wall	Dyn four-point bending
1.2-10	IPIRG-1	Through-wall	Dyn Cyc four-point bending $R = 0$
1.2-6	IPIRG-1	Through-wall	Dyn Cyc four-point bending $R = -1$

During the course of the Degraded Piping and IPIRG-1 programs, these materials were extensively characterized. Figures 2.1 and 2.2 show stress-strain curves for the DP2-A23 and DP2-F30 materials, respectively, at several different strain rates. It can been seen from these figures that the stainless steel has a lower ultimate strength than the carbon steel and shows less rate sensitivity at 288 C (550 F) than does the carbon steel.

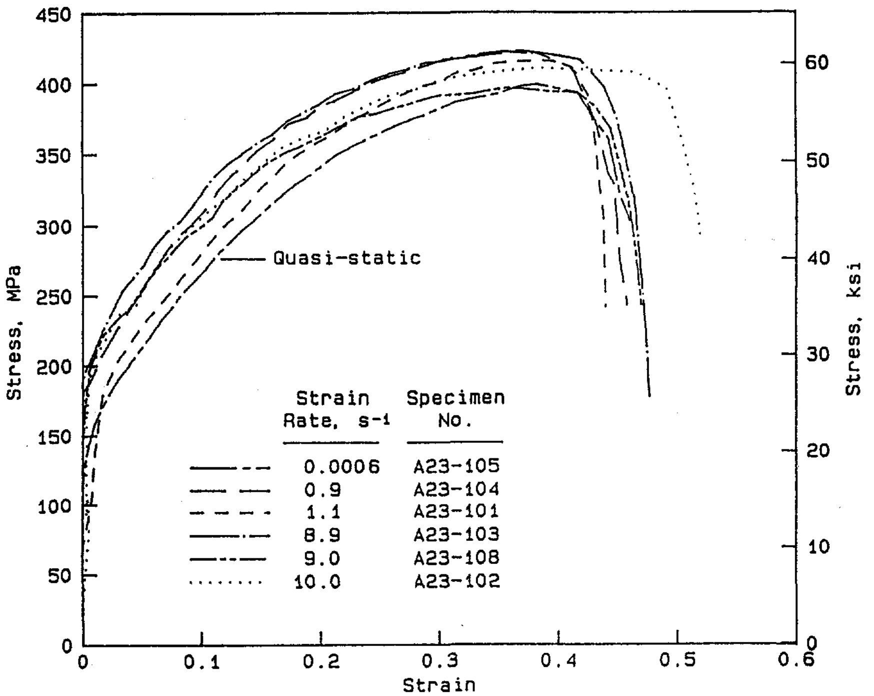

Figure 2.1 Engineering stress-strain curves at 288 C (550 F) for Pipe DP2-A23 (A376 Type 304 stainless steel) tested at several different strain rates

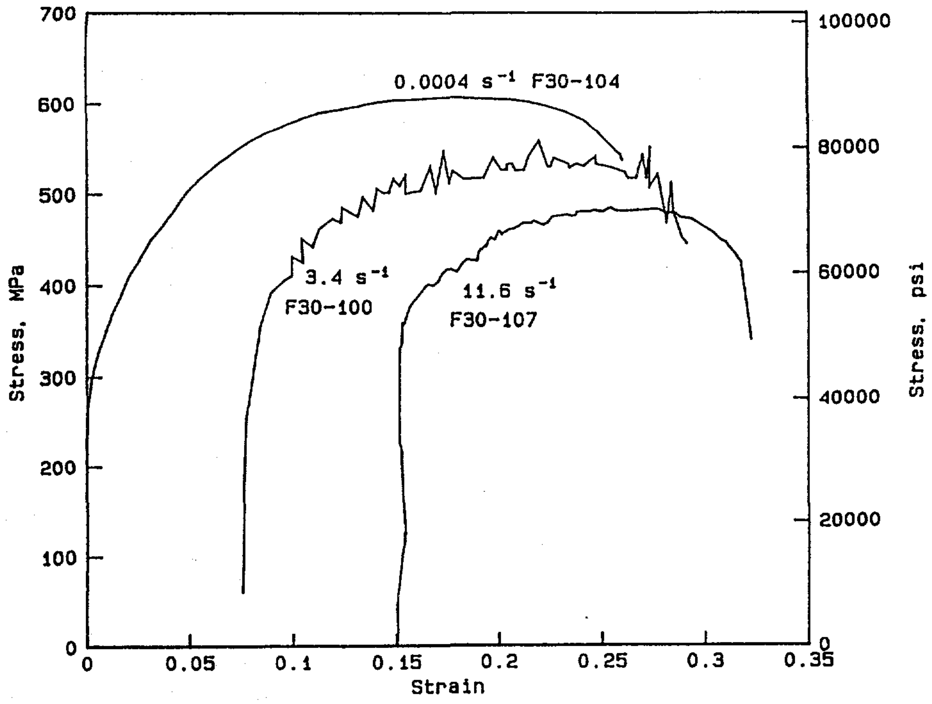

Figure 2.2 Engineering stress-strain curves at 288 C (550 F) for Pipe DP2-F30 (A106 Grade B carbon steel) tested at several different strain rates

Figures 2.3 and 2.4 show J-resistance curves for these materials at two different rates of loading at 288 C (550 F). From these figures, the stainless steel shows only a slight effect of loading rate, while the carbon steel shows a more pronounced effect. Also, crack instabilities were noted in the carbon steel fracture tests, which could be due to dynamic strain aging (DSA) in that material (see Section 3.0). Full details on the characterization of these materials can be found in Reference 2.2.

2.1.2.2 Weld Metal

The DP2-A8W weld was tested in the following circumferential cracked pipe experiments at 288 C (550 F) in the Degraded Piping, IPIRG-1, and IPIRG-2 programs shown in Table 2.3.

Table 2.3 Circumferential cracked pipe experiments with DP2-A8W pipe weld

Experiment No.	Program	Crack Type	Loading
4141-3	Degraded Piping	Through-wall	Four-point bending
4141-4	Degraded Piping	Surface crack	Four-point bending and pressure
4141-6	Degraded Piping	Surface crack	Four-point bending and pressure
1.3-5	IPIRG-1	Surface crack	Single frequency
1-6	IPIRG-2	Short surface crack	Four-point bending
1-5	IPIRG-2	Short surface crack	Single frequency

The carbon steel SAW procedure (DP2-F29W) was used in the following experiments at 288 C (550 F) in the Degraded Piping, IPIRG-1, and IPIRG-2 programs shown in Table 2.4.

Table 2.4 Circumferential cracked pipe experiments with DP2-F29W1 pipe weld

Experiment No.	Program	Crack Type	Loading
4141-9	Degraded Piping	Through-wall	Four-point bending and pressure
4141-8	Degraded Piping	Surface crack	Four-point bending and pressure
1.3-4	IPIRG-1	Surface crack	Single frequency
1-4	IPIRG-2	Surface crack in elbow girth weld	Four-point bending
1-3	IPIRG-2	Surface crack in elbow girth weld	Single frequency

Figures 2.5 and 2.6 show stress-strain curves for the stainless steel SAW (DP2-A8W4) and the carbon steel SAW (DP2-F29W1), respectively, at several different strain rates. The stainless steel SAW shows a slight increase in yield strength, but no significant change in the ultimate strength with increasing strain rate. The carbon steel SAW shows a decrease in both the yield and ultimate strength with increasing strain rate. The response to increasing strain rate in these SAWs is very similar to the response in the base metals.

Figures 2.7 and 2.8 show J-resistance curves for these weld materials at two different rates of loading at 288 C (550 F). These figures show the fracture resistance of both the stainless and carbon steel SAW increase with increasing load rate. This result is different than the result for the base metals, whose

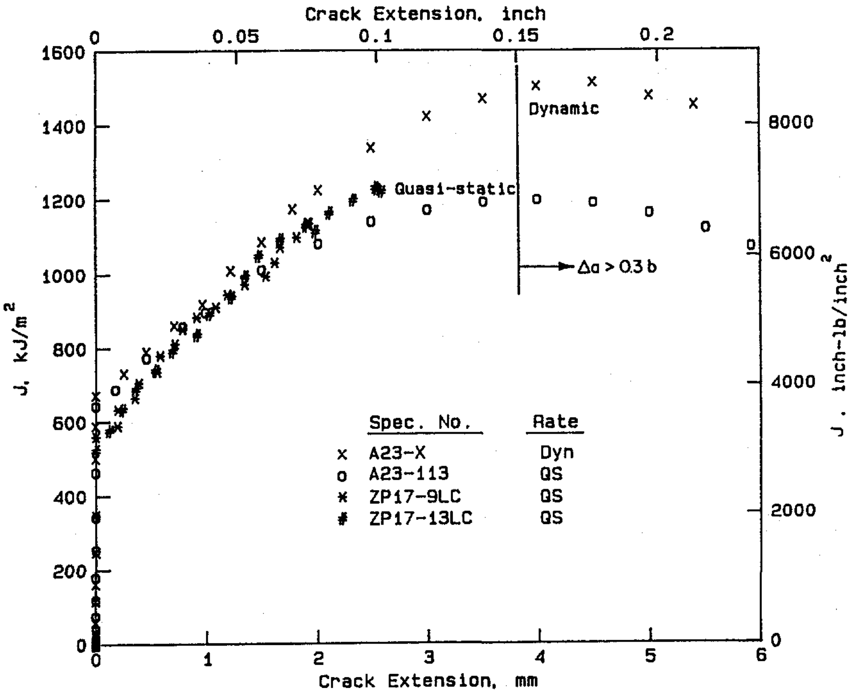

Figure 2.3 J-resistance curves for compact specimens from Pipe DP2-A23 (Type 304 stainless steel) tested at 288 C (550 F) in L-C orientation

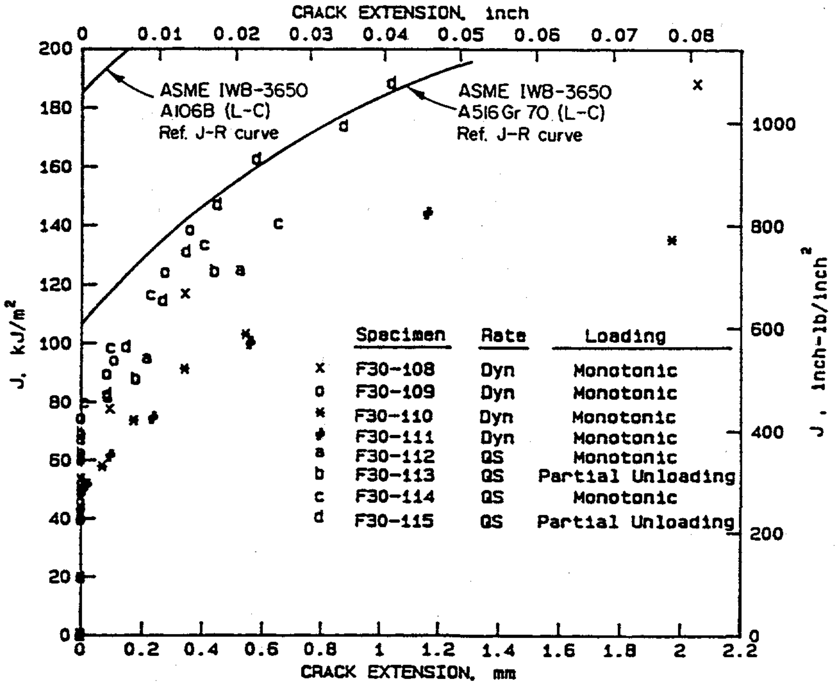

Figure 2.4 J-resistance curves for compact specimens, up to the point of the first large crack instability, from Pipe DP2-F30 (A106 Grade B carbon steel) tested at 288 C (550 F) in L-C orientation

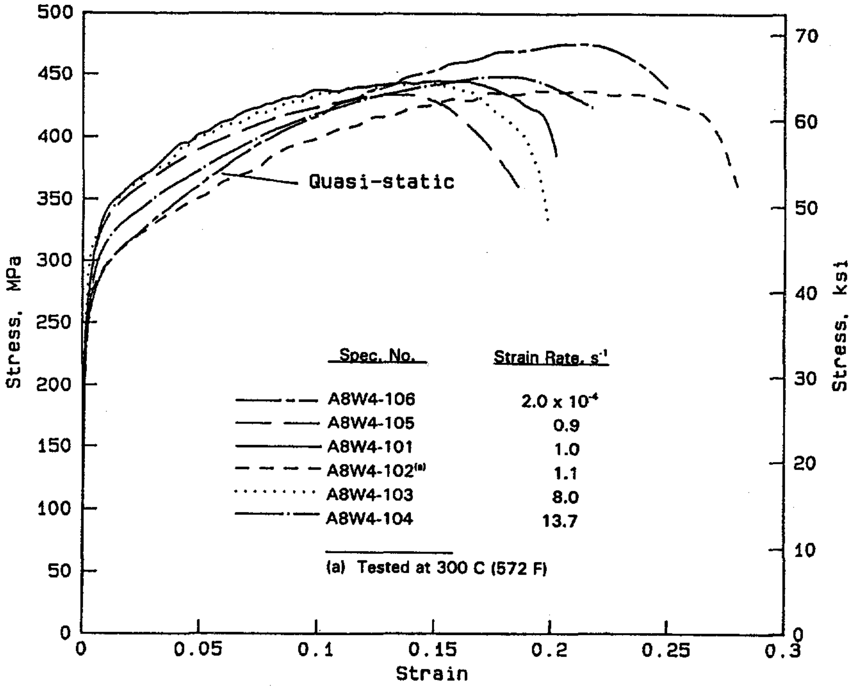

Figure 2.5 Engineering stress-strain curves at 288 C (550 F) for a submerged-arc weld (DP2-A8W4) in Type 304 stainless steel, tested at several different strain rates

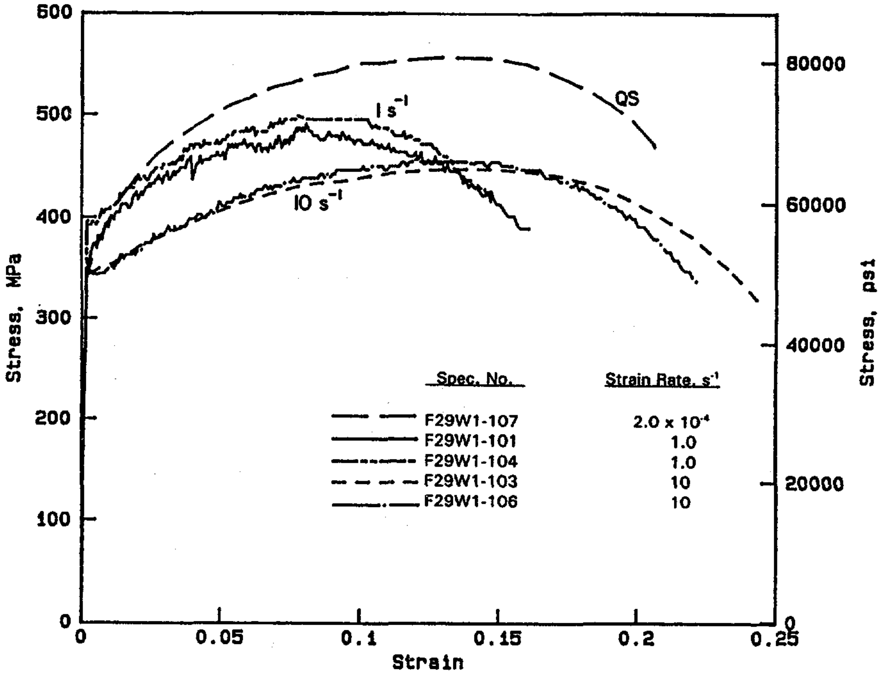

Figure 2.6 Engineering stress-strain curves at 288 C (550 F) for a submerged-arc weld (DP2-F29W1) in an A106 Grade B carbon steel pipe, tested at several different strain rates

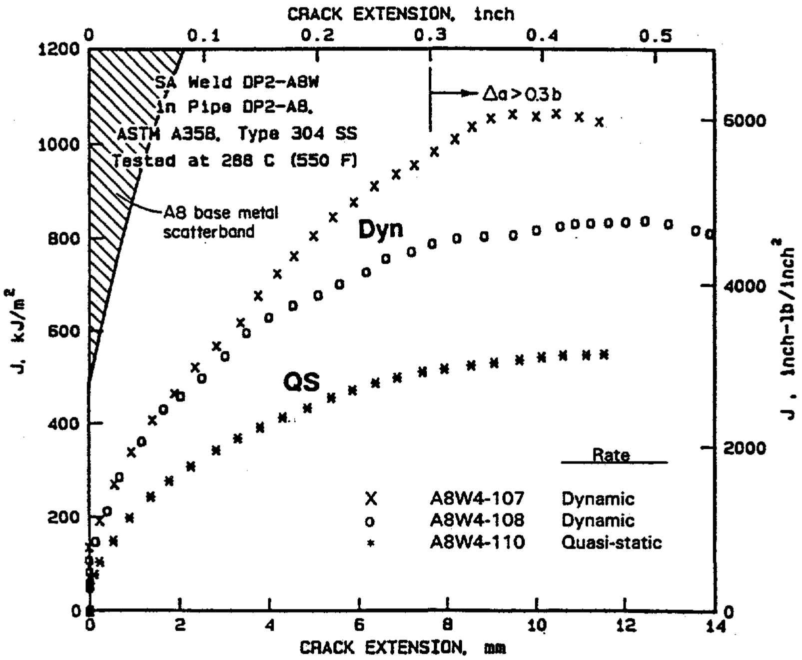

Figure 2.7 J-resistance curves at 288 C (550 F) for compact specimens from a submerged-arc weld (DP2-A8W4) in a Type 304 stainless steel pipe

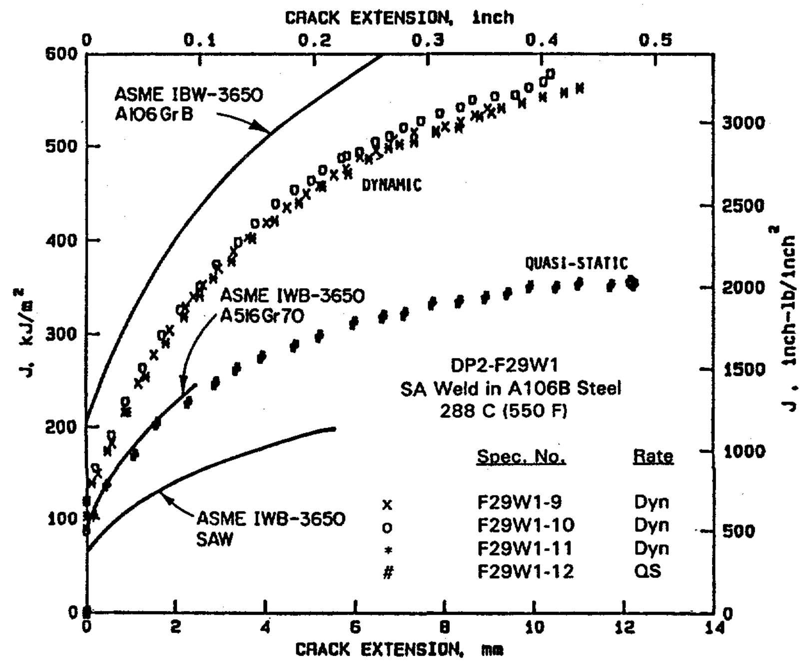

Figure 2.8 J-resistance curves for compact specimens from a submerged-arc weld (DP2-F29W1) in A106 Grade B carbon steel pipes tested at 288 C (550 F)

fracture resistance decreased with increasing loading rate. Full details on the characterization of these materials can be found in Reference 2.2.

2.1.3 Description of Experimental Procedure

The C(T) specimens that were machined from pipe were fabricated without flattening the pipe and were in the L-C orientation, i.e., loads were applied in the direction of the pipe axis and the crack growth direction was circumferential. The C(T) specimens that were machined from a plate weld were machined in the L-T orientation; that is, the longitudinal direction was the loading direction while the width direction (along the length of the weld) was the crack growth direction. The base metal specimens and the carbon steel weld specimens were of the 0.5T C(T) size, while the stainless steel weld specimens were of the 1T C(T) size. The carbon steel base metal specimens and the stainless steel weld specimens were about 80 percent of the standard thickness because of the smaller wall thickness of those particular pipes.

The specimens were fatigue precracked according to the specification in ASTM E1152-87, Standard Test Method for Determining J-R Curves, to produce an initial crack length of 0.52w to 0.57w, where w is the specimen width. The base metal C(T) specimens were not sidegrooved in order to better simulate the crack growth behavior of a TWC pipe. The weld specimens were sidegrooved to a depth of 10 percent per side in order to match previous material characterizations.

2.1.3.1 Test Facility and Specimen Preparation

In order to eliminate dynamic-loading effects and isolate the effect of cyclic loads on fracture resistance, most of the cyclic-load tests were conducted using quasi-static loading rates. However, in addition, dynamic, cyclic tests were conducted on the weld specimens in order to investigate the combined cyclic/dynamic effect on these weld metals. The rate chosen for the quasi-static cyclic tests is the same as for a monotonic test where the time to crack initiation is about 10 minutes. For the dynamic, cyclic tests, the rate was similar to a typical pipe system test, approximately 4 Hz. All specimens were tested in a 90 kN (20,000 lb) servohydraulic test system.

Direct-current electric potential (d-c EP) was used to monitor crack growth during these tests. This method of crack initiation detection and crack growth measurement has been used successfully in both the IPIRG-1 and Degraded Piping Programs (Refs. 2.1 and 2.2). The load cell in the servo-hydraulic test machine was electrically isolated to prevent a current path through the load train. The potential leads were iron wires in the case of the carbon steel and stainless steel wires in the case of the stainless steel specimens in order to reduce thermally induced voltages that can arise from dissimilar materials in contact. As shown in Figure 2.9, the potential leads were placed at locations C and D in order to detect an average crack front in those specimens where the crack front might not be straight. For the quasi-static tests, the direct-current magnitude was adjusted to give a potential of about 400 μV at the start of the tests. The tests continued until a 400 μV shift in the electric potential was observed. For the dynamic tests, the direct-current magnitude was adjusted to give a potential of approximately 4,000 μV at the start of the tests, to minimize the effect of an electric-potential pulse arising from a piezoelectric effect, seen in carbon steel materials at the onset of rapid loading (Ref. 2.2).

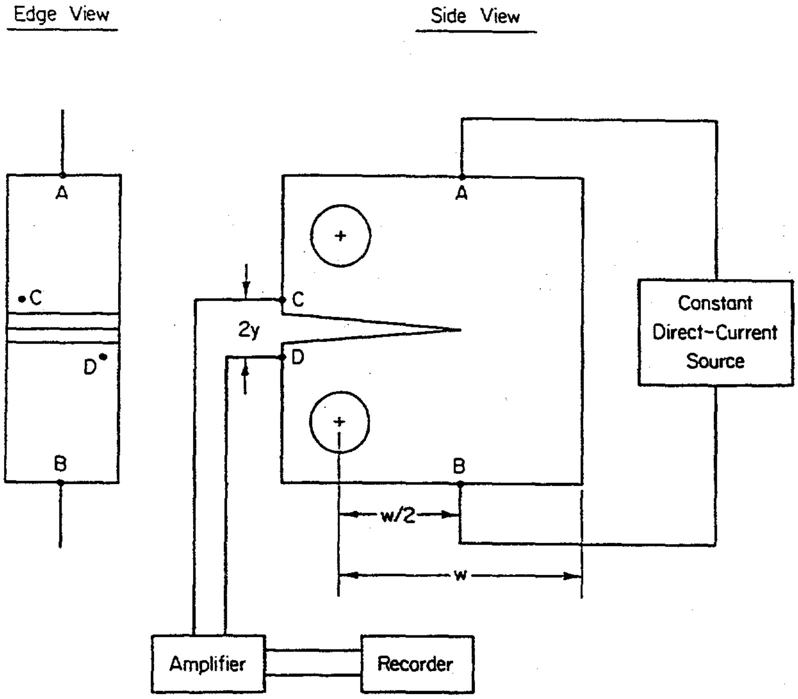

Figure 2.9 Schematic illustration of d-c EP method employed at Battelle to monitor crack growth in C(T) tests

An onset strain-gaged high temperature clip gage was used to measure load-line displacements. The clip gage attached to the specimens by seating on razor blades welded directly to the specimen load-line. (This clip gage was calibrated with a linear range up to 20 mm [0.8 inch].)

The data recorded during these tests included load, ram displacement, load-line displacement, and d-c EP. All data were taken with LABTECH® NOTEBOOK software in conjunction with a Metrabyte DAS-20 card. A standard X-Y plotter and a linear strip chart recorder were used as backup.

2.1.3.2 Description of Cyclic-Load Tests and Additional Tests

Table 2.5 shows the test matrix for the cyclic-loaded C(T) specimens. In this test matrix, δ_{cyc}/δ_i is the plastic load-line displacement increment of each cycle. δ_{cyc} is the displacement per cycle and δ_i is the load-line displacement at crack initiation in a monotonic test. These values were chosen to match those in the TWC cyclic-load pipe experiments conducted as part of the IPIRG-1 program (Ref. 2.3). All of the base metal specimens were run at quasi-static loading rates (approximately 10 min. to crack initiation). Half of the weld specimens were run with quasi-static rates and half were run at dynamic rates. For the dynamic experiments, the rate was chosen to be 4 Hz. Since these tests are increasing amplitude tests at a constant ramp rate, an average of 4 Hz was used.

In order to conduct experiments that required cyclic loading, a computer was used for real-time control of the experiments. Since these tests were conducted in displacement control at a constant ramp rate, and cyclic loading is a function of stress ratio, real-time control was necessary to regulate the loading in displacement control and to evaluate the load during unloading to achieve a desired stress ratio. A

Table 2.5 Cyclic-load C(T) test matrix

Material	Loading rate	δ_{cyc}/δ_i	Stress Ratio	Specimen Identification
TP304 DP2-A23	Quasi-static	n/a	1	A23-2c
		0.1	0	A23-4c, A23-21c
			-0.3	A23-13c
			-0.6	A23-14c
			-0.8	A23-17c
			-1	A23-5c, A23-20c
		0.2	0	A23-6c
			-0.6	A23-16c
			-0.8	A23-18c
			-1	A23-7c
		0.025	0	A23-11c, A23-22c
			-0.6	A23-15c
			-0.8	A23-19c
			-1	A23-12c
A106B DP2-F30	Quasi-static	n/a	1	F30-1c
		0.1	0	F30-2c, F30-7c
			-0.3	F30-12c
			-0.6	F30-4c
			-0.8	F30-5c
			-1	F30-3c, F30-6c
TP304 SAW DP2-A8W4	Quasi-static	0.1	-0.6	A8W4-103c, A8W4-104c
			-1	A8W4-101c, A8W4-102c
	Dynamic (4 Hz)	0.1	-0.6	A8W4-108c
			-1	A8W4-106c, A8W4-107c
A106 B SAW DP2-F40W	Quasi-static	n/a	1	F40W-1c
		0.1	-0.6	F40W-7c
			-1	F40W-5c, F40W-8c
	Dynamic (4 Hz)	n/a	1	F40W-4c
		0.1	-0.6	F40W-12c, F40W-13c
			-1	F40W-10c, F40W-11c

computer code written in BASIC was used to achieve this real-time control. The program used in these experiments was identical to the control program used in the IPIRG-1 program. This BASIC program performs the cyclic loading by loading the specimen to a prescribed displacement in tension, recording the peak load, and then reversing the test-machine crosshead until the compressive load is equal to the previous peak load value multiplied by the stress ratio. These loading/unloading cycles were continued throughout the experiment.

In addition to the test matrix shown in Table 2.5, a series of additional tests was run in order to metallographically inspect the damage caused by fully reversed loading. Three additional tests were performed on both the carbon steel and stainless steel base materials. Figure 2.10 shows a schematic loading path for these additional specimens. The first specimen (A) was loaded to a displacement just beyond crack initiation and unloaded to zero load. The second specimen (B) was loaded to a displacement just past crack initiation, the load recorded, reverse loaded to a negative load equal to the recorded tensile load, and unloaded to zero load. The third specimen (C) was loaded to a displacement just past crack initiation, the load recorded, reverse loaded to a negative load equal to the recorded tensile load, reloaded in tension to a displacement equal to 110 percent of the crack initiation displacement, and unloaded to zero load. These specimens were then sectioned through the thickness and examined metallographically. The findings are discussed in Section 2.2.

2.1.4 Experimental Results of Cyclic-Load C(T) Tests

Experimental data were reduced using the Quattro-Pro® software. Initial data reduction included converting data from voltages to engineering units and generating plots of the converted data. Since the J-estimation scheme used to calculate the J-R curves from the experimental record (see Section 2.3.1) requires an upper envelope of the load-displacement record, these peaks where chosen during the initial data reduction procedures. Figure 2.11 shows an example of a stainless steel specimen tested at a stress ratio equal to -1. Also included in this figure are the upper envelope points used in the J-estimation scheme. The dimensions of each of the specimens tested in this investigation are given in Appendix A

2.1.4.1 Base Metal Results

Stable crack growth occurred in both the carbon and stainless steel cyclic-loaded C(T) specimens. Crack growth for the stainless steel specimens remained in the initial crack plane. The cracks in the carbon steel specimens on the other hand, level off from the initial crack plane. This behavior was observed also in the TWC pipe tests made from the same material (Ref. 2.3). It is believed that this effect is due to the fracture-toughness anisotropy present in this carbon steel material (Ref. 2.4).

Figure 2.12 shows the reduction in maximum load and displacement at maximum load for both the stainless and carbon steels as a function of displacement increment and stress rates. Complete upper envelope load-deflection plots for these specimens can be found in Appendix B. In all cases, the reduction in maximum load ranged from zero to a maximum of 20 percent in several of the R = -1 cases. However, the load-line displacement (LLD) at maximum load decreased significantly, especially at the larger negative stress ratios. For the stainless steel specimen tested at a displacement increment of 0.025, the load-line displacement at maximum load decreased by about 80 percent of the monotonic value. The trend of the data for the stainless steel in Figure 2.12 is not linear with stress ratio. For example, there is a relatively small decrease in the load-line displacement at maximum load between the stress ratios of 0 and -0.6, and then a steep decrease between -0.6 and -1. However, this observation is dependent on the displacement increment. For the case with the displacement increment of 0.2, no significant load-displacement differences were seen at stress ratios up to -0.6, but at a displacement increment of 0.025, a 10 percent decrease in the maximum load was observed at a stress ratio of -0.6. Even though a test at R = -0.3 and a displacement increment of 0.025 was not run in this study, it can be assumed from the trends of the other tests that this test probably would have produced a lower load-displacement record. This trend agrees with the linear summation law proposed by Landes and Liaw (Ref. 2.5). They suggest that the amount of total crack growth can be broken down into crack growth due to stable ductile tearing

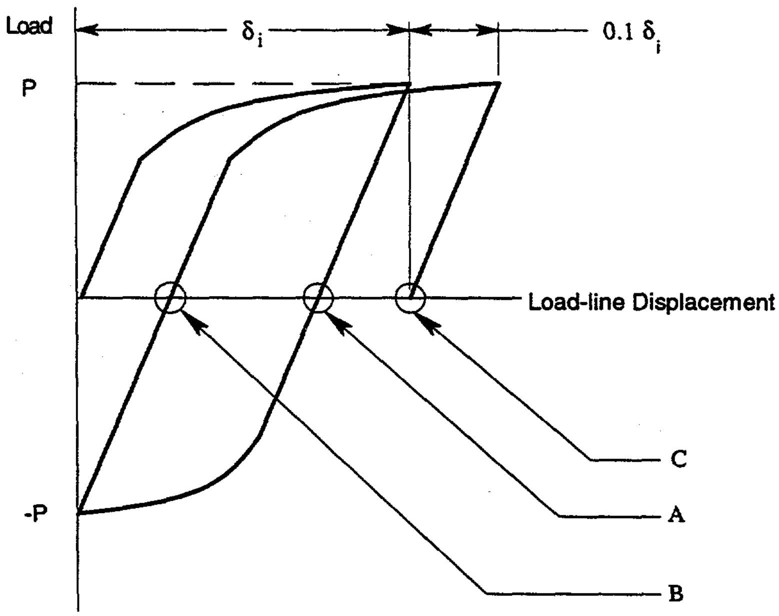

Figure 2.10 Schematic of loading path for additional metallographic C(T) specimens

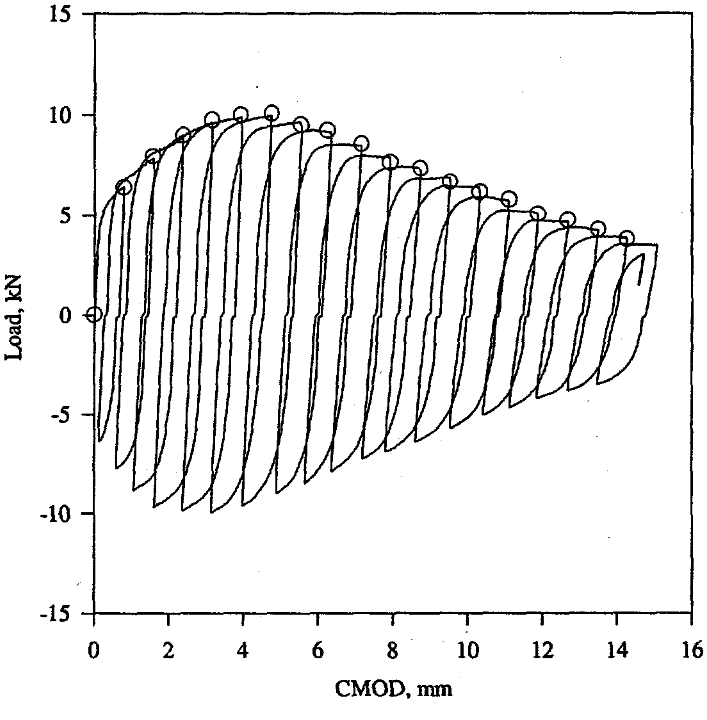

Figure 2.11 Load-displacement curve for stainless steel specimen tested with $\delta_{cyc}/\delta_i = 0.1$, R = -1. Circled points indicate upper envelope of load-displacement curve. All specimens tested at 288 C (550 F) (Specimen A23-5c)

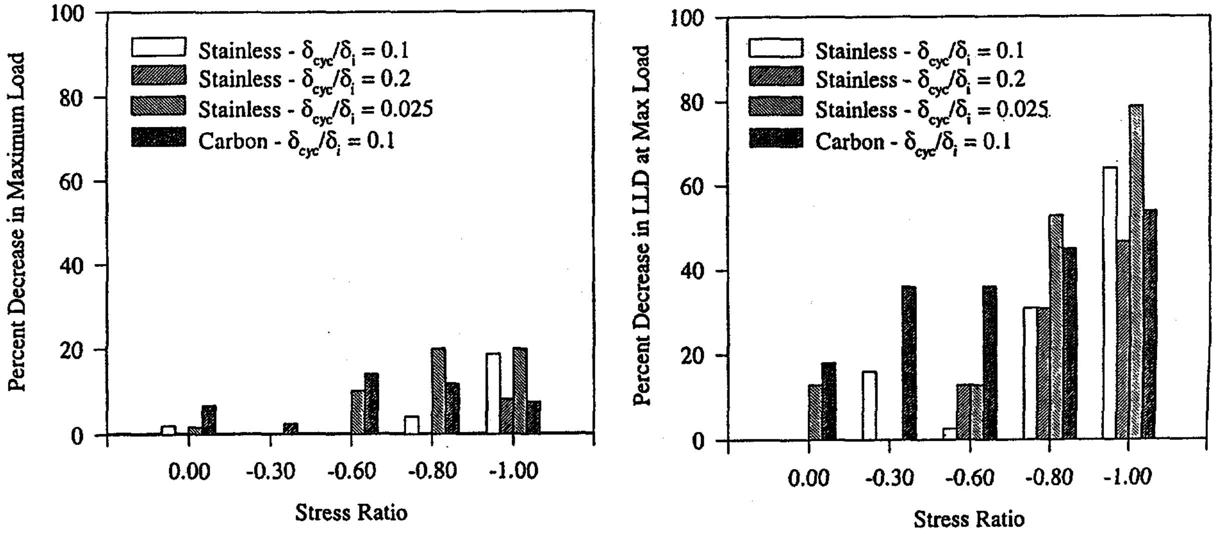

Figure 2.12 Percent decrease in maximum load and load-line displacement (LLD) at maximum load relative to monotonic C(T) specimen data

and fatigue for every case except R = -1. As the number of cycles is increased (smaller displacement increments) the load-displacement record is lowered, thus causing a reduction of the apparent fracture toughness. However, another hypothesis, not investigated by Landes and Liaw, is that the crack is growing in a more damaged region.

Since only one displacement increment was run for the carbon steel material, only conclusions about the effect of stress ratio can be made. In comparing the carbon steel results with the stainless steel results at the same displacement increment, the carbon steel seems to be more affected by cyclic loading at each stress ratio investigated, except at R = -1. For example, at a stress ratio of -0.3, where no decrease in the load and only a slight decrease in displacement were observed in the stainless steel material, a significant drop in the load-displacement record is shown for the carbon steel material. Also, there seems to be a threshold in the effect of stress ratio in the carbon steel. At stress ratios of -0.8 and -1, the percentage decrease in both the maximum load and the displacement at maximum load were nearly identical, which was not true for the stainless steel, where the effects of cyclic loading tended to be greater at R = -0.8.

A considerable amount of through-thickness deformation was observed in stainless steel specimens that were loaded monotonically. Figure 2.13 shows the fracture surface of such a specimen. However, as the stress ratio was made increasingly negative in cyclic-load tests, the amount of through-thickness deformation decreased. Figure 2.14 shows the fracture surface of a stainless steel specimen tested at a stress ratio of -1 and a displacement increment of 0.1. This reduction in through-thickness deformation suggests that the cyclic loading affects the constraint in the specimen. It is also consistent with the load-displacement curve which implies that the ductile crack growth resistance is lower for cyclic loading.

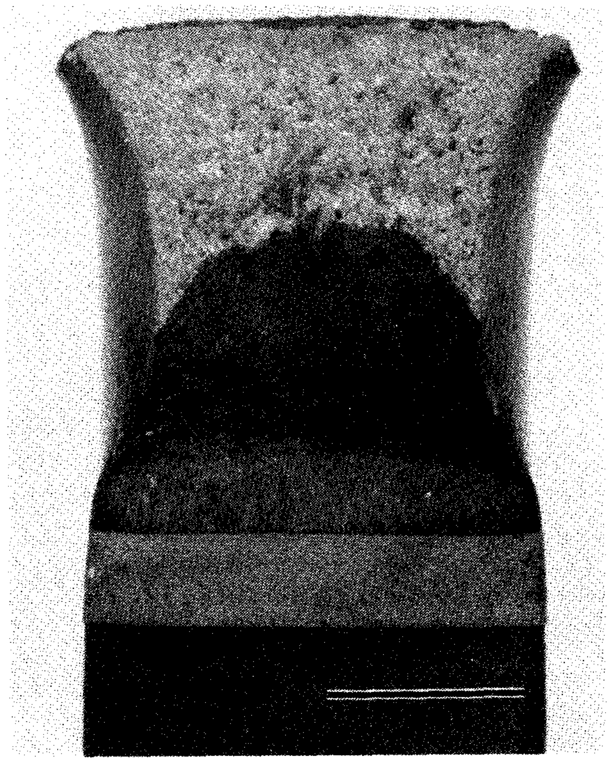

Figure 2.13 Fracture surface for stainless steel base metal C(T) specimen tested monotonically with quasi-static loading rates (Specimen A23-2c)

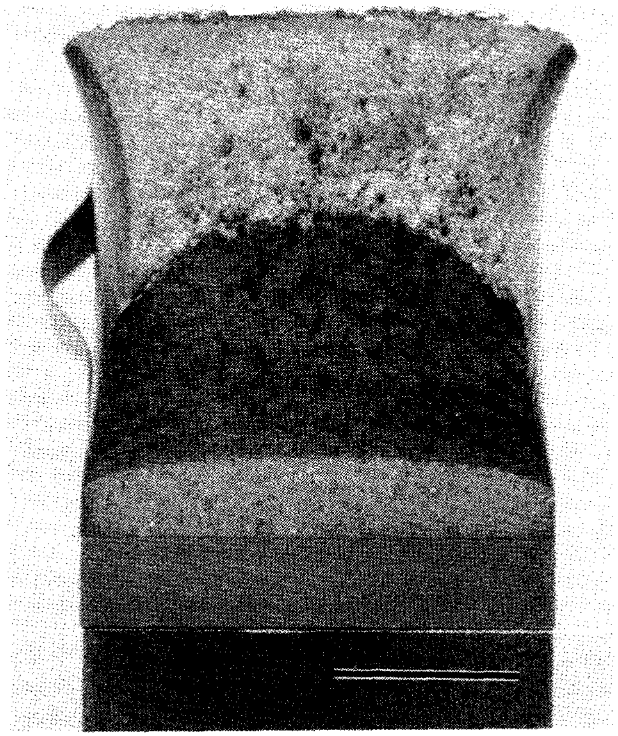

Figure 2.14 Fracture surface for stainless steel base metal C(T) specimen tested cyclically with quasi-static loading rates at R = -1 (Specimen A23-5c)

Figure 2.15 shows the fracture surfaces for two carbon steel specimens, one tested monotonically and one tested cyclically with a stress ratio of -1. In these carbon steel specimens, the crack left its initial plane. This behavior is typical of circumferentially cracked carbon steel pipes under ductile tearing and was seen in the TWC pipe tests on the same material (Ref. 2.4). There was no evidence of significant through-thickness deformation in any of the carbon steel specimens. Thus, something other than a change in constraint is degrading the materials toughness during cyclic loading. Section 2.2 discusses a metallographic study of these materials conducted to better understand the cyclic degradation mechanisms.

2.1.4.2 Weld Metal Results

Stable crack growth occurred in both the carbon steel and stainless steel SAW cyclic-loaded C(T) specimens. All cyclic-loaded weld specimens were tested with $\delta_{cyc}/\delta_i = 0.1$. A special note should be made about these experiments. The base metal cyclic-load specimens, all of which employed quasi-static loading rates, were conducted in clip gage control (the clip gage was used to measure the load-line displacement), so that the δ_{cyc}/δ_i value would remain strictly consistent throughout the test. However, for the weld specimens, the experiments were conducted in stroke control, necessitated by the fact that half of the tests would employ dynamic loading at an average of 4 Hz. Because of this use of stroke control and the compliance of the test frame, the displacement increment at the load-line (clip gage) was not strictly consistent. As the crack began to grow, the load-line displacement became larger for the same amount of stroke displacement. The dynamic tests had to be run in stroke control since clip-gage control would become unstable at this high frequency. In order to be consistent, the quasi-static SAW specimens were also run in stroke control. Since all of these specimens had 20 percent sidegrooves, the crack remained in the original crack plane.

Figure 2.16 shows the reduction in maximum load and displacement at maximum load for both welds as a function of stress ratio. Note that these reductions are based on the monotonic counterparts for both the quasi-static and dynamic loading tests. Complete upper-envelope load-displacement plots can be found in Appendix B.

For the quasi-static experiments, the reduction in maximum load for the cyclic experiments relative to the monotonic experiments was minimal for both SAWs. The greatest reduction of maximum load was 10 percent, observed in the stainless steel SAW tested at $R = -1$. Interestingly, the reduction in maximum load for the dynamic-cyclic experiments was greater than the reduction for the quasi-static-cyclic experiments. In all of the dynamic-cyclic cases, the reductions in the $R = -1$ maximum load were at least 10 percent when compared to the dynamic, monotonic experiments, and a reduction of 18 percent was observed in the stainless steel SAW, dynamic, $R = -1$ experiment. These findings indicate that dynamically cycling a specimen increases the cyclic degradation as compared to cycling at quasi-static rates.

It is important to note that the dynamic monotonic loading increased the maximum load for both welds as compared to the quasi-static monotonic loading. For the stainless steel SAW (A8W4), that increase was 20 percent, while for the carbon steel SAW (F40W) that increase was 13 percent. Note that the quasi-static and dynamic monotonic J-R curves for the A8W4 were taken from Reference 2.2. In that report, three dynamic, monotonic experiments were conducted with the A8W4 material. Those three experiments had dramatically different results; the increase in load described above is the maximum increase for the three experiments run in Reference 2.2. Therefore, the percent decrease in maximum load for the A8W4 shown in Figure 2.16 is based on the experiment from Reference 2.2 that yielded the highest maximum load.

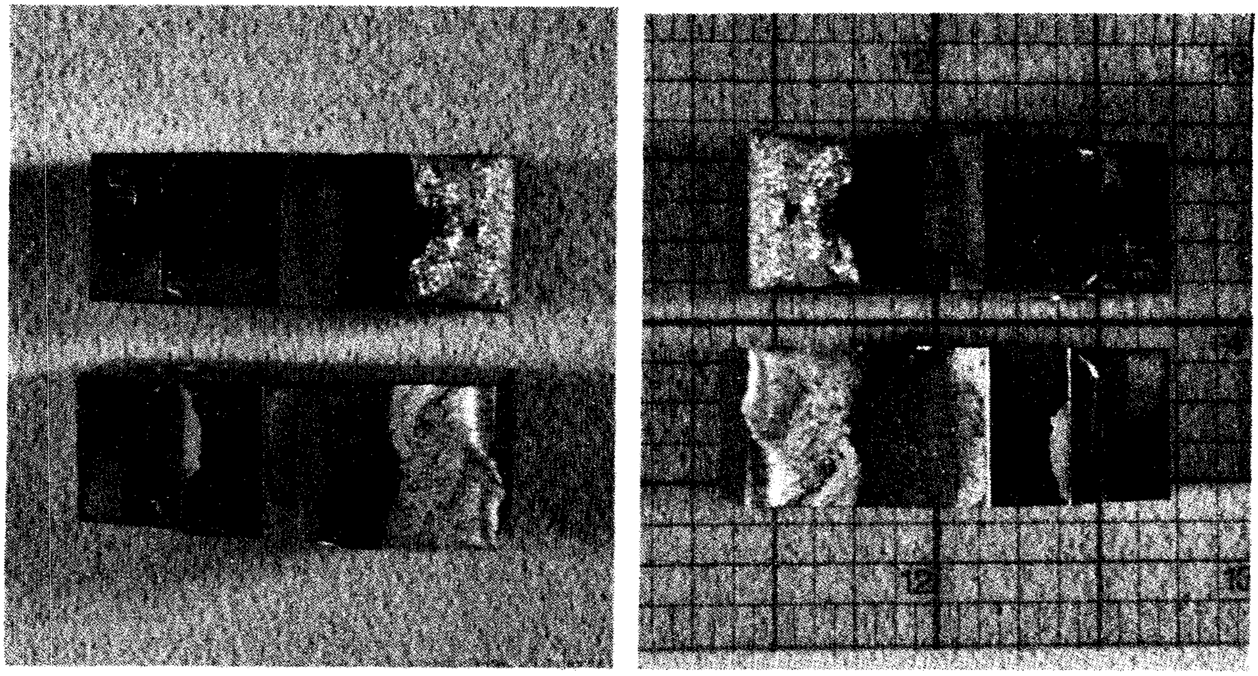

(a) Monotonic (Specimen F30-1c) **(b) Cyclic R = -1 (Specimen F30-3c)**

Figure 2.15 Fracture surfaces of carbon steel specimens tested with quasi-static loading rates

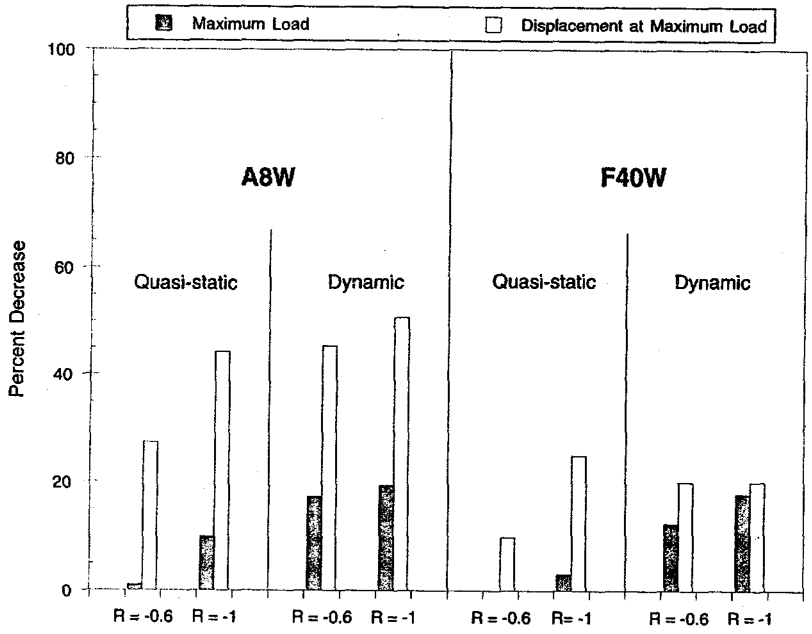

Figure 2.16 Percent decrease in maximum load and displacement at maximum load for stainless steel SAW (A8W4) and carbon steel SAW (F40W) versus stress ratio. Quasi-static, cyclic results are relative to quasi-static monotonic experiments while dynamic cyclic results are relative to dynamic monotonic experiments

In terms of displacement at maximum load, the trends indicate that the stainless steel SAW experienced an overall larger decrease in displacement than did the carbon steel SAW; on average, the relative decrease was about 35 percent for the stainless steel SAW and about 20 percent for the carbon steel SAW.

2.2 Results of Metallographic Examination of Cyclic-Load C(T) Specimens

2.2.1 Review of Additional Cyclic-Load Tests

As was described in Section 2.1.3.2, three additional C(T) specimens of each of the two base metals were subjected to cyclic loading, following the loading paths shown schematically in Figure 2.10. Each specimen was then sectioned at mid-thickness and the mid-thickness surface was metallographically polished and etched to reveal the microstructure in the vicinity of the crack formed during the cyclic loading. If there are microstructural changes occurring in the crack tip process zone, then these changes would contribute to a degradation mechanism that could not be solely accounted for by sophisticated continuum mechanics approaches, e.g., detailed FEM analyses.

2.2.2 Stainless Steel Base Metal

Figure 2.17 shows a typical microstructure of an unstressed region of the TP304 stainless steel material. Figure 2.18 shows a general view of the three specimens and their completion points along the load-displacement curve. Clearly, the crack tip for Specimen A23-9c is much sharper than the crack tip for Specimen A23-8c. This sharpening, which occurs because of compressive plasticity, raises the crack tip stress intensity and lowers the apparent fracture resistance. Additionally, a local residual stress field is created from the reverse plastic flow that can change constraint conditions. These aspects make it easier to tear in the next positive load cycle, as shown in the view of the crack tip for Specimen A23-10c.

A magnified view of the crack tip for Specimen A23-8c is shown in Figure 2.19. The surface shown in this figure has been etched to reveal the grain boundaries. As expected, due to the high toughness of stainless steel, the crack tip is blunted and several voids, about 50 µm in diameter, are present ahead of the crack tip. Also, a zone of heavily deformed material containing numerous smaller voids surrounds the crack tip. The extensive plastic strain and the presence of voids significantly reduce the ductility of the material surrounding, and immediately ahead of, the crack tip. Thus, it is customary to described the material in this zone as "damaged".

A magnified view of the crack tip for Specimen A23-9c from Figure 2.18 is shown in Figure 2.20. When compared with the crack tip in Specimen A23-8c, the sharpness of the crack tip in Specimen A23-9c is striking. The density of the damage surrounding the crack tip appears to be larger than in Specimen A23-8c. Due to the compressive loads, the material ahead of the crack yielded in both tension and compression, thereby increasing the dislocation density. Also, it is important to note that the crack-mouth-opening displacement was decreased by a factor of 10 after the compressive loading. Note that the voids in this TP304 material are not flattened after compressive loading. Perhaps more negative loading would have caused the voids to flatten.

A magnified view of the crack tip for Specimen A23-10c from Figure 2.18 is shown in Figure 2.21. This figure shows evidence of ductile tearing and void coalescence. In the center of the figure, the dominant

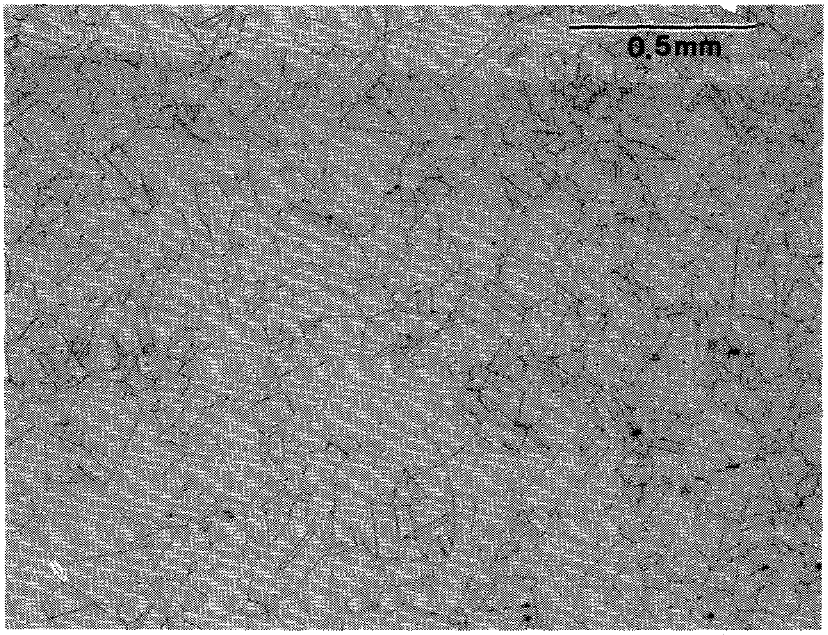

Figure 2.17 Photomicrograph of unstressed region of TP304 stainless steel C(T) specimen

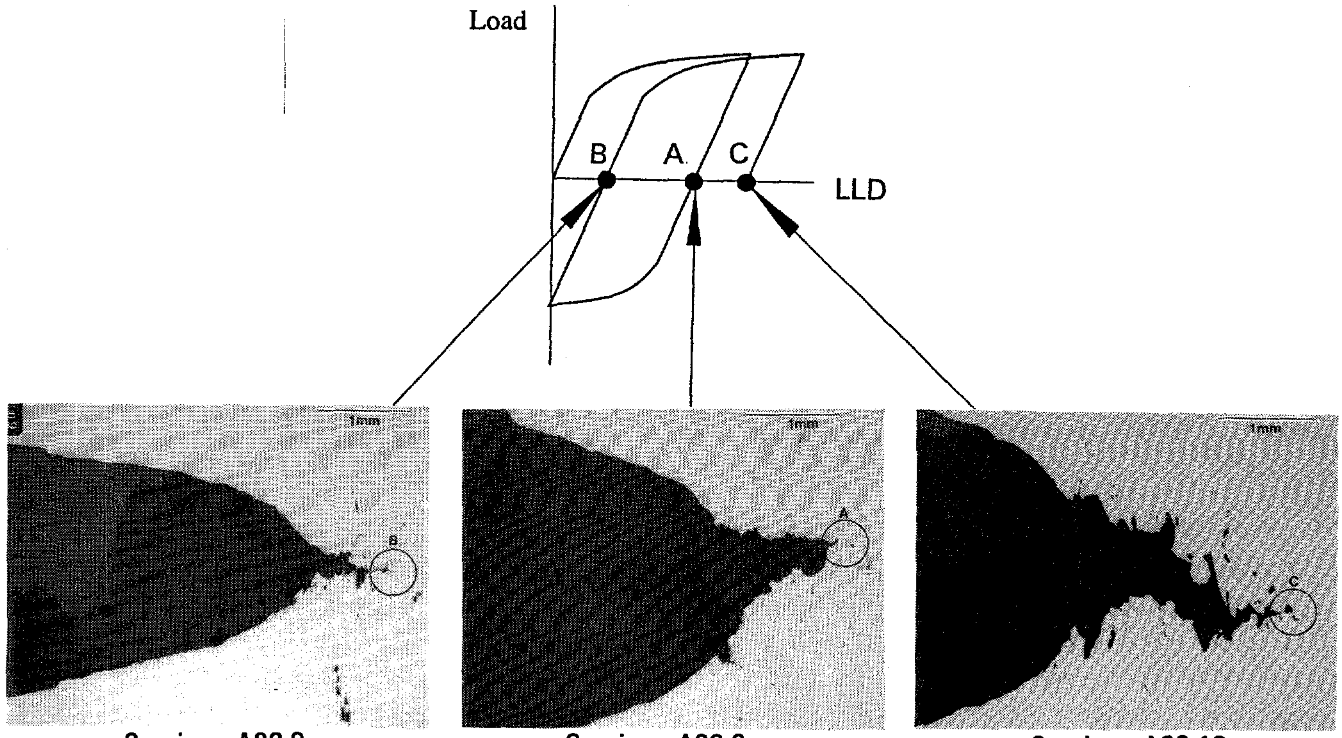

Specimen A23-9c

Specimen A23-8c

Specimen A23-10c

Figure 2.18 Mid-thickness cross sections showing crack-tip region in three additional stainless steel cyclic-load specimens (unetched)

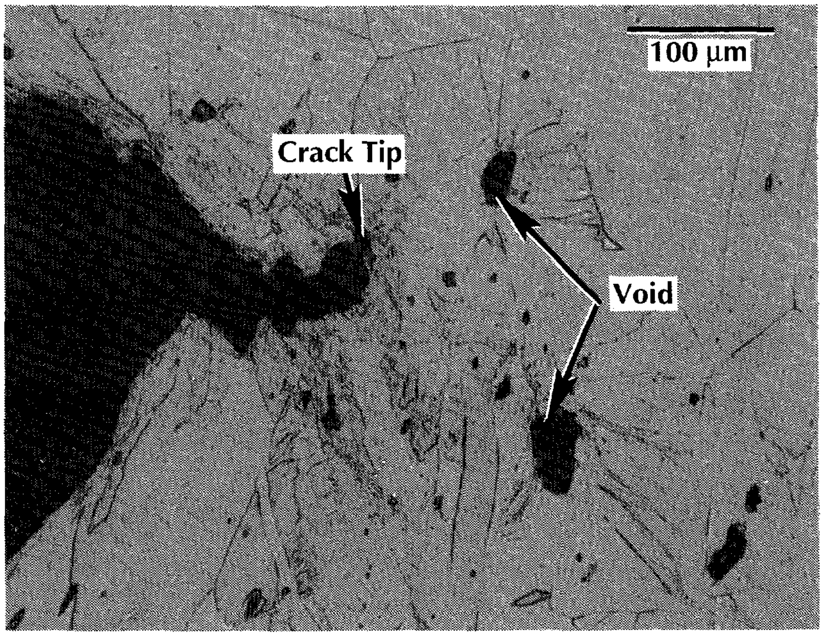

Figure 2.19 Magnified view of crack tip for stainless steel Specimen A23-8c loaded to Point A

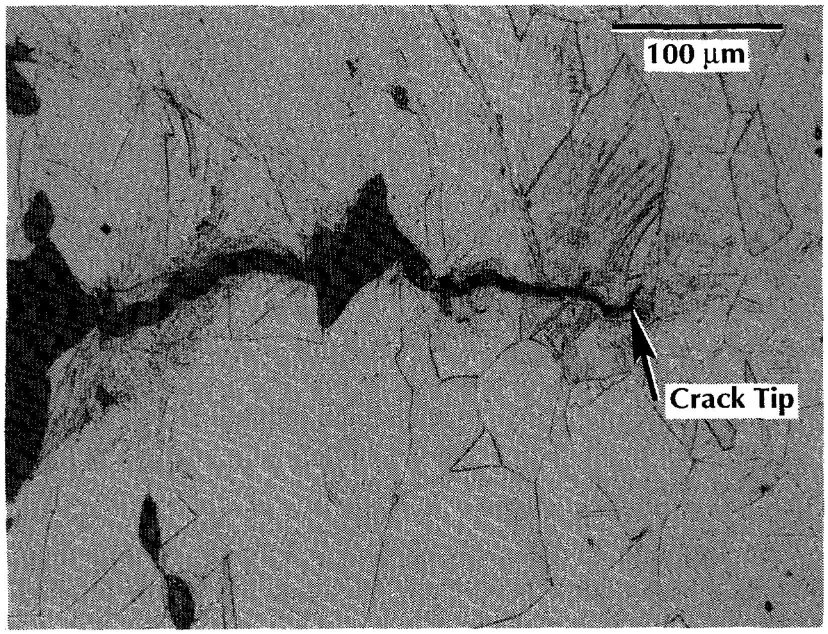

Figure 2.20 Magnified view of crack tip for stainless steel Specimen A23-9c loaded to Point B

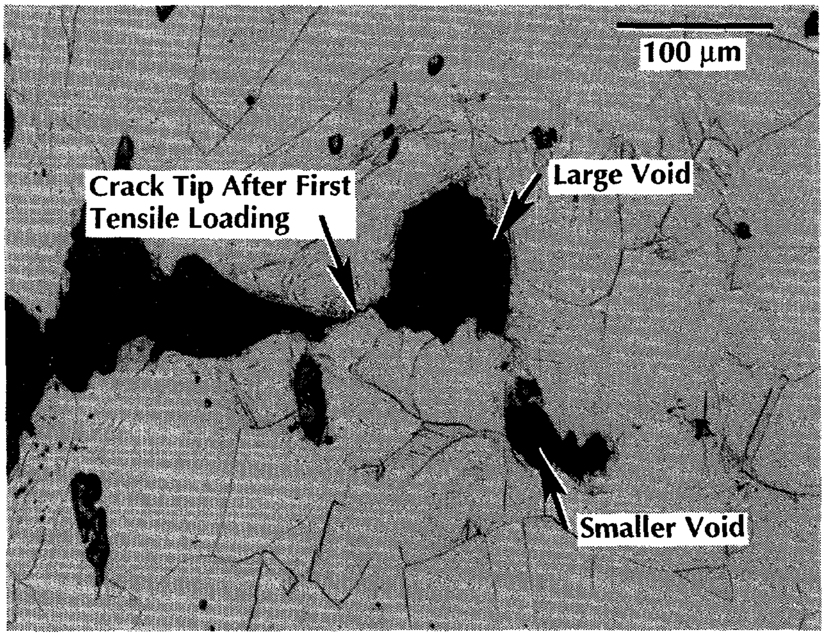

Figure 2.21 Magnified view of crack tip for stainless steel Specimen A23-10c loaded to Point C

crack has joined with a large void. The tip of the dominant crack shows evidence of being sharpened before joining with the large void. There is evidence that the main crack was sharpened, due to the compressive cycle, which upon reloading, caused a microcrack to join the main crack to the void ahead of the crack. Also a smaller void directly ahead of the large void has an elongated shape, indicating that this void was also slightly flattened by the fully reversed cycle. The large void contains a sharp edge leading toward the smaller void, indicating that void coalescence was about to occur. Even though there is damage around the microcrack and void, the density of this damage appears to be somewhat less than in the previous two cases. It is possible that the damage ahead of the crack tip only enhances the degradation in toughness, with crack-tip sharpening causing the major reduction in toughness.

2.2.3 Carbon Steel Base Metal

Figure 2.22 shows an etched surface of an unstressed region of the A106 Grade B carbon steel material. The ferrite and pearlite structure, typical for this material, can be clearly identified. A polished, unetched surface showed a relatively voidless material with void diameters about one-tenth of those seen in the stainless material. Figure 2.23 shows an overall view of the three carbon steel specimens tested. As in the stainless material, Specimen F30-10c, which underwent the compressive cycle, had a much sharper crack tip than either of the other specimens. Also, in the carbon steel, the crack-mouth-opening displacement is a factor of 10 smaller than in the stainless steel.

Figure 2.24 shows the crack tip for Specimen F30-9c (stopped at Point A) from Figure 2.23. There are several voids formed ahead of the main crack. From this figure, there is evidence that the crack growth process was due to void coalescence. There is no visible evidence of significant damage near the crack surface.

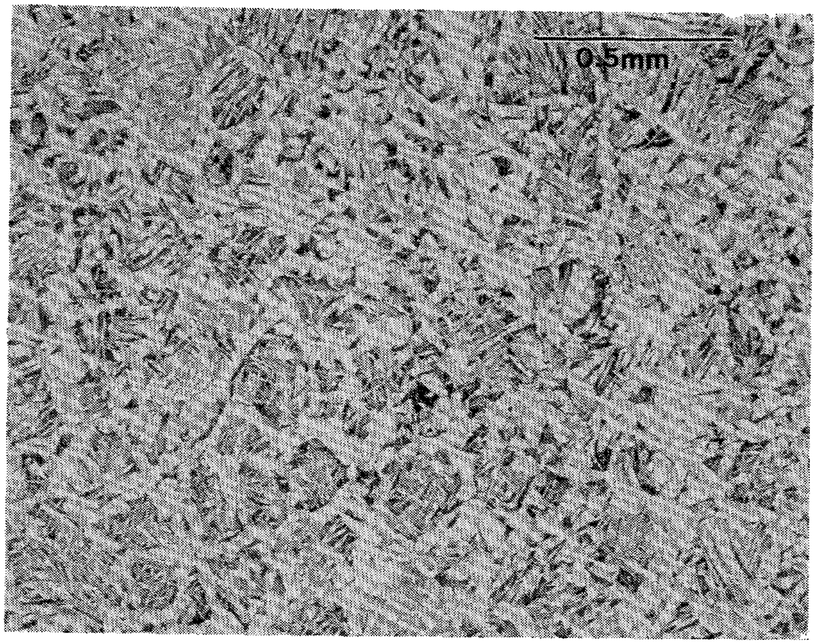

Figure 2.22 Photomicrograph of unstressed region of A106 Grade B carbon steel C(T) specimen

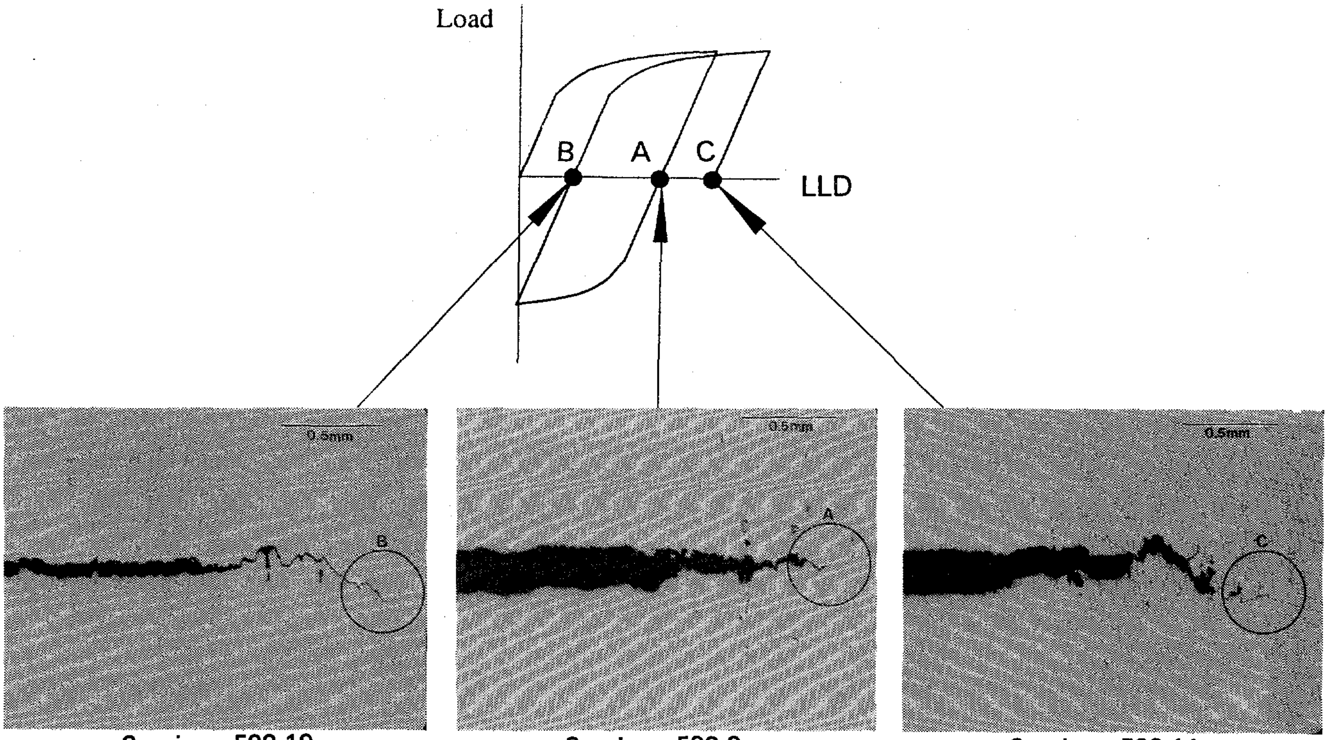

Specimen F30-10c Specimen F30-9c Specimen F30-11c

Figure 2.23 Mid-thickness cross sections showing crack-tip region in three additional carbon steel cyclic-load specimens

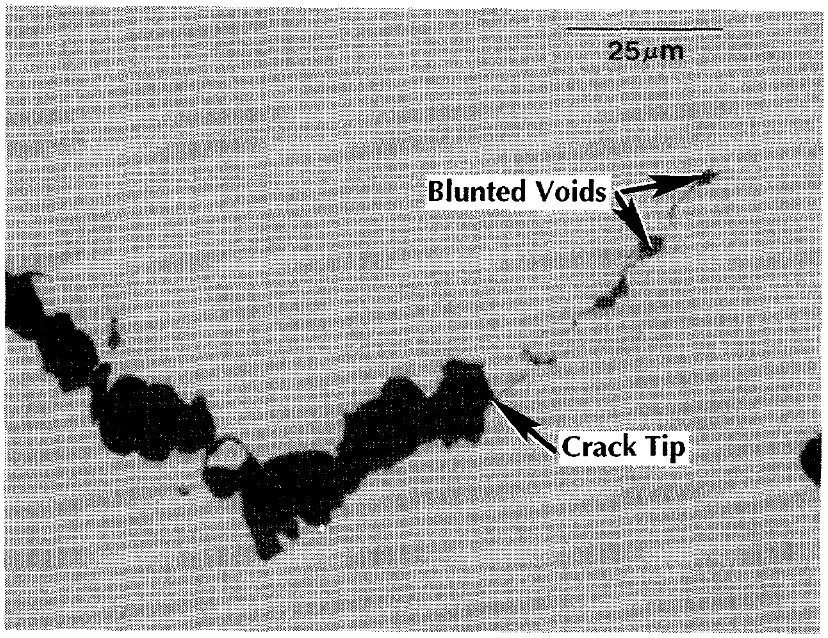

Figure 2.24 Magnified view of crack tip for carbon steel Specimen F30-9c loaded to Point A

The magnified view of the crack tip for Specimen F30-10c (stopped at Point B) from Figure 2.23 is shown in Figure 2.25. Notice that the main crack tip is significantly sharper than in Specimen A. Also, there are small compressed voids extending about 100 μm ahead of the main crack tip. These sharp voids will promote large stress intensities which will promote easier crack extension on the next cycle of loading.

The magnified view of the crack tip for Specimen F30-11c (stopped at Point C) from Figure 2.23 is shown in Figure 2.26. It appears that the main crack had just joined with a large void ahead of the crack. It is possible that the main crack and the void appeared after the first tensile load, were sharpened by the fully reversed load, and were joined upon application of the final tensile load.

2.2.4 Vickers Hardness Results

Metallographic examination of the crack-tip region cannot easily provide an estimate of the plastic zone size ahead of a crack tip. Therefore, a series of indentation hardness tests were conducted on the sectioned stainless steel specimens from the additional tests in order to estimate the size of the plastic zone and its movement during the cyclic process. Figure 2.27 shows the paths in which hardness values were taken. The hardness values were taken at the specimen center thickness along lines parallel, perpendicular, and at 45 degrees to the crack plane. They were taken from the crack tip to 7.6 mm (0.3 inch) ahead of the crack tip in 0.76 mm (0.03 inch) increments. These hardness values, along with the specimen geometry, were inputted into a finite element post processor, which interpolated between the measured hardness values producing smooth contours. Figure 2.28 shows the hardness contours for the three specimens. Note, the crack tips for these three specimens are not in the same absolute coordinate position in space, i.e., the crack length for Specimen A23-8c is longer than for Specimen A23-9c.

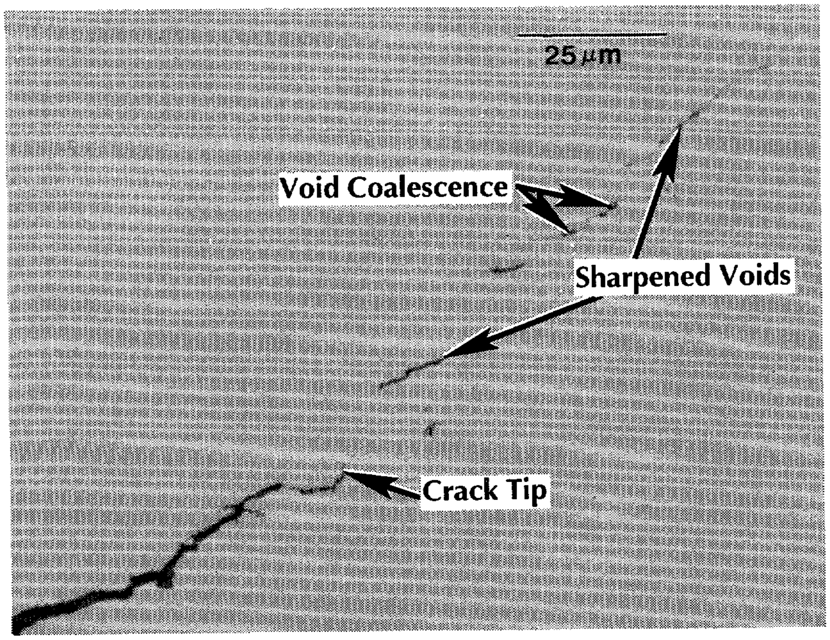

Figure 2.25 Magnified view of crack tip for carbon steel Specimen F30-10c loaded to Point B

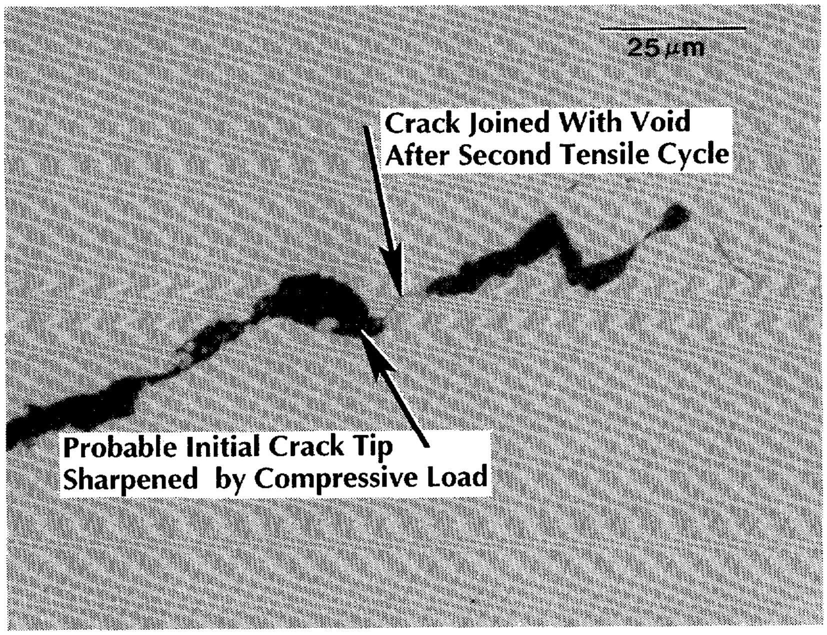

Figure 2.26 Magnified view of crack tip for carbon steel Specimen F30-11c loaded to Point C

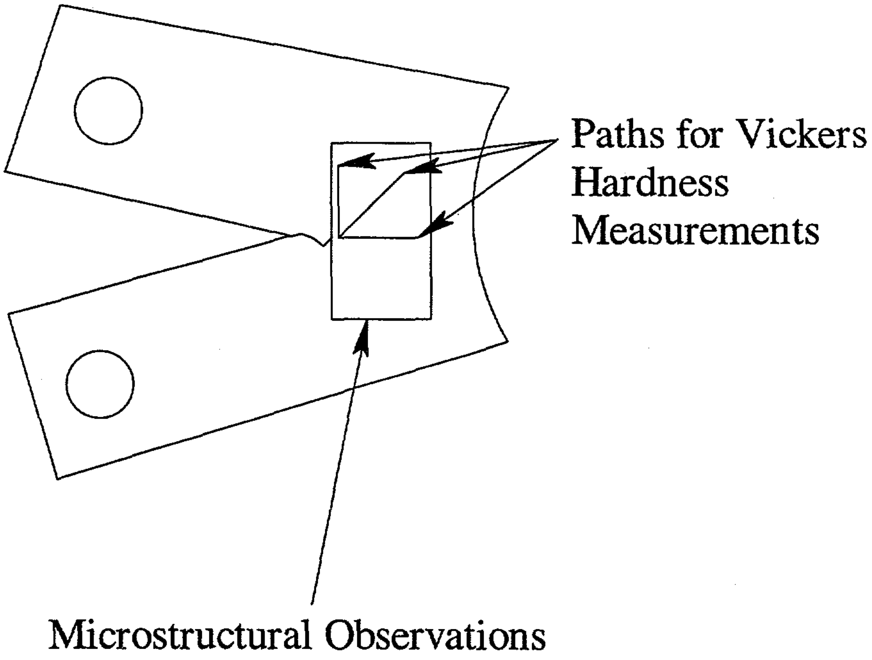

Figure 2.27 Schematic illustration of locations of Vickers hardness readings

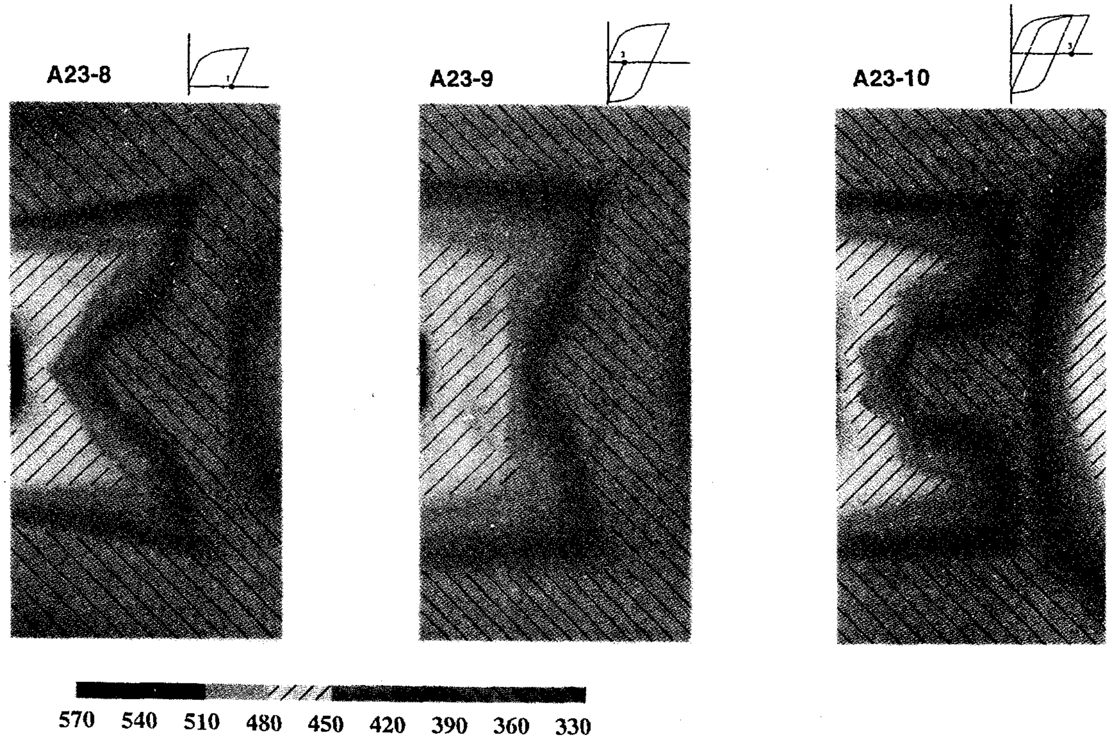

Figure 2.28 Hardness contours for three additional stainless steel specimens

Upon inspection of Specimen A23-8c, it is clear that the hardness values are the highest closest to the crack tip. This led to the conclusion that the material is strongest closest to the tip, which is expected for strain-hardening materials. The shape of the plastic zone has von-Mises characteristics, i.e., it has the approximate shape of the classical von-Mises, maximum distortion energy, plastic-zone size approximation.

The hardness values shown in Figure 2.28 for Specimen A23-9c represent the plastic zone shape of the specimen that was loaded in tension, compression and then unloaded. Clearly, the plastic zone has been affected by this fully reversed loading. The overall shape still has von-Mises characteristics, but there seems to be a slight softening that occurred about 3/4 of the way around the plastic zone. This could be a consequence of the fully reversed loading or could be a material flaw. Section 2.3.2 discusses the finite element strain contour results and compares its results with the Vickers hardness plastic-zone approximations. Surprisingly, the same softening effect is seen in the finite element results that was shown in the hardness results. This result leads to the conclusion that the effect seen is a real material response and not a single specimen anomaly. Also, from these hardness contours, it is impossible to differentiate between tensile and compressive plastic strains.

Finally, the specimen that has undergone two loading cycles, Specimen A23-10c, is shown in Figure 2.28. The plastic zone shape ahead of the crack is similar to that of Specimen A23-8c. However, the shape is somewhat altered, suggesting that the fully reversed loading may effect the plastic zone ahead of the crack.

It is important to note that the hardness values shown in Figure 2.28 cannot be directly converted to the amount of plastic strain in the C(T) specimens. A calibration factor for relating plastic strain to Vickers hardness would have to be developed first. This calibration could be determined experimentally by conducting hardness tests on a series of tensile specimens that had been plastically strained to various known levels. The deformation of such a hardness-strain calibration curve was beyond the scope of this investigation.

2.2.5 Discussion of Cyclic-Loading Degradation Mechanisms

From the metallographic results presented, it appears that there are two main mechanisms present in the cyclic-loading degradation process -- crack-tip sharpening and void sharpening. Both the stainless and the carbon steel showed evidence of crack-tip sharpening. Because of the more ductile nature of stainless steel, the increased amount of crack-tip blunting in this material caused the sharpening to be less severe than in the carbon steel specimens. This sharpening acts to increase the crack-tip stress intensity which would promote crack extension, thus lower the apparent fracture resistance. From the load-displacement record, the carbon steel specimens were strongly affected by the intermediate stress ratios. Since the carbon steel has a lower toughness than the stainless steel, it has less crack-tip blunting. Hence, it may take less compressive load to sharpen the crack tip. Therefore, intermediate stress ratios could decrease the load-carrying capacity in the carbon steel, but have little effect on the stainless steel. This behavior was observed in the cyclic C(T) tests in this study. Using this hypothesis, there should be a limit to the amount the load and displacement are decreased by the cyclic loading. In the carbon steel base metal tested in this investigation, that limit seems to occur at a stress ratio of -0.8. For this material, decreasing the stress ratio from -0.8 to -1 did not decrease the load-displacement curve any further. Theoretically, the same effect should be observed in the stainless steel base metal; however, tests at stress ratios more negative than -1 were not conducted in this study.

With respect to void sharpening, only the carbon steel experienced this phenomenon. Sharp voids tend to enhance void coalescence and should thereby lower the apparent fracture toughness. The argument for this mechanism is similar to the one just made for the crack-tip sharpening, the higher the material's toughness, the larger the compressive load needed to promote void sharpening. The crack tip and void sharpening mechanisms probably work together in degrading the material's fracture resistance under cyclic loading.

Another possibility is that the cyclic degradation effect is due to a change in the constitutive behavior of the material. If this is the case, then it should be possible to model the behavior using the finite element method. Vickers hardness tests on the stainless steel material showed that the shape of the plastic zone is modified as the specimen loads are fully reversed. Section 2.3.2 discusses a series of FE analyses that attempt to model this cyclic degradation effect.

2.3 Analysis of Cyclic-Load C(T) Tests

In order to determine the extent of toughness degradation due to cyclic loading, an estimate for the J-integral has to be made for this specimen geometry. For C(T) specimens under monotonic loading, estimations of J have been made and published in ASTM 1152, Standard Test Method for Determining J-R curves. However, classical J, based on deformation theory, is undefined when unloadings occur. Therefore, an engineering approximation of J was required to assess the cyclic effects on fracture toughness. In previous work on cyclically loaded 1T C(T) specimens, Landes and McCabe (Ref. 2.6) used an upper envelope of the load-displacement record to calculate J. Later, Landes and Liaw (Ref. 2.5) used the same procedure except that they calculated the cyclic crack growth component by taking into account the amount of crack closure per cycle. In the IPIRG-1 program (Ref. 2.3), pipe J-R curves were calculated from the load-displacement record using the η-factor approach. When it came to cyclic pipe tests, the upper envelope of the load-displacement curve was used in the analysis. Even though the formal definition of J is violated when unloadings occur, calculating J from the upper envelope of the load-displacement record can provide a useful tool in the determination of cyclic effects on fracture toughness.

Crack initiation and growth in the cyclic-load C(T) tests were determined from the direct-current electric potential (d-c EP) data taken during the experiments. The electric potential corresponding to the upper envelope of the load-displacement curve was used in all crack growth analyses. The procedure for calculating crack initiation and growth was as follows. First, the point of crack initiation was estimated from the departure from linearity of the d-c EP versus load-line displacement curve. Note that this curve would correspond to the upper envelope of the load-displacement record. Engineering judgement was employed in final selection of the crack initiation point, making certain that it lay somewhat beyond the elastic portion of the load-displacement curve and before maximum load. In cyclic-load tests, small errors may arise in determing the point of crack initiation if the crack in a particular specimen initiates before the maximum d-c EP reading of the previous cycle. In the cyclic-load pipe tests conducted in IPIRG-1, a distinct change in the d-c EP readings was seen at the point of crack initiation and re-initiation; however, during crack growth in the cyclic-load C(T) tests, the change in slope of the d-c EP readings between blunting and crack growth was not as evident. Therefore, using the upper envelope curve was based on the assumption that the crack initiated and re-initiated at a displacement equal to the maximum displacement of the previous cycle.

Once the decision was made on the crack initiation point, the d-c EP value at this point was called U_o. Approximately 30 to 50 data sets (load, load-line displacement, and d-c EP) were then selected from the continuous upper envelope test record. In the cases where this many data points were unavailable, all of the data points were used. Some of the data sets were taken from the test record prior to crack initiation and some were taken from the growing-crack part of the test. Due to crack-tip blunting, which changes the electrical resistivity of the material (electric resistance changes with cold-working), the d-c EP values increase before crack initiation occurs. The change in the d-c EP is misleading in that it implies that the crack is growing. Therefore, the values of d-c EP prior to crack initiation were set to the initiation value, U_o. After crack initiation, new values of the crack length were calculated using the Johnson equation (Ref. 2.7):

$$a = \left(\frac{2w}{\pi}\right) \cos^{-1}\left[\frac{\cosh\left(\frac{\pi y}{2w}\right)}{\cosh\left[\left(\frac{U}{U_o}\right) \cosh^{-1}\left(\frac{\cosh\left(\frac{\pi y}{2w}\right)}{\cos\left(\frac{\pi a_i}{2w}\right)}\right)\right]}\right] \tag{2-1}$$

where a is the crack length, a_i is the original crack length, w is the specimen width, and 2y is the spacing of the electric potential probes. Battelle has modified Equation 2-1 to permit 2y to increase in proportion to the load-line displacement during the test, because experience has shown that this modification provides a more accurate estimate of the actual crack extension (Ref. 2.8).

J values were calculated from each data set using the procedure specified in ASTM E1152-87, Standard Test Method for Determining J-R Curves. The procedure is as follows for compact tension specimens. J is separated into elastic and plastic components as indicated in Equations 2-2, 2-3 and 2-4:

$$J = J_e + J_p \tag{2-2}$$

$$J_e = \frac{K_e^2\left(1-\nu^2\right)}{E} \tag{2-3}$$

$$J_{p_i} = \left[J_{p_{i-1}} + \frac{\eta_i\left(A_{p_i} - A_{p_{i-1}}\right)}{b_i B_N}\right]\left[1 - \frac{\gamma_i\left(a_i - a_{i-1}\right)}{b_i}\right] \tag{2-4}$$

where K_e is the elastic stress intensity parameter (defined in ASTM E1152), ν is Poisson's ratio, E is the elastic modulus, a is the crack length, b is the ligament length, B_N is the net thickness at the side grooves, A is the area under the load-displacement curve, $\eta = 2 + 0.522\ b/w$, $\gamma = 1 + 0.76\ b/w$, and the subscripts i and i-1 relate to consecutive test record increments.

These equations have been automated by use of the EXCEL® spreadsheet program. The user inputs the load, load-line displacement and d-c electric potential data, physically measured initial and final crack lengths, crack initiation values of load, load-point displacement and EP, and tensile properties data into the spreadsheet program. EXCEL® then calculates the corresponding J-R curve. Figure 2.29 shows an example of the spreadsheet format and input lines. The only difference between this J-R curve and the one presented in ASTM E1152 is the presence of a blunting line in the latter. Also, J_{Ic} from the ASTM method is calculated from a 0.2 mm offset of Δa from this blunting line. The blunting line represents apparent and not physical crack extension. Past work at Battelle (Refs. 2.1 and 2.2) has shown that the J_i and J-Δa values calculated with this spreadsheet program are similar to those calculated with the ASTM procedure.

2.3.1 Stainless Steel Base Metal

Figures 2.30, 2.31, and 2.32 show the calculated J-R curves for the stainless steel base metal C(T) specimens tested at $\delta_{cyc}/\delta_i = 0.1$, 0.2 and 0.025, respectively. Tabulated J-R curves for each experiment can be found in a future update of the PIFRAC database, Ref. 2.10. Table 2.6 shows a summary of the fracture toughness results for the stainless steel specimens. Note that in the following figures and discussion the maximum allowable crack extension in a C(T) specimen is shown as 30 percent of the original ligament. In ASTM E1152, the maximum allowable crack extension is listed as 10 percent of the original ligament. However, recent studies (Ref. 2.9) have shown that in C(T) specimens the crack extensions are valid up to 30 percent of the original ligament.

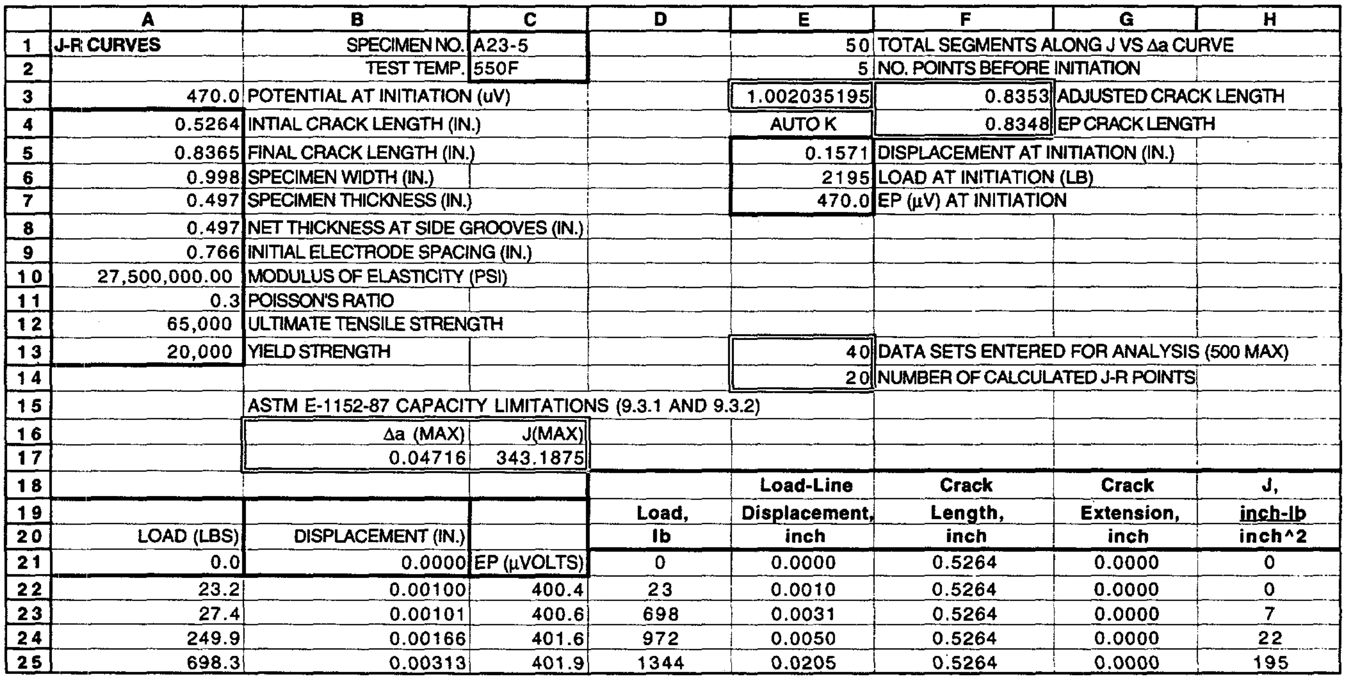

	A	B	C	D	E	F	G	H
1	J-R CURVES	SPECIMEN NO.	A23-5		50	TOTAL SEGMENTS ALONG J VS Δa CURVE		
2		TEST TEMP.	550F		5	NO. POINTS BEFORE INITIATION		
3	470.0	POTENTIAL AT INITIATION (uV)			1.002035195	0.8353	ADJUSTED CRACK LENGTH	
4	0.5264	INTIAL CRACK LENGTH (IN.)			AUTO K	0.8348	EP CRACK LENGTH	
5	0.8365	FINAL CRACK LENGTH (IN.)			0.1571	DISPLACEMENT AT INITIATION (IN.)		
6	0.998	SPECIMEN WIDTH (IN.)			2195	LOAD AT INITIATION (LB)		
7	0.497	SPECIMEN THICKNESS (IN.)			470.0	EP (μV) AT INITIATION		
8	0.497	NET THICKNESS AT SIDE GROOVES (IN.)						
9	0.766	INITIAL ELECTRODE SPACING (IN.)						
10	27,500,000.00	MODULUS OF ELASTICITY (PSI)						
11	0.3	POISSON'S RATIO						
12	65,000	ULTIMATE TENSILE STRENGTH						
13	20,000	YIELD STRENGTH			40	DATA SETS ENTERED FOR ANALYSIS (500 MAX)		
14					20	NUMBER OF CALCULATED J-R POINTS		
15		ASTM E-1152-87 CAPACITY LIMITATIONS (9.3.1 AND 9.3.2)						
16		Δa (MAX)	J(MAX)					
17		0.04716	343.1875					
18					Load-Line	Crack	Crack	J,
19				Load,	Displacement,	Length,	Extension,	inch-lb
20	LOAD (LBS)	DISPLACEMENT (IN.)		lb	inch	inch	inch	inch^2
21	0.0	0.0000	EP (μVOLTS)	0	0.0000	0.5264	0.0000	0
22	23.2	0.00100	400.4	23	0.0010	0.5264	0.0000	0
23	27.4	0.00101	400.6	698	0.0031	0.5264	0.0000	7
24	249.9	0.00166	401.6	972	0.0050	0.5264	0.0000	22
25	698.3	0.00313	401.9	1344	0.0205	0.5264	0.0000	195

Figure 2.29 Example of J-R curve EXCEL® program input screen

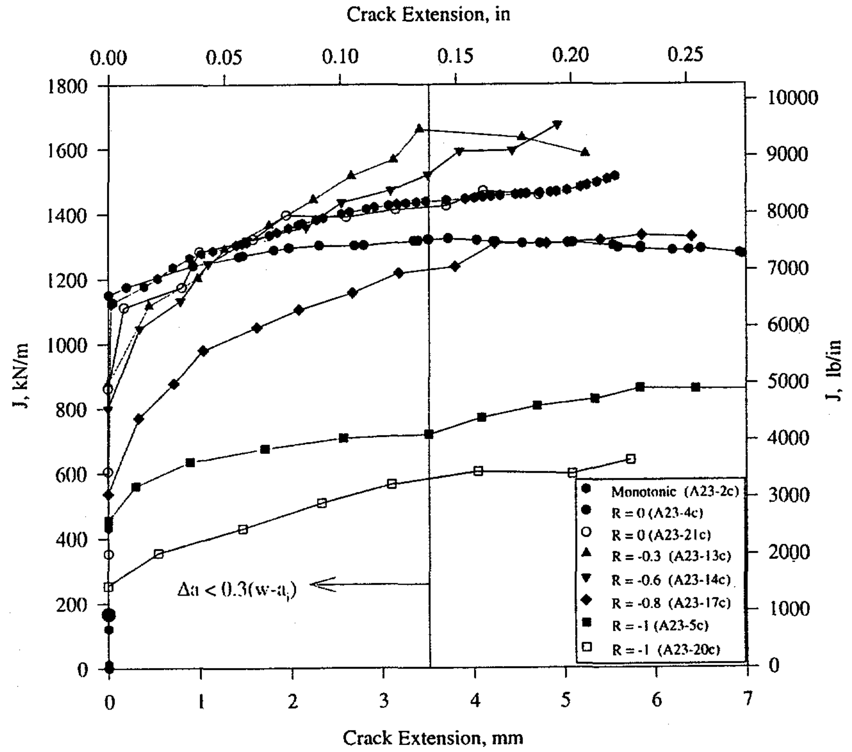

Figure 2.30 Stainless steel cyclic-load J-R curves tested with $\delta_{cyc}/\delta_i = 0.1$

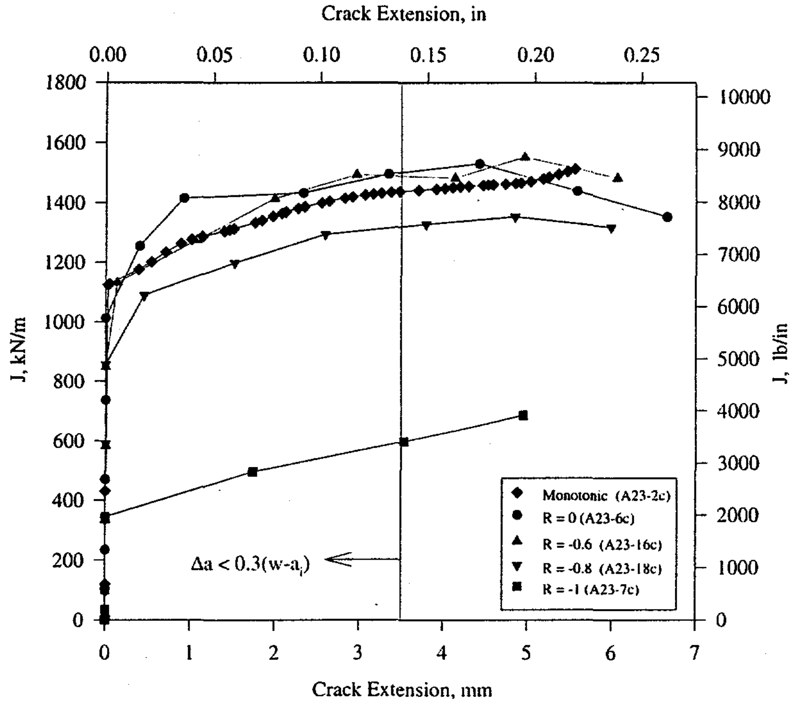

Figure 2.31 Stainless steel cyclic-load J-R curves tested with $\delta_{cyc}/\delta_i = 0.2$

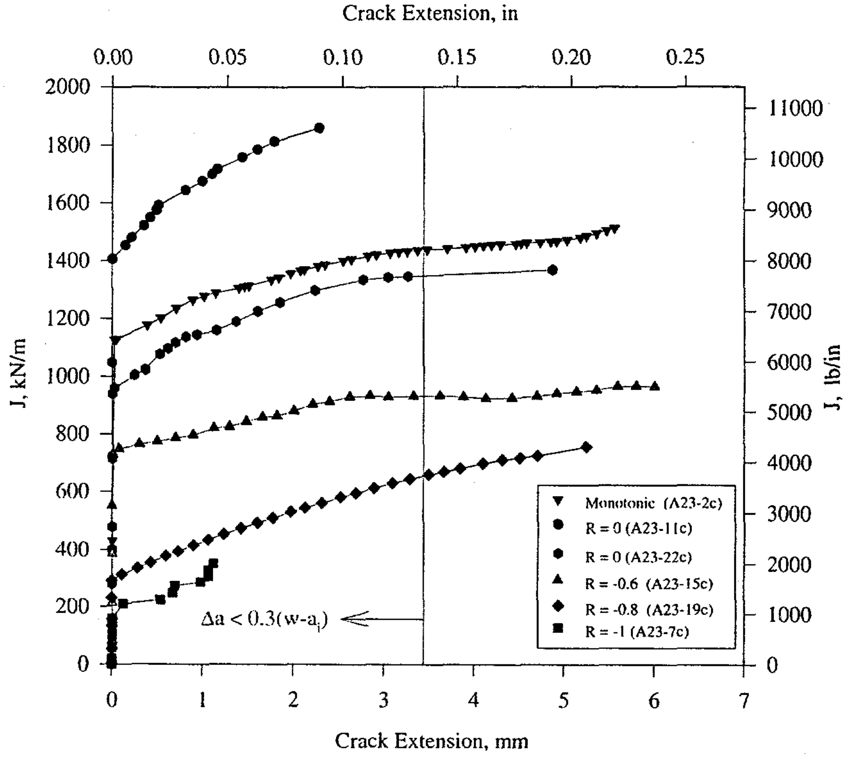

Figure 2.32 Stainless steel cyclic-load J-R curves tested with $\delta_{cyc}/\delta_i = 0.025$

Table 2.6 Cyclic-load fracture toughness summary for stainless steel (DP2-A23) base metal

Specimen	Stress		J at Initiation,		dJ/da,	
Identification	**Ratio, R**	δ_{cyc}/δ_i	**kN/m**	**lb/in**	**MN/m^2**	**lb/in^2**
A23-2c	1	N/A[(a)]	1124	6,418	130.1	18,870
A23-4c	0	0.1	1150	6,566	75.6	10,960
A23-21c	0	0.1	862	4,924	156.0	22,620
A23-13c	-0.3	0.1	877	5,010	194.0	28,140
A23-14c	-0.6	0.1	799	4,565	177.6	25,760
A23-17c	-0.8	0.1	536	3,061	219.5	31,830
A23-5c	-1	0.1	455	2,598	79.0	11,460
A23-20c	-1	0.1	253	1,449	85.8	12,440
A23-6c	0	0.2	1013	5,788	400.0	58,010
A23-16c	-0.6	0.2	850	4,858	203.0	29,440
A23-18c	-0.8	0.2	857	4,896	202.0	29,300
A23-7c	-1	0.2	343	1,963	72.5	10,510
A23-11c	0	0.025	1405	8,025	230.6	33,440
A23-22c	0	0.025	959	5,479	164.2	23,810
A23-15c	-0.6	0.025	726	4,146	68.0	9,860
A23-19c	-0.8	0.025	291	1,665	120.9	17,530
A23-12c	-1	0.025	157	900	132.8	19,260

(a) Monotonic test.

As expected, the J-R curves show the same trends as the load-displacement curves. Figure 2.33 shows a plot of J_i versus stress ratio for the stainless steel cyclic-load tests. From this figure, it is clear that the decrease in stress ratio decreases the value of J at crack initiation. In the extreme case, R = -1 and δ_{cyc}/δ_i = 0.025, J_i decreased by 86 percent in comparison with monotonic tests. Note that the displacement at the maximum load decreased by 80 percent (see Figure 2.12). Also, from Figure 2.33, the effect of displacement increment can be seen. For the specimens where the number of cycles is large, i.e., δ_{cyc}/δ_i = 0.025, the initiation resistance seems to decrease almost linearly with stress ratio. However, when the displacement increment is large, i.e., δ_{cyc}/δ_i = 0.2, there is only a small decrease in J_i until a stress ratio of -1 is reached. This finding suggests that there are two cyclic degradation effects present, fatigue and reverse plasticity. For the case of the large displacement increment, where fatigue has a minimal effect, the resistance is not significantly affected until the crack tip undergoes fully reversed plasticity. Apparently, for this material, there is not enough plastic damage at the crack tip until the loads are fully reversed.

Figure 2.34 shows the ratios of $J_{QS,cyc}/J_{QS,mono}$ versus stress ratio for the stainless steel material. The values of J in this figure are taken at the maximum allowable crack extension (30 percent of the initial ligament). If it is assumed that the J-R curves obtained from compact tension specimens are valid until the crack extension reaches 30 percent of the uncracked ligament, this value can be used as a comparison tool. The results in Figure 2.34 are similar to the results in Figure 2.33. For the larger displacement increments, the decrease in resistance due to cyclic loading is not significant until a stress ratio of -1. At R = -0.8, the J values were about 85 percent of the monotonic values, but at R = -1, the J values were only about 30 percent of the monotonic values. As shown before, when the displacement increment is small, the resistance decreases linearly with stress ratio, indicating that fatigue is playing a larger role in the apparent decrease in fracture resistance.

2.3.2 Carbon Steel Base Metal

Figure 2.35 shows the calculated J-R curves for the carbon steel base metal (DP2-F30) C(T) specimens tested in this study. Note, the carbon steel specimens were tested with only one displacement increment, δ_{cyc}/δ_i = 0.1 Table 2.7 shows a summary of the fracture toughness results for the carbon steel specimens. A detailed listing of each of the J-R curves will be listed in a future version of the PIFRAC database, Ref. 2.10.

From Figure 2.35, the carbon steel appears more sensitive to intermediate stress ratios than the stainless steel for the same displacement increment. Figure 2.36 shows the J_i values as a function of stress ratio for the carbon steel. The decrease in J_i is approximately linear with decreasing stress ratio. However, for the fully reversed case, the decrease in J_i is about the same between the two materials. At R = -1, the J_i value was decreased by 36 percent in the carbon steel. This amount compares to the 40 percent decrease in J_i reported for the stainless steel at the same displacement increment.

Figure 2.37 shows the ratios of $J_{QS,cyc}/J_{QS,mono}$ versus stress ratio for the stainless steel material. The values of J in this figure are taken at the maximum allowable crack extension. After some crack extension, the J value at R = -1 is about 30 percent of the monotonic-loading value, similar to the stainless steel case. However, the decrease in resistance occurs at a much larger stress ratio. At a stress ratio of -0.3 the resistance for cyclic loading is approximately 60 percent of the monotonic-loading value.

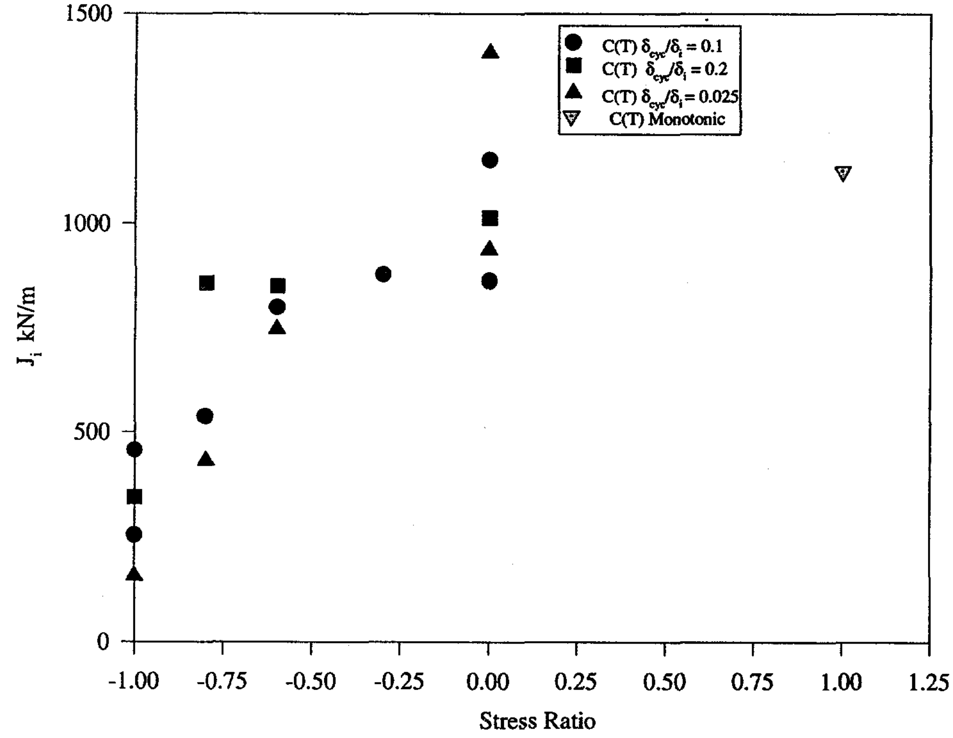

Figure 2.33 J at crack initiation for stainless steel cyclic-load C(T) specimens

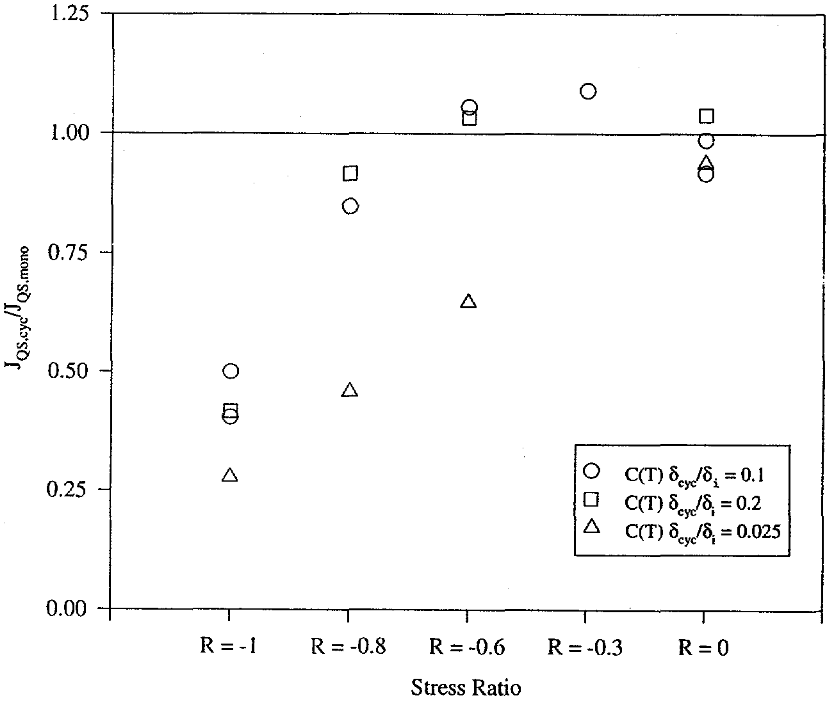

Figure 2.34 $J_{QS,cyc}/J_{QS,mono}$ for stainless steel cyclic-load C(T) specimens

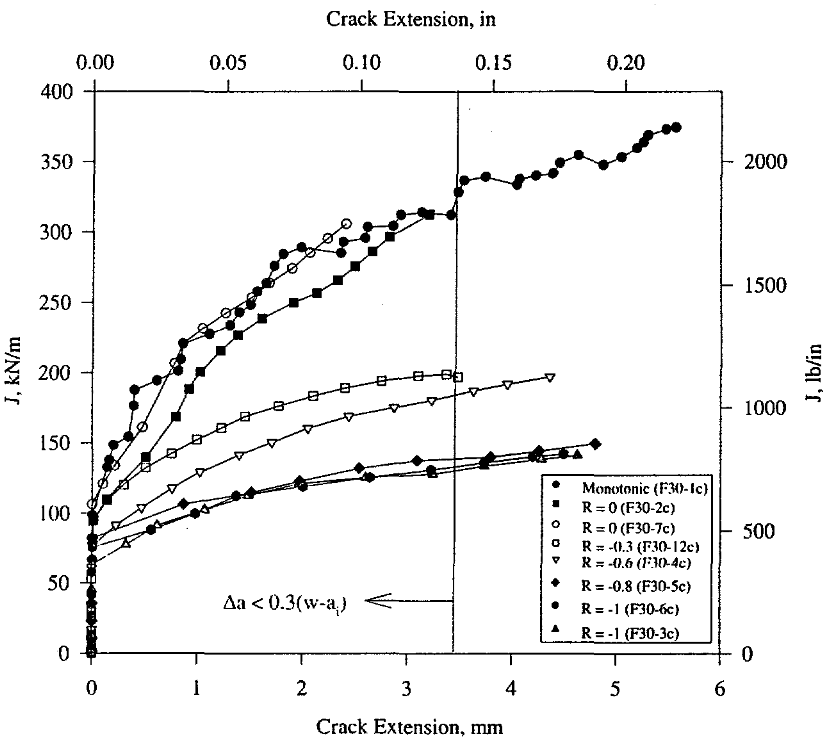

Figure 2.35 Carbon steel cyclic-load J-R curves tested at $\delta_{cyc}/\delta_i = 0.1$

Table 2.7 Cyclic-load fracture toughness summary for carbon steel (DP2-F30) base metal

Specimen	Stress		J at Initiation,		dJ/da,	
Identification	Ratio, R	δ_{cyc}/δ_i	kN/m	lb/in	MN/m^2	lb/in^2
F30-1c	1	N/A[(a)]	98.3	561	79.8	11,430
F30-2c	0	0.1	94.2	537	93.2	13,530
F30-3c	-1	0.1	63.2	360	32.7	4,750
F30-4c	-0.6	0.1	76.4	436	46.2	6,700
F30-5c	-0.8	0.1	82.1	468	21.6	3,150
F30-6c	0	0.1	75.5	431	26.6	3,870
F30-7c	-1	0.1	106.3	606	100.8	14,62
F30-12c	-0.3	0.1	81.4	464	44.2	6,420

(a) Monotonic test.

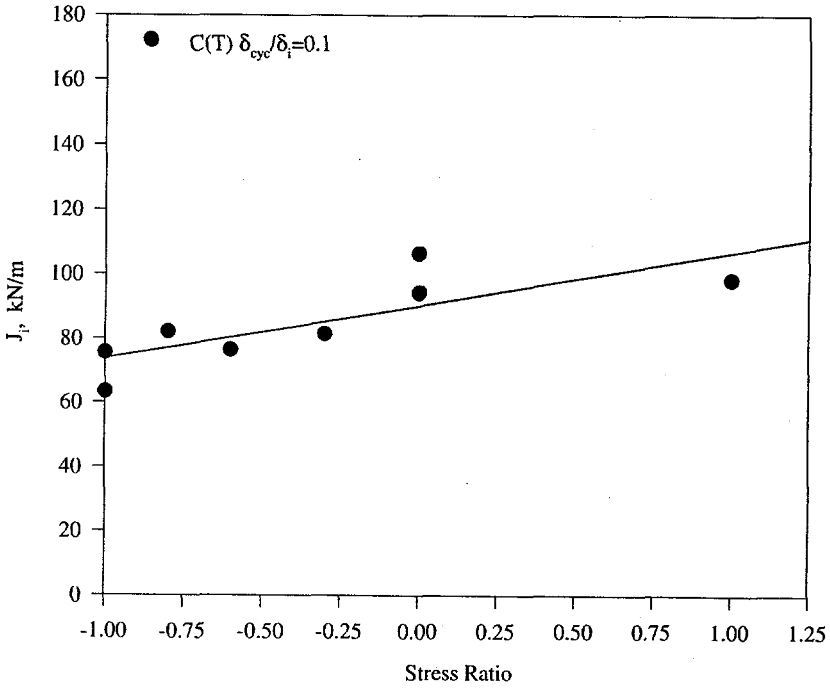

Figure 2.36 J at crack initiation for carbon steel cyclic-load C(T) specimens

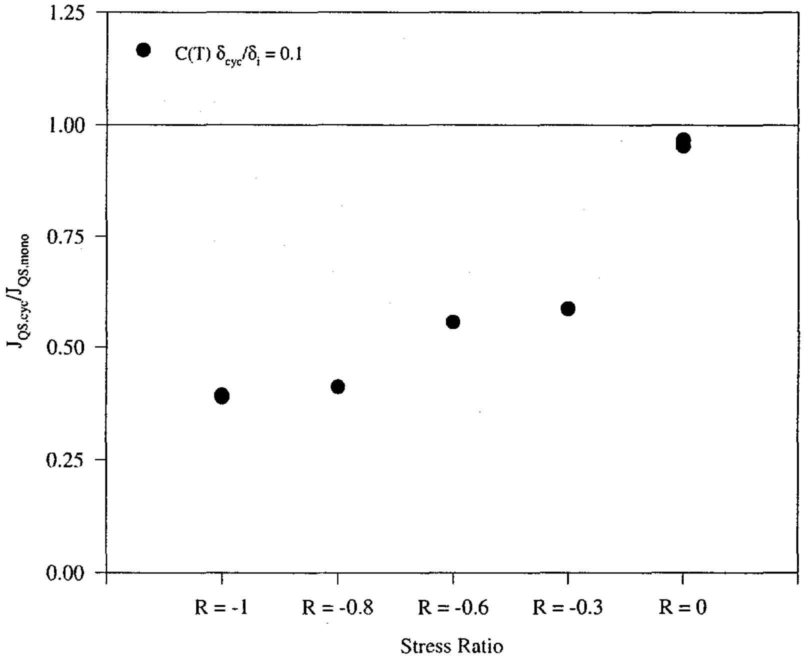

Figure 2.37 $J_{QS,cyc}/J_{QS,mono}$ for carbon steel cyclic-load C(T) specimens

2.3.3 Stainless Steel Weld Metal

Figures 2.38 and 2.39 show the quasi-static and dynamic J-R curves, respectively, for the stainless steel SAW, A8W4. Table 2.8 shows a fracture toughness summary for these tests. The detailed J-R curve will be listed in a future release of the PIFRAC database, Ref. 2.10. From these figures, dynamic monotonic loading increases the resistance of this material as compared to quasi-static loading. Also, there is a noticeable variability in toughness between nominally identical specimens. The differences between the two dynamic, monotonic loading experiments and between the two quasi-static, $R = -1$ specimens is quite large. These differences may be due to weld inhomogeneity.

Figure 2.40 shows the values of J at crack initiation-versus-stress-ratio for the stainless steel SAW. In this figure, the J_i values from the duplicate specimens have been averaged. The dynamic loading in monotonic tests increased the J_i value of this material by a factor of about 2.5. As mentioned before, these data were taken from Reference 2.2 and a high degree of variability existed between the three dynamic C(T) specimens tested in that reference. Cycling this material at quasi-static rates did not influence the J at crack initiation considerably. As shown in Figure 2.40, the J_i values decreased only slightly when tested at $R = -1$. However, there was a considerable change in J_i when the material was cycled at dynamic loading rates. Under these conditions, the J_i value decreased by more than a factor of 3 when it was cycled at $R = -1$. Even when the lower bound J_i value from Reference 2.2 is considered, the J_i value still decreased by a factor of 2.2. This result indicates that for this weld, the beneficial increase in resistance due to dynamic loading is counteracted by a larger decrease due to cyclic loading.

Figure 2.41 shows $J_{QS,cyc}/J_{QS,mono}$ for the quasi-static and dynamic cyclic-load stainless steel SAW specimens. This normalized toughness value was taken at a crack extension of $0.3(w-a_i)$. Since several of the specimens did not have this amount of crack extension, the J-R curve was extrapolated to this value in order to make this comparison. For the specimens loaded at quasi-static rates, the trend is similar to that seen in the base metal specimens. As the stress ratio is decreased, the relative value of J also decreases. However, under dynamic loading the trend is slightly different. It appears that the dynamic loading makes this material more sensitive to intermediate stress ratios. There is a much larger decrease in J at dynamic $R = -0.6$ rates than at quasi-static $R = -0.6$ rates. This contradicts the trends seen in the base metals. The carbon steel base metal, which was less tough than the stainless steel base metal, was more sensitive to intermediate stress ratios. For the stainless steel SAW, the dynamic loading increased the toughness, yet also increased the materials sensitivity to intermediate stress ratios. Also, the relative decrease in resistance at $R = -1$ was the same for both the quasi-static and dynamic loading conditions.

Since most engineers in industry have only quasi-static, monotonic loading data from which to perform their analyses, it is useful to plot these data normalized by the quasi-static, monotonic J values. Figure 2.42 shows these results. This figure shows that the damage done by the cyclic loading outweighs the beneficial increase in resistance due to dynamic loading. As shown in this figure, dynamic loading increased the resistance by 88 percent, while the quasi-static, $R = -1$ loading decreased the resistance 65 percent as compared to the monotonic value. If the combined dynamic, cyclic effect was a linear combination of the two individual effects, the result would be a 23 percent increase ($1.88 - 0.65 = 1.23$) in resistance compared to the quasi-static monotonic resistance. However, as shown in Figure 2.42 the dynamic, cyclic resistance was 40 percent lower than the quasi-static monotonic resistance. This indicates that the separate effects from dynamic and cyclic loading are not additive, and the combined effect is detrimental.

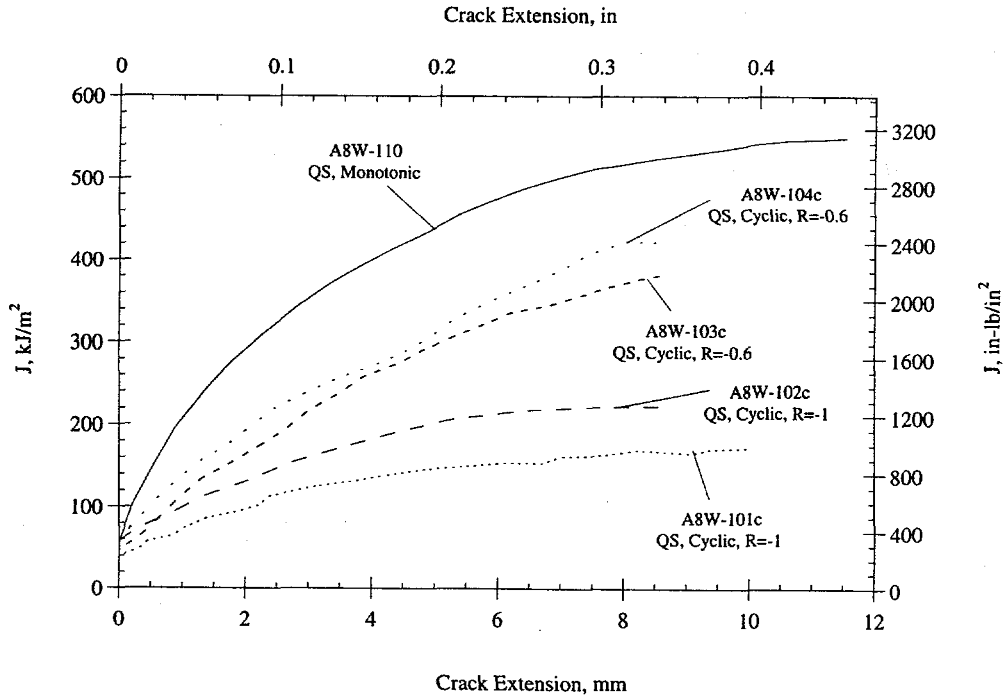

Figure 2.38 Quasi-static J-R curves for the stainless steel SAW (A8W4)

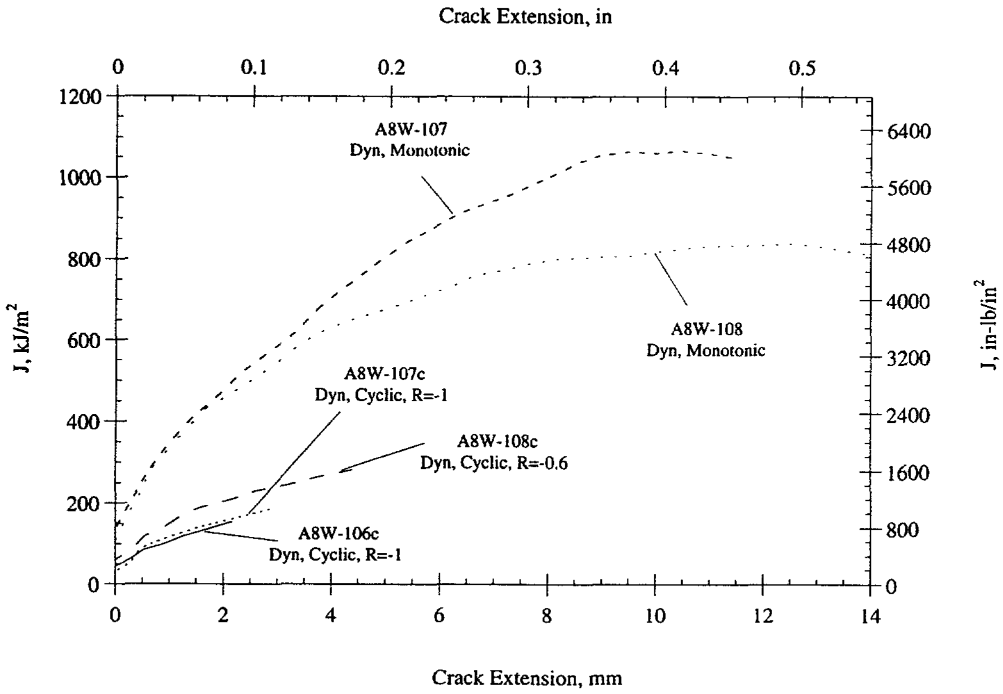

Figure 2.39 Dynamic J-R curves for the stainless steel SAW (A8W4)

Table 2.8 Fracture toughness summary for stainless steel SAW (A8W4)

Specimen ID	Loading Rate	Stress Ratio, R	δ_{cyc}/δ_i	J at Initiation, kN/m	J at Initiation, lb/in	dJ/da, MN/m²	dJ/da, lb/in²
A8W4-110[a]	QS	1	N/A[b]	55	315	135	19,550
A8W4-107[a]	Dyn	1	N/A[b]	140	800	180	26,140
A8W4-101c	QS	-1	0.1	39	225	30.2	4,380
A8W4-102c	QS	-1	0.1	57	328	38.3	5,560
A8W4-103c	QS	-0.6	0.1	46	265	72.9	10,570
A8W4-104c	QS	-0.6	0.1	59	336	62.6	9,080
A8W4-106c	Dyn (4Hz)	-1	0.1	47	254	55.0	7,980
A8W4-107c	Dyn (4Hz)	-1	0.1	34	192	46.8	6,790
A8W4-108c	Dyn (4Hz)	-0.6	0.1	61	343	72.6	10,530

(a) Data taken from Reference 2.2
(b) Monotonic test.

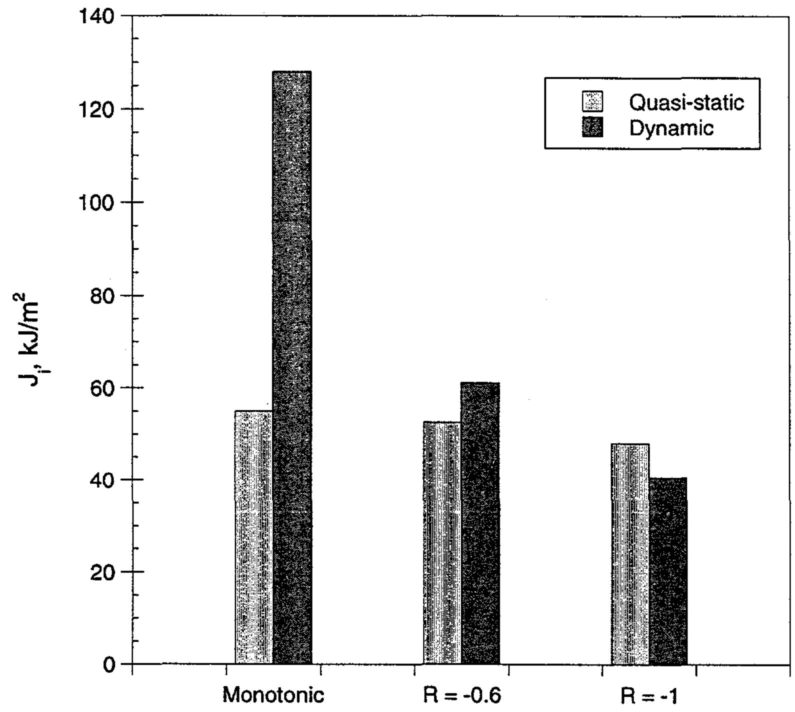

Figure 2.40 J at crack initiation versus stress ratio for the stainless steel SAW (A8W4)

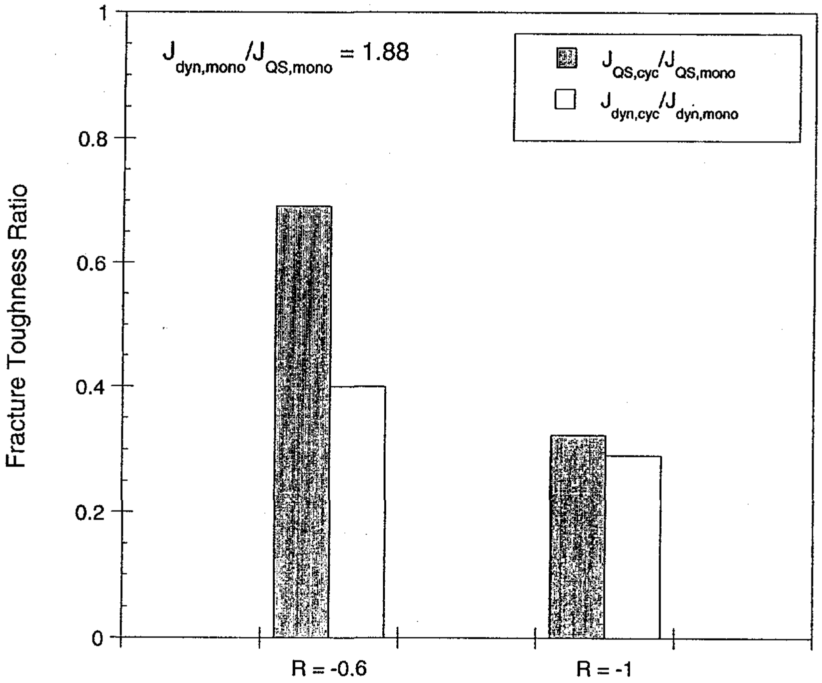

Figure 2.41 Fracture toughness ratios at corresponding load rates versus stress ratio for the stainless steel SAW (A8W4)

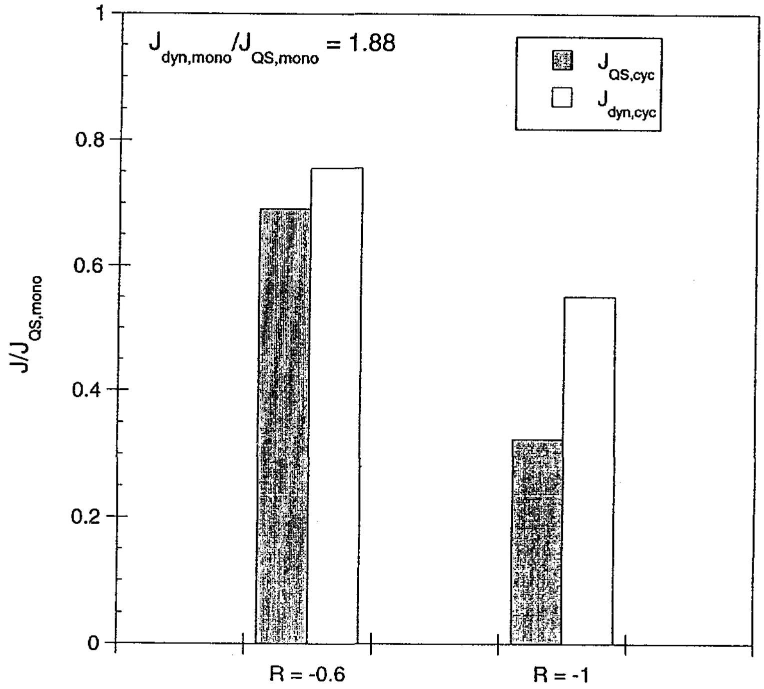

Figure 2.42 $J_{QS,cyc}/J_{QS,mono}$ versus stress ratio for the stainless steel SAW (A8W4)

2.3.4 Carbon Steel Weld Metal

Figures 2.43 and 2.44 show the quasi-static and dynamic J-R curves, respectively, for the carbon steel weld metal, F40W. Table 2.9 shows a fracture toughness summary for these specimens. The tabulated J-R curves will be listed in a future release of the PIFRAC database (Ref. 2.10). As in the stainless steel SAW, the dynamic loading increased the resistance significantly, as compared to the quasi-static monotonic loading experiment. Also, there is some variability in toughness between nominally identified specimens.

Figure 2.45 shows the values of J at crack initiation versus stress ratio for the carbon steel SAW. In this figure, the J_i values from the duplicate specimens have been averaged. For this weld, the dynamic loading slightly decreased J_i as compared to the quasi-static, monotonic loading. As the stress ratio was decreased, the J_i value decreased for both the quasi-static and dynamic loading. In contrast to the stainless steel SAW, the initiation resistance decreases whether the specimen was loaded at quasi-static or dynamic loading rates.

Figure 2.46 shows $J_{QS,cyc}/J_{QS,mono}$ for these carbon steel SAW specimens. This normalized toughness value was taken at a crack extension of 0.3(w-a_i), which is the maximum allowable crack extension in a C(T)

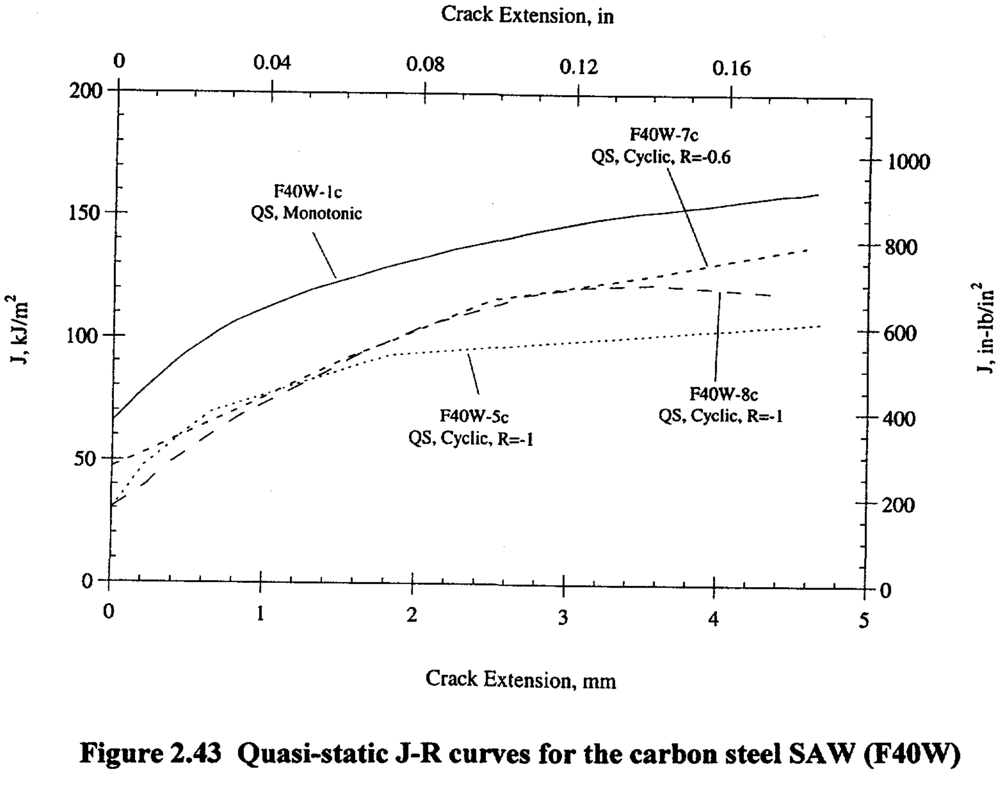

Figure 2.43 Quasi-static J-R curves for the carbon steel SAW (F40W)

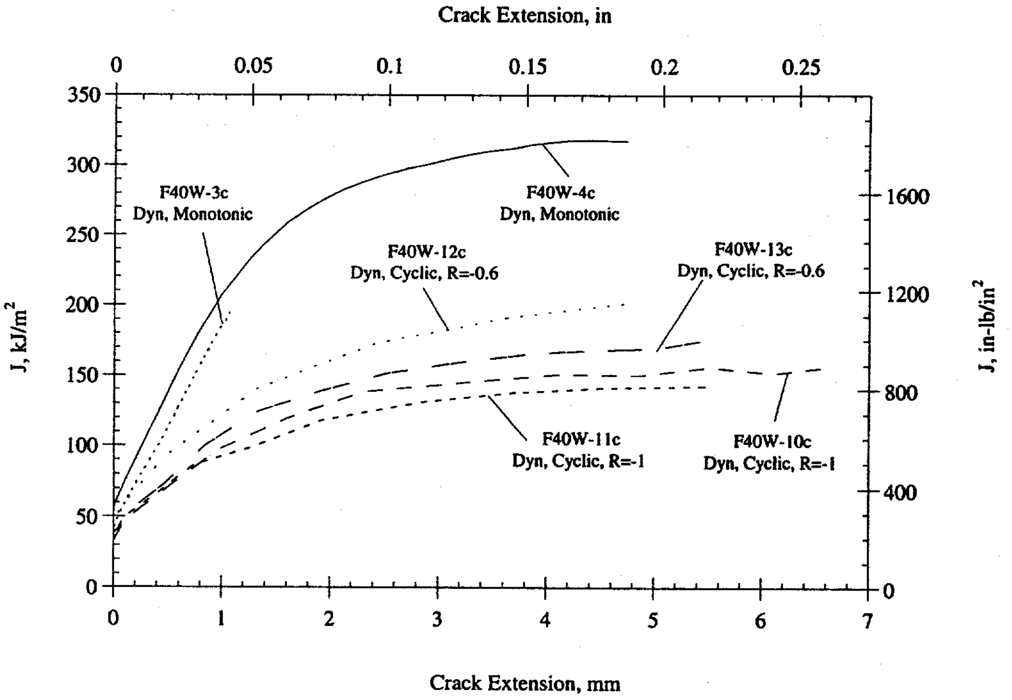

Figure 2.44 Dynamic J-R curves for the carbon steel SAW (F40W)

Table 2.9 Fracture toughness summary for carbon steel SAW

Specimen ID	Loading Rate	Stress Ratio, R	δ_{cyc}/δ_i	J at Initiation, kN/m	J at Initiation, lb/in	dJ/da, MN/m^2	dJ/da, lb/in^2
F40W-1c	QS	1	N/A[(a)]	65.5	374	29.3	4,250
F40W-4c	Dyn	1	N/A[(a)]	56.4	322	113.2	16,400
F40W-5c	QS	-1	0.1	30.1	172	26.2	3,800
F40W-7c	QS	-0.6	0.1	47.3	270	29.3	4,250
F40W-8c	QS	-1	0.1	30.3	173	33.6	4,870
F40W-10c	Dyn (4 Hz)	-1	0.1	38.6	220	43.3	6,280
F40W-11c	Dyn (4Hz)	-1	0.1	33.7	192	37.2	5,390
F40W-12c	Dyn (4Hz)	-0.6	0.1	48.5	277	56.5	8,190
F40W-13c	Dyn (4Hz)	-0.6	0.1	33.4	191	58.8	8,530

(a) Monotonic tests.

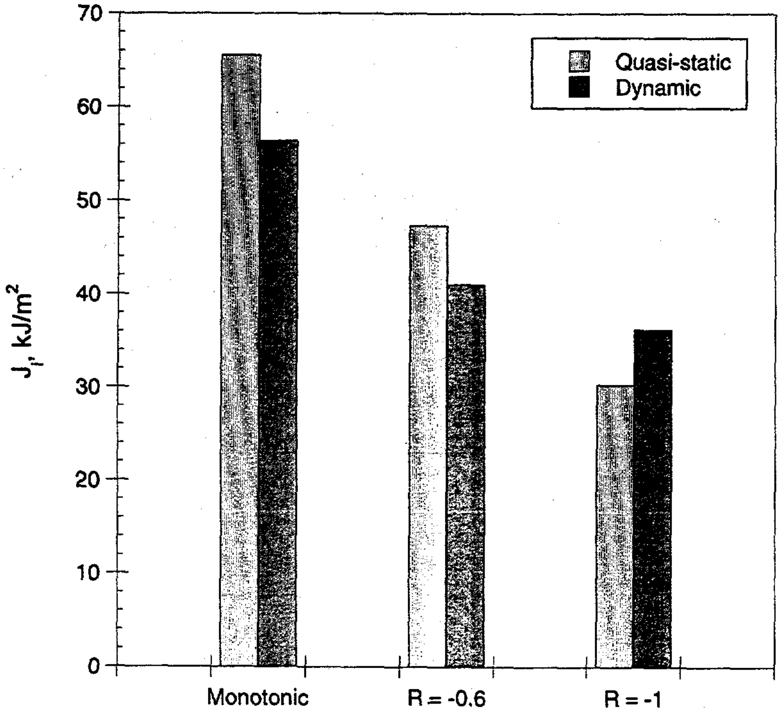

Figure 2.45 J at crack initiation versus stress ratio for the carbon steel SAW

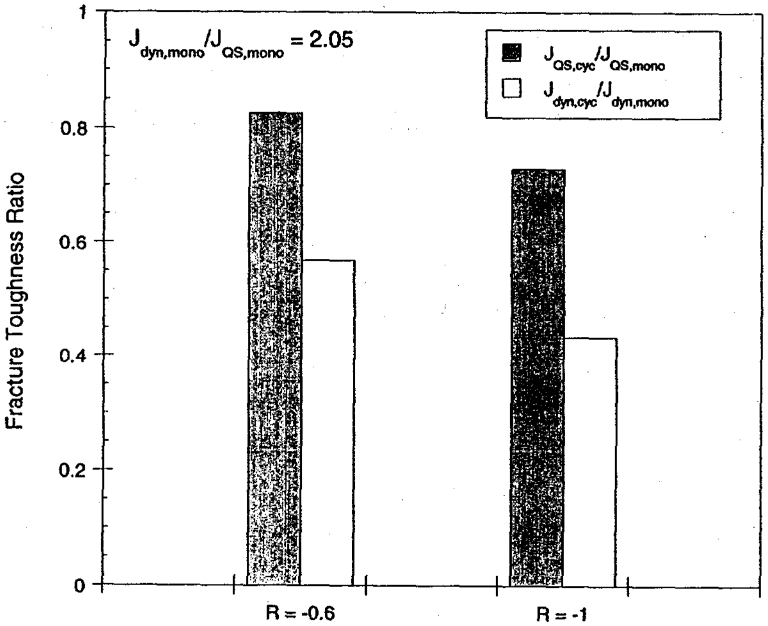

Figure 2.46 Fracture toughness ratios at corresponding load rates versus stress ratio for the carbon steel SAW (F40W)

experiment (Ref. 2.9). In relative terms, the cyclic loading was more detrimental under dynamic loading than it was under quasi-static loading. A 20-percent difference in the amount of toughness degradation is present just by increasing the loading rate. Even though the dynamic loading produced a resistance that was 105 percent higher than the quasi-static resistance, the quasi-static, R = -1 loading produced a resistance that was 25 percent lower than the monotonic resistance. Using the same logic as before, if the effects can be summed, then the dynamic, cyclic loading would produce a resistance that was 80 percent higher than the quasi-static, monotonic loading resistance; however, as shown in Figure 2.46, the resistance at R = -1 dynamic loading was 60 percent lower than the resistance under dynamic, monotonic loading.

Figure 2.47 shows $J/J_{QS\ mono}$ versus stress ratio for the carbon steel SAW. Interestingly, the resistance during the dynamic, R = -1 loading was 5 percent lower than the quasi-static monotonic loading. This shows that this material had the same trend as the stainless steel SAW. The effect of cyclic, dynamic loading on the resistance of these welds is not equal to the sum of the effect of dynamic, monotonic loading and quasi-static, cyclic loading.

2.3.5 Mechanism of Toughness Degradation from Cyclic Loading

In this investigation, a series of cyclic-load C(T) tests was conducted to help define the mechanism that leads to the toughness degradation that occurs during cyclic loading. These cyclic tests were conducted on stainless and carbon steel base and weld metals. The majority of these tests were performed at quasi-static rates in order to study only the cyclic-load effects. However, a group of experiments was conducted at

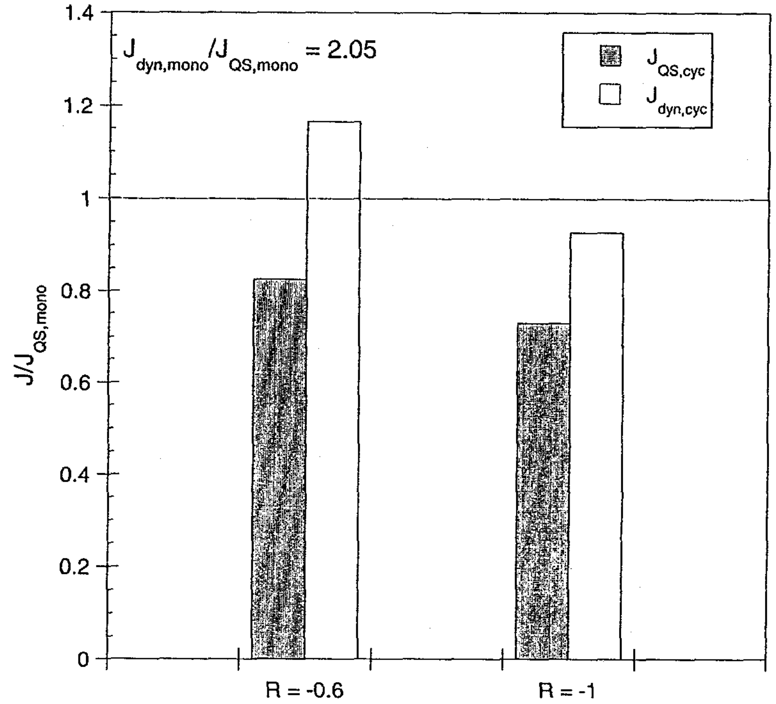

Figure 2.47 $J/J_{QS,mono}$ versus stress ratio for the carbon steel SAW (F40W)

dynamic, cyclic loading rates on carbon steel and stainless steel welds in order to study the interaction between the dynamic effects and the cyclic effects on the fracture toughness of these materials. Accordingly, this discussion is separated into two parts, the first on the cyclic effects and the second on the combined cyclic and dynamic effects.

2.3.5.1 Quasi-static Cyclic-Loading Effects

As a specimen is cycled, fatigue damage is accumulated. In the specimens tested in this study for which $\delta_{cyc}/\delta_i = 0.025$, the maximum number of cycles was approximately 100. At this number of cycles, it is likely that fatigue crack growth is a small portion of the amount of crack extension. However, for the $\delta_{cyc}/\delta_i = 0.2$ case where the maximum number of cycles is approximately 10, fatigue crack growth is not an issue. If these two cases are used as a guideline, then there are two effects that are contributing to the decrease in the apparent crack resistance. The first is fatigue. As stated earlier, Landes and McCabe (Ref. 2.6) developed a model which accounts for this effect. They stated that the crack extension from fatigue can be summed directly with the ductile tearing crack extension to obtain the total crack extension.

The second effect is damage due to reverse plasticity. For the $\delta_{cyc}/\delta_i = 0.2$ case, where the number of cycles is small, fatigue crack growth is not an issue. However, at $R = -1$ there is a severe drop in apparent fracture toughness. It has been shown metallographically that the fully reversed loading severely sharpens the crack and flattens the voids ahead of the crack tip. This sharpening tends to increase the crack tip stress intensity, promote crack growth, hence lowering the apparent fracture toughness.

The main difference between the behavior of the two base materials under cyclic loading is the effect of an intermediate stress ratio. Both materials were unaffected at $R = 0$ and both were significantly affected at $R = -1$. In the carbon steel, which is less ductile than the stainless steel, the slightest amount of negative load seems to decrease the apparent fracture toughness. From these results, it can be hypothesized that the amount of damage caused by intermediate stress ratios is highly dependent on the individual material properties. The stainless steel base metal is a very ductile material. During the tensile cycles, the crack tip is severely blunted, as was shown in the metallographic analysis. Upon unloading, it takes a fully reversed condition to compress the blunted crack enough to cause damage. On the other hand, the carbon steel did not blunt as severely upon tensile loading. During the compressive cycle, not as much reverse plasticity is required to damage the crack tip. For both materials tested at $R = -1$, the apparent fracture toughness decreased the same percentage as compared to the monotonic result, indicating that there is a threshold to the reduction in load-carrying capacity.

The trends observed for the quasi-static, cyclic-load weld specimens were similar to those for the base metal. The quasi-static stainless steel weld experiments showed practically no effect of stress ratio on the initiation value of J, while the carbon steel SAW showed an almost linear decrease in J_i with decreasing stress ratio. After some crack extension, both materials showed a decrease in the relative value of J with decreasing stress ratio. The stainless steel SAW showed a much larger degradation, with a J value at $R = -1$ of approximately 30 percent of the quasi-static monotonic J value. The degradation in the carbon steel SAW was smaller, with the $R = -1$ experiment producing a J value about 66 percent of the quasi-static, monotonic J value. Even though no microstructural analyses were performed on these welds, it can be assumed that the same mechanisms described above are causing the cyclic degradation.

These quasi-static cyclic results are plotted versus the material's yield-to-ultimate strength ratio in Figure 2.48. Note that the data shown in Figure 2.48 represents only the data at $R = -1$, and at a crack

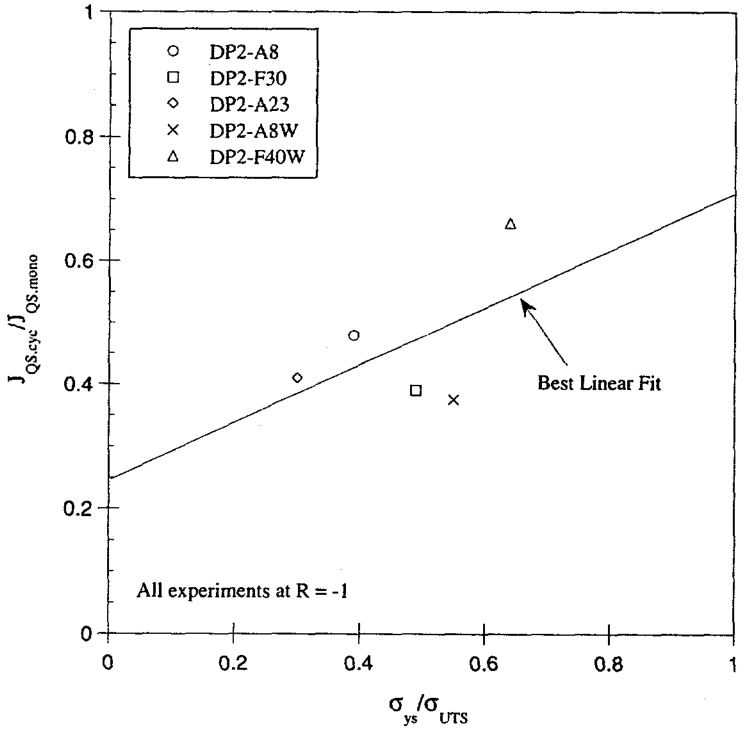

Figure 2.48 Quasi-static $J_{QS,cyc}/J_{QS,mono}$ versus yield-to-ultimate strength ratio

extension equal to 30 percent of the original ligament with the average of duplicate test data taken. The solid line in Figure 2.48 represents the best linear fit for the data shown. There appears to be a linear trend forming between the material's yield-to-ultimate strength and its reduction in toughness due to cyclic loading. However, the limited data hinder the formulation of a reliable criterion to predict the cyclic effects on fracture toughness.

2.3.5.2 Dynamic, Cyclic Loading Effects

Even though Section 3 deals directly with the effects of loading rate on the tensile and fracture toughness properties, it is necessary to discuss the combined effects of cyclic and dynamic loading here. As described earlier, the tests performed in Task 3 showed that the combined effects of dynamic and cyclic loads are not strictly additive. For example, the stainless steel weld, whose dynamic monotonic resistance was 88 percent higher than its quasi-static monotonic resistance, had a quasi-static, R = -1 resistance that was 65 percent lower than the quasi-static monotonic resistance. A direct summation of these effects would produce a dynamic, R = -1 resistance that was 23 percent higher (1.88 - 0.65 = 1.23) than the quasi-static resistance; however, the dynamic, R = -1 experiment had a resistance that was 40 percent lower than the quasi-static, monotonic resistance.

In Reference 2.3, a series of dynamic, cyclic-load experiments was conducted on 6-inch TWC pipe. Figure 2.49 shows a comparison of those results with the dynamic cyclic-load, weld results from this investigation. The trends shown in the dynamic, cyclic-load C(T) experiments are similar to the base metal TWC pipe experiments. The main difference is that in the base metal, the dynamic, monotonic loading did not significantly increase the resistance of those materials as compared to the quasi-static monotonic loading experiments. Actually, for the carbon steel base metal, the resistance dropped significantly. This

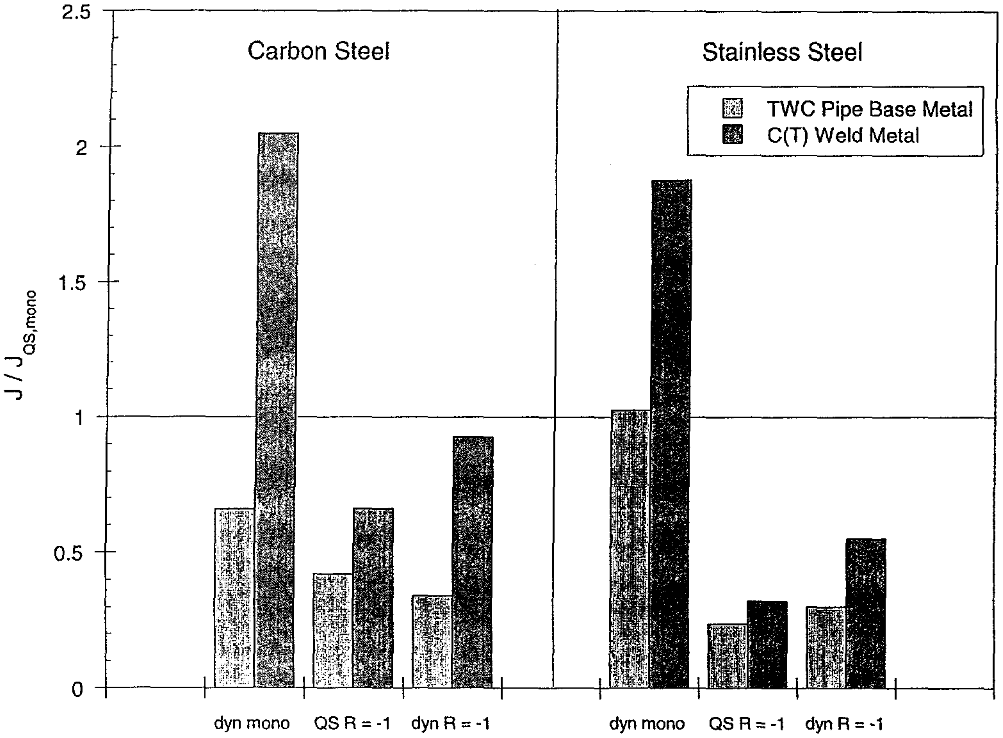

Figure 2.49 Comparison of SAW C(T) J-R results with IPIRG-1 base metal TWC pipe J-R results

effect is due to dynamic strain aging and is discussed in Section 3.0 of this report. Taking this difference into account, the trends shown are very similar. For the carbon steel base metal, the J at $\Delta a = 0.3\ (w-a_i)$ under dynamic loading was 65 percent of the quasi-static, monotonic J at the same Δa, while the J at $\Delta a = 0.3\ (w-a_i)$ quasi-static, cyclic loading was 40 percent of the quasi-static, monotonic J at the same Δa. Under dynamic cyclic loading, the J at $\Delta a = 0.3\ (w-a_i)$ was 30 percent of the quasi-static monotonic J at the same Δa. Even though the effects are not strictly additive, the trends are consistent.

In Section 4.0 of this report, the base metal cyclic-load J-R curves are compared to the base metal TWC pipe J-R curves from Reference 2.3. Also, a series of moment predictions using a variety of J-estimation schemes using the cyclic-load J-R curves is presented. In Reference 2.11, the cyclic weld J-R curves presented here are used in making moment predictions for surface-cracked pipe experiments conducted in the IPIRG-1 and IPIRG-2 programs. The conclusions from those analyses suggest that even though using quasi-static J-R curves predicted welded pipe maximum loads within 15 percent, using the dynamic, cyclic-load J-R curves predicted the welded pipe response within 5 to 10 percent. However, since the standard deviation of these estimation schemes is between 5 and 15 percent (Ref. 2.12) it is difficult to make a general conclusion about which J-R curve produces the best prediction of experimental moments.

2.3.6 Finite Element Analysis

In order to predict the experimental loads and verify the calculations of J from the ASTM E813/1152 Standard, a series of two-dimensional finite element analyses was conducted. Questions addressed as part of the analysis studies include:

- Can the load response be predicted accurately using the finite element method?

- How do the constitutive laws affect the predicted response?
- How are the plastic zones affected by cyclic loading?
- How does the J-resistance curve as predicted from analysis compare with the experimental results?
- Is the engineering method for accounting for cyclic tearing effects on pipeline steels adequate?

Two plasticity laws were selected for use in these studies; the classical isotropic and kinematic hardening laws. The first C(T) specimen chosen to be modeled in these analyses was a stainless steel specimen tested at 288 C (550 F) with a displacement increment of 0.1 and a stress ratio of -1 (Specimen A23-5c). This specimen experienced crack initiation on the sixth loading cycle. Test data from this specimen are shown in Figure 2.11. The second specimen modeled was the specimen used in the metallographic study for loading up to Point C (A23-10c) in Figure 2.10. Each specimen was modeled with both plasticity laws and assuming plane stress conditions. The first specimen was also modeled assuming generalized plane strain conditions. The results of these models were then compared directly with the experimental data.

2.3.6.1 Analysis Procedure

The ABAQUS finite element code was used to perform the analyses. Eight-noded isoparametric quadrilateral elements were used with reduced integration and the plane-stress assumption. Classical plasticity theory and isotropic and kinematic hardening were used. Originally, the Ohno cyclic plasticity constitutive law (Ref. 2.17) was intended to be used for one of the analyses. The material constants for the Ohno law were developed for the TP304 stainless steel material at 288 C. The law was coded as an ABAQUS USER routine. However, it was found that the law, while performing well for simple geometries such as the uniaxial bar or biaxially loaded specimen, was numerically unstable for the crack problem since the stresses near the crack tip become so large. Hence, the analyses using the Ohno law were abandoned.

Crack growth for Specimen A23-5c was modeled using a node release technique. Since the eight-noded elements were used, both nodes along the crack plane were released simultaneously during crack growth through an element. The finite element mesh used is shown in Figure 2.50a. As can be seen, only one half of the specimen is modeled to take advantage of symmetry. Observing the load pin region in Figure 2.50a, it is seen that four triangular elements are used for the positive (upward in Figure 2.50a) load application in the model and four are used for the negative load application. Two nodes are at the center of the hole; one attached to the top four triangular elements and one attached to the bottom four elements so that, as the load pin region deforms, the two sets of triangular elements separate, as occurs in an experiment performed using load pins. The stiffness and yield stress of these load elements was made artificially high so that plastic straining of the "load pins" could not occur. This provides a more realistic representation of the experiments. Other approaches were used to model the load pin effect such as using rigid surfaces and load elements for the load pin; however these approaches did not perform as well. The symmetry plane (at the bottom of Figure 2.50a) had gap elements placed in case crack face contact occurred during the unloading phase. However, as will be seen in the results presented later, the zone of contact was very small and occurred only after crack growth very near the crack tip. This small zone of contact is a consequence of the very ductile nature of TP304 stainless steel at 288 C.

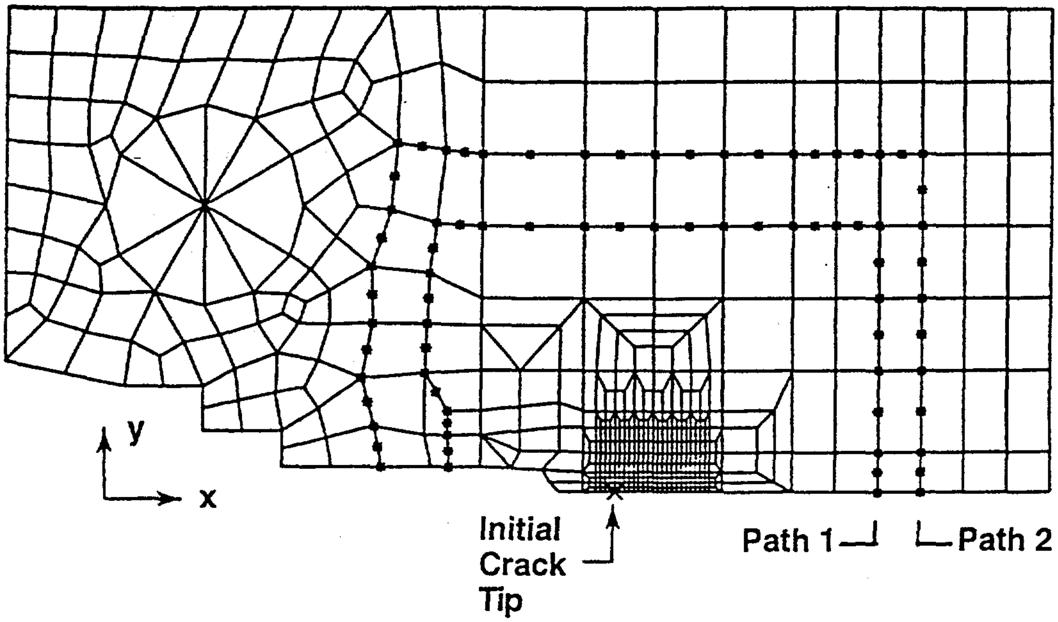

Figure 2.50a Finite element mesh used in analyses illustrating far field path definition

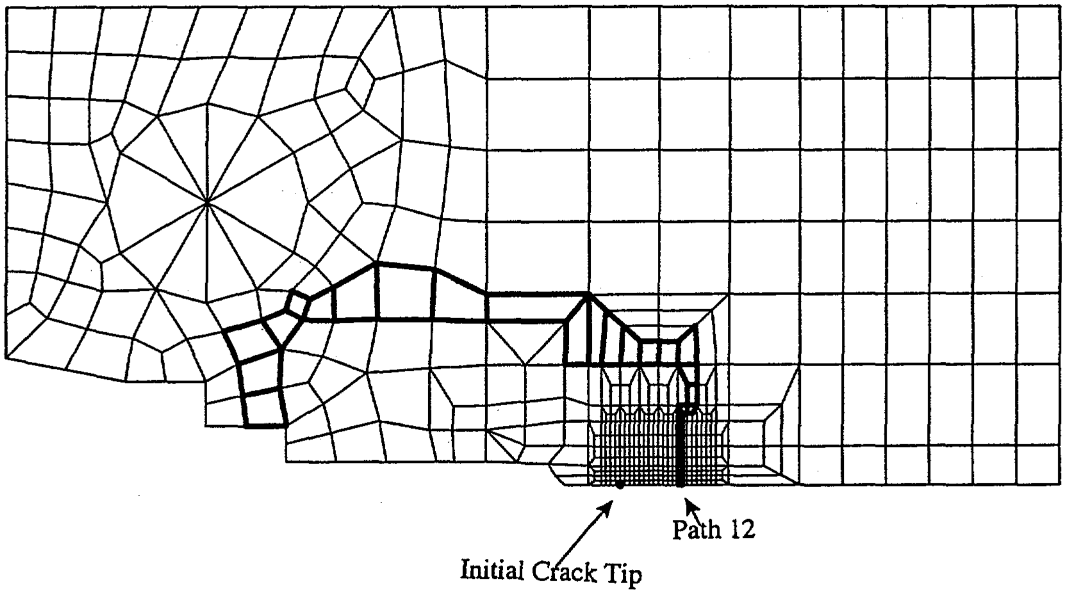

Figure 2.50b ABAQUS J-path definition for Path 12

The J-integral was evaluated using Battelle's T-Post ABAQUS post processor, which evaluates integral parameters for growing crack tips (e.g., J, CMOD, T^*, etc.). T-Post uses a domain integral method to calculate the integral parameters. The ABAQUS J-integral routine could not be used here because of the large amount of crack growth that was modeled and the method ABAQUS uses to define the paths. With T-Post, truly far-field paths could be defined. The crack-tip-opening angle was also evaluated using the displacements of the corner nodes behind the growing crack tip divided by the distance to the crack tip.

It is useful to point out the issues regarding the calculation of the J-integral by ABAQUS at this point. ABAQUS defines its own paths for evaluating J as follows. For a two-dimensional problem, the user inputs the crack-tip location as well as the number of paths along which the user wishes to calculate J. ABAQUS then defines the paths by taking rings of elements which are increasingly larger and encircle the crack tip. The rings are not uniformly sized because they depend on the mesh definition. Figure 2.50b illustrates the definition of the 12th path, as defined by ABAQUS using this procedure. The crack tip is also illustrated. At the inner surface of this 'ring' the 's' value for the Equivalent Domain Integral (EDI) (or the virtual crack vector) is defined as 1. All values of 's' within this region are likewise defined as 1. At the outer 'ring' the 's' value is zero, and 's' varies linearly within the element. As can be seen, for Path 13, the path definition would reach the load pin. The value of J for paths reaching the load pin are incorrect. Hence, 12 is the maximum path definition for this mesh. However, as can be seen, for Path 12, the path passes elements only 12 elements ahead of the original crack tip, i.e., the path definition ahead of the crack tip is only 1.8 mm (0.07 inch) (since the crack tip elements are only 0.15 mm (0.006 inch) in size). While this poses no problems for monotonic load problems (unless the crack grows to a size larger than the largest path), for cyclic load problems, the far field values for J cannot be obtained from this mesh since J is extremely path dependent. Hence, the Battelle TPOST program was used as a post processor to evaluate far-field J along the user defined path illustrated in Figure 2.50a. While the far-field value of J was adequately evaluated here, the important issue of the meaning of J under cyclic-load conditions was not addressed. This aspect will be discussed later in this section.

2.3.6.2 Analysis Results for Specimen A23-5c

The input to the analysis of Specimen A23-5c consisted of the crack-opening (load-line) displacement (COD) versus crack growth record, as illustrated in Figure 2.51a. The crack began to grow during the sixth load cycle. Therefore, the first displacement unload shown in Figure 2.51a represents the unload after the sixth load period. The applied displacement for the first five load/unload sequences (before crack growth) are not shown in Figure 2.51a. The analysis was performed up to about 3.5 mm (0.138 inch) of crack growth, after the tenth load period. Note that Figure 2.51a is one-half of the total COD (since the analysis included symmetric boundary conditions). Hence, the crack began growing at a total COD of about 7.9 mm (0.311 inch) (or ½ COD = 3.95 mm (0.156 inch)).

Figure 2.51b illustrates the stress-strain curve for the Pipe DP2-A23 material. As is seen, two curves are shown; one is the actual stress-versus-plastic-strain curve and the other is a straight line which provides an accurate estimate of the stress-strain response up to about 8-percent strain. The linear stress-strain relation was used for most of the analyses provided here. ABAQUS permits only a linear-hardening definition for the stress versus plastic-strain curve when kinematic hardening plasticity is used. Since the objective is to obtain solutions for both kinematic and isotropic hardening, a linear curve was fit (quite accurately as seen in Figure 2.51b) over the early portion of the curve. It is seen that this linear curve is very accurate up to about 8-percent strain. The analysis using the exact stress-strain relation provided load predictions that

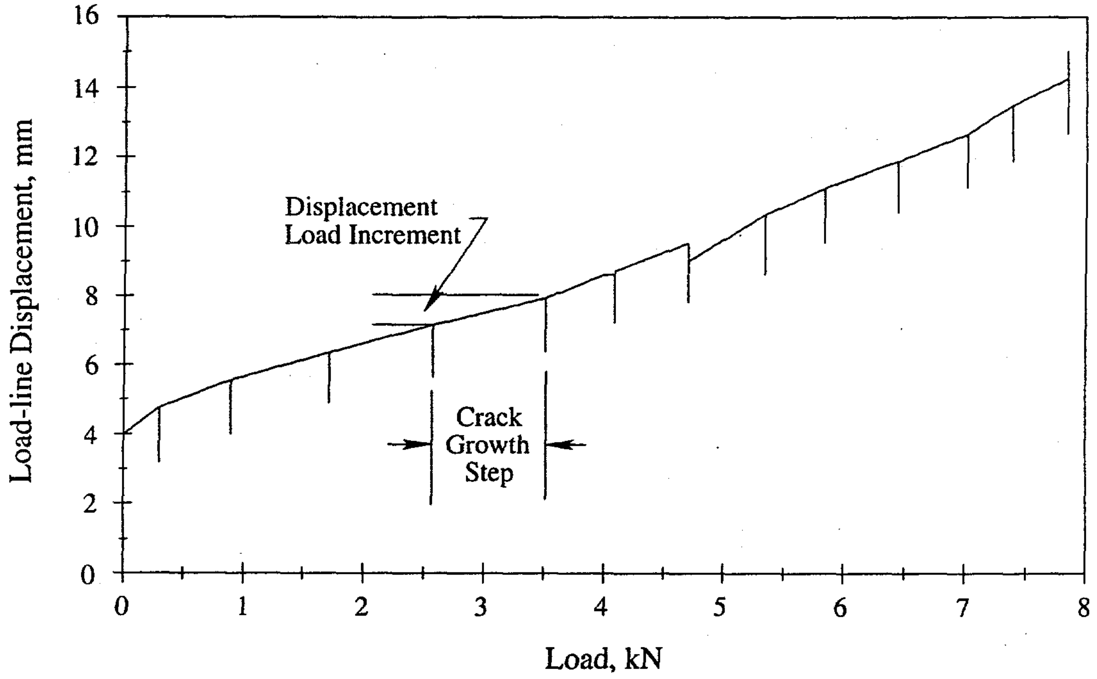

Figure 2.51a Experimental load-line displacement versus crack growth record for Experiment A23-5c used as input to the finite element analysis (Note: load-line displacement shown is one-half the total load-line displacement)

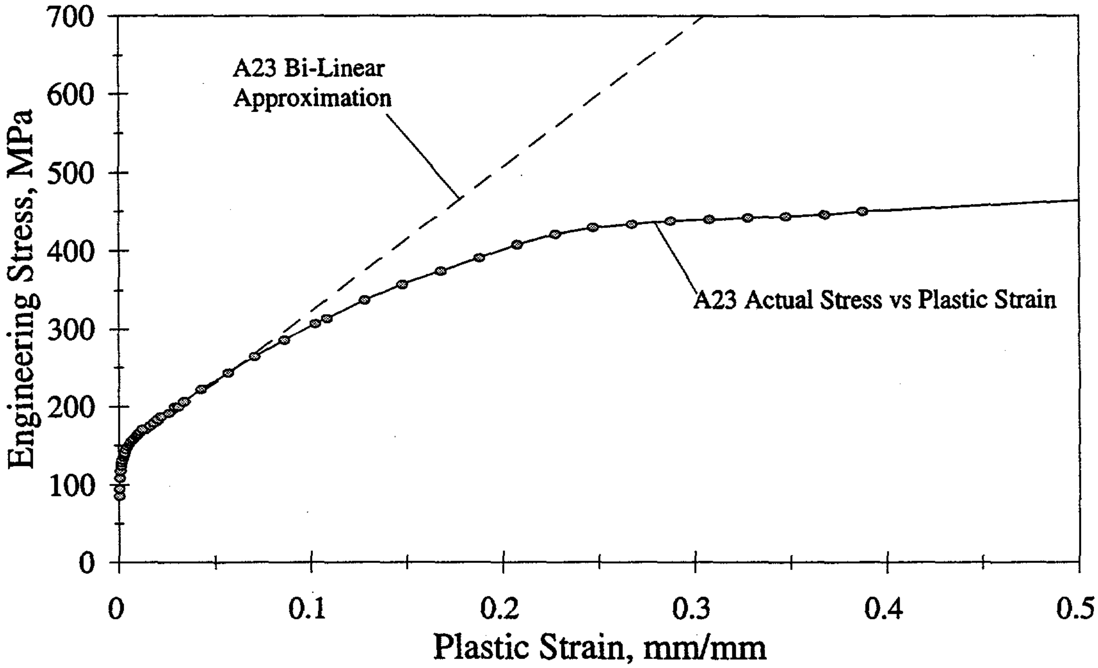

Figure 2.51b Stress-strain curves for TP304 stainless steel (DP2-A23)

were about ten percent lower than the linear curve; however, J values were not affected significantly. This finding will be discussed in some detail later.

Although the analysis was displacement controlled and, hence, loads were predicted and compared to experimental data, the following procedure was found to be most convenient in an ABAQUS framework. Each displacement load sequence was broken into four steps:

(Step 1) The displacement increment, along with the crack growth increment, was applied simultaneously as displacement control to the node attached to the top triangular elements shown in Figure 2.51a. For instance, for the sixth load cycle, a total (half) displacement of 4.8 mm (0.189 inch) was applied while permitting crack growth of 0.3 mm (0.012 inch).

(Step 2) A model change to the ABAQUS input deck was enforced, and the load in this node reduced to zero.

(Step 3) A model change was enforced (changing the condition of the load points from load control back to displacement control) and the displacement of the node attached to the lower set of triangular load point elements was applied based on the experimental unload displacement. Some parts of the crack may close during this phase. For the sixth unload case here, the unload (half) load-line displacement applied was 3.16 mm (0.124 inch), see Figure 2.51a.

(Step 4) A model change to the ABAQUS input deck was then enforced, and the load applied to the lower set of triangles was reduced to zero.

Step 1 was then repeated for the next load and crack growth increment. This approach proved to be by far the most efficient computational method for modeling the cyclic load problem with ABAQUS. None of the other approaches attempted were very efficient for this problem.

Load Versus COD Predictions Figures 2.52a and 2.52b illustrate the finite element predictions of the A23-5c test compared to the experimental results. Figure 2.52a is the predicted result using classical plasticity theory and kinematic hardening while Figure 2.52b illustrates the prediction using isotropic hardening and a bilinear stress-strain curve. Here the total load-line displacement is plotted. For all other results, the total load-line displacement will be plotted in the load curve comparisons.

As seen in Figure 2.52a, the maximum-load prediction using kinematic hardening compares reasonably well to experimental data. All analyses which use the kinematic hardening assumption use a bilinear stress-strain curve. However, the minimum load comparison was very poor. In fact, because the minimum load prediction was so small (in absolute value), the compressive plastic-zone size prediction was extremely small. Notice that during the ninth unloading, the displacement began to move to the left at a load of zero. This prediction was clearly inadequate.

It is believed that the predictions using kinematic hardening are poorer than the corresponding prediction using isotropic hardening since the magnitude of compressive plasticity is greatly underpredicted. Note that because kinematic hardening forces the size of the yield surface to be constant, although translating in space, the opposite effect would occur if a compressive load were performed first, followed by the tensile load; i.e., the compressive loads would compare rather well with experiment while the tensile loads would be greatly underpredicted.

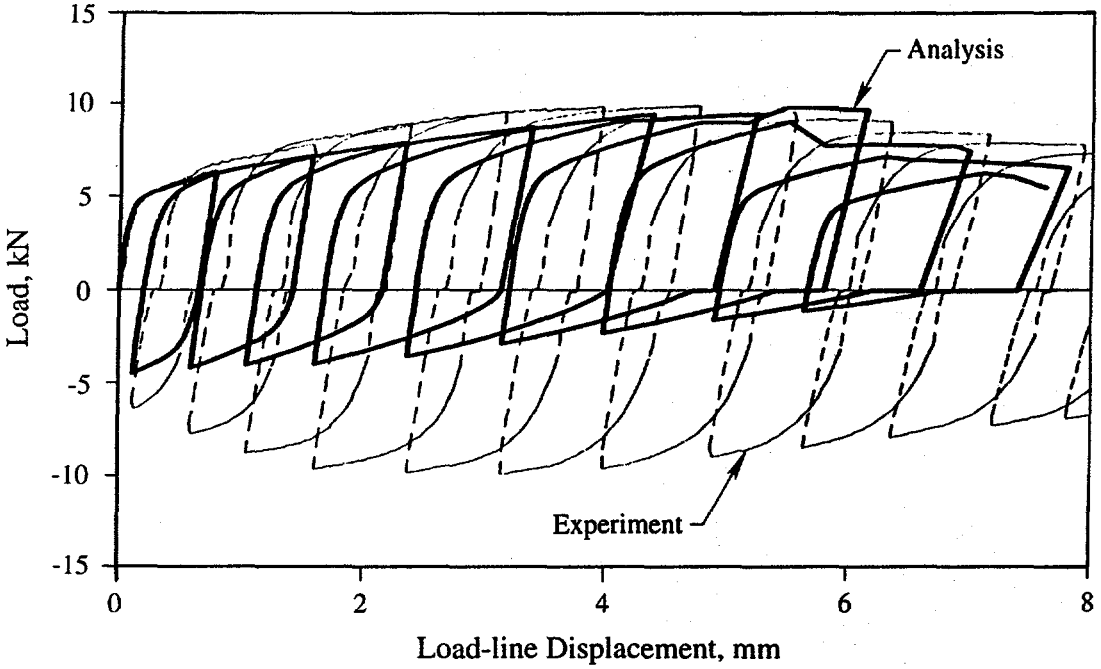

Figure 2.52a Predicted and experimental load-versus-load-line displacement comparison. The plotted load-line displacement represents one-half of the experimental load-line displacement. Classical plasticity theory with kinematic hardening was used

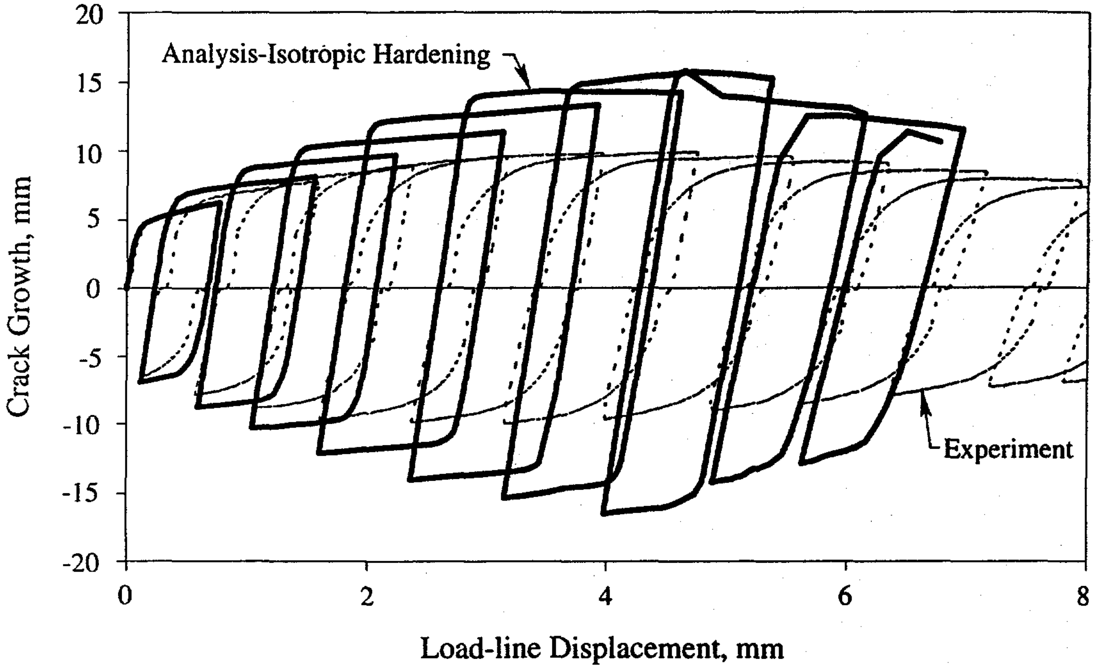

Figure 2.52b Predicted and experimental load-versus-load-line displacemet comparison. The plotted load-line displacement represents one-half of the experimental load-line displacement. Classical plasticity theory with isotropic hardening was used

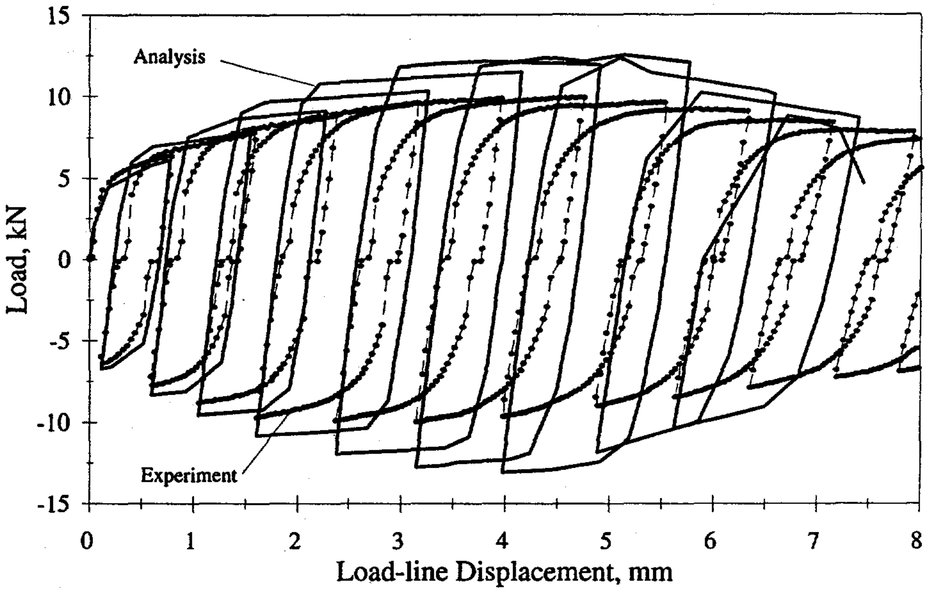

Figure 2.52c Predicted load versus load-line displacement response; actual stress-strain curve used

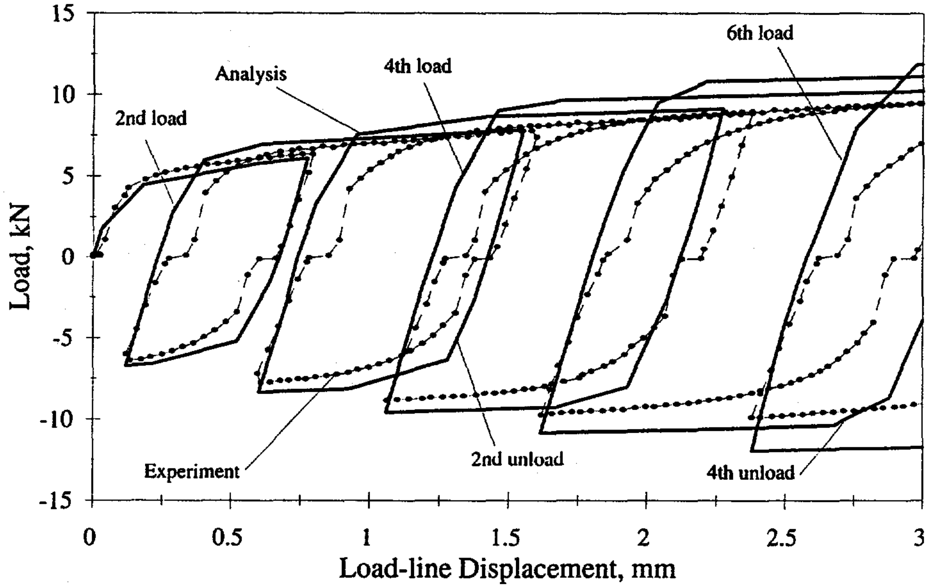

Figure 2.52d Predicted load response over the first six cycles; actual stress-strain curve used

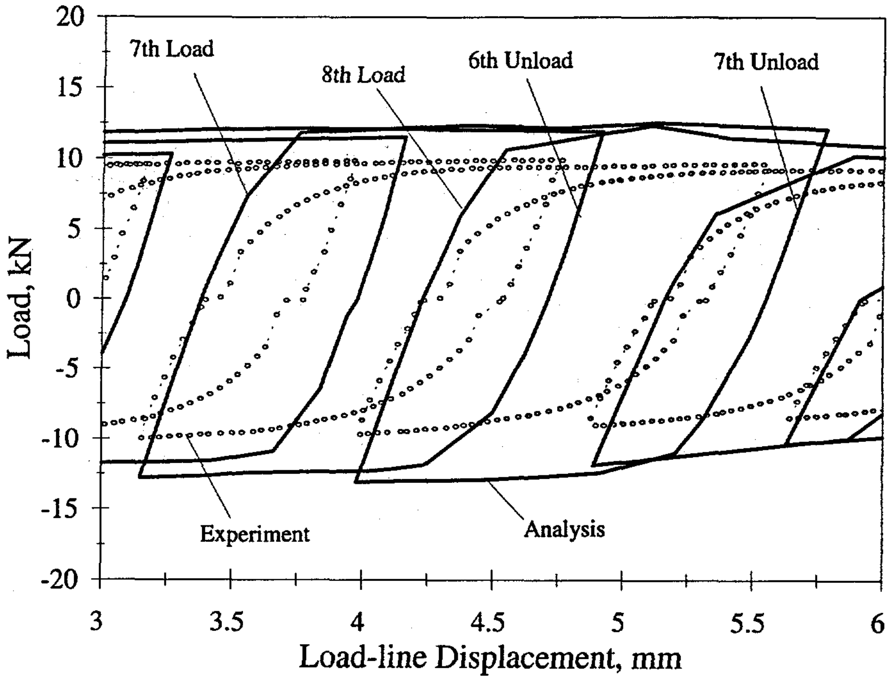

Figure 2.52e Predicted response over the middle portion of analysis, actual stress-strain curve used

The predictions using isotropic hardening, see Figure 2.52b, overpredicted the experimental loads (in absolute value) for both tensile and compressive loads. However, the predictions were quite good for the first several cycles. Moreover, the general trend, while overpredicting, follows the experimental trend better than kinematic hardening and the compressive (reverse) plasticity was captured better. It is clear that a combined isotropic/kinematic hardening law which permits the yield surface to expand (but less so than full isotropic hardening) and translate (but less so than full kinematic hardening) should better capture the trends observed here. However, ABAQUS does not have a combined hardening law.

One additional analysis was performed using the actual stress-strain curve (Figure 2.51b). This actual stress-strain curve represents the material response throughout the entire strain regime. As seen in Figure 2.51b, the bilinear-hardening relation represents the material response up to strains of about 8 percent. The load versus load-line displacement prediction is compared to the experiment in Figure 2.52c. As is seen, predictions are lower in absolute value compared with the analysis results shown in Figure 2.52b (both analyses used isotropic hardening). The predictions using the actual stress-strain response are also closer to the experimental results, although the trends of results in Figures 2.52b and 2.52c are similar. It is seen from Figure 2.52b that the stresses beyond about 8-percent strain can reach higher values with the linear representation compared with the actual curve. Thus, it is not surprising that the predictions (Figure 2.52b) are higher with the linear curve compared with the actual curve (Figure 2.52c). What this also suggests is that a small region within the plastic zone attains strains greater than 8 percent. Figures 2.52d and e provide more detailed predictions of the results when using the actual stress-strain curve. As is seen, these results appear reasonable, although about 20 percent higher in load (in absolute magnitude) compared with the experiment.

Crack-Opening Profiles The crack-opening profiles for both the isotropic and kinematic hardening (linear stress-strain) cases are illustrated in Figures 2.53a and 2.53b, respectively. In Figure 2.53a, the crack profile after the sixth load period (for total crack growth of 0.3 mm (0.012 inch)), and the corresponding sixth unload period can be seen. Notice that, with the isotropic hardening assumption, a contact zone upon unloading is observed. In addition, Figure 2.53a shows the crack profile after the end of the eighth load period (with total crack growth of 1.8 mm (0.071 inch)), the corresponding eighth unload profile, and the profile after the ninth load period. Again, note that a contact zone is predicted very near the crack tip. The analysis using kinetic hardening, as seen in Figure 2.53b for the sixth and ninth load/unload sequences, does not predict crack-face contact at any point. This is not surprising since the compressive loads upon unloading are predicted to be so small. Hence, for kinematic hardening, the effect of crack face contact, which is observed experimentally, is not predicted. Moreover, the size of the compressive plastic zone is likewise greatly underpredicted. For this reason, the plastic-zone-size plots as well as the stress-contour plots discussed in the next subsection do not include predictions using kinematic hardening. Finally, the crack-opening profiles for the analysis using isotropic hardening and the actual stress-strain curve are quite similar to those in Figure 2.53, but slightly larger.

Plastic Zones and Stress Contour Plots Figures 2.54a and 2.54b illustrate the y-direction component of the plastic strain, ϵ_y^p, after the eighth load and unload sequences, respectively. The y-direction is illustrated in Figure 2.50a, and represents the direction perpendicular to the crack. The current crack tip positions, as well as the crack tip position after the sixth and seventh load steps, are also illustrated. Notice that the plastic strains 'pinch' at the region of the seventh unload crack tip position. Moreover, the contours for smaller plastic strains away from this region appear to pinch towards this region as well. This pinching is clearly caused by the unload at the seventh cycle. Notice that the strains are attempting to pinch (Figure 2.54b) near the crack tip region at the location of the crack tip at the 8th load position. Figure 2.55 shows the plastic strain (y-direction) after the ninth load. Again, note the pinching effect at the location of the eighth load crack tip position. This type of plastic zone is not observed for monotonic loaded specimens which experience crack growth. This pinching effect affects the residual stress patterns which develop at the end of the unload points, but its effect on the crack growth process is uncertain at this point.

The y-direction stresses, σ_y, at the end of the fifth load and unload periods (no crack growth as yet) are illustrated in Figures 2.56a and 2.56b, respectively. Figure 2.56a illustrates the classical plane stress condition, apparently not affected significantly by the previous unloads. Figure 2.56b illustrates the large zone of compressive stresses that develop and emanate from the crack tip region. It is also interesting to observe the stress state near the load-pin region in these figures. Note, in Figure 2.56a the upper triangular load elements are stressed (end of load period), and Figure 2.56b shows the lower triangular elements are stressed.

Finally, Figures 2.57a and 2.57b illustrate the stress state after the ninth load and unload sequence, respectively, after 2.7 mm (0.106 inch) of crack growth has occurred. Note that the contours 'skew' to the left, or in the direction opposite to the crack growth direction. Again, note the large zone of compressive stresses which develop after the unload periods. These contours, too, are skewed to the left.

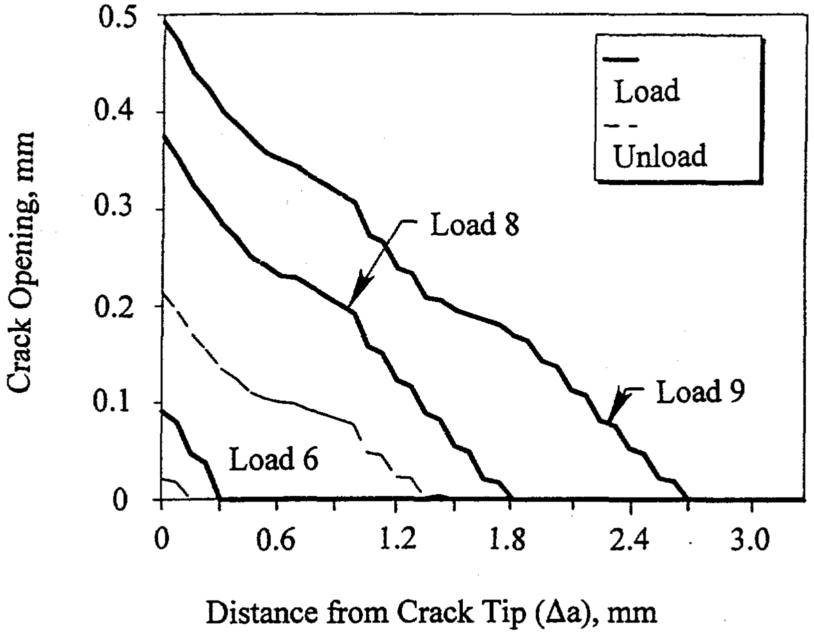

(a) Isotropic hardening

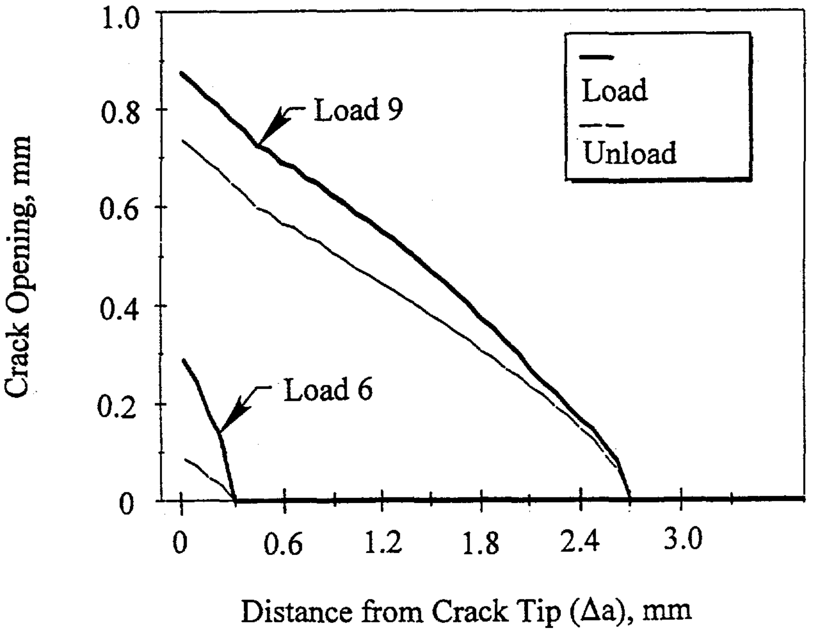

(b) Kinematic hardening

Figure 2.53 Crack-opening profiles for Specimen A23-5c analysis

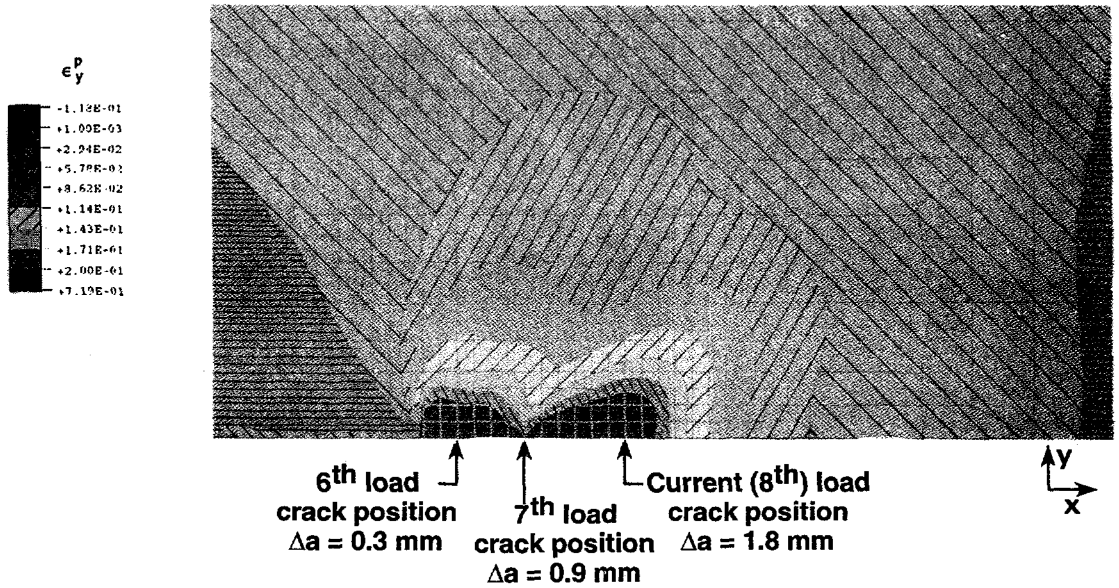

(a) At the end of the eighth load

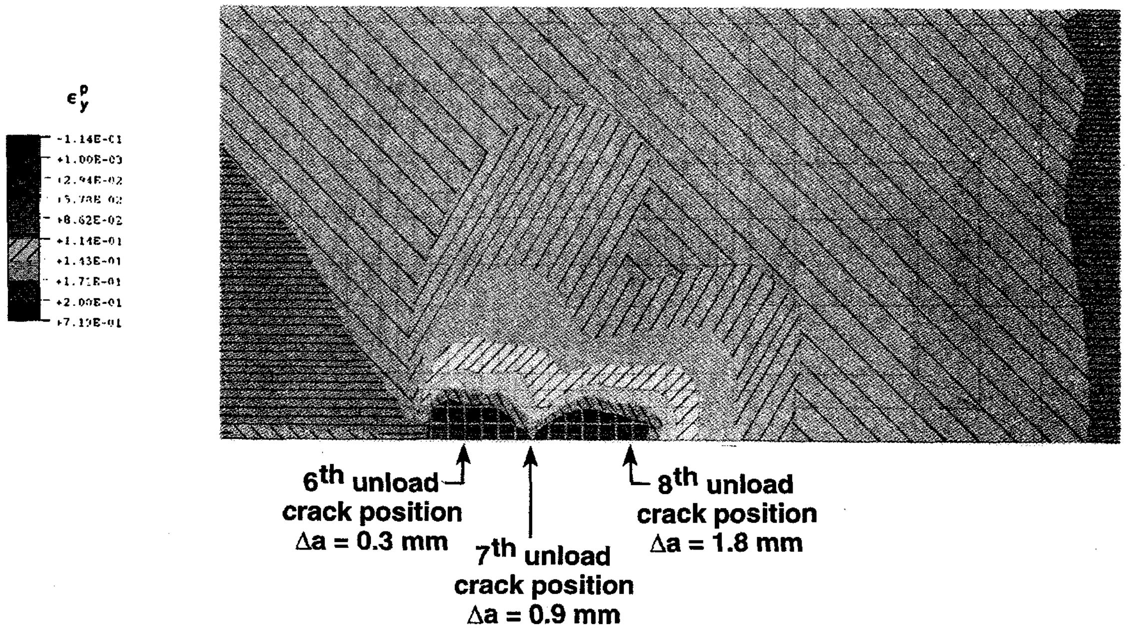

(b) At the end of the eighth unload

Figure 2.54 y-direction component of plastic strain

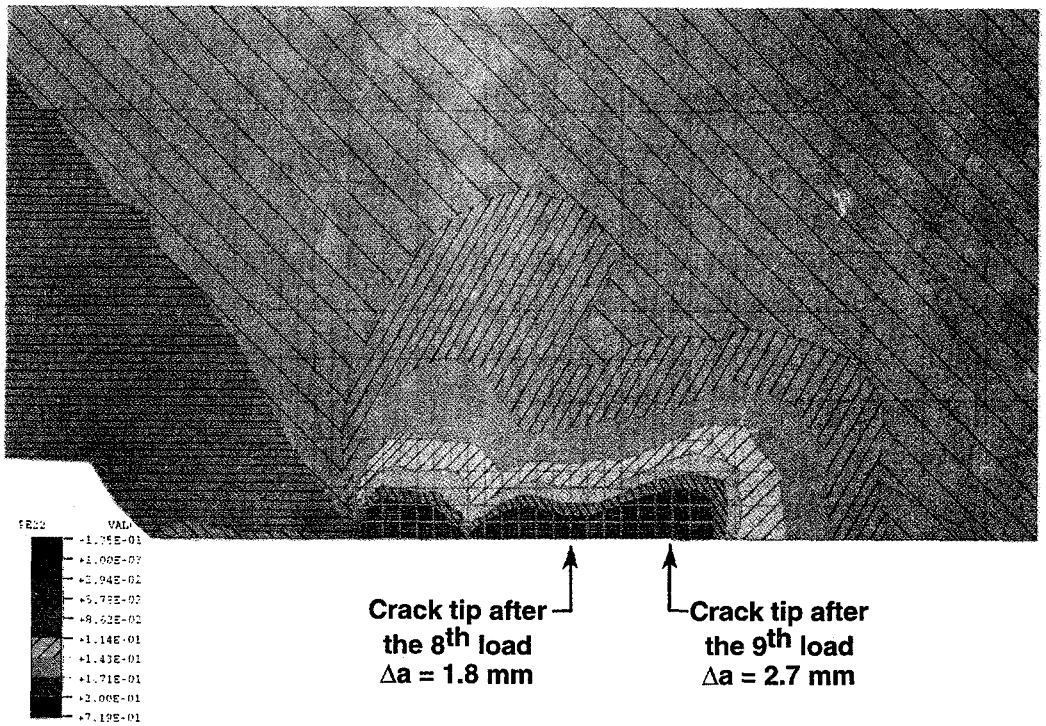

Figure 2.55 y-direction component of plastic strain after ninth load

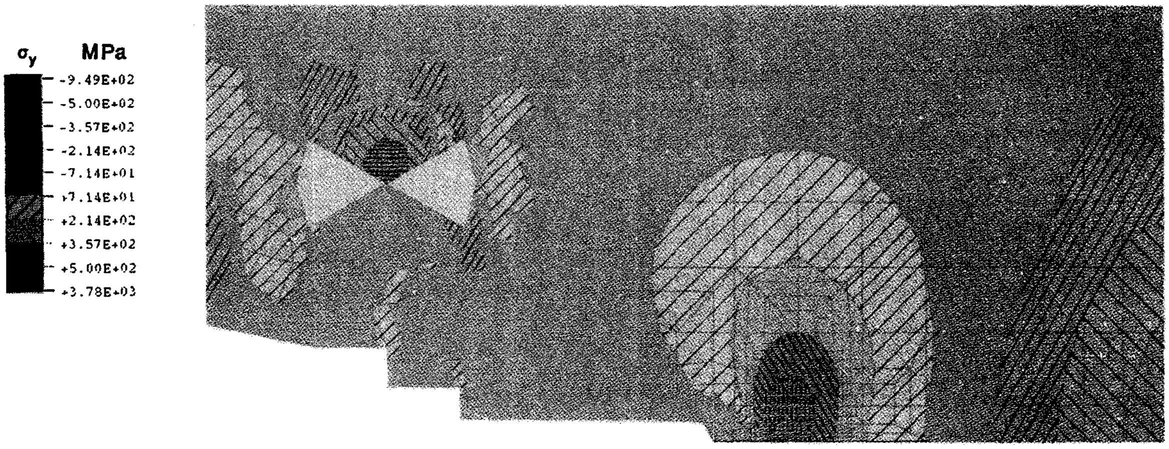

(a) At the end of the fifth load

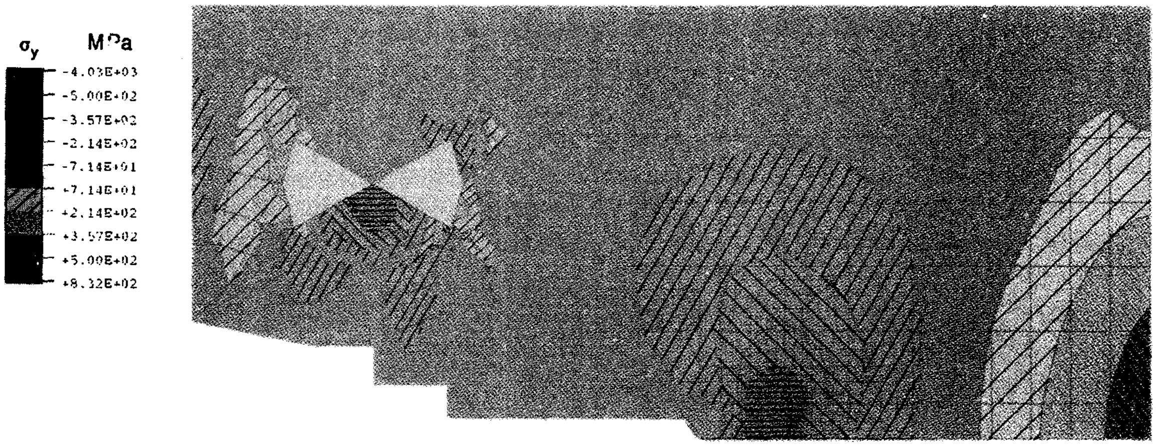

(b) At the end of the fifth unload

Figure 2.56 y-direction component of stress

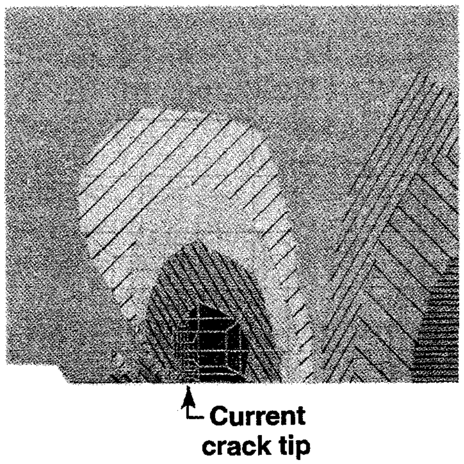

(a) At the end of the ninth load

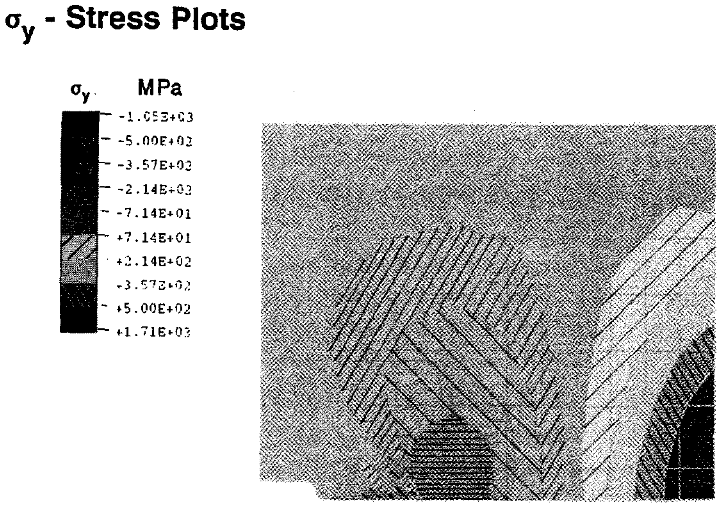

(b) At the end of the ninth unload

Figure 2.57 y-direction component of stress

Crack-Tip-Opening Angle The crack-tip-opening angle (CTOA) resistance curves for both the isotropic and kinematic hardening case analyses are illustrated in Figure 2.58. The values of CTOA are quite different depending on which hardening law was used: kinematic hardening produces much higher crack tip angles compared with the isotropic hardening analysis. Figure 2.58 used the linear stress-strain curve. The main source of this difference appears to be that, with kinematic hardening, the crack appears to be blunted even during crack growth. This blunting may be seen by re-examining Figure 2.52 which illustrates the crack profiles. It is seen that the prediction with kinematic hardening shows a more blunted crack tip. Also, from Figure 2.58, the CTOA does not appear to be strictly a constant. For monotonic loaded specimens which experience crack growth, the CTOA reaches a constant value after a short period of crack growth. Note that Figure 2.58 has a large scale variation along the ordinate, and differences between the angles do not appear large, but they are large compared to similar monotonic loaded specimens. Note also that the angles are quite large - significantly larger than those typically observed from monotonic load analyses. The cyclic loading appears to render CTOA a less useful fracture resistance parameter compared with the corresponding monotonic loaded case. This result is not unexpected considering that CTOA is a geometric parameter that is typically dependent on mesh size. Although an analysis was not performed here, it is expected that CTOA will also depend on R-ratio. Recall that here R = -1.

Before discussing the results regarding the J-integral, it is first useful to describe the analysis of the additional stainless steel Specimen A23-10c and show the results for both tests together.

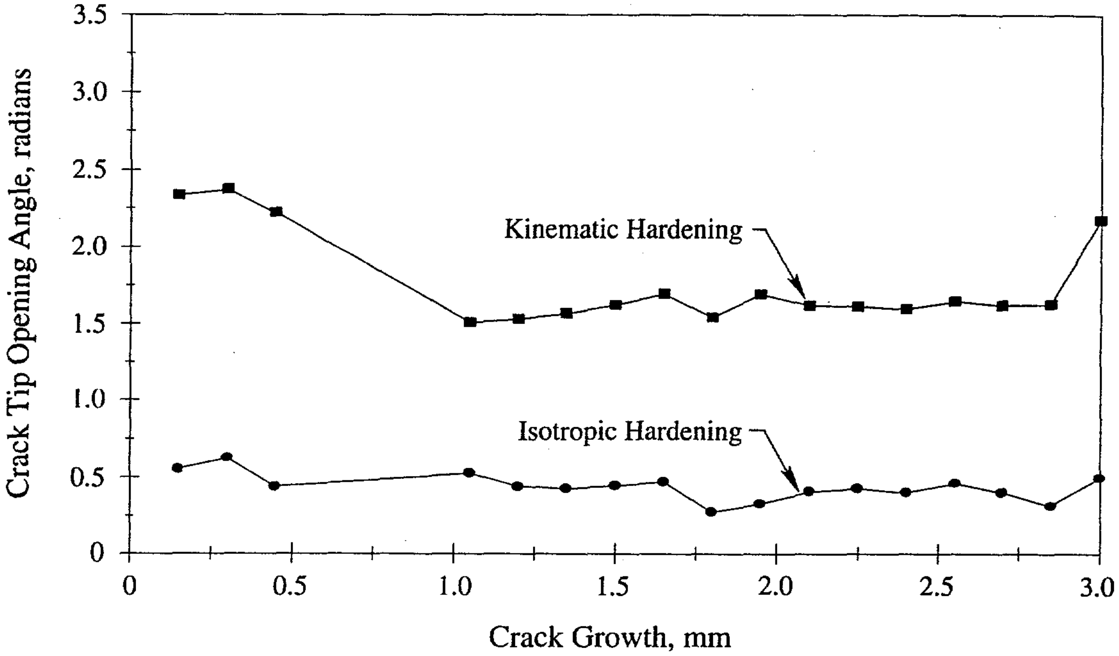

Figure 2.58 Crack-tip-opening angle resistance curves for Specimen A23-5c

2.3.6.3 Analysis Results for Stainless Steel Specimen A23-10c

The analysis of the stainless steel Specimen A23-10c was performed to investigate three separate experiments that were performed and discussed earlier. Figure 2.10 illustrates the three tests performed. One analysis for Specimen A23-10c is sufficient to obtain results for test Specimens A23-8c and A23-9c also. Figure 2.59 illustrates the experimental load versus load-line displacement for this test. Also shown is the experimental maximum load for Specimen A23-5c, which is seen to be about 20 percent lower than the present test because of the cyclic loading effect. Also, the points along the curve where the Specimen A23-8c and A23-9c tests were stopped are also illustrated. The input to the analysis consisted of the load-line displacement versus crack-growth curve illustrated in Figure 2.60. The only unload occurred after about 0.37 mm (0.015 inch) of crack growth as seen in Figure 2.60. Note that for analysis purposes, the first unload occurred at 0.3 mm (0.012 inch) of crack growth since the mesh size (or crack growth increment size) is 0.15 mm (0.006 inch). After the unload/reload sequence, an additional 1 mm (0.039 inch) of crack growth occurred. For Specimens A23-8c and A23-9c, the amount of crack growth before unloading may have been slightly different from the 0.37 mm (0.015 inch) of growth here before unloading, but any differences are considered to be negligible for the purposes of this analysis. Hence, the analysis of the Specimen A23-10c test provides results at the intermediate points for Specimen A23-8c and A23-9c illustrated in Figures 2.10 and 2.59.

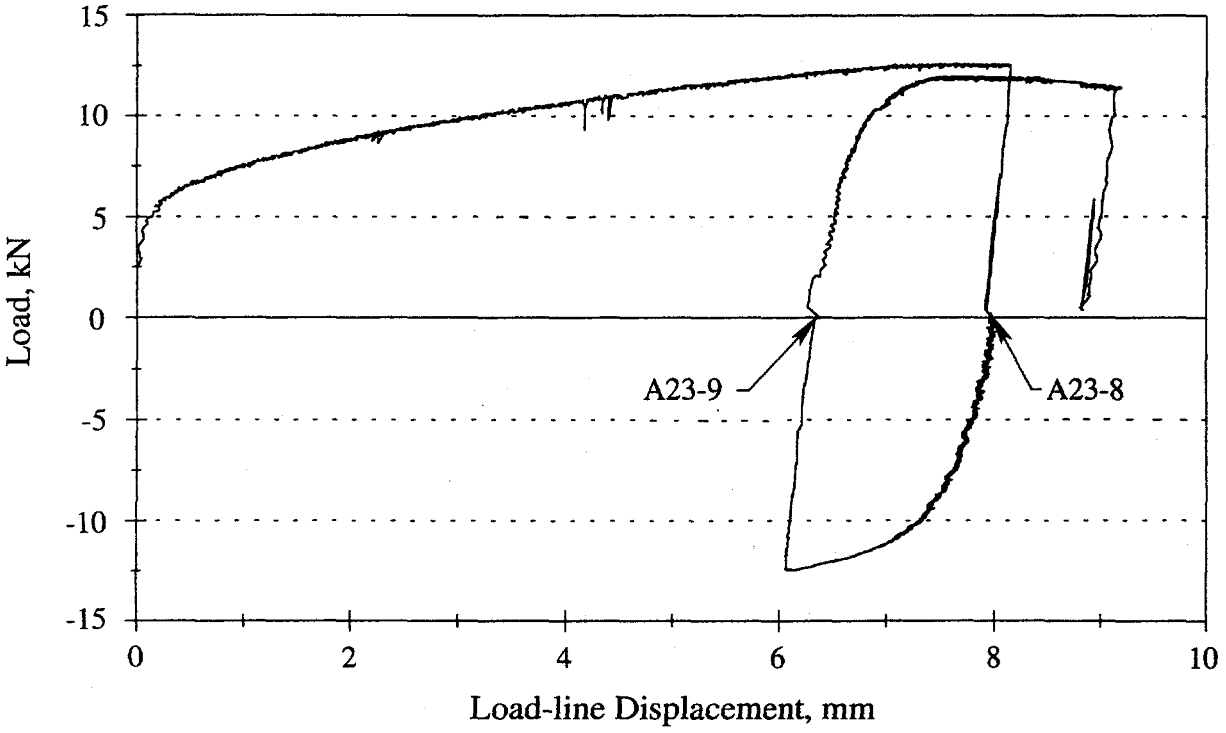

Figure 2.59 Experimental record for additional stainless steel cyclic-load experiment (Specimen A23-10c)

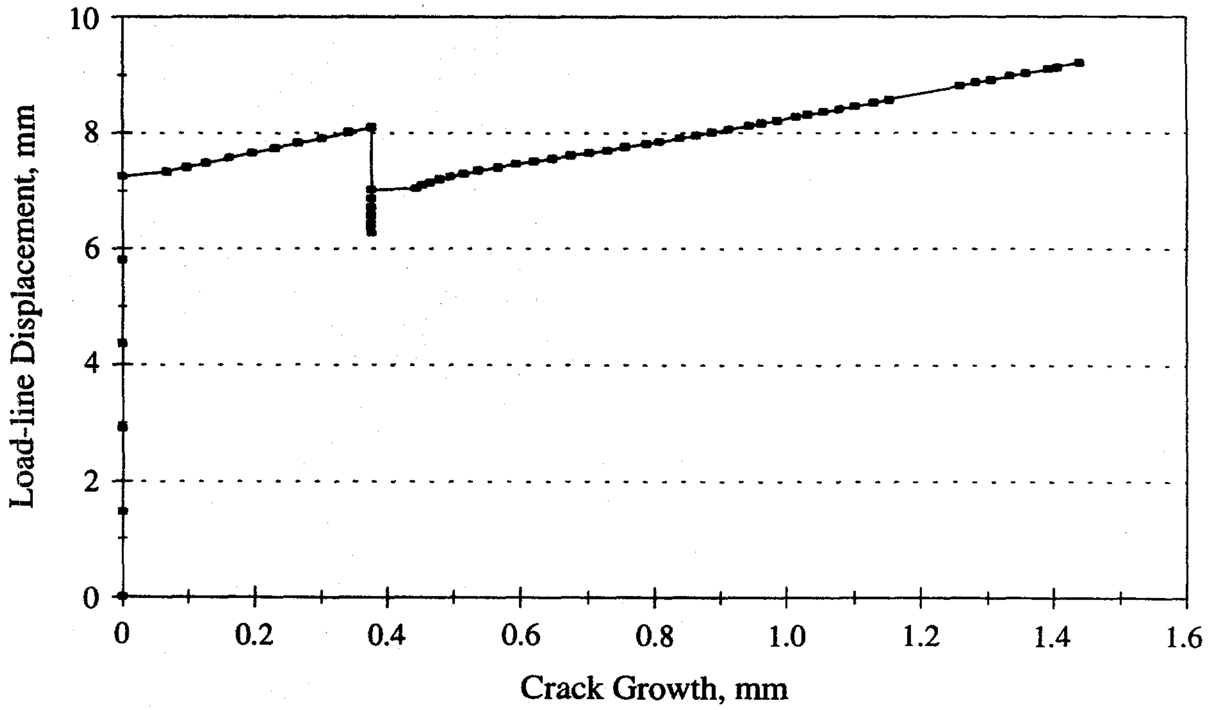

Figure 2.60 Load-line displacement versus crack growth record used as input for the analysis of additional stainless steel cyclic-load experiment (Specimen A23-10c)

Load Versus Displacement Comparison Figure 2.61 shows the predicted load versus load-line displacement (using both kinematic and isotropic hardening and a linear stress-strain curve) compared with the experimental results. All analyses for stainless steel Specimen A23-10c used the linear stress-strain curve in Figure 2.51b. It is seen that the results for kinematic hardening were very poor on the compression side while the predictions using isotropic hardening were very good throughout the one cycle. The kinematic hardening results were very poor since the unload occurred just after crack initiation. As such, the yield surface was translated very far from the origin before unloading occurred. Hence, upon unloading, the opposite side of the yield surface was reached even before the global load reached zero. Observe the physically unrealistic result for the kinematic hardening predictions where the predicted curve, upon unloading, begins to curve at a load of about 4 kN (i.e., greater than zero). Note from Figure 2.52a that the predicted results for the A23-5c test using kinematic hardening became increasingly worse as the crack initiation point was approached. It is clear that kinematic hardening is inappropriate for 304 stainless steel. Results for isotropic hardening are adequate until many cycles occur. Here the predicted results are excellent for the isotropic hardening analysis.

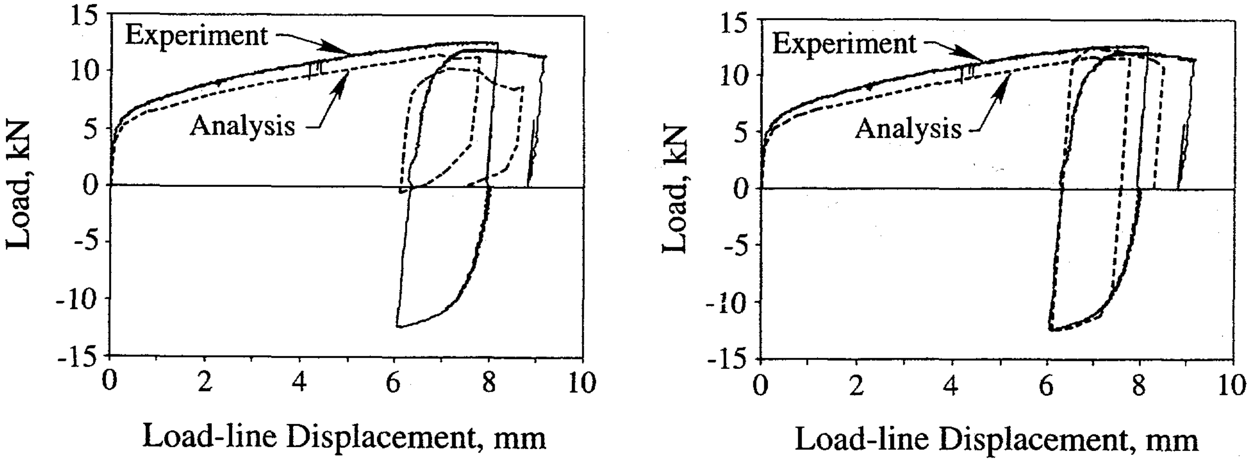

(a) Kinematic (b) Isotropic

Figure 2.61 Predicted load versus load-line displacement curves compared with experiment for the stainless steel Specimen A23-10c

Crack Opening Profiles The crack opening profiles for the isotropic analysis case are shown in Figures 2.62 and 2.63. The results for kinematic hardening are not shown since they are unrealistic. The crack profile at Points A, B, and C (see inset in figure) are shown in Figure 2.62. The profile for Points A and B correspond to Specimens A23-8c and A23-9c, in Figure 2.10, respectively. Unfortunately, the corresponding experimental profile is not available. As seen in Figure 2.62, crack closure is predicted at Point F. Also note that the crack closes significantly from Point B to C. Also, the crack is open only slightly at Point D. Recognize that these profiles are blowups very close to the crack tip. Experimentally, the crack appeared to be nearly closed for Specimen A23-9c, which corresponds to Point B in Figure 2.62. Figure 2.63 illustrates the crack profiles for the maximum load points and the corresponding unload points. Note that the crack tip at Point C is pinched slightly. This pinching is due to the unloading effect and the unload compressive plasticity.

Plastic Zones The solutions using isotropic hardening compared very well with experimental data obtained from hardness tests. As was observed regarding the solutions for the Specimen A23-5c analyses, isotropic hardening performs well for lower numbers of cycles applied, as was the case. Some examples of plastic zone sizes and stress contour plots are provided for the Specimen A23-10c case with the isotropic hardening analyses.

The plastic strain profile at the end of the test is illustrated in Figure 2.64. Note again that the plastic strains tend to 'pinch' at the location of the crack tip prior to and during the unloading phase. This characteristic pinch effect can also be observed experimentally. Figure 2.65 illustrates the hardness

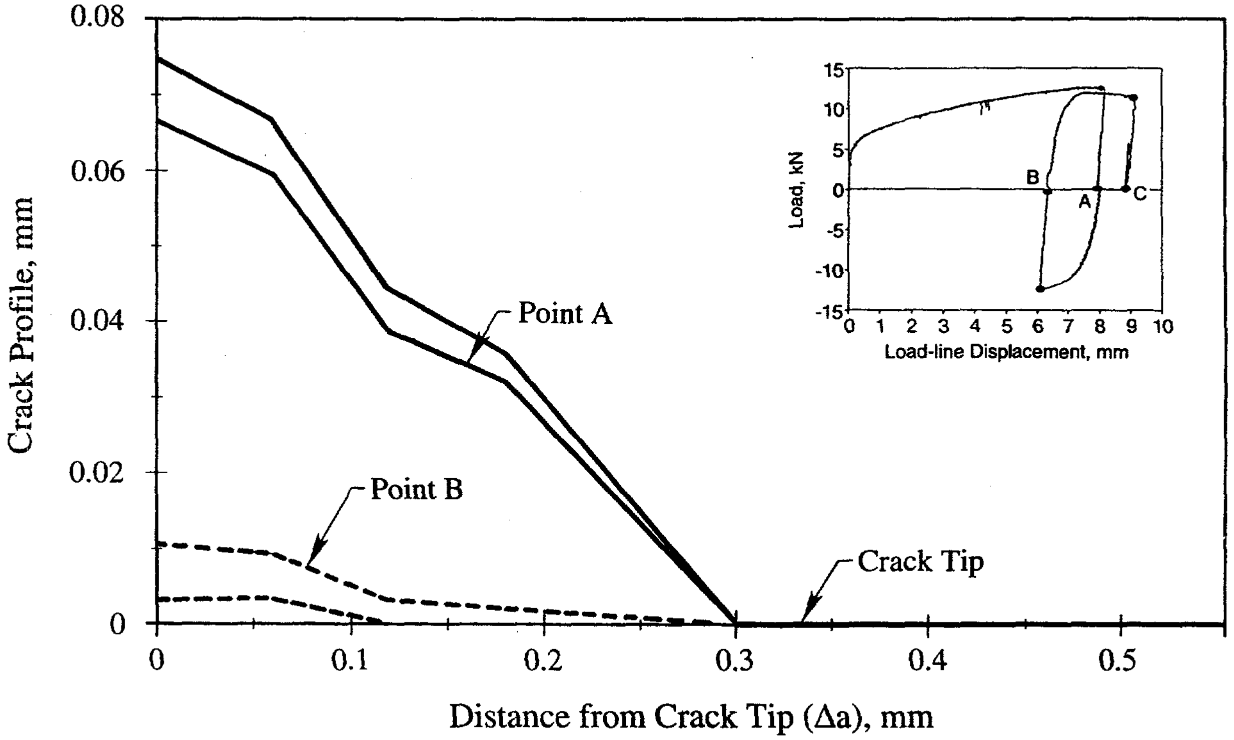

Figure 2.62 Crack profiles for stainless steel Specimen A23-10c analysis, isotropic hardening

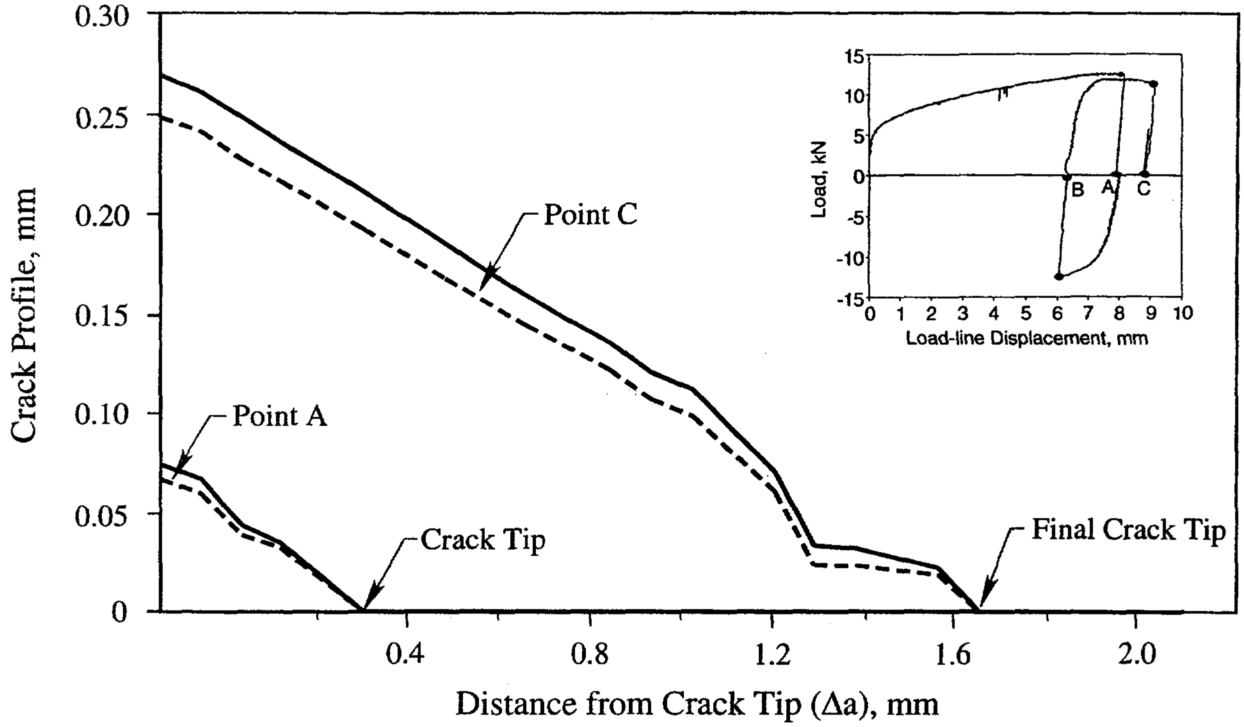

Figure 2.63 Crack profiles for stainless steel Specimen A23-10c

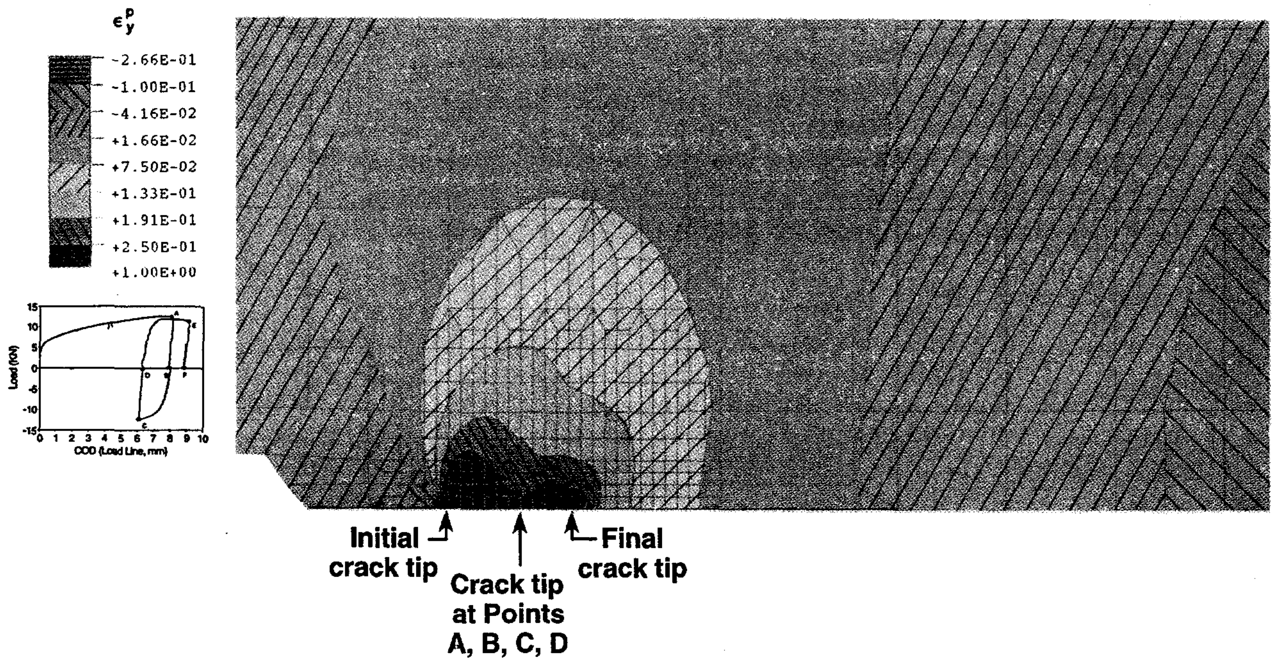

Figure 2.64 Plastic strain at Point C (end of test) in stainless steel Specimen A23-10c

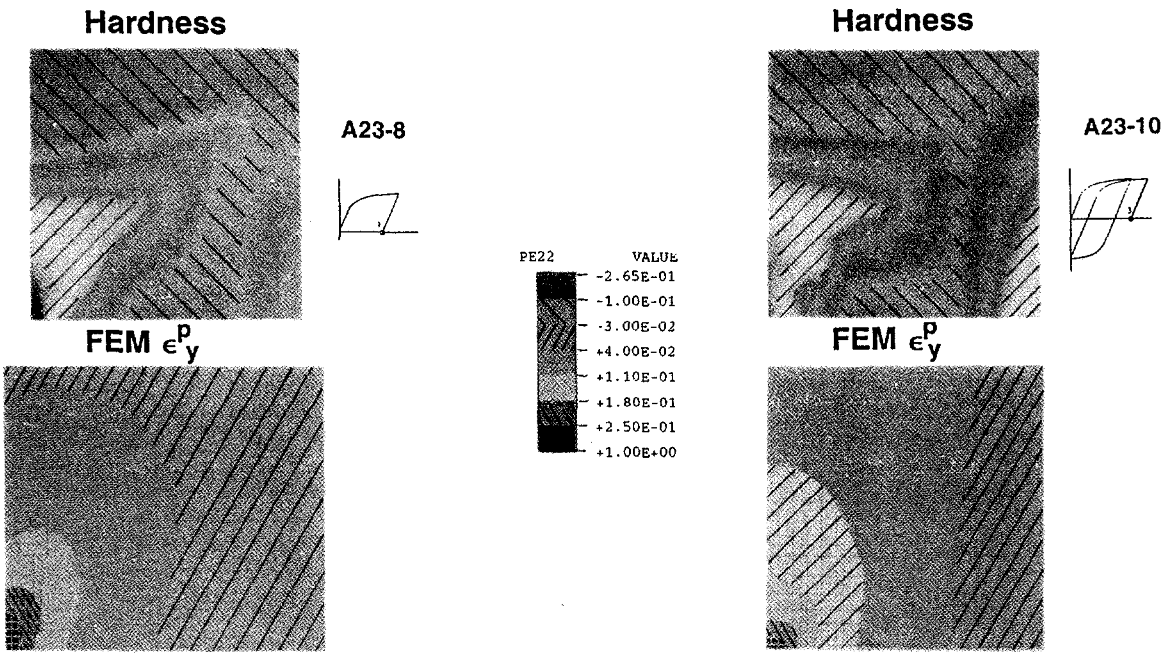

Figure 2.65 Plastic zone profiles (bottom figures) compared to hardness measurements

profiles for Specimen A23-8c (the case where the specimen was loaded, the crack grew, and then the load was removed and the specimen sectioned, etc.) and for Specimen A23-10c (the case where the specimen was sectioned after a complete cycle was completed). Directly beneath these hardness profiles the predicted plastic strains in the y-direction, ϵ_y^p, are illustrated. For the left side figures, note that the profiles are expected for the monotonic load case. As discussed in Section 2.2.4, the uniform plastic zone features typical of monotonic loading are seen. On the right side figures, the pinching effect is clearly seen for both the hardness measurements and for the analysis. While the hardness measurements do not provide quantitative plastic zone results, it can be seen that the general profiles for both the top and bottom figures are similar. Even though hardness is not a direct measure of plastic strain, it is related to the plastic strains and the predictions are seen to be qualitatively adequate here.

Finally, stress contour plots are illustrated in Figure 2.66. Figure 2.66a illustrates the y-component of stress at Point C, after a complete unload cycle has occurred. Again, also note the load pin stress here. A large zone of tensile stresses is observed ahead of the crack tip, and the typical compressive zone beyond this region. Figure 2.66b illustrates the x-component of stress which is the stress in the direction of crack growth. Note the compressive wake zone behind the growing crack tip which persists despite the unloading cycle which occurred. Finally, Figure 2.66c illustrates the y-direction component of stress at point C, i.e., at the end of the complete test. Again, as with the Specimen A23-5c hardness results, note that a large zone of compressive stresses is present. This compressive residual stress zone persists despite the lack of global load. Note also the tensile zone above the region where crack growth has occurred.

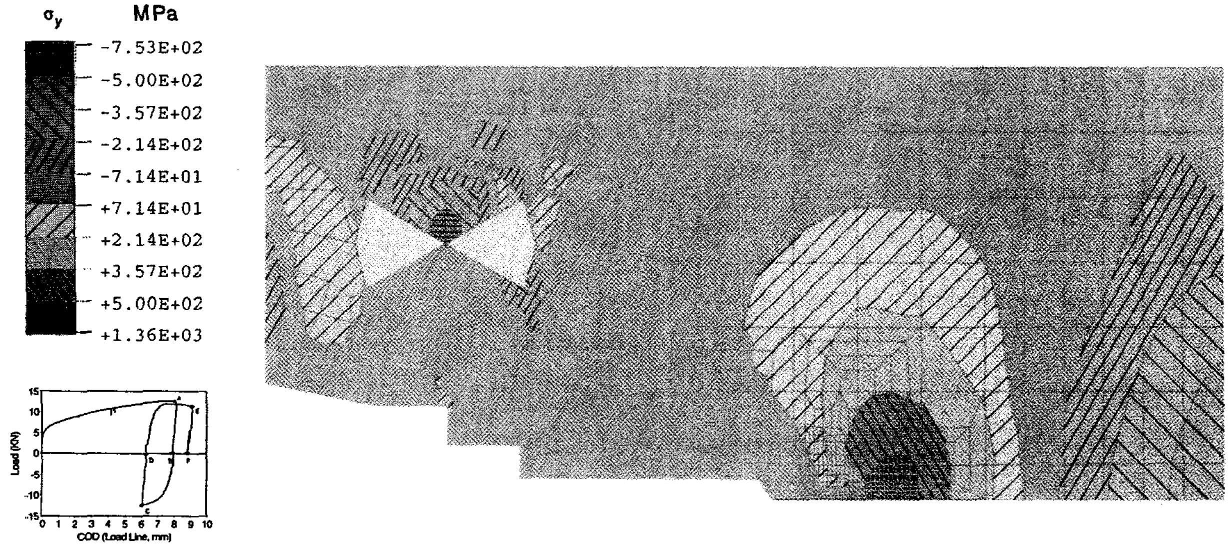

(a) y-direction component, Point C

Figure 2.66 Stress contour plots

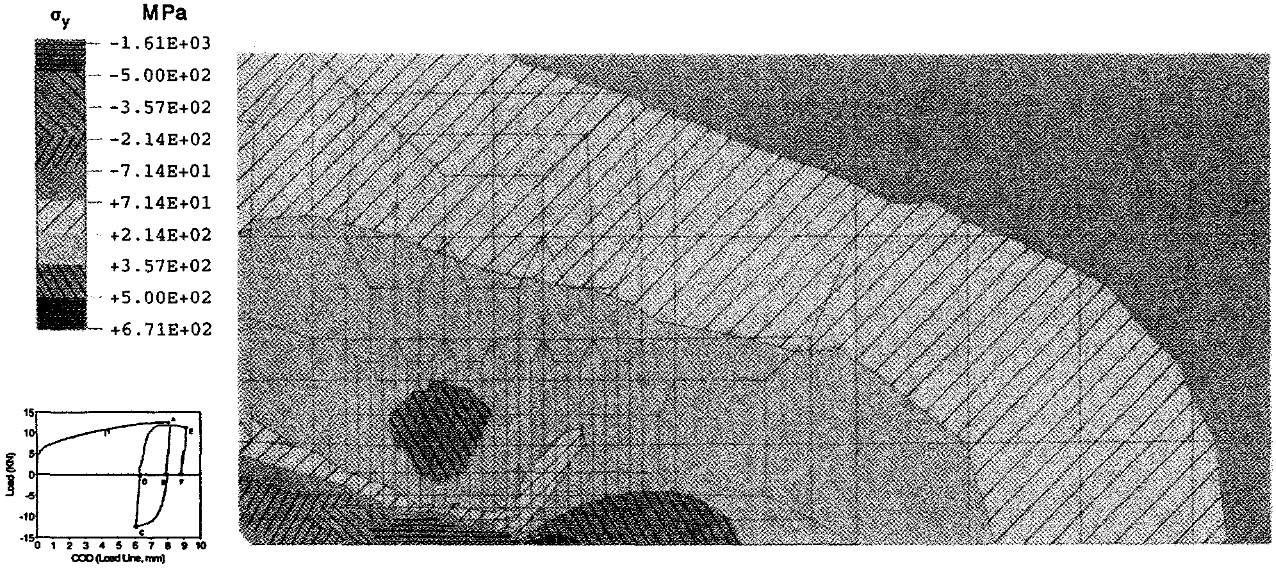

(b) x-direction component, Point C

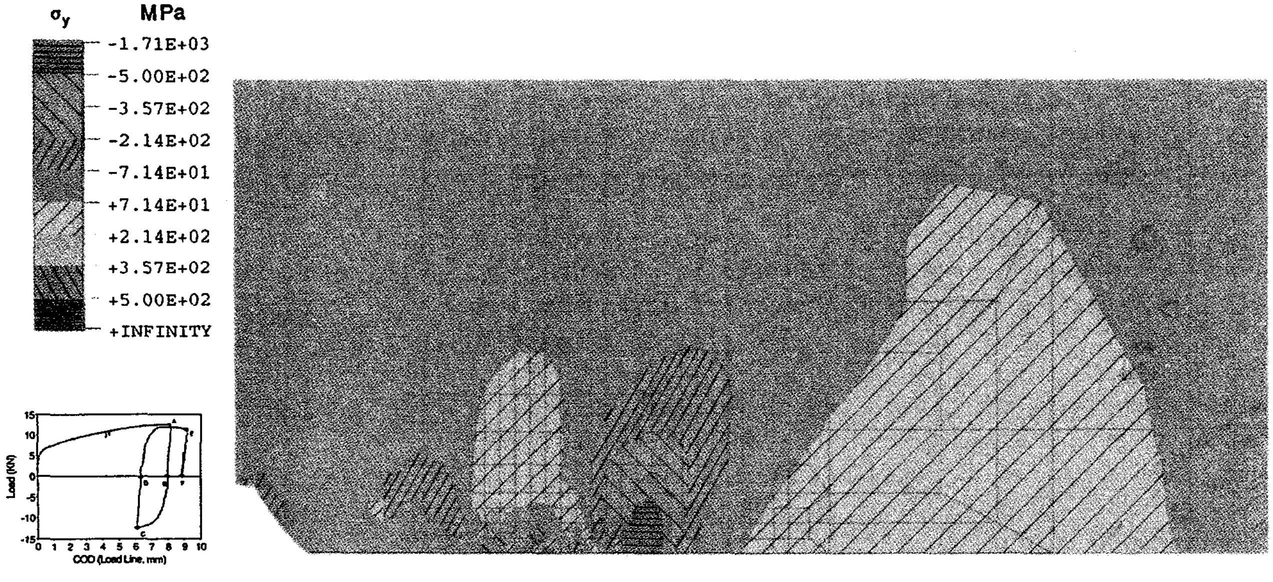

(c) y-direction component, Point C

Figure 2.66 (continued)

2.3.6.4 Fracture Parameters

The J-integral fracture parameter had its development, from a practical applications standpoint, in the nuclear industry where very ductile materials are typically used. The limitations of J from theoretical considerations are well known and include:

- The crack must be stationary, i.e., no crack growth is permitted.
- Only monotonic loading of the cracked structure is permitted. Cyclic loading is not permitted since J becomes path dependent.

These theoretical limitations are overcome by several practical considerations. The first limitation is overcome from a practical standpoint by obtaining the material's J-resistance curve from a bend type (usually compact tension) specimen. Bend specimens produce lower-bound J-R curves. Therefore, such predictions, even when permitting crack growth, tend to be conservative and, are accepted. The wealth of comparisons of fracture predictions with experimental data for through-wall and surface cracks in pipes subjected to tension, bending, and both tension and bending (Refs. 2.3 and 2.11) indicate that good and conservative predictions can be made using J-tearing theory.

The second major limitation, that cyclic loading cannot be permitted, is more troublesome. When J is calculated during the analysis of a cyclically loaded specimen, it becomes markedly path dependent. The path dependence persists both before and after crack growth occurs. Thus, the far field value of J is no longer related to the processes near the crack tip which led to crack propagation and ultimate failure.

Moreover, all of the J-estimation schemes predict the value of J assuming a stationary crack and monotonic loading. The philosophy to render the prediction of cyclic fracture practical is as follows.

- The J-resistance curve, as determined from a cyclically loaded fracture specimen, is obtained from the envelope of the maximum load-displacement curve. Since J is related to the area under the load-displacement curve, and cyclic loading lowers the load displacement curve, the cyclic J-R curve is lower than the corresponding monotonic J-R curve.
- To predict failure in a cyclically loaded specimen, the cyclic-load J-R curve is assumed to be the new J-R curve, which may be lower than its monotonically loaded counterpart. The J value (for the pipe) is then estimated using the normal J-estimation schemes. Of course, these schemes are based on deformation theory plasticity, monotonic loading, etc.

Hence, the lower predictions using this approach are caused by the J-R curve being reduced rather than by modifying the prediction of crack-driving force. While this approach is certainly not complete from a theoretical standpoint since there are many unknown limitations, from a practical standpoint it is attractive. Moreover, many of the predictions made using this approach have been adequate from an applications perspective.

Other methods to predict ductile cyclic fracture have a more sound theoretical basis, but are not yet practical. The approach based on the T*-integral, which has received much attention in the U.S. aerospace arena recently, has potential. The Elastic-Plastic Finite Element Alternating method (EPFEAM) combined with the T*-integral parameter (see Refs. 2.13 to 2.15) shows practical promise since EPFEAM permits the analysis of crack growth *without having a crack explicitly in the FEM mesh.* The aerospace industry is now using this method to predict residual strength in the presence of Multi-Site-Damage (MSD). It should be mentioned that EPFEAM is useful to predict J as well. Damage-based approaches also show promise (Ref. 2.16), but are not practical because very fine finite element meshes and large computation times are required. The CTOA parameter is not useful since it appears to be inappropriate under cyclic load conditions and again, a fine finite element mesh is required.

J-Integral Results The J-integral value during the cyclic load event for stainless steel Specimen A23-10c was calculated from the analyses. Figure 2.50a shows the two far-field paths where J was evaluated. These two paths were chosen close together to evaluate the path dependence of J. Figure 2.67 shows a comparison between the numerically and experimentally calculated J for Specimen A23-10c in Figure 2.10. At crack initiation, the predicted and experimental J values differ by about 30 percent. This may be due to the fact that the analyses were performed using a 2-dimensional plane stress assumption and the ASTM E813/1152 analysis was performed using a plane strain assumption in the elastic calculation of J (see Equation 2.3). After the unload, the predicted value of J at reloading is considerably lower than the value before unloading. This effect cannot be seen in the experimental data since J was calculated from an upper envelope of the load-displacement curve. The far-field values of J over the two paths do not differ greatly. However, after the unload, the two paths seem to deviate slightly, indicating that unloadings cause J to become path dependent.

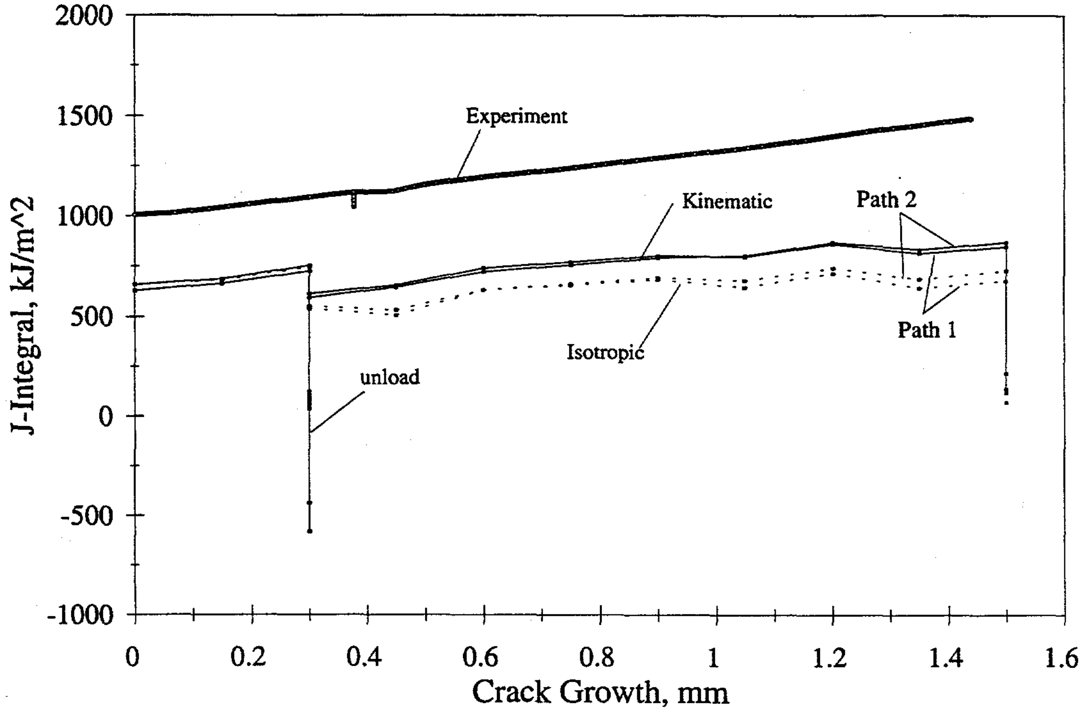

Figure 2.67 Predicted and experimental J-R curve for additional stainless steel Specimen A23-10c

Figure 2.68 shows a comparison of the numerical J-R curve with the experimental data from the stainless steel specimen shown in Figure 2.11 (A23-5c). Recall that the crack initiated during the sixth loading cycle in this experiment. As in the previous analyses, J was evaluated along the two paths shown in Figure 2.50a.

As shown in Figure 2.68a, the predicted value of J at crack initiation compares well with the ASTM estimate for both the kinematic and isotropic analyses. Recall that the ASTM estimate from the experiment is based on the envelope of the experimental load-versus-displacement curve.

After the first unloading, J became very path dependent in these analyses, even for the closely spaced paths shown in Figure 2.50a. The path dependence is due to the global unloadings that occur at each cycle. For the monotonic case with crack growth, the J values evaluated along the far-field paths do not deviate greatly from path independence because the unloadings are localized at the crack tip. After an unload, the crack re-initiation value of J is smaller than that before unloading. Moreover, the difference between the load and reload values of J appears to increase with the number of cycles.

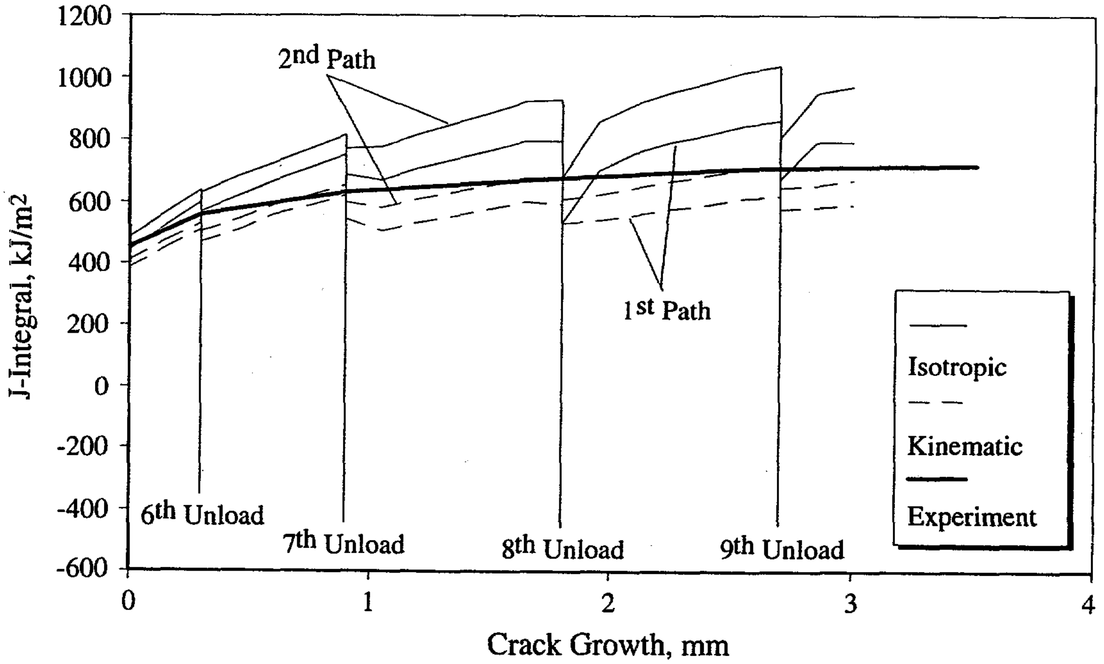

Figure 2.68a J-R curve comparison for stainless steel specimen tested with R = -1 and $\delta_{cyc}/\delta_i = 0.1$ (A23-5c), linear stress-strain curve used

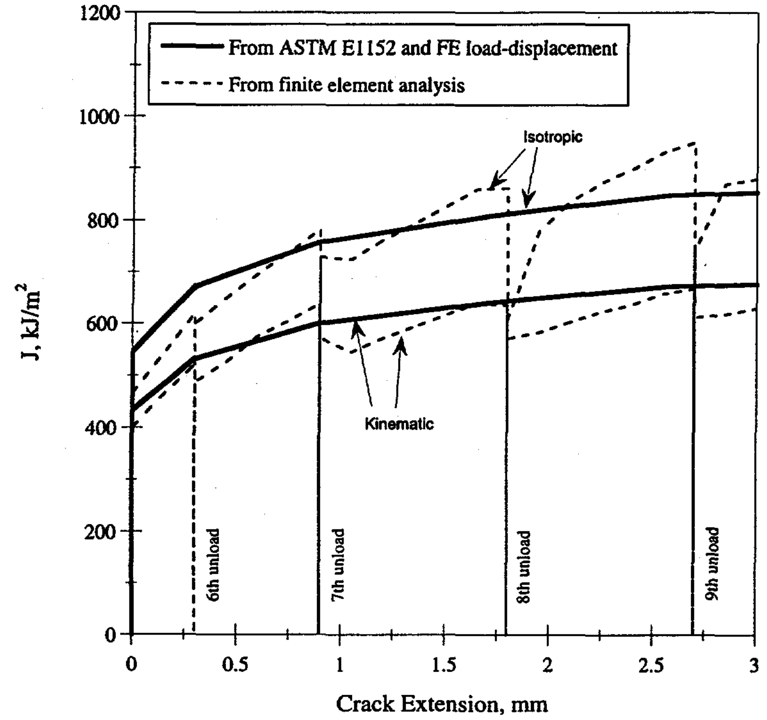

Figure 2.68b Comparison of J-R curves from FEM and ASTM using predicted load-displacement response

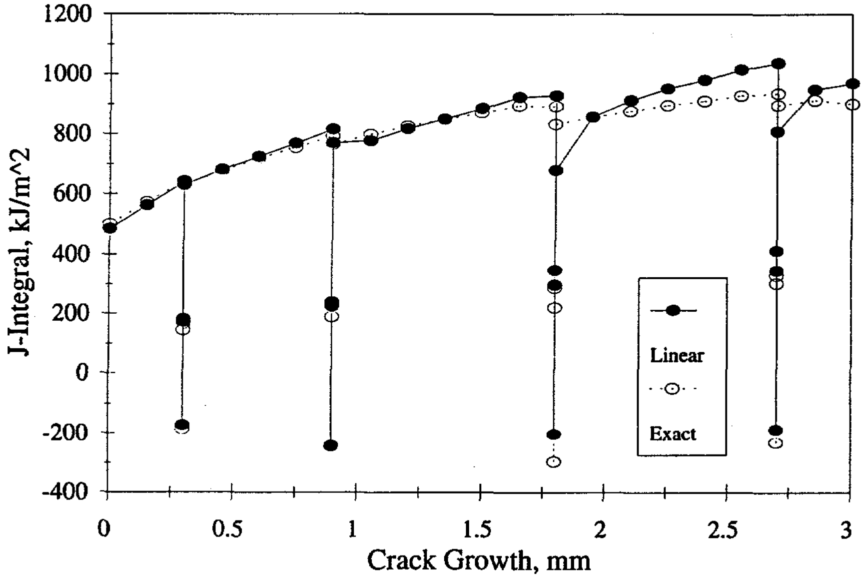

Figure 2.68c Comparison of J for Specimen A23-5c; linear and actual stress-strain curves

After crack growth, the kinematic-hardening analysis, which slightly underpredicted the tensile loads, slightly underpredicted the J values. The isotropic analysis predicted slightly higher J values. Since the kinematic hardening analysis underpredicted the compressive loads, and the isotropic analysis overpredicted the tensile loads, and the compressive loads, it would seem likely that an analysis that accurately predicted the load-displacement response would also accurately predict the J-R response. However, since the hardening laws used could not model the cyclic load-deflection behavior, the accuracy of the J-integral results are unknown. A hardening law based on the Ohno-Kachi two-surface plasticity model (Ref. 2.17) was developed as an ABAQUS subroutine in hopes that cyclic load-displacement history could be accurately predicted. Unfortunately, this law had numerical convergence problems for the cyclic-loaded-crack problem.

In all of the finite element analyses discussed, a post processor was used to calculate J from the geometry and the predicted load-displacement behavior. Since neither hardening law was sufficient in predicting the experimental load-displacement response, the J values calculated from these analyses can not be expected to correspond to J values calculated from the experimental results. Therefore, the ASTM procedure for calculating J was used with the finite element predictions of load and displacement to produce predictions of the J-R curve that can be directly compared with the finite element J-R curve. These results are shown in Figure 2.68b. In this figure, the solid lines represent the ASTM calculated J-R curves using the predicted load-displacement behavior, while the dashed lines represent the finite element calculated J-R results. Note that the finite element results represent an average of the results from the two paths shown in Figure 2.50a. The results shown in Figure 2.68b illustrate that the ASTM method of calculating J from the upper envelope of the load-displacement response can be used to predict the fracture toughness response due to cyclic loading.

As discussed earlier with regard to Figure 2.68a, some differences were observed between the predictions using the linear approximation to the stress-strain curve and the actual curve (Figure 2.51b). Figure 2.68c illustrates the comparison between the calculated J-R curves using the two stress-strain curves. As can be seen, little difference is observed. Hence, while using the exact stress-strain curves results in better load predictions, the prediction of J is not affected here. This result is probably because J is evaluated along far-field paths, where the strains are rather small. Hence, the differences illustrated in Figure 2.68c are not seen far from the crack tip region.

Finally, based on the comparison of the predicted and experimental J-R curves in Figure 2.68, it appears that the engineering procedure considered here to predict cyclic fracture has promise. This postulate is investigated in Section 4.0 where moment predictions, using the J-R curves from this method, are compared with TWC pipe experimental moments.

2.4 References

2.1 Wilkowski, G. M., and others, "Degraded Piping Program - Phase II," Summary of Technical Results and Their Significance to Leak-Before-Break and In-Service Flaw Acceptance Criteria, March 1984-January 1989, by Battelle Columbus Division, NUREG/CR-4082, Vol. 8, March 1989.

2.2 Marschall, C. W., Landow, M. P., and Wilkowski, G. M., "Loading Rate Effects on Strength and Fracture Toughness of Pipe Steels Used in Task 1 of the IPIRG Program," NUREG/CR-6098, BMI-2175, October 1983.

2.3 Scott, P., Kramer, G., Vieth, P., Francini, R., and Wilkowski, G., "The Effect of Dynamic and Cyclic Loading During Ductile Tearing on Circumferential Cracked Pipe - Experimental Results," ASME PVP Vol. 280, pp 207-220, June 1994.

2.4 Mohan, R., Marschall, C., Krishnaswamy, P., Brust, F., Ghadiali, N., and Wilkowski, G., "Effects of Toughness Anisotropy and Combined Tension, Torsion, and Bending Loads on Fracture Behavior of Ferritic Nuclear Pipe," NUREG/CR-6299, April 1995.

2.5 Landes, J. D., and Liaw, P. K., "Effect of Cyclic Loading on Fracture Toughness of a Modified 4340 Steel," *Effect of Load and Thermal Histories on Mechanical Behavior of Materials*, P. K. Liaw and T. Nicholas, Eds., a publication of the Metallurgical Society, Inc., 1987.

2.6 Landes, J. D., and McCabe, D. E., "Load History Effects on the J_R-Curve," *Elastic Plastic Fracture: Second Symposium, Volume II-Fracture Resistance Curves and Engineering Applications,* ASTM STP 803, C. F. Shih and J. P. Gudas, Eds., American Society for Testing and Materials, pp II723-II738, 1983.

2.7 Schwalbe, K.H. and Hellman, D., "Application of the Electric Potential Method to Crack Length Measurements Using Johnson's Formula," *Journal of Testing and Evaluation,* Vol. 9, No. 3, pp 218-221, 1981.

2.8 Landow, M. P., and Marschall, C. W., "Experience Using Direct Current Electric Potential to Monitor Crack Growth in Ductile Metals," ASTM STP1114, pp 163-172, 1991.

2.9 Wilkowski, G. M., Marschall, C. W., and Landow, M., "Extrapolation of C(T) Specimens J-R Curves for use in Pipe Flaw Evaluations," ASTM STP1074, pp 56-84, 1990.

2.10 Wilkowski, G. M., and others, "Short Cracks in Piping and Piping Welds," NUREG/CR-4599, Vol. 4, No. 1, April 1995.

2.11 Scott, P., and others, "IPIRG-2 Task 1 - Pipe System Experiments With Cracks in Straight-Pipe Locations," NUREG/CR-6389, BMI-2187, December 1996.

2.12 Krishnaswamy, P., and others, "Fracture Behavior of Short Circumferentially Surface-Cracked Pipe," NUREG/CR-6298, BMI-2183, November 1995.

2.13 Okada, H., Suzuki, Y., Ma, L., Lam, P. W., Pyo, C. R, Atluri, S. N., Kobayashi, A. S., and Tan, P., "Plane Stress Crack Growth and T*-Integral on Experimental-Numerical Analysis," Computational Mechanics '95, Proceedings of the International Conference on Computational Engineering Science, Vol. 2, pp 2148-2153, Hawaii, USA, July 30-August 3, 1995.

2.14 Pyo, C. R., Okada, H., and Atluri, S. N., “Elastic-Plastic Residual Strength Analysis of Aircraft Structures with Wide-Spread Damage,” Computational Mechanics ‘95, Proceedings of the International Conference on Computational Engineering Science,Vol. 2, pp 2154-2159, Hawaii, USA, July 30-August 3, 1995.

2.15 Wang, L., and Atluri, S. N., “On Schwartz - Neumann Alternating Method for the Elastic-Plastic Analysis of Elliptical Cracks in 3D Body,” Computational Mechanics ‘95, Proceedings of the International Conference on Computational Engineering Science, Vol. 2, pp 2160-2164, Hawaii, USA, July 30-August 3, 1995.

2.16 Lawaitre, J., and Chaboche, J. L., *Mechanics of Solid Materials*, Cambridge University Press, 1990.

2.17 Ohno, N., and Kachi, Y., “A Constitutive Model of Cyclic Plasticity for Nonlinear Hardening Materials,” *Journal of Applied Mechanics*, Vol. 53, pp 395-403, June 1986.

3.0 TESTING AT DYNAMIC RATES OF LOADING

During the IPIRG-1 program, it was found that the toughness of nuclear piping steels at plant operating temperatures was different at quasi-static rates than at loading rates typical of a seismic event (Ref. 3.1). Austenitic materials showed a slight increase in toughness, while ferritic base metals showed a decrease in toughness. This decrease in ferritic steel toughness was believed to be due to dynamic strain aging (Ref. 3.2). Since quasi-static toughness values are typically used in LBB and in-service flaw evaluation criteria, this was a point of interest to explore further in the IPIRG-2 program. The purpose of the investigation described in this section is to present results on additional dynamic-load tests carried out on ferritic nuclear piping steels.

3.1 Test Matrix for Dynamic Loading

Since the purpose of this work was to expand on the carbon steel dynamic material property database, a series of different carbon steel materials was tested. Table 3.1 shows a list of the pipe steels used in this investigation.

Table 3.1 Dynamic loading test matrix

Material	Battelle Designation	Pipe Size	Number of Dynamic C(T) Tests	Number of Dynamic Tensile Tests
Japanese STS49	IP-F1	30-inch Sch. 80	2	2
A333 Gr. 6	DP2-F9	10-inch Sch. 100	2	2
A106 Gr. B	DP2-F22	6-inch Sch. 80	2	2
Japanese STS410	IP-F13	6-inch Sch. 120	4	6[a]

(a) The dynamic tensile tests at strain rates of 1/s and 10/s for this material were completed in Reference 3.1. Three quasi-static (10^{-4}/s) and two intermediate-strain-rate (10^{-2}/s) stress-strain curves were generated in this task.

Additional dynamic toughness and strength data were developed during the IPIRG-1 program on two other A106 Grade B pipes, one carbon steel SAW, two TP304 stainless steels, one stainless steel SAW, and one aged cast stainless steel (Ref. 3.1). Also, dynamic toughness test were conducted on elbows made from A106 Grade B pipe and TP304 stainless steel in IPIRG-2, Task 2 (Ref. 3.3). Dynamic tests were conducted on the Japanese STS410 (IP-F13) pipe and TIG weld in Reference 3.4. All together, the dynamic data available (including data from this effort) are:

6 carbon steel base metals
2 carbon steel welds
3 TP304 base metals
1 stainless steel weld
1 aged cast stainless steel

These data are being implemented into a future version of the PIFRAC database (Ref. 3.5).

3.2 Dynamic Tensile Tests

Tensile specimens were machined from the pipes such that their tensile axis was parallel to the pipe axis. All specimens were machined without flattening the pipe and were taken from the midwall location of the pipe. These dynamic tensile tests employed flat, pin-loaded specimens of the design shown in Figure 3.1. Typically, the dynamic tensile specimens had a gage length of 25.4 mm (1.00 inch), a gage width of 6.35 mm (0.25 inch), and a gage thickness of 3.18 mm (0.125 inch). However, the IP-F13 specimens had a gage length of 8.89 mm (0.35 inch). In Reference 3.4, an STS410 carbon steel base metal (IP-F13) pipe and an associated TIG weld (IP-F16W) were characterized. Due to the small size of the TIG weld, the gage length for the weld dynamic specimens was reduced. The base metal specimens were manufactured with the same gage length in order to eliminate material property scatter due to specimen geometry differences. However, one specimen from the IP-F13 material was machined with a 25.4 mm (1-inch) gage length to document any difference in the stress-strain response.

All tensile tests were performed in either a 22 kN (5,000 lb) or a 44 kN (10,000 lb) capacity servohydraulic MTS testing machine. Data were taken continuously during the tests using the LABTECH® NOTEBOOK software. Two different methods were used to measure strain during the course of these tests. An optical extensometer, identical to that used in IPIRG-1 (Ref. 3.1) was initially used. However, it was found that the data from this device obtained during IPIRG-2 were erroneous. Therefore, another device that makes use of a high temperature clip gage was implemented. The following is a description of each of these strain measuring methods.

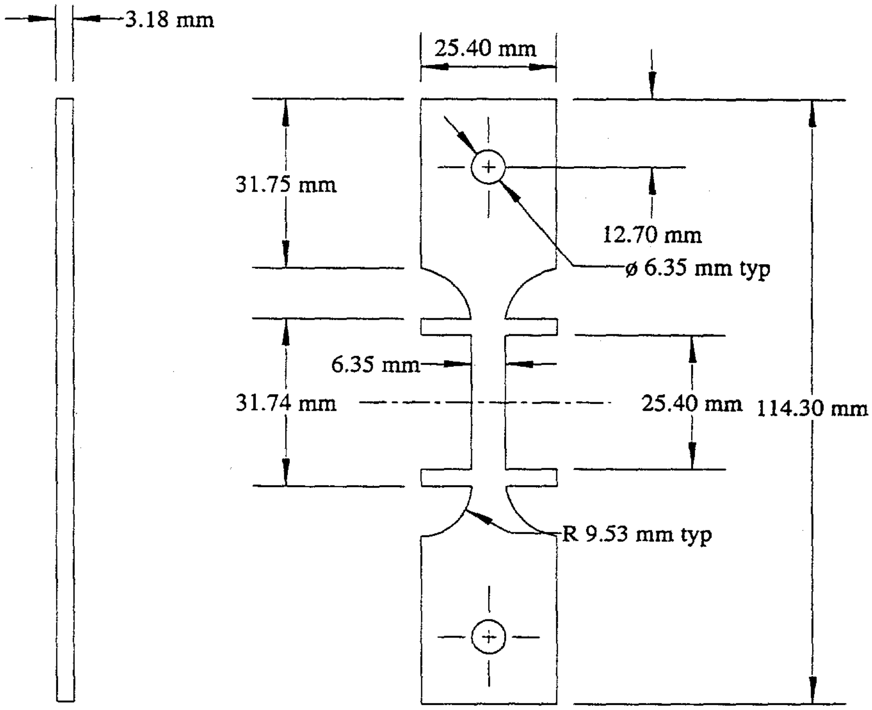

Figure 3.1 Tensile specimen for dynamic-loading-rate tests

3.2.1 Description of Optical Strain-Measurement System

The specimens tested using this device were enclosed in a circulating-air oven which had windows in the front and back to allow the transmission of light. Temperatures were maintained in this furnace within ±2 C (±4 F) of the test temperature. For these specimens, strains were measured using a noncontacting optical strain-measuring device, shown schematically in Figure 3.2. Light was transmitted though the back window of the oven, which produced a sharp contrast at the integral flags on the specimens. With the device focused on these flags, the test was run. As the specimen was strained, the device followed the flags and provided an electrical signal whose magnitude was proportional to the change in the distance between the flags.

These data, as well as the ram displacement and load, were recorded using the LATECH® NOTEBOOK software and a digital oscilloscope. During the course of IPIRG-1, this strain-measuring method proved to be a reliable tool (Ref. 3.1). However, in IPIRG-2, the data produced by the optical device was erroneous. Curiously, the data appeared acceptable upon initial investigation, and the measured final elongations matched the final strain reading within a reasonable amount of scatter. However, upon full analysis of the data, problems with the optical device output were discovered.

Figure 3.3 shows an example of the strain- and stress-versus-time for a carbon steel elbow specimen tested using the optical device; the measured elongation from the experiment was 30 percent. Note that the final elongation values as measured from the broken specimen are usually higher than the elongation values measured from the optical device, since it is difficult to place the fracture surfaces back to the exact location at the time of failure. Figure 3.3 shows the strain steadily increasing as the load increased. However, at the point of maximum load, the strain rate began to decrease. By the time failure occurred, the strain had stopped increasing. Curiously, at the point of specimen separation, the optical device showed no increase in strain rate. Had the device been working properly, the strain rate should have increased at the point of maximum load and again at the point of failure. Clearly, the optical device was not operating properly. Since for several specimens it was the only means of measuring strain, no accurate strain data exist for these specimens.

3.2.2 Description of Modified Strain-Measurement System

Since the optical device was producing unreliable strain data, a modified high-strain-rate measurement system was developed. A high temperature MTS clip gage was used to measure the deflection between the flags on the specimen. The specimen geometry was not altered for this new method. Knife edges were welded to the integral flags on one side of the specimens. At the time of this investigation, only one high temperature clip gage was available for use, so strain was measured from one side of the specimen only (The optical device also measures strain from only one side of the specimen.) This system is very similar to the method for measuring load-line displacement in the fracture toughness tests.

Since the MTS clip gage was rated to only 149 C (300 F), the circulating air oven could not be used to heat the specimen. Therefore, two 12.7 mm (0.5 inch) wide heater tapes were used. One heater tape was used to wrap the lower portion of the specimen and one tape was used to wrap the upper portion of the specimen. Two heater tapes provided uniform temperature distribution along the gage length. Four thermocouples were used to measure the temperature distribution across the gage section. Three of these thermocouples were on the back side of the gage section and the fourth, the control thermocouple, was on

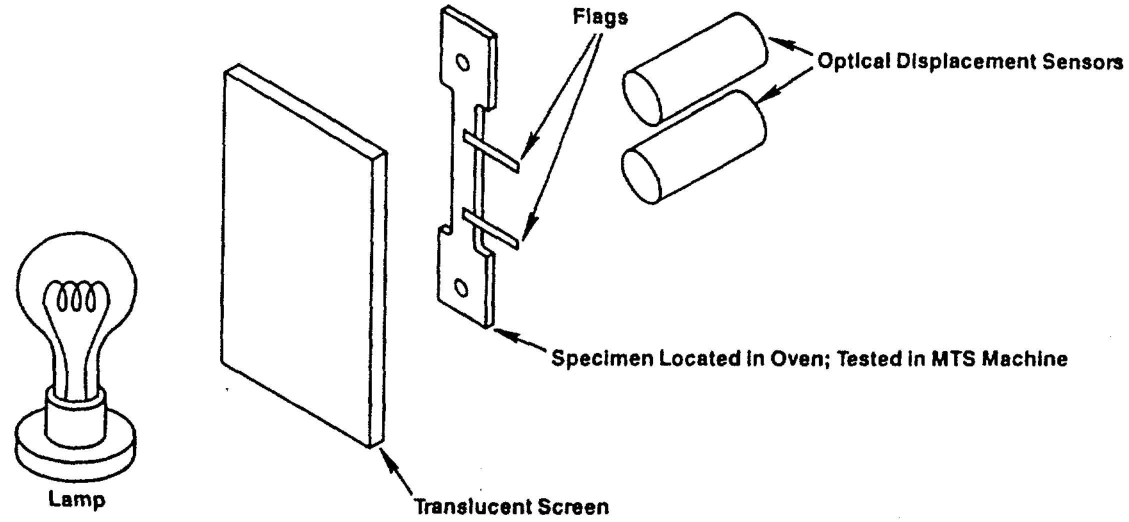

Figure 3.2 Schematic illustration of optical displacement sensors used in dynamic tensile tests

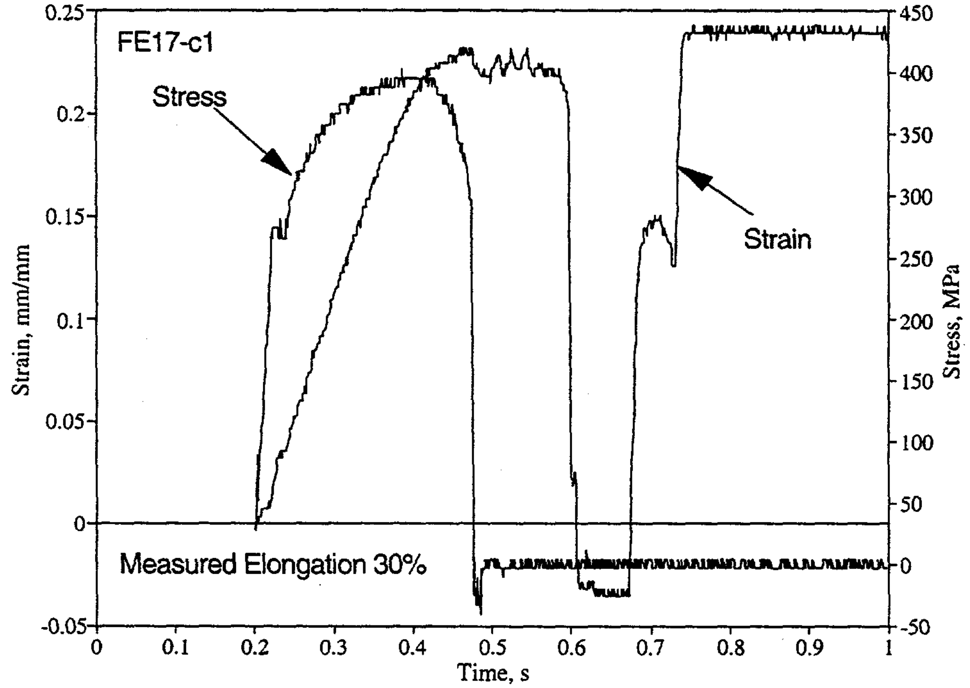

Figure 3.3 Stress and strain response from the optical extensometer

the front side in the center of the gage length. Figure 3.4 shows a schematic view of the instrumentation for the high speed tensile tests.

Figure 3.5 shows an example of the stress- and strain-versus-time using this method. The specimen was a carbon steel elbow specimen and its measured elongation was 22 percent, which agrees well with the final strain reading of 0.214. Also, at maximum load, the strain rate increased as expected. Clearly, this method for measuring strain is more reliable than the optical device.

3.2.3 Test Results

Table 3.2 shows a summary of the dynamic tensile test results. The quasi-static tensile results for each material type are also shown in the table for comparison purposes. Specimens IP-F13-T1, -T6 and -T8 are fully documented in Reference 3.4. A detailed listing of the stress-strain results for Specimens IP-F13-9, -10, -11, -12, and -13 can be found in a future release of the PIFRAC database (Ref. 3.5). No detailed listing of the stress-strain curves for the remaining specimens is given due to the erroneous strain data recorded.

The yield strengths for all dynamic specimens except the IP-F13 specimens were estimated using a strain derived from the stroke indicator since the optical device did not produce usable strain data.

From Table 3.2, as the strain rate was increased, the ultimate strength was decreased, by as much as 15 percent for IP-F1. Also, in most cases, the final elongation was significantly decreased with an increasing strain rate. Finally, the yield strength increased, by as much as 32 percent as the strain rate was increased

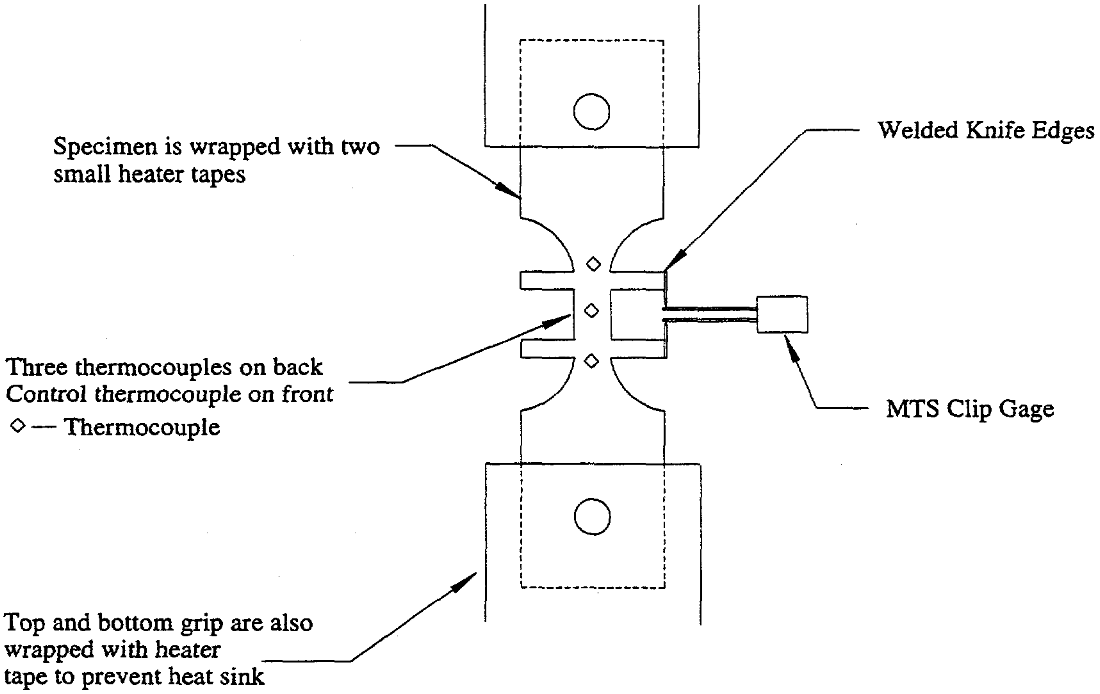

Figure 3.4 Schematic illustration of modified strain-measurement system

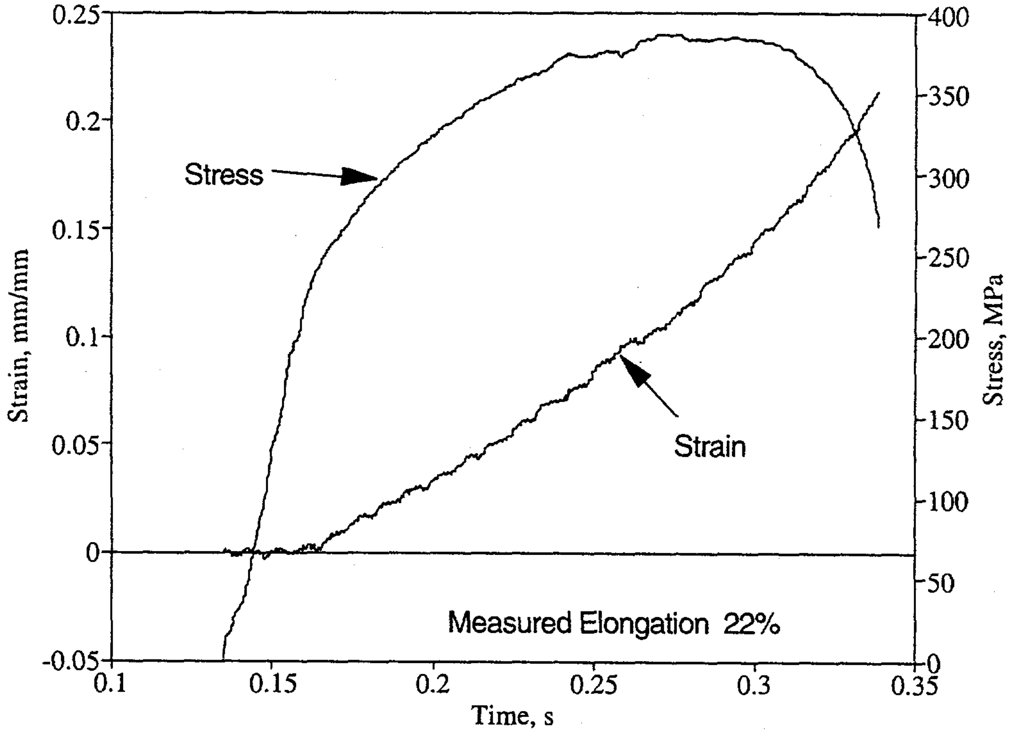

Figure 3.5 Example of stress-strain data obtained with modified strain-measurement procedure

Table 3.2 Summary of tensile data for carbon steels tested at various strain rates

Specimen Number	Test Temperature, C	Strain Rate, s^{-1}	UTS,		σ_{ys},		Final Elong., Percent
			ksi	MPa	ksi	MPa	
F22B	288	0.99	76.3	526.0	47.5	327.5	20.7
F22-1(a)	288	4×10^{-4}	85.3	588.1	37.5	258.6	26.1
F9A	288	0.91	62.9	433.5	42.7	294.4	29.5
F9B	288	1.05	68.1	469.8	44.7	308.2	24.3
F9-5(a)	288	4×10^{-4}	76.6	528.1	34.7	239.3	26.5
IPF1-1h	288	1.1	76.1	524.8	46.7	322.1	28.7
IPF1-2h	288	1.1	72.0	496.4	44.6	307.7	27.0
IP-F1-1(a)	288	4×10^{-4}	84.6	583.0	35.1	242.0	31.2
IPF13-T1(a)	300	4×10^{-4}	71.4	492.6	31.3	215.8	28.5
IPF13-T6	300	9.9	61.4	423.5	32.5	224.1	42.6
IPF13-T8	300	1.4	62.5	430.9	37.8	260.6	48.0
IPF13-T9	288	8×10^{-2}	63.0	434.4	29.1	200.6	50.5
IPF13-T10	288	3×10^{-2}	65.0	448.2	28.0	193.1	50.5
IPF13-T11	300	4×10^{-4}	72.3	498.8	32.2	221.7	53.0
IPF13-T12	300	4×10^{-4}	72.1	497.0	28.9	199.1	52.2
IPF13-T13	300	3×10^{-4}	71.1	490.4	30.4	209.8	33.4

(a) Round bar tensile specimens.

by a factor of 5,000. In Reference 3.1, dynamic tensile tests performed on other carbon steels showed similar trends, with some exceptions. For example, DP2-F30 showed the tensile strength, as well as the ductility, diminished significantly with increasing strain rate. However, it was shown that for this material, the yield strength was not affected by the increasing strain rate. Another material tested in Reference 3.1, DP2-F29 showed slightly different results. The ultimate strength decreased with increasing strain rate, but the ductility increased. When a SAW in the same material was tested, the ultimate strength again decreased, but this time the ductility decreased at a strain rate of 1/s but increased at a strain rate of 10/s.

Figure 3.6 shows the stress-strain curves for the IP-F13 material. Note that all of these high speed tests were completed using the modified strain-measuring procedure described above and not the optical device. Also, testing details for Specimens IP-F13-T1, T6 and T8 can be found in Reference 3.4. As the strain rate was increased, the ultimate strength was decreased. In going from quasi-static rates (10^{-4}/s) to intermediate rates (10^{-2}/s) the ultimate strength decreased approximately 10 percent. Increasing the strain rate to 10/s did not add significantly to the decrease in ultimate strength. A comment needs to be made about the differences in the stress-strain curves for the four quasi-static tensile tests beyond maximum load. IP-F13-T1 was a round-bar specimen with a 12.7 mm (0.5 inch) gage length, IP-F13-T13 was a flat specimen with a 25.4 mm (1.0 inch) gage length, and IP-F13-T11 and -T12 were flat specimens with an 8.9 mm (0.35 inch) gage section. The differences shown in the stress-strain behavior for these four tests can be attributed to the differences in specimen geometry. In all specimens, the maximum stress was approximately the same; however, for the flat specimens, the increase in gage length decreased the elongation by 37 percent. Also, there was a slight decrease in elongation when going from a flat specimen to a round-bar specimen. This difference is attributed to the size of the necked region relative to the gage length. In the flat specimens with the 8.9 mm (0.35 inch) gage section, the local necking is constrained by the material outside of the gage section; therefore, it requires a greater amount of elongation than does a longer specimen before the same amount of necking occurs. However, if the four quasi-static specimens

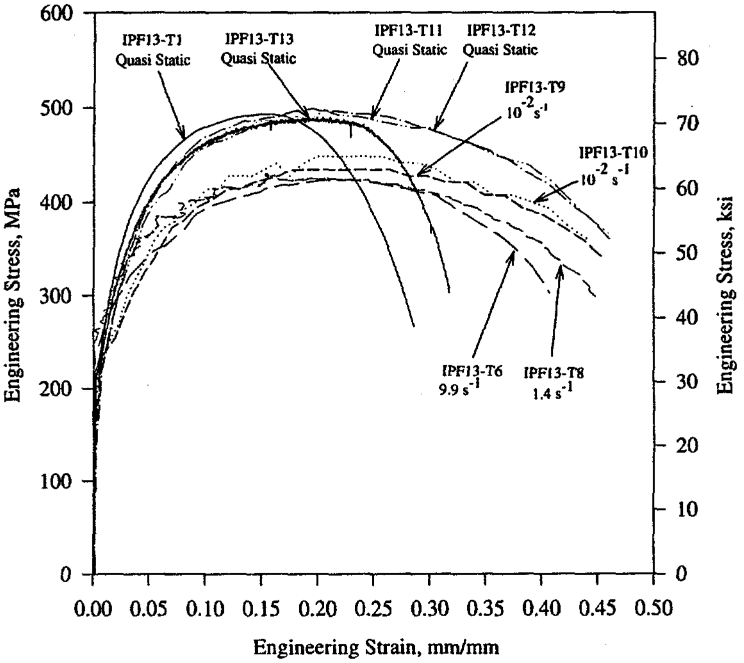

Figure 3.6 Stress-strain curves for carbon steel pipe material, IP-F13

are compared to the point of maximum load for the IP-F13-T1 specimen, they are nearly identical, indicating that the stress-strain response up to the onset of necking is not affected by the geometry of the specimen. Consequently, a Ramberg-Osgood fit of these curves should produce similar coefficients.

3.3 Dynamic Fracture Toughness Tests

All dynamic fracture toughness specimens were of the compact tension, C(T), design. They were machined from sections of pipe without mechanical flattening and were in the L-C orientation.

The C(T) specimens were of three different planform sizes, 0.5T, 1T and 1.5T, depending on the size of the pipe. The standard thicknesses for the 0.5T, 1T, and 1.5T specimens are 12.7 mm (0.5 inch), 25.4 mm (1.0 inch), and 38.1 mm (1.5 inch), respectively. Because of the pipe curvature, some of the specimens tested were less than the standard thickness. Specimen dimensions are shown in Appendix A, where w, B, B_N, and a_i denote width, thickness, net thickness at side grooves, and initial crack length, respectively.

Because of the different specimen sizes, different testing machines were used. For the 1T specimens and larger, a 222 kN (50,000 lb) servohydraulic Instron testing machine was used. For the 0.5T specimens a 22.2 kN (5,000 lb) servohydraulic MTS testing machine was used. The dynamic rate chosen for these tests was 0.2 seconds to crack initiation. This rate was chosen in IPIRG-1 to closely match the strain rate at the crack tip of a full-scale pipe experiment. As explained in Reference 3.1, finite element analyses were run and it was determined that 0.2 seconds to crack initiation in a monotonic C(T) test would represent a typical crack initiation time in a pipe system test.

All dynamic fracture toughness tests employed the direct-current electric potential (d-c EP) method to monitor crack growth. This method has been shown to provide an excellent measure of the crack growth at high strain rates (Ref. 3.1). Also, it is more practical to use the d-c EP method than the unloading-compliance method since it is difficult to measure the crack extension using the latter method for tests that last a fraction of a second.

The load cells in the servohydraulic testing machines were electrically isolated to prevent a current path through the load train. The potential leads were iron wires in order to reduce thermally induced voltages that could arise from dissimilar materials. An MTS strain-gaged clip gage was used to measure load-line displacements. This clip gage attached to the specimen by seating on razor blades welded to a lip on the specimen load-line.

All dynamic fracture toughness tests were run in stroke control. The tests terminated when the actuator displacement reached the value of the actuator displacement of a quasi-static test on the same material. The actuator speed was calculated from the desired 0.2 seconds to crack initiation and the quasi-static actuator displacement.

The data recorded during these tests included load, actuator displacement, load-line displacement, and d-c EP. All data were taken with the LABTECH® NOTEBOOK software in conjunction with a Metrabyte® DAS-20 card. A digital oscilloscope was used as a backup.

The analysis of these dynamic fracture toughness specimens was identical to that described in Section 2.3. All testing procedures and analysis follow the ASTM E813/1152 standard.

Figures 3.7 through 3.9 show the J-R results for the F22, F9, and IP-F1 specimens, respectively. A detailed listing of the J-R results will be found in a future release of the PIFRAC database (Ref. 3.5). The F22 and F9 specimens showed a significant decrease in fracture resistance as the strain rate was increased. At a crack extension equal to 30 percent of the original uncracked ligament, the F22 material showed a decrease of approximately 50 percent in J, while the F9 material showed a decrease of approximately 55 percent. The IP-F1 material showed no significant change in resistance as the strain rate was increased. The J-R curves for the IP-F13 material are not shown here since they are fully documented in Reference 3.4. However, that material showed no change in resistance with increasing strain rate.

Table 3.3 show a summary of the dynamic C(T) fracture results from this investigation. Quasi-static results are also shown in Table 3.3 for comparison purposes.

Table 3.3 Loading-rate effect on fracture resistance of carbon steel C(T) specimens

Specimen Identification	Approximate Time to Crack Initiation, s	J at Initiation		dJ/da[a]	
		kN/m	lb/in	MN/m^2	lb/in^2
F22-2	0.2	51	291	42	6200
F22-3	600	79	451	105	15300
IP-F1-1d	0.2	386	2210	131	19100
IP-F1-2d	0.2	278	1590	167	24300
IP-F1-8	600	366	2090	153	22300
F9-1d	0.2	96	549	43	6240
F9-2d	0.2	137	785	27	3970
F9-19	600	147	840	103	15050

(a) Calculated between crack lengths of 0.15 mm (0.006 inch) and 1.5 mm (0.06 inch).

For the F22 material, dynamic loading reduced the J at initiation by 34 percent and the dJ/da by 60 percent. For the F9 material, the dynamic loading reduced the average J at crack initiation by 20 percent and the average dJ/da by 66 percent. However, for the IP-F1 material, the dynamic loading did not significantly affect the J-R curve.

In Section 2 of this report, C(T) specimens machined from a carbon steel SAW were tested using cyclic loading at both quasi-static and dynamic loading rates. In addition to these cyclic tests, quasi-static and dynamic monotonic C(T) tests also were performed. This weld (DP2-F40W) was manufactured with the same weld procedure as the DP2-F29W SAW from Reference 3.1. It showed a dramatic increase in toughness as the strain rate was increased. As is shown in Figure 2.46, after some crack extension [$\Delta a=0.3(w-a_i)$] the J value under dynamic loading was 105 percent higher than the J value under quasi-static loading. The same effect was shown in Reference 3.1 for the DP2-F29W pipe indicating that dynamic loading has a different effect in carbon steel SAW than in the base metals examined. The reason for this carbon steel SAW behavior being different than the base metal behavior was explored in Reference 3.2 where the same weld procedure was used. In Reference 3.2, it was found that this weld was

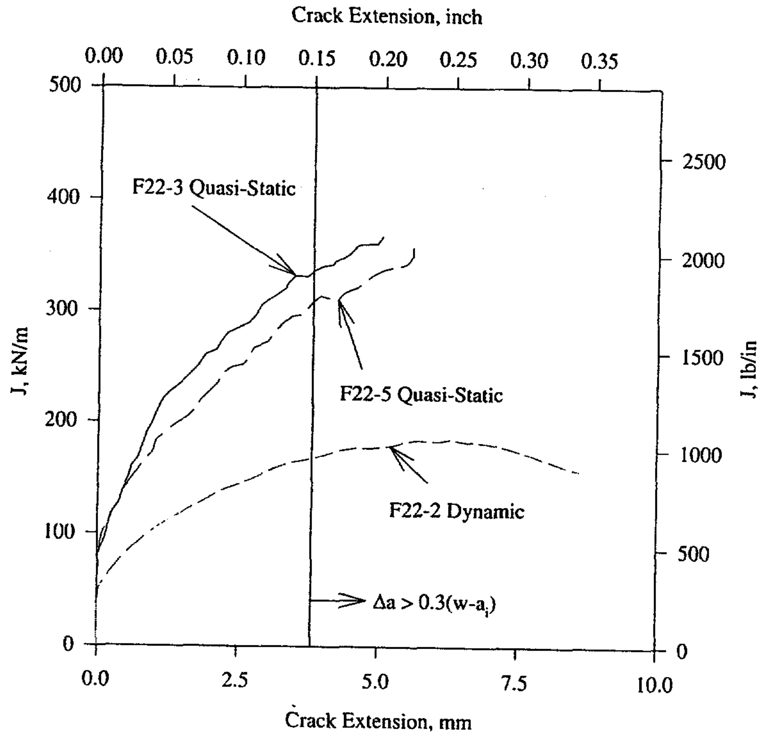

Figure 3.7 J-R curves for carbon steel pipe, DP2-F22

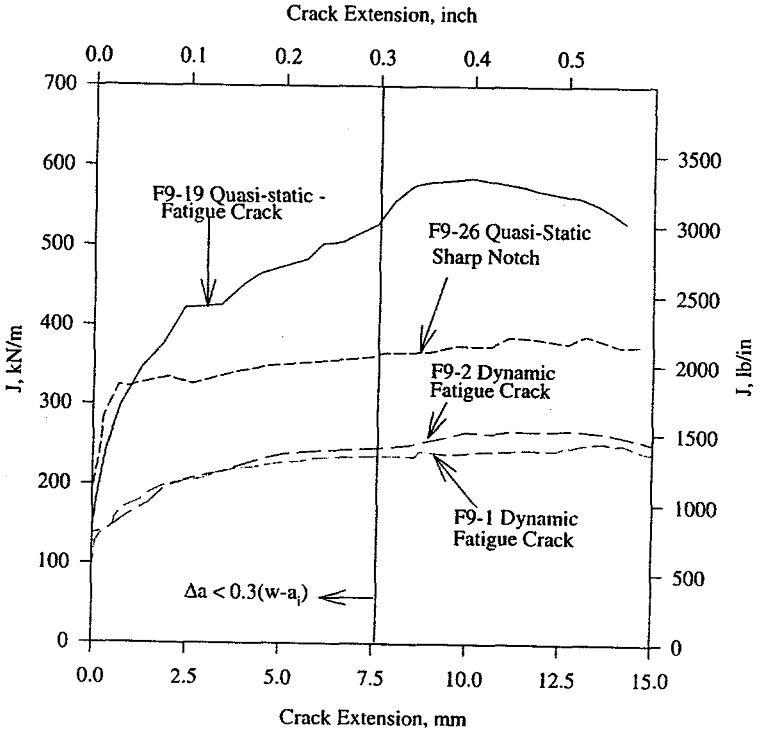

Figure 3.8 J-R curves for carbon steel pipe, DP2-F9

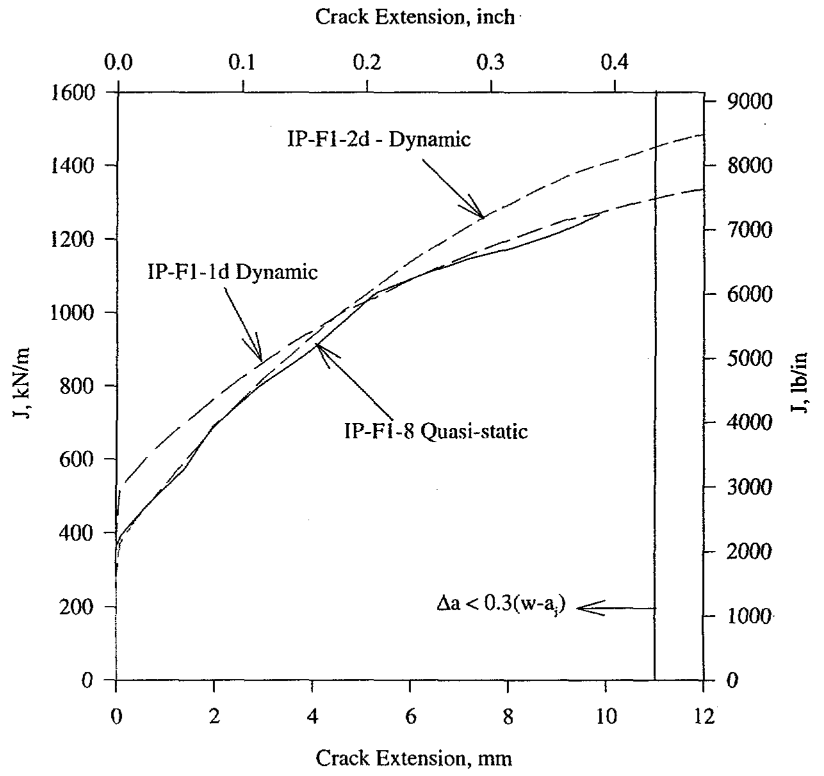

Figure 3.9 J-R curves for carbon steel pipe IP-F1

susceptible to dynamic strain aging over a much higher temperature range than all the base metals examined. It is not known if this is generally true for all carbon steel weld procedures, or just an anomaly for this weld procedure.

3.4 High Temperature Brinell Hardness Tests

Reference 3.2 discusses a simple screening criterion to measure a material's susceptibility to dynamic strain aging. In this reference, a series of high-temperature Brinell hardness tests were used to predict when crack instabilities occurred in C(T) specimen. It was found that when the ratio of the hardness value at test temperature to the hardness value at room temperature BHN_{288}/BHN_{RT} was greater than 1.09, crack instabilities occurred. In this study, the same criterion was used to find a trend for the decrease in fracture resistance due to dynamic loading.

The high temperature hardness tests conducted as part of this investigation were performed identically to the tests performed in Reference 3.2. Figure 3.10 shows the hardness values as a function of temperature for the materials tested in this study. Also included in the figure are hardness values for DP2-F23 (A106 Grade B 16-inch straight pipe), DP2-FE17 (A106 Grade B 16-inch elbow), and IP-F16W (STS410 TIG

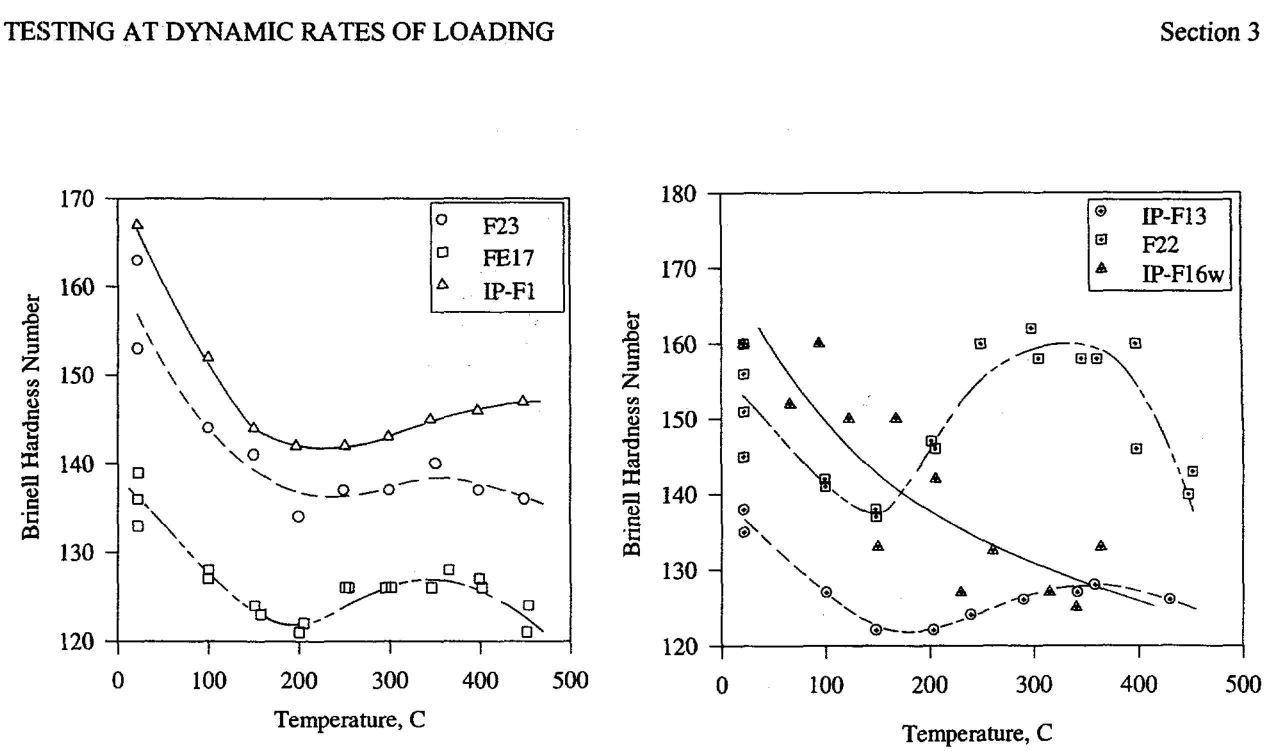

Figure 3.10 Brinell hardness versus temperature for a variety of carbon steel materials

weld in 6-inch straight pipe). The hardness data for the DP2-F9 and DP2-F29W materials are found in Reference 3.2.

A plot of the Brinell hardness ratio versus the dynamic-to-quasi-static toughness ratio for the specimens tested in this study is found in Figure 3.11. This toughness ratio is taken at a crack extension of 0.3(w-a_i). In ASTM E1152, the maximum allowable crack extension is defined as 10 percent of the original ligament for a C(T) specimen; however, recent studies (Ref. 3.6) have shown that the crack extension in a C(T) specimen is valid up to 30 percent of the original ligament. From Figure 3.11, it appears that materials whose hardness ratio is greater than 1.0 have toughness degradation due to dynamic effects. This trend seems to hold true for all of the base metals. However, DP2-F29W, a 16-inch SAW, appears to act differently. Even though its hardness did not change much with temperature, its dynamic resistance is much higher than its quasi-static resistance. It is possible that this screening criterion is not applicable to submerged-arc welds.

Figure 3.12 shows the same fracture toughness ratio as a function of the yield-to-ultimate strength ratio. Included in this figure are both base metal and weld metal materials. A trend seems to be forming that as the yield-to-ultimate-strength ratio is increased, the dynamic J-R curve also increases as compared to the monotonic J-R curve. This trend suggests that if a metal's yield-to-ultimate strength ratio is greater than 0.5, the dynamic J-R curve will be equal to or greater than the monotonic J-R curve. However, most carbon steel base metal materials have a yield-to-ultimate strength ratio less than 0.5 and will show a detrimental effect of the J-R curve with increasing strain rate. Interestingly, the two SAWs tested showed a large increase in resistance, but also had a yield-to-ultimate strength ratio greater than 0.5. However, the STS410 TIG weld also had a yield-to-ultimate ratio greater than 0.5 but showed no change in fracture

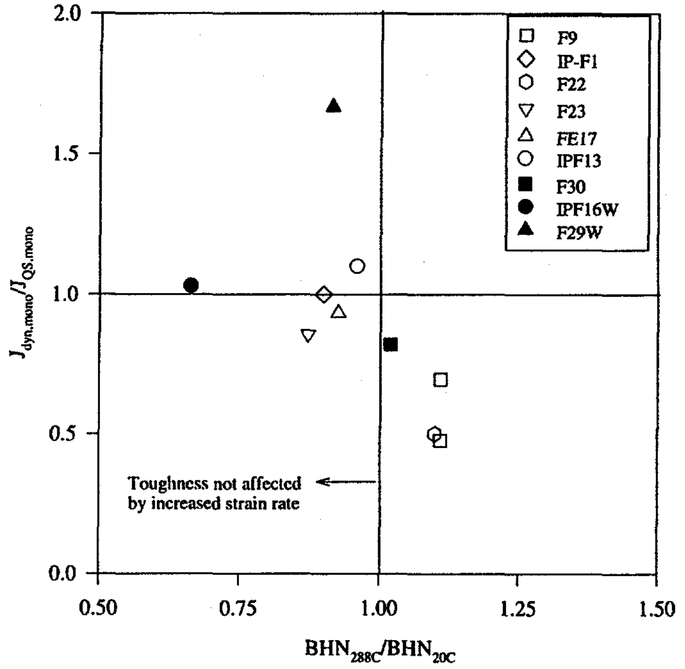

Figure 3.11 $J_{dyn,mono}/J_{QS,mono}$ versus BHN_{288}/BHN_{RT} for a variety of carbon steel base and weld metals

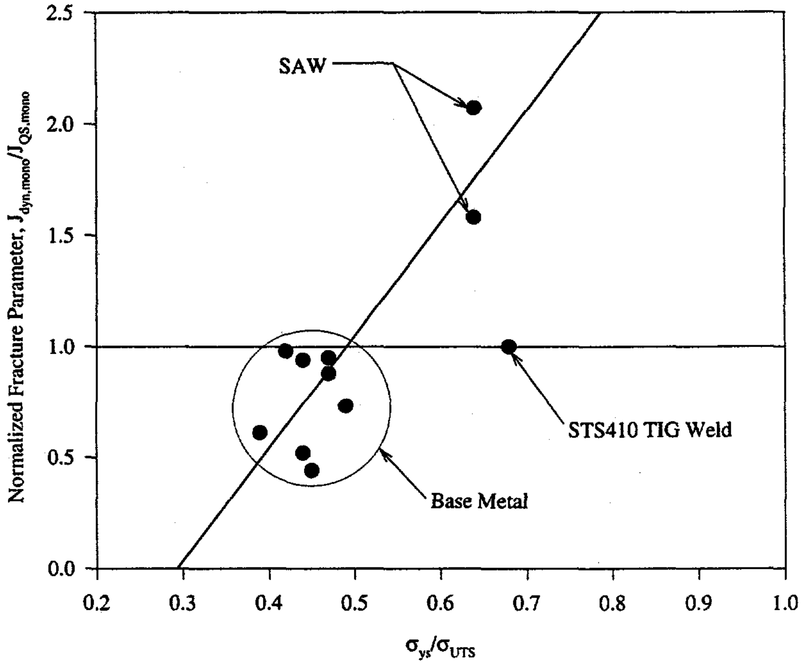

Figure 3.12 $J_{dyn,mono}/J_{QS,mono}$ versus yield-to-ultimate ratio for a variety of carbon steel base metals and weld metals

resistance with increasing strain rate. This result suggests that there are not enough data available to make a solid conclusion about the trend shown in Figure 3.12.

3.5 Discussion of Dynamic-Loading Rate Effects on Carbon Steel Material Properties

In a quasi-static tensile test, carbon steel materials can age either statically or dynamically. If a tensile specimen is strained, unloaded, and allowed to age at an elevated temperature, it will have a higher yield and ultimate strength than if it was not aged. This phenomenon is called static strain aging. As noted in Reference 3.2, carbon steel materials also age dynamically, i.e., a quasi-static tensile test at elevated temperatures produces different yield and ultimate strengths than do room temperature tests. This change in strength is attributed to the diffusion of carbon and nitrogen atoms to moving dislocations. Since it takes time for these atoms to diffuse, the effects of this aging will be dependent on the strain rate as well as the temperature. Also affecting the strain aging process will be the amount of carbon and nitrogen in the material.

From the carbon steel materials tested in this investigation and in Reference 3.1, the effects of increased loading rate on the stress-strain behavior were similar in all carbon steel materials tested. All showed a decrease in ultimate strength with an increase in strain rate at 288 C (550 F). As the strain rate is increased, the interstitial atoms have less time to diffuse to the moving dislocation; thus, the plastic strains are greater and the limit load is less. Interestingly, even though the ultimate strength decreased in all cases, the yield strengths increased or were unchanged in all cases.

Even though the stress-strain response was similar for the materials tested, the effects of dynamic loading on the fracture resistance were inconsistent. While some base metal specimens showed a decrease in fracture resistance with increasing loading rate, others showed no change in resistance with the same increase in rate. The submerged-arc weld tested in Reference 3.1 and in Section 2 of this report showed a significant increase in fracture resistance with increasing loading rate. However, the STS410 TIG weld tested in Reference 3.4 showed no change in resistance with increasing loading rate.

Possibly, this change in fracture resistance is also related to the materials yield-to-ultimate strength ratio. The trends shown in Figure 3.12 suggest that dynamically loaded carbon steel materials whose yield-to-ultimate-strength ratio is greater than 0.5 will have toughness values that are equal to or higher than those tested with quasi-static loading rates. This dependency on yield-to-ultimate strength ratio may aid in the creation of a criterion that would characterize a material's fracture toughness response to dynamic loading; however, the amount of data available is still too limited to create a reliable criterion given the scatter seen in Figure 3.12. Another possibility is that in order to reduce the scatter in predicting the dynamic toughness from quasi-static properties, multiple parameters may be needed, e.g., σ_{ys}, σ_{UTS}, BHN_{288}, BHN_{RT}, etc.

3.6 References

3.1 Marschall, C. W., Landow, M. P., and Wilkowski, G. M., "Loading Rate Effects on Strength and Fracture Toughness of Pipe Steels Used in Task 1 of the IPIRG Program," NUREG/CR-6098, BMI-2175, October 1993.

3.2 Marschall, C. W., Mohan, R., Krishnaswamy, P., and Wilkowski, G. M., "Effect of Dynamic Strain Aging on the Strength and Toughness of Nuclear Ferritic Piping at LWR Temperatures," NUREG/CR-6226, BMI-2176, October 1994.

3.3 Kilinski, T. J., Mohan, R., Rudland, D. L., Wilkowski, G. M., and Choi, Y-H., "Fracture Analysis of Cracked Elbows: Part 2 - Comparison of Experimental Results with Estimation Predictions," ASME PVP, Vol. 323, pp 97-107, 1996.

3.4 Rudland, D. L., Scott, P., and Wilkowski, G. W., "The Effect of Cyclic and Dynamic Loads on a Carbon Steel Pipe," NUREG/CR-6438, BMI-2188, February 1996.

3.5 Wilkowski, G. M., and others, "Short Cracks in Piping and Piping Welds," NUREG/CR-4599, Vol. 4, No. 1, April 1995.

3.6 Wilkowski, G. M., Marschall, C. W., and Landow, M., "Extrapolations of C(T) Specimens J-R Curves for Use in Pipe Flaw Evaluations," ASTM STP1074, pp 56-84, 1990.

4.0 COMPARISON OF C(T)-SPECIMEN RESULTS TO TWC PIPE TESTS

This section compares the fracture toughness results of the C(T)-specimen experiments conducted in this effort to the cyclic and dynamic pipe experiments conducted in the IPIRG-1 and IPIRG-2 programs. Also, using a variety of J-estimation schemes, a series of TWC and surface-cracked pipe moment predictions using the cyclic and dynamic C(T) J-R curves are presented. Finally, a series of sensitivity calculations are presented that aid in the assessment of pipe diameter effects on the maximum failure loads for cyclically and dynamically loaded pipes. These results are presented in two parts: (1) cyclic-loading effects, and (2) dynamic-loading effects.

4.1 Cyclic-Loading Effects

4.1.1 Review of TWC Pipe Fracture Studies

In the IPIRG-1 program, twelve displacement-controlled cyclic-load TWC pipe tests were conducted on both stainless steel (TP304) and carbon steel (A106 Grade B) 6-inch nominal diameter Schedule 120 pipes. The objective of that study was to compare the dynamic- and cyclic-load effects on the fracture resistance of these pipe materials. The pipe tests were conducted at stress ratios of 0 and -1 with quasi-static and dynamic loading rates. Dynamic loading refers to loading rates comparable to those in high amplitude seismic events, i.e., 2 to 4 Hz. Only the quasi-static tests are discussed in this section of the report. Full details of these tests can be found in Reference 4.1.

The J-resistance curves for these pipe tests were calculated using the η-factor approach. The η-factor analysis is a general analytical procedure where the fracture resistance is estimated using the experimental load, the pipe displacement at the load point, and the crack extension data from the experiment. The analysis method for a circumferential through-wall-cracked pipe was first developed by Zahoor (Ref. 4.2) and later improved by Pan (Ref. 4.3). The J-R curve calculated is based on the deformation theory of plasticity. Battelle has incorporated this method into a computer code called ETAFACTR, which was substantially improved during the IPIRG-2 program(*). The procedures behind the code are explained in Reference 4.4.

As in the cyclic C(T)-specimen experiments, only the upper envelope of the load-displacement record was used to calculate the J-R curves for the cyclic-load experiments. The possible contributions of fatigue crack growth were not accounted for. Even though the formal definition of J is violated when unloadings occur, these resistance curves can be used to evaluate the apparent effect of cyclic loading on the fracture resistance of these materials.

Figure 4.1a shows the J-R curves for the quasi-static, monotonic- and cyclic-load carbon steel TWC pipe tests conducted in IPIRG-1, while Figure 4.1b shows the J-R curves for the stainless steel TWC pipes from the same program (Ref. 4.1). For these pipe steels, the fracture resistance of the material was lowered significantly as the stress ratio was decreased to -1. There was no significant change in the resistance in

---

(*) Improvements made by Mr. N. Miura of CRIEPI while a visiting scientist at Battelle.

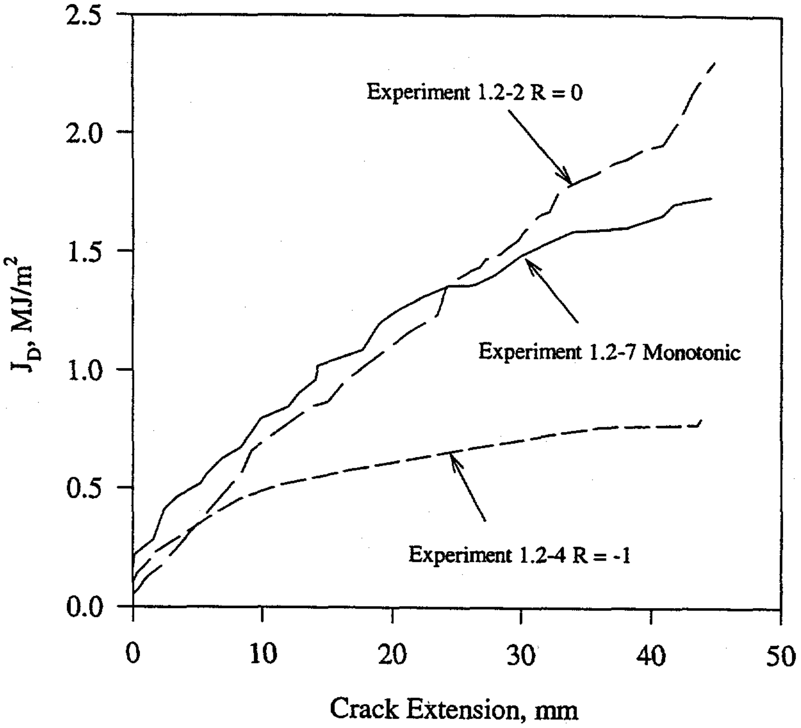

(a) Carbon steel (A106 Grade B)

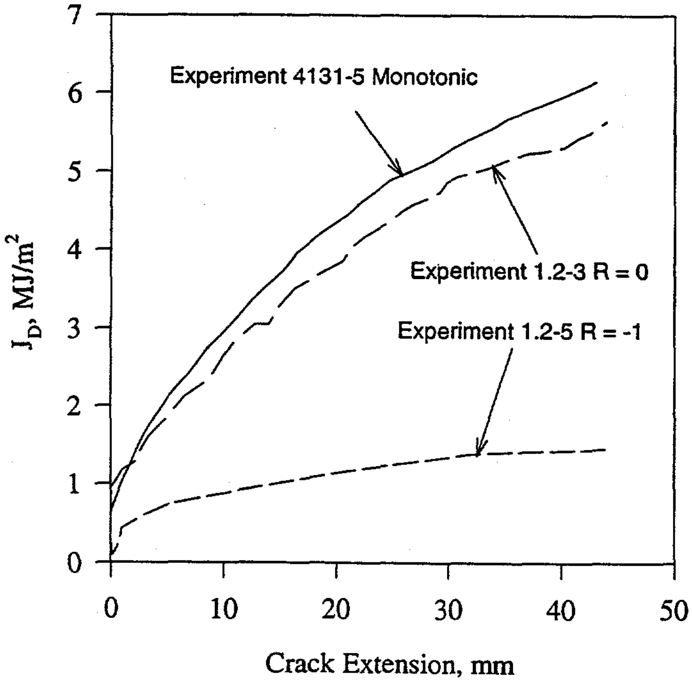

(b) Stainless steel (TP304)

Figure 4.1 J-R curves for quasi-static, monotonic, and cyclic-load 6-inch nominal diameter TWC pipe tests

going from a monotonic experiment to one with a stress ratio of zero. Note that angled crack growth from the circumferential plane occurred in all of the carbon steel experiments. For the angled crack growth cases, the crack length used in the J calculations was the crack length projected back onto the circumferential crack plane.

4.1.1.1 Intermediate Stress Ratio Test on A106 Grade B Carbon Steel Pipe

As discussed in Section 2.3.1, the fracture resistance of the carbon steel pipe tested in this investigation was more sensitive to intermediate stress ratios than was the stainless steel tested. This conclusion was based on observations made from the cyclic-load C(T) tests conducted. To verify this effect in cracked pipe, a quasi-static, cyclic-load, TWC pipe test was conducted with a stress ratio of -0.6. Except for the stress ratio, this pipe test was identical to the quasi-static, cyclic-load, TWC pipe tests conducted as part of Subtask 1.2 of the IPIRG-1 program (Ref. 4.1). The test specimen for this experiment was fabricated from a 6-inch nominal diameter, Schedule 120, A106 Grade B carbon steel pipe. The test specimen contained a circumferential through-wall crack. The test temperature for this experiment was 288 C (550 F). The pertinent experimental parameters and test results are listed in Table 4.1.

Table 4.1 Parameters and results from Experiment 3.3-2

Experimental Parameters	
Test material	A106 Grade B carbon steel
Material identification	DP2-F31
Crack location	Base metal
Average outside pipe diameter	167.8 mm (6.605 inch)
Average pipe wall thickness	13.7 mm (0.540 inch)
θ/π	0.369
Loading conditions	Quasi-static, R = -0.6
Outer span for four-point bending	1.524 m (60 inches)
Inner span for four-point bending	0.610 m (24 inches)
Test temperature	288 C (550 F)
Experimental results	
Moment at crack initiation (based on initiation at Tip A)	31.81 kN-m (245.1 x 10^3 in-lb)
Maximum moment	40.05 kN-m (354.5 x 10^3 in-lb)

Figure 4.2 shows the experimental moment-rotation curve. As in the IPIRG-1 TWC displacement-controlled pipe tests, the fracture toughness of the cyclic test was estimated using the η-factor approach. The upper envelope of the load-displacement record was used in this analysis. Figure 4.3 shows the upper envelope of the load-displacement record for Experiment 3.3-2. Also included in this figure are the load-displacement records for the quasi-static, monotonic-load (Experiment 1.2-7) , the quasi-static, R = 0 (Experiment 1.2-2) and the quasi-static, R = -1 (Experiment 1.2-4) experiments. In comparing these tests it is important to note that for each of the experiments the angle from the circumferential plane at which the cracks grew was different. Table 4.2 shows these angles and the J at crack initiation for each experiment.

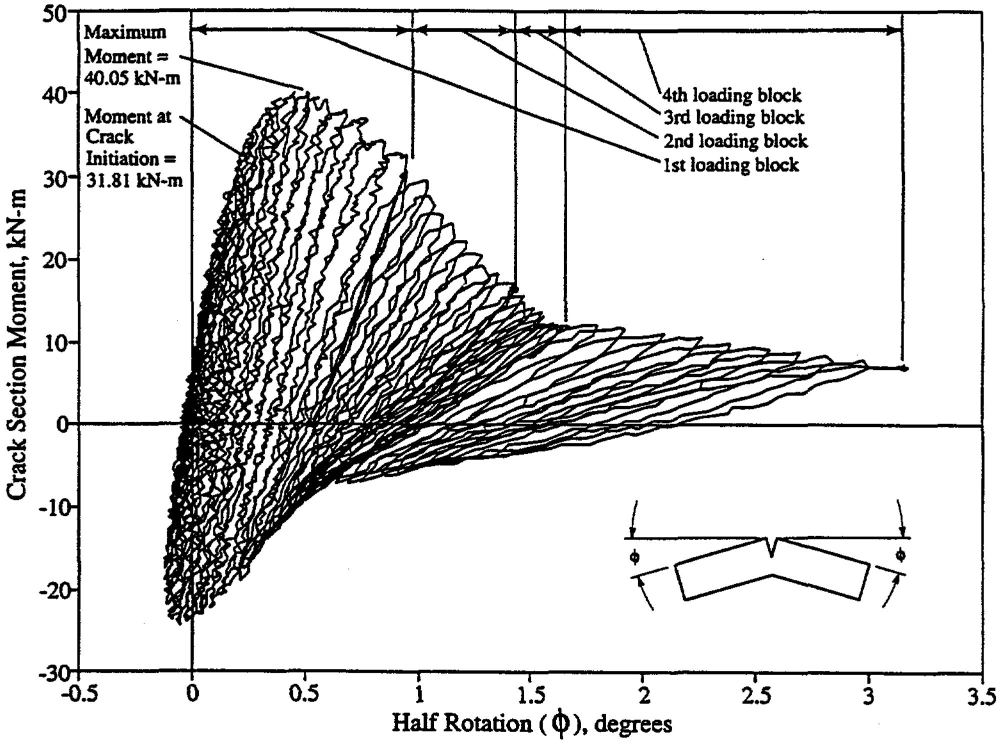

Figure 4,2 Crack-section moment versus half rotation for Experiment 3.3-2

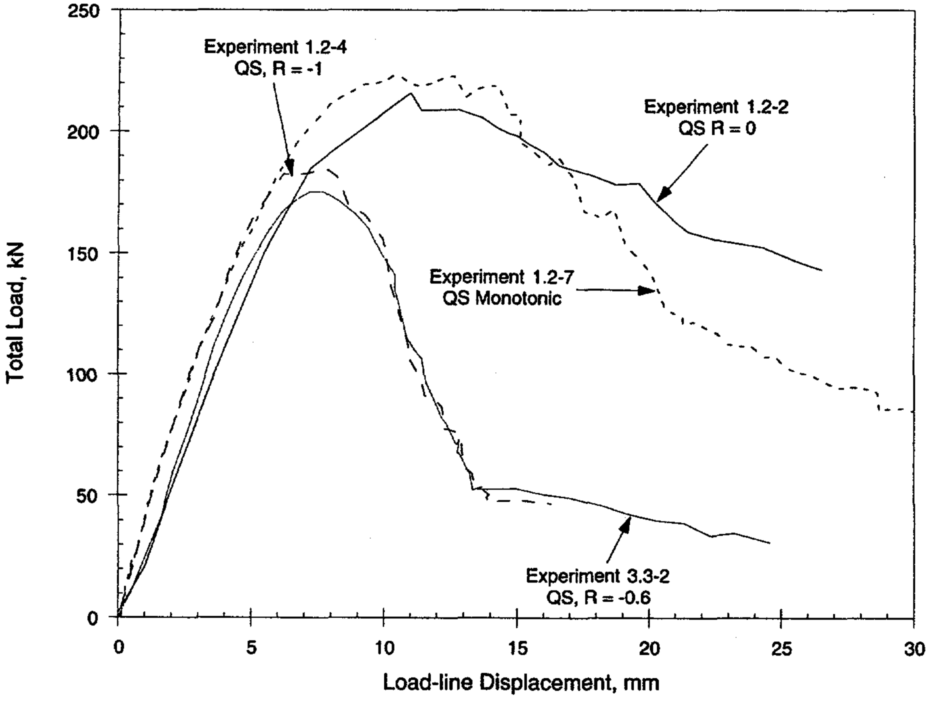

Figure 4.3 Load-displacement records for 6-inch nominal diameter carbon steel pipe experiments

Table 4.2 Crack growth angle from the circumferential plane for quasi-static TWC carbon steel experiments

Experiment	Stress Ratio	Angle from circumferential plane, degrees	J_i, kJ/m^2
1.2-7	1	40	160
1.2-2	0	46	49
3.3-2	-0.6	32	97
1.2-4	-1	45	99

Previous work on the angled-crack-growth phenomenon (Ref. 4.5) suggests that as the crack growth becomes more axial, the area under the moment-rotation curve increases, thus increasing the apparent fracture resistance. Also, the work in Reference 4.5 suggests that most carbon steels will experience this type of crack growth because of the inherent anisotropy in the material. This particular heat of pipe had inherent anisotropy due to the forming process of the seamless pipe. This anisotropy also causes a large scatter in the material properties of this particular pipe. For example, Figure 4.1a shows that after some crack extension, the R = 0 experiment had a resistance approximately equal to the monotonic experiment. However, at crack initiation, the J value (J_i) for the R = 0 experiment was even lower than the J_i value for the R = -1 experiment. This may be due to the variability in this material as was discussed in Reference 4.1.

Figure 4.4 shows the calculated J-R curve for Experiment 3.3-2. Also included in this plot are the J-R curves for Experiments 1.2-4 and 1.2-7. The J_i value calculated for this experiment was almost identical to that calculated for Experiment 1.2-4 (see Table 4.2). However, because of the differences in the angled crack growth, the resistance for the R = -0.6 experiment appears as slightly lower than the R = -1 experiment.

4.1.2 Comparison of Cyclic-Load Pipe and Cyclic-Load C(T)-Specimen J-R Curves

4.1.2.1 Stainless Steel

Figures 4.5, 4.6, and 4.7 show a comparison between the IPIRG-1 stainless steel cyclic-load TWC pipe and the IPIRG-2 cyclic-load C(T) J-R curves for displacement increments of 0.1, 0.2, and 0.025, respectively. From these plots, the conclusion was that there is some agreement between the C(T) and TWC pipe tests. In some cases, the C(T) specimens tested at a stress ratio of -1 produce J-R curves similar to the TWC pipe at a stress ratio of -1. However, for the case when the displacement increment is 0.025, the C(T) R = -1 specimen produced a J-R curve that was slightly lower than the pipe J-R curve. The main discrepancy between the C(T) and the TWC pipe J-R curves is the dJ/da values at the higher stress ratios. In all cases, the pipe J-R curves had a much higher dJ/da than the C(T) tests at the same stress ratio. In the pipe tests, the cyclic loads decreased the dJ/da value considerably. However, this was not the case for the C(T) specimens. From Table 2.2, the dJ/da values for the C(T) specimen did decrease slightly for all displacement increments; however, Figures 4.5, 4.6 and 4.7 show that the effect was not as obvious as in the pipe tests.

In general, the J_i values calculated for the C(T) specimens were slightly higher than those for the TWC pipes. Figure 4.8 shows a plot of these J_i values versus stress ratio for the stainless steel material. As the

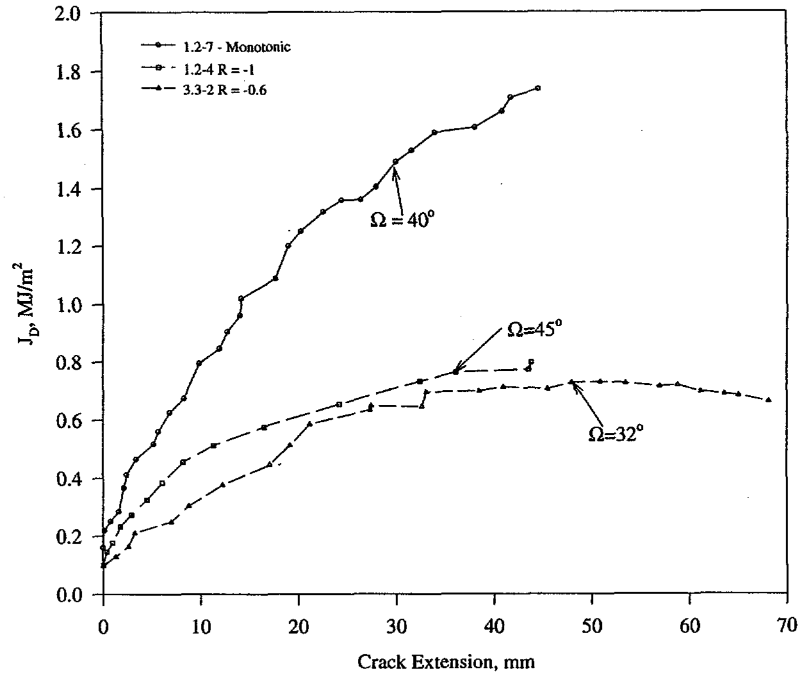

Figure 4.4 Comparison of J-R curves for carbon steel TWC pipe experiments

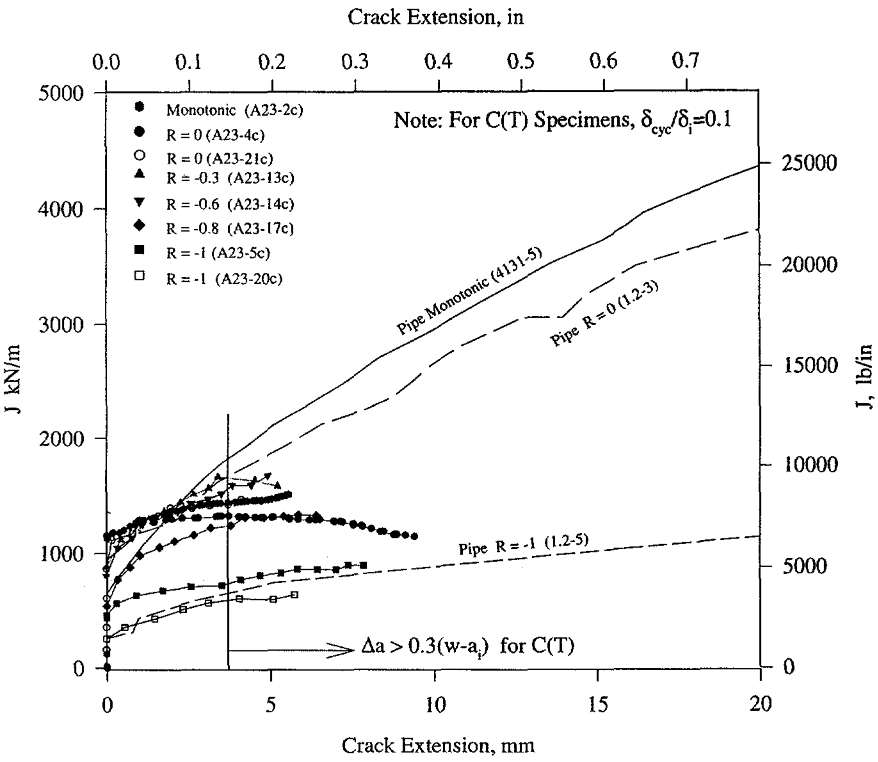

Figure 4.5 Comparison of cyclic-load J-R curves for stainless steel C(T) specimens tested with $\delta_{cyc}/\delta_i = 0.1$ and stainless steel TWC experiments

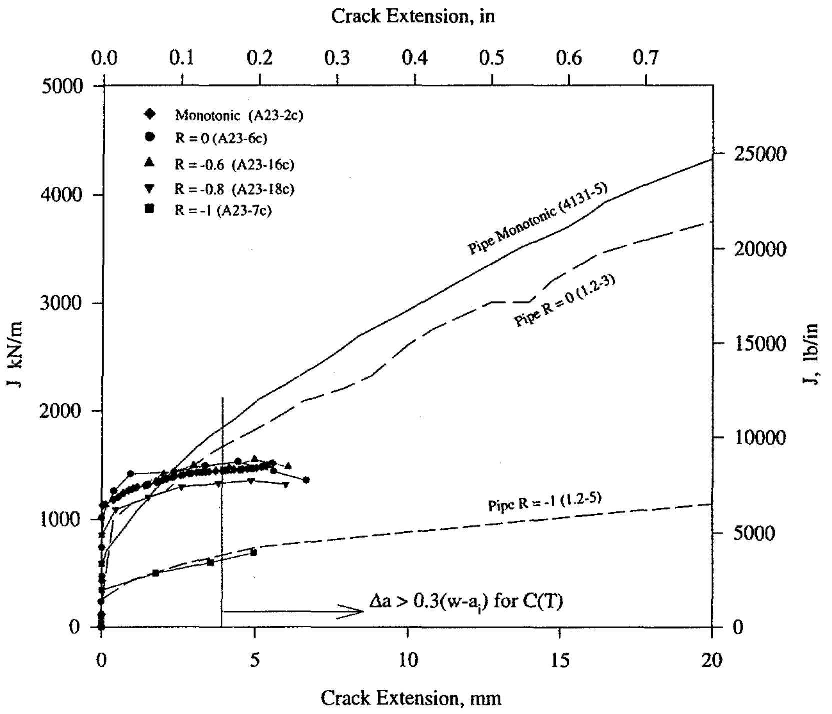

Figure 4.6 Comparison of cyclic-load J-R curves for stainless steel C(T) specimens tested with $\delta_{cyc}/\delta_i = 0.2$ and stainless steel TWC experiments

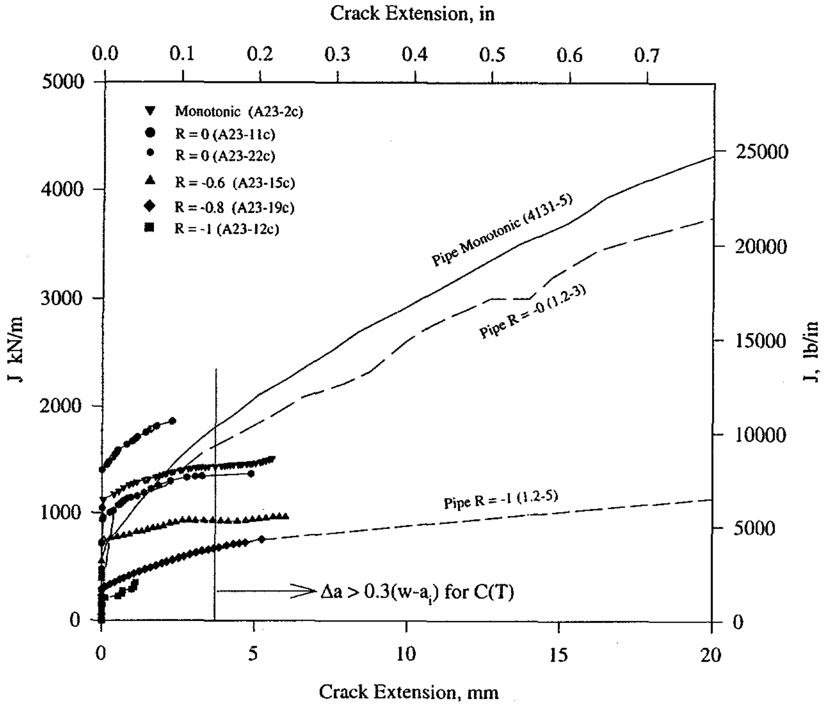

Figure 4.7 Comparison of cyclic-load J-R curves for stainless steel C(T) specimens tested with $\delta_{cyc}/\delta_i = 0.025$ and stainless steel TWC experiments

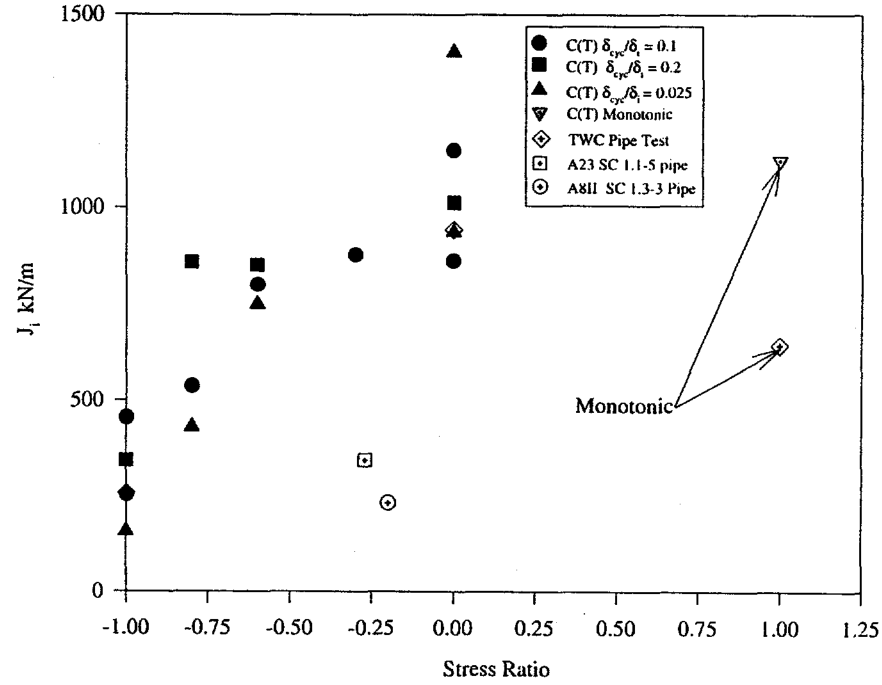

Figure 4.8 J at crack initiation versus stress ratio for stainless steel C(T) and pipe experiments

stress ratio was increased, the value of J at crack initiation was also significantly increased. The displacement increment may play a small role in the amount of increase that accompanies the increase in stress ratio. Figure 4.8 shows that at a displacement increment of 0.2, there was a large increase in the J_i value, going from a stress ratio of -1 to -0.8, with only a slight additional increase in J_i when the stress ratio became zero. At a displacement increment of 0.025 there was a relatively constant increase in the J_i value as the stress ratio was increased from -1 to 0. It is difficult to compare these results to the TWC pipe tests since there are only two TWC stainless steel cyclic-load pipe tests for comparison. However, these two pipe test J_i values fall in the range of data predicted from the C(T) tests. From these data, the conclusion that the cyclic-load C(T) data can be used to predict TWC cyclic-load crack initiation toughness values for stainless steel is reasonable.

After crack initiation, all C(T) J-R curves had lower dJ/da values than the TWC pipe J-R curves. The differences in the dJ/da are due to the differences in crack growth between the pipe and C(T) specimen. Figure 4.9 shows a comparison between the cyclic-load TWC pipe and the cyclic-load C(T) crack growth per cycle for this stainless steel. In Figure 4.9, labels A, C, and E show R = -1 crack growth comparison results for the stainless steel specimens at displacement increments of 0.1, 0.2, and 0.025, respectively. Labels B, D, and F show the same comparisons but for the R = 0 case. Note that the R = -1 and R = 0 TWC pipe tests were not conducted at a constant displacement increment; a displacement increment of 0.1 was used up to maximum moment. Therefore, three different displacement increments were used. A crack-growth-per-cycle value was taken from the each of the displacement increments, i.e., each cyclic-load TWC pipe test produced three crack-growth-per-cycle values.

From Figure 4.9, the cyclic-load C(T) tests severely underpredicted the crack growth per cycle in the TWC pipe tests. This result is expected since the absolute displacement per cycle is much smaller for the C(T)

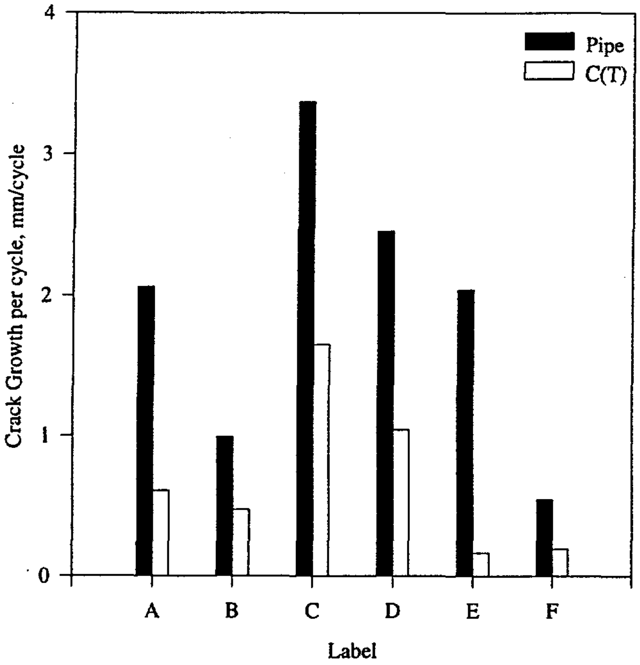

Label	R	δ_{cyc}/δ_i	Material
A	-1	0.1	A23
B	0	0.1	A23
C	-1	0.2	A23
D	0	0.2	A23
E	-1	0.025	A23
F	0	0.025	A23

Figure 4.9 Crack growth per cycle for stainless steel C(T) and TWC pipe experiments

experiments. In all cases, the C(T) specimens produced at least 50 percent less crack growth per cycle than its pipe test counterpart. However, if the C(T) results from Label D ($R = 0$, $\delta_{cyc}/\delta_i = 0.2$) are compared to the pipe results of Label B ($R = 0$, $\delta_{cyc}/\delta_i = 0.1$) an interesting observation can be made. The C(T) test at the larger displacement increment produced a crack growth per cycle that is nearly identical to that of the pipe test at the lower displacement increment. The same result is observed if the C(T) result from Label C ($R = -1$, $\delta_{cyc}/\delta_i = 0.2$) is compared to the pipe results from Label A ($R = -1$, $\delta_{cyc}/\delta_i = 0.1$). It is likely that the differences in crack growth per cycle are a function of specimen size. From this comparison, the size difference may be accounted for by increasing the displacement increment for the smaller specimen, i.e., possibly having one displacement increment up to crack initiation, and a different displacement increment during crack growth. The trends shown in Figure 4.9, that suggest that doubling the displacement increment after crack initiation will create better similitude between the TWC pipe and C(T) J values during crack growth, have been reproduced by calculating the crack growth per cycle from an NRCPIPE run of a TWC pipe test and determining the displacement increment needed to match that crack growth per cycle from the C(T) experimental data. These calculations give confidence that is it possible to have similitude between the C(T) and TWC pipe J values both before and after crack initiation.

Figure 4.10 shows $J_{QS,cyc}/J_{QS,mono}$ as a function of stress ratio. The ratio $J_{QS,cyc}/J_{QS,mono}$ is a measure of the decrease in J when going from a monotonic to a cyclic loading history. In order to make a comparison between the C(T) and TWC pipe experiments, the J values were taken at a crack extension equal to 30 percent of the initial ligament. The trends in the figure are similar to the trends observed in the initiation values of Figure 4.8. The amount J decreases with decreasing stress ratio is a function of the displacement increment. For small increments, the J value drops significantly at the intermediate stress ratios, while at large displacement increments, the decrease in J is minimal until a stress ratio of -0.8. It is possible that

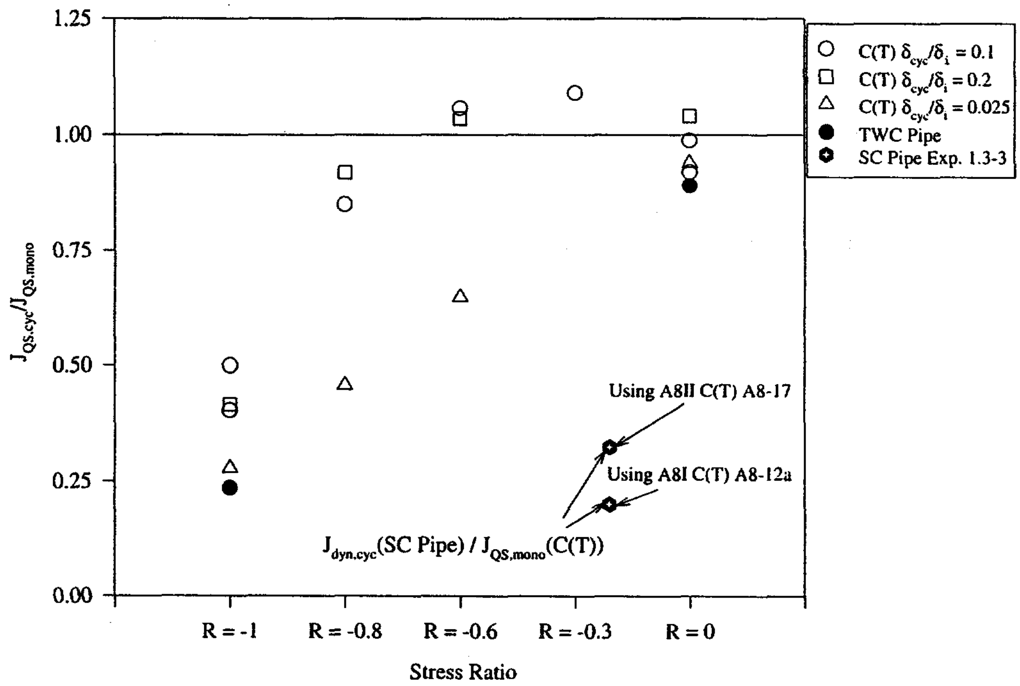

Figure 4.10 $J_{QS,cyc}/J_{QS,mono}$ versus stress ratio for stainless steel C(T) and pipe experiments

fatigue is playing a role in the apparent decrease in J at the smaller displacement increments. However, it is more likely that with smaller crack growth increments, the crack is growing in a more severely damaged region of material than if it was allowed to grow further during each cycle. Since there is less crack growth per cycle, it is reasonable to assume that the damage ahead of the crack is greater which would cause apparent crack extension at lower values of J.

Each of the stainless steel TWC pipe results fall below any of the C(T) predictions in Figure 4.10. Therefore, for the stainless steel, the cyclic-load C(T) experiments tended to overpredict the TWC pipe $J_{QS,cyc}/J_{QS,mono}$ response at this particular crack extension. Overall, the C(T) tests did a reasonable job in predicting the decrease in toughness under cyclic loading. Note, however, that the $J_{QS,cyc}/J_{QS,mono}$ ratio is a relative measure of the decrease in J due to cyclic loading. From Figures 4.5, 4.6, and 4.7, it is evident that the cyclic-load C(T) J-R curves cannot be used to predict absolute values of J for the pipe tests during crack growth.

In both Figures 4.8 and 4.10, two surface-cracked pipe results are shown along with the TWC pipe and C(T) results. These tests were conducted as part of IPIRG-1. Experiment 1.1-5 was conducted using the same pipe material that was used to manufacture the stainless steel C(T) specimens from this study. The pipe specimen contained a circumferential external surface crack and was inertially loaded in two-point bending. The J_i value shown in Figure 4.8 was calculated in Reference 4.6. Experiment 1.3-3 was a single-frequency pipe system experiment on a 180-degree, 66-percent-deep, internal, surface flaw. The material used in this experiment was a section of 16-inch nominal diameter, Schedule 100 stainless steel seamless pipe. The J values used in Figures 4.8 and 4.10 were calculated in Reference 4.7.

An interesting observation can be made from the comparison between the TWC and the surface-cracked pipe results. Conclusions from Reference 4.7 indicated that the difference between the C(T) J-R curve and the J-R curve for Experiment 1.3-3 was possibly a function of the loading history. It was suggested that the surface-crack geometry and the radial crack growth direction under cyclic loading may inherently produce a lower J-R curve than from a compact tension specimen under monotonic loading. However, work performed in Reference 4.8 suggests that the apparent resistance produced by the single-edge-notch (tension) [SEN(T)] geometry is dependent on the crack depth. In Reference 4.8, a series of SEN(T) experiments were conducted in order to investigate the cyclic-loading and crack depth effect using the SEN(T) geometry. The material used in the Reference 4.8 investigation was the same material (DP2-A8) used in the Reference 4.7 investigation. In Reference 4.8, it was discovered that the three original lengths of Pipe DP2-A8 had two distinct chemical compositions and toughnesses. The two heats of material were labeled DP2-A8I and DP2-A8II, which explains the differences in the two data points for Experiment 1.3-3 in Figure 4.10. From Reference 4.8, it was found that the SEN(T) specimens produced cyclic-load J-R curves that were similar to the J-R curve calculated for the SC pipe experiments when loading history and crack depth were accounted for. This finding indicated that for stainless steels, the large differences seen between the surface-cracked pipe experiments and the C(T) results are an effect of crack depth and cyclic-load effects.

4.1.2.2 Carbon Steel

Figure 4.11 shows a comparison between the carbon steel cyclic-load C(T) J-R curves and the cyclic-load TWC pipe J-R curves. Both the pipe J-R curves and the C(T) J-R curves show a decrease in resistance under cyclic loading, but the absolute values of J after some crack growth are much lower for the C(T) specimens than for the TWC pipe experiments.

Figure 4.12 shows a plot of the J_i values from both the TWC pipe and C(T) experiments. The J_i values calculated from the C(T) experiments are reasonably similar to the J_i values from the pipe tests. There appears to be a large amount of scatter in the data. It should be pointed out that this particular length of pipe has been found to be extremely anisotropic and inhomogeneous (Ref. 4.9). This inhomogeneity was found to occur in a helical pattern, possibly from the seamless pipe manufacturing process, and could cause the scatter in the data that is observed in Figure 4.12.

Figure 4.13 shows the ratio $J_{QS,cyc}/J_{QS,mono}$ for the C(T) and TWC pipe experiments. Again, note that this ratio is a measure of the relative decrease in resistance due to cyclic loading and can not be used to directly compare the cyclic-load C(T) J-R curves to the cyclic TWC pipe J-R curves. The cyclic-load C(T) results follow the same trend as the TWC pipe experimental results. This finding indicates that for this material the decrease in resistance due to cyclic loading is approximately the same for the C(T) and TWC pipe geometries.

Figure 4.14 shows the average crack growth per cycle for the carbon steel specimens tested. Clearly, at a displacement increment of 0.1, the C(T) specimens cannot predict the crack growth per cycle in a TWC pipe experiment. Since only one displacement increment was used for the carbon steel in this investigation, it is impossible to make further conclusions about the possibility of making accurate through-wall crack growth predictions using C(T) results.

4.1.2.3 Discussion of Comparison Between Cyclic-Load Pipe and C(T) Fracture Toughness Results

For both materials tested, the cyclic-load C(T) experiments produced J_i values that were in reasonable agreement with the cyclic-load TWC pipe J_i values. However, as shown in the preceding figures, the

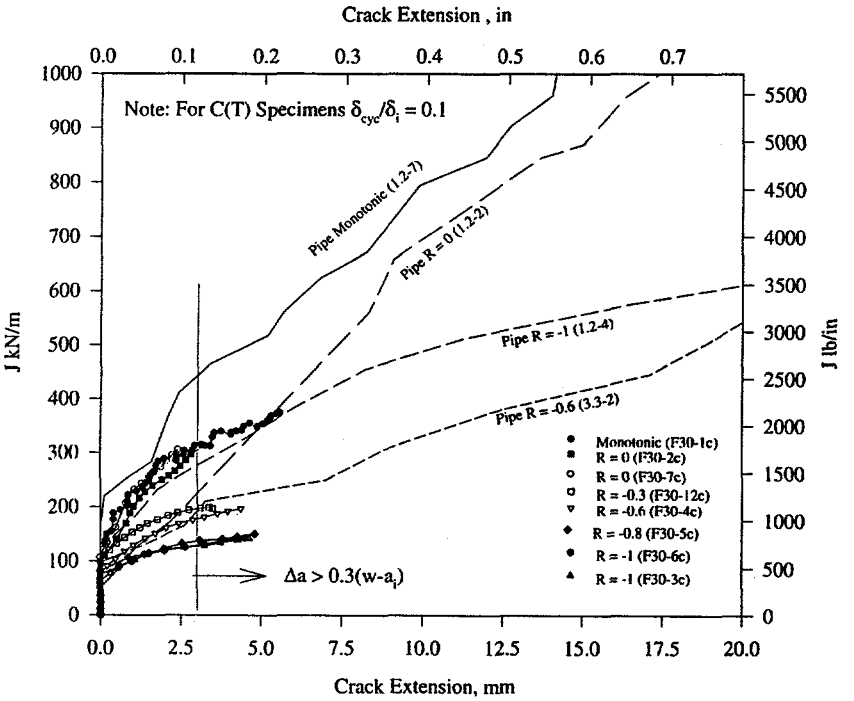

Figure 4.11 Comparison of cyclic-load J-R curves for carbon steel C(T) specimens tested with $\delta_{cyc}/\delta_i = 0.1$ and carbon steel TWC experiments

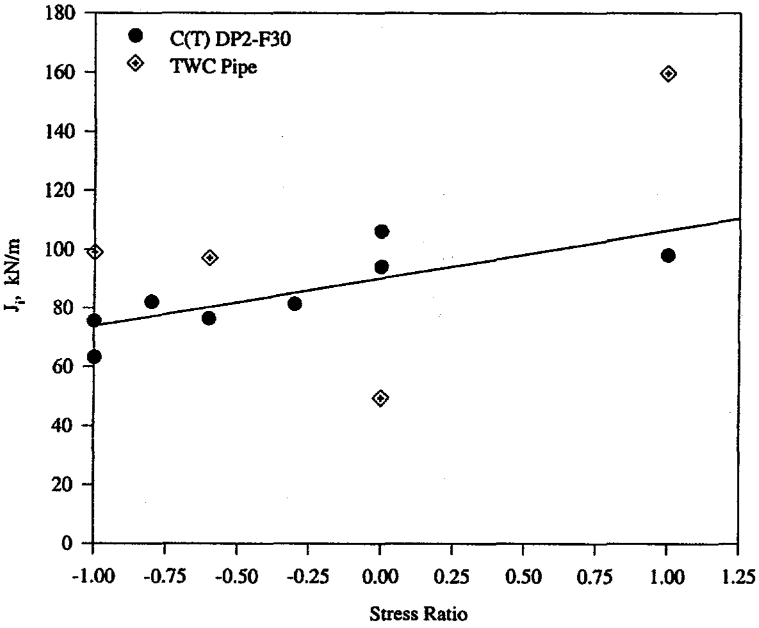

Figure 4.12 J at crack initiation versus stress ratio for carbon steel C(T) and TWC pipe experiments

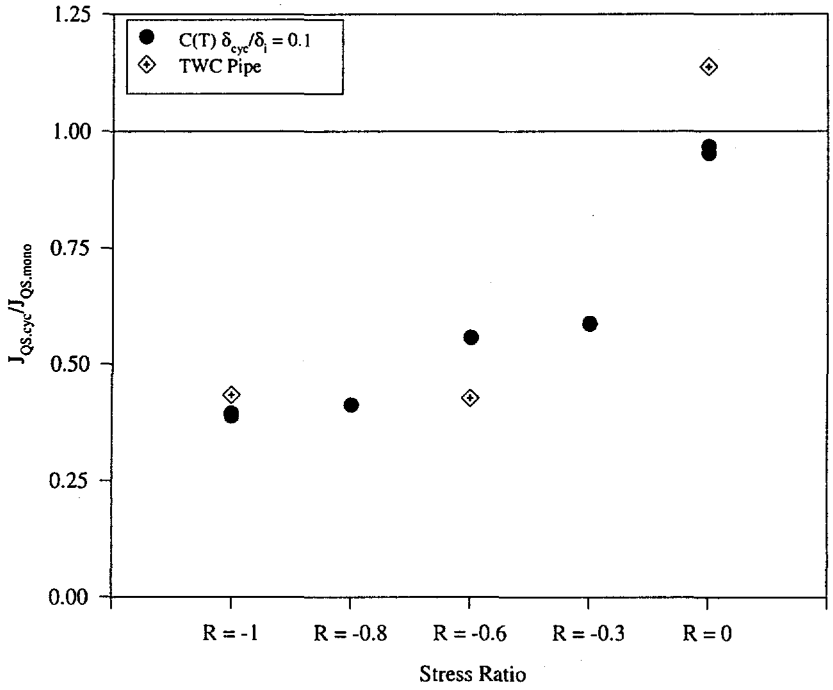

Figure 4.13 $J_{QS,cyc}/J_{QS,mono}$ **versus stress ratio for carbon steel C(T) and TWC pipe experiments**

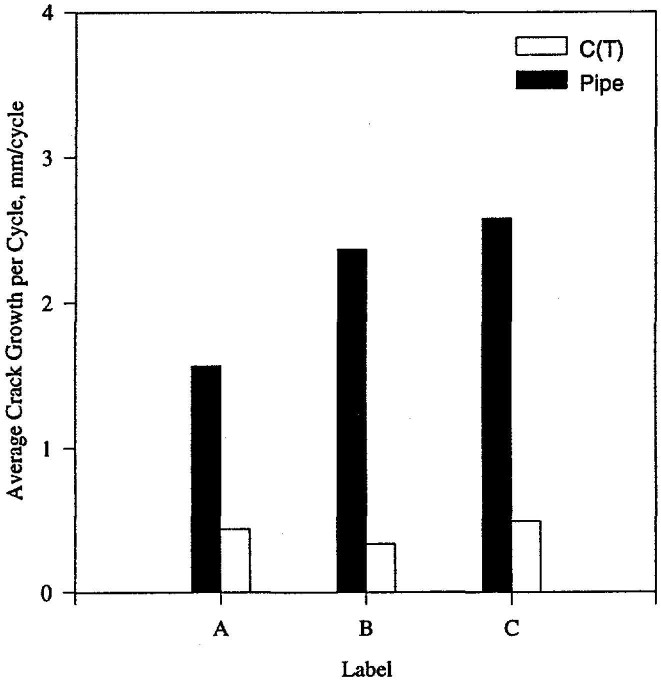

Label	R	δ_{cyc}/δ_i	Material
A	0	0.1	F30
B	-0.6	0.1	F30
C	-1	0.1	F30

Figure 4.14 Crack growth per cycle for carbon steel C(T) and TWC pipe experiments

agreement was not very good after some crack growth. The relative decrease in crack growth resistance from cyclic loading between the specimen types was comparable even if the absolute comparison was poor. The trend in $J_{QS,cyc}/J_{QS,mono}$ for both the TWC pipe and C(T) experiments during crack growth suggests that the C(T) specimen can predict the relative decrease in crack growth resistance that may be observed in a cyclic-load TWC pipe experiment. It is believed that if the C(T) specimen cyclic displacement increment was changed after crack initiation, to give the same cyclic crack growth per cycle as in a cyclic TWC pipe, then there would be better similitude between the C(T) specimen and TWC pipe J-R curves during crack growth. If this hypothesis is true, then if the monotonic-load fracture toughness of a TWC pipe is known, conducting a simple C(T) experiment with a known cyclic loading history is all that is needed to make an estimate of the decrease in resistance in the TWC pipe system due to that loading history. At this point, the constant cyclic displacement increment parameter gives good similitude between the C(T) and TWC pipe tests with the same load history up to crack initiation, but the resulting C(T) specimen J-R curve will be lower than the TWC pipe J-R curve. However, a study to validate an approach to provide similitude between C(T) specimen and TWC pipe results was beyond the scope of this investigation.

4.1.3 Predictions of Cyclic-Load TWC Pipe Test Loads Using Cyclic-Load C(T)-Specimen Results

The purpose of this section is to determine whether the cyclic-load J-R curves calculated from the C(T) experiments can be used to accurately predict the displacement-controlled, cyclic-load TWC pipe response. In order to make a solid conclusion about the usefulness of the cyclic-load J-R curves, several different analysis methods were used in making this assessment.

4.1.3.1 Description of Analysis Methods

The circumferential through-wall cracked pipe analysis methods used in the study are:

- Net-Section-Collapse analysis prediction of maximum moments (Ref. 4.10)
- J-estimation scheme analysis predictions of maximum and initiation moments using
  - LBB.NRC (Ref. 4.11)
  - LBB.ENG2 (Ref. 4.12)
  - GE/EPRI (Ref 4.13).

The Net-Section-Collapse (NSC) analysis is a limit-load analysis that was first proposed for application to stainless steel with circumferential through-wall cracks (Ref. 4.10). The NSC analysis assumes that the material is tough enough so that no crack growth occurs before maximum load. It also assumes that the net section becomes fully plastic and has a constant stress value. The critical net-section stress is called the flow stress. In this analysis, the flow stress is defined as the average between the material's yield and ultimate strengths. Since the pipes used in this study were analyzed in IPIRG-1, the NSC values shown in this section of the report come directly from Reference 4.1.

Since there are many cases where the NSC analysis produces higher-than-actual loads, a series of elastic-plastic analyses was developed. Several closed-form solutions exist to gave approximate elastic-plastic solutions for circumferential-through-wall-cracked pipe. In this investigation, the LBB.NRC, LBB.ENG2, and GE/EPRI J-estimation schemes were used. These J-estimation schemes have been coded into an IBM-PC compatible program called NRCPIPE, Reference 4.14. For these analyses, Version 1.4g of the NRCPIPE code was used. The GE/EPRI method was selected since it typically underpredicts the experimental loads more than all of the other J-estimation schemes, the LBB.NRC method typically gives the highest predictions of maximum load, and the LBB.ENG2 method typically gives reasonably accurate experimental load predictions (Ref. 4.14).

Stress-strain behavior, fracture toughness, and pipe geometry are needed as inputs to these analyses. The yield and ultimate strength of each material were well documented in Reference 4.1. The full stress-strain curve was fit using the Ramberg-Osgood curve fit. The curve fits defined in Reference 4.1 were used in these analyses. Table 4.3 shows a summary of the tensile inputs from Reference 4.1. For the fracture toughness inputs, the C(T) J-R curves were used that corresponded to the particular pipe test being analyzed, i.e., when the quasi-static R = -1 stainless steel pipe experiment was being analyzed, all of the cyclic C(T) J-R curves that had a stress ratio of -1 were used in the analyses. Since the C(T) specimens were too small to reach the values of crack growth in the pipe tests, the J-R curves had to be extrapolated. Since only the J_D-R curve was used in these analyses, a power-law extrapolation procedure was used. This procedure is identical to the one found in Reference 4.15. The procedure is as follows:

Table 4.3 Tensile properties used in cyclic moment predictions

Material	Specimen Number	σ_o, MPa	ϵ_o	α	n
A106 Gr. B	F30-104	294	0.00152	1.97	5.3659
TP304	A23-105	139	0.00076	11.23	3.5646

- The experimental J_D-R curve was used for crack growth up to 30 percent of the original ligament, which Reference 4.15 showed the J_D-R curve data to be valid. These data were fit with the following power-law curve

$$J = J_i + C\Delta a^m \tag{4-1}$$

- The value of J_i is the initiation value of J as chosen using the d-c electric potential method.
- In the analysis, the actual J values from the experiments were used for the crack extension up to 30 percent of the remaining ligament, while the extrapolated values of J were used for the larger crack extensions.

Note that since the TWC pipe tests conducted in Subtask 1.2 of the IPIRG-1 program were fully analyzed in that program, the NSC values shown in this report come directly from that report (Ref. 4.1). Table 4.4 shows the constants for the power law extrapolated J-R curves used in these analyses.

4.1.3.2 Stainless Steel Results

The results for the stainless steel pipe J-estimation scheme predictions are discussed below. The results are presented as a ratio of the experimental moments to the predicted moments. Three different combinations of J-R results were used in these analyses. First, the cyclic-load J-R curves calculated from the C(T)

Table 4.4 Constants for J-R extrapolation used in cyclic moment predictions

Specimen or Pipe Test No.	Material, Geometry	Stress Ratio, R	δ_{cyc}/δ_i	J_i, kJ/m^2	C	m
4131-5	TP304, TWC pipe	1	N/A	642	557.10	0.6205
1.2-3	TP304, TWC pipe	0	0.1*	943	343.34	0.7028
1.2-5	TP304, TWC pipe	-1	0.1*	258	178.98	0.5244
A23-2c	TP304, C(T)	1	N/A	1124	144.82	0.6515
A23-4c	TP304, C(T)	0	0.1	1150	98.82	0.4551
A23-21c	TP304, C(T)	0	0.1	862	399.95	0.2873
A23-6c	TP304, C(T)	0	0.2	1013	353.20	0.2580
A23-11c	TP304, C(T)	0	0.025	1405	296.12	0.6894
A23-22c	TP304, C(T)	0	0.025	938	208.09	0.6129
A23-5c	TP304, C(T)	-1	0.1	455	175.98	0.3791
A23-20c	TP304, C(T)	-1	0.1	253	145.03	0.6437
A23-7c	TP304, C(T)	-1	0.2	343	96.15	0.7886
A23-12c	TP304, C(T)	-1	0.025	157	150.45	0.9900
1.2-7	A106B, TWC pipe	1	N/A	159	141.31	0.6540
1.2-2	A106B, TWC pipe	0	0.1*	49	86.32	0.8445
1.2-4	A106B, TWC pipe	-1	0.1*	99	111.04	0.5060
F30-1c	A106B, C(T)	1	0.1	98	123.62	0.5097
F30-2c	A106B, C(T)	0	0.1	94	97.68	0.7008
F30-6c	A106B, C(T)	0	0.1	75	25.72	0.6666
F30-3c	A106B, C(T)	-1	0.1	63	37.09	0.5118
F30-7c	A106B, C(T)	-1	0.1	106	111.62	0.6540

* Up to maximum load only, but since these were pipe tests, the Δa values were much larger than in the C(T) tests.

experiments were used to predict the cyclic-load pipe response. For example, when predicting the moment response of the IPIRG-1 Experiment 1.2-5, quasi-static R = -1, stainless steel, TWC experiment, each of the cyclic-load C(T) experiments with a stress ratio of -1 was used. In addition, the η-factor calculated J-R curves from the pipe experiments were also used to predict the experimental pipe response. Finally, the monotonic-load C(T) results were used to predict the cyclic-load TWC pipe response. Quasi-static, monotonic-load stress-strain properties were used in all analyses. Table 4.5 shows the stainless steel experimental-to-predicted moment ratios.

Crack Initiation A comparison of the experimental-to-predicted moment at crack initiation versus the loading parameter for the stainless steel material is shown in Figure 4.15. In all cases, the LBB.NRC method slightly overpredicted the experimental moments, while the GE/EPRI method slightly underpredicted the experimental moments. The LBB.ENG2 method, on the other hand, yielded mixed results, sometimes slightly overpredicting and sometimes slightly underpredicting. For the cyclic-load cases, the C(T) J_i values provided very similar predictions to the TWC pipe J_i values, indicating that the small-scale specimens could be used in making larger-pipe predictions. Also, the difference in the predictions due to the different displacement increments was minimal.

In examining the predictions of moment at crack initiation using the pipe J_i values, the differences between the experimental and the predicted results can be attributed to the assumptions and conservatism in the

Table 4.5 Cyclic initiation moment and maximum moment predictions for stainless steel quasi-static TWC pipe experiments

			Experimental-to-Predicted Moment Ratios						
J-R Curve	Specimen	Displacement	GE/EPRI		LBB.ENG2		LBB.NRC		NSC
Specimen #	Load History	Increment	Initiation	Maximum	Initiation	Maximum	Initiation	Maximum	Maximum
Analysis of Monotonic Pipe Experiment 4131-5 (Initiation Moment = 29.72 kN-m, Maximum Moment = 37.74 kN-m)									
4131-5	Pipe, Monotonic	N/A	1.391	1.443	1.295	1.379	0.995	1.156	1.099
A23-2c	C(T) Monotonic	N/A	1.223	1.532	1.142	1.434	0.911	1.153	1.099
Analysis of R = 0 Pipe Experiment 1.2-3 (Initiation Moment = 28.98 kN-m, Maximum Moment = 34.60 kN-m)									
1.2-3	Pipe, R = 0	0.1*	1.202	1.315	1.115	1.246	0.887	1.033	0.972
A23-2c	C(T) Monotonic	N/A	1.193	1.404	1.113	1.315	0.889	1.057	0.972
A23-4c	C(T), R = 0	0.1	1.084	1.291	0.997	1.191	0.819	0.977	0.972
A23-6c	C(T), R = 0	0.2	1.115	1.251	1.008	1.155	0.834	0.961	0.972
A23-11c	C(T), R = 0	0.025	1.035	1.198	0.953	1.110	0.796	0.943	0.972
A23-21c	C(T), R = 0	0.1	1.089	1.500	0.996	1.398	0.771	1.097	0.972
A23-22c	C(T), R = 0	0.025	1.035	1.198	0.953	1.110	0.796	0.943	0.972
Analysis of R = -1 Pipe Experiment 1.2-5 (Initiation Moment = 22.00 kN-m, Maximum Moment = 32.99 kN-m)									
1.2-5	Pipe R = -1	0.1*	1.164	1.469	1.064	1.369	0.818	1.060	0.871
A23-2c	C(T) Monotonic	N/A	0.906	1.339	0.845	1.254	0.675	1.008	0.871
A23-5c	C(T), R = -1	0.1	1.019	1.430	0.934	1.319	0.729	1.036	0.871
A23-7c	C(T), R = -1	0.2	1.089	1.500	0.996	1.398	0.771	1.097	0.871
A23-12c	C(T), R = -1	0.025	1.226	1.580	1.118	1.493	0.857	1.123	0.871
A23-20c	C(T), R = -1	0.1	1.170	1.487	1.068	1.392	0.822	1.071	0.871

* Displacement increment changed after maximum load exceeded

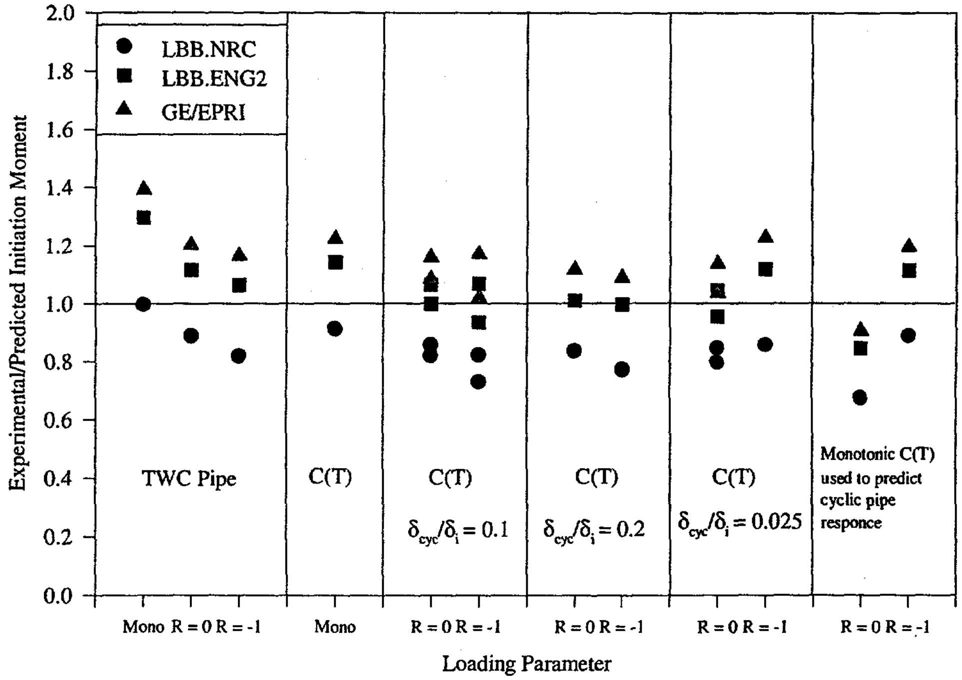

Figure 4.15 Stainless steel experimental/predicted initiation moments using a variety of cyclic-load C(T) and TWC pipe J-R curves

estimation schemes. It would be expected that using the actual pipe J_i values would give the most accurate predictions.

However, as seen in Figure 4.15, using the cyclic-load C(T) results produced predictions of moments at crack initiation within the same scatter as using the TWC pipe J_i values. Interestingly, the monotonic-load C(T) J_i values gave initiation moment predictions for the R = -1 TWC pipe test that were similar to the results using the R = -1 pipe J_i values. However, all of the analysis schemes overpredicted the R = 0 moments at crack initiation when using the quasi-static, monotonic-load C(T) J_i values.

Maximum Moment A comparison of the experimental-to-predicted maximum moment versus the loading parameter for the stainless steel material is shown in Figure 4.16. Also included in this figure are the crack extension values at maximum moment for the stainless steel TWC experiments. The trends in these predictions are the same as they were for the initiation moments. The NSC predictions in all cases were close to the experimental moments. This result is typical for high toughness materials in small diameter pipe. The GE/EPRI method greatly underpredicted the experimental moments in all cases, while the LBB.NRC method gave results that were close to the experimental moments.

In examining the stainless steel pipe maximum moment predictions, it is clear that the accuracy of the maximum moment predictions is not sensitive to the J-R curve used. Whether a J-R curve with a plastic displacement increment of 0.1 or 0.2 is used made no significant difference in the predictions. Even when the monotonic-load C(T) J-R curve was used, the predictions of crack initiation and maximum moment for the R = -1 pipe test were nearly identical, within engineering scatter, to the predictions using the cyclic-load J-R curves. It appears that the inaccuracies in the predictions do not come from the material

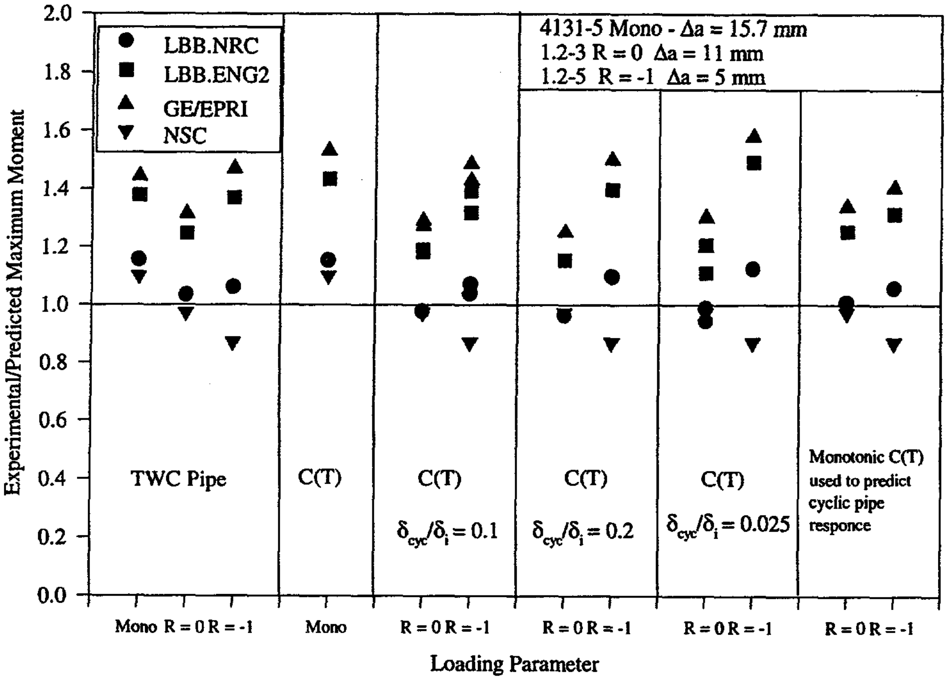

Figure 4.16 Stainless steel experimental/predicted maximum moments using a variety of cyclic-load C(T) and TWC pipe J-R curves

properties but are inherent in the application of the J-estimation schemes to a case that is at limit load due to the high toughness of the material.

4.1.3.3 Carbon Steel Results

The results for the carbon steel J-estimation scheme predictions are discussed below. They are presented as a ratio of the experimental moments to the predicted moments. The same three combinations of J-R results were used in these analyses as were used in the stainless steel analyses. Table 4.6 presents the carbon steel experimental-to-predicted moment ratios.

Crack Initiation Figure 4.17 shows the ratio of experimental-to-predicted initiation moment values versus the loading parameter for the carbon steel material. In most cases, the GE/EPRI analysis underpredicted the experimental initiation moments while the LBB.NRC analysis overpredicted the initiation moments. The effect of the material-property scatter is apparent in these prediction. For example, the GE/EPRI analysis of the R = -1 pipe test using the C(T) specimen R = -1 J_i values gave initiation moment ratios ranging from 0.95 to 1.45. This range in the moment ratios is due to the differences between the two C(T) specimen J_i values; only one pipe test with these test conditions is available for comparison. Drawing conclusions about the validity of predictions based on material property values is difficult when the variability of the material properties is high.

Maximum Moment Figure 4.18 shows the ratio of experimental-to-predicted maximum moment values versus the loading parameter for the carbon steel material. Also included in this figure are the crack

Table 4.6 Cyclic initiation moment and maximum moment predictions for quasi-static carbon steel TWC pipe experiments

			Experimental-to-Predicted Moment Ratios						
J-R Curve	Specimen	Displacement	GE/EPRI		LBB.ENG2		LBB.NRC		NSC
Specimen #	Load History	Increment	Initiation	Maximum	Initiation	Maximum	Initiation	Maximum	Maximum
Analysis of Monotonic Pipe Experiment 1.2-7 (Initiation Moment = 37.08 kN-m, Maximum Moment = 51.33 kN-m)									
1.2-7	Pipe, Monotonic	N/A	1.128	1.224	0.944	1.092	0.839	0.938	0.844
F30-1c	C(T), Monotonic	N/A	1.314	1.330	1.079	1.168	0.992	0.992	0.844
Analysis of R = 0 Pipe Experiment 1.2-2 (Initiation Moment = 27.26 kN-m, Maximum Moment = 48.18 kN-m)									
1.2-2	Pipe, R = 0	0.1*	1.243	1.174	1.002	1.058	0.968	0.918	0.793
F30-1c	C(T), Monotonic	N/A	0.966	1.249	0.793	1.097	0.729	0.931	0.793
F30-2c	C(T), R = 0	0.1	0.981	1.218	0.803	1.084	0.741	0.919	0.793
F30-7c	C(T), R = 0	0.1	0.942	1.195	0.775	1.064	0.708	0.906	0.793
Analysis of R = -1 Pipe Experiment 1.2-4 (Initiation Moment = 34.57 kN-m, Maximum Moment = 42.70 kN-m)									
1.2-4	Pipe, R = -1	0.1*	1.223	1.114	1.003	0.987	0.922	0.834	0.702
F30-1c	C(T), Monotonic	N/A	1.225	1.107	1.005	0.972	0.924	0.825	0.702
F30-3c	C(T), R = -1	0.1	1.434	1.423	1.160	1.205	1.103	1.052	0.702
F30-6c	C(T), R = -1	0.1	1.343	1.408	1.092	1.199	1.025	1.038	0.702

* Displacement increment changed after maximum load exceeded

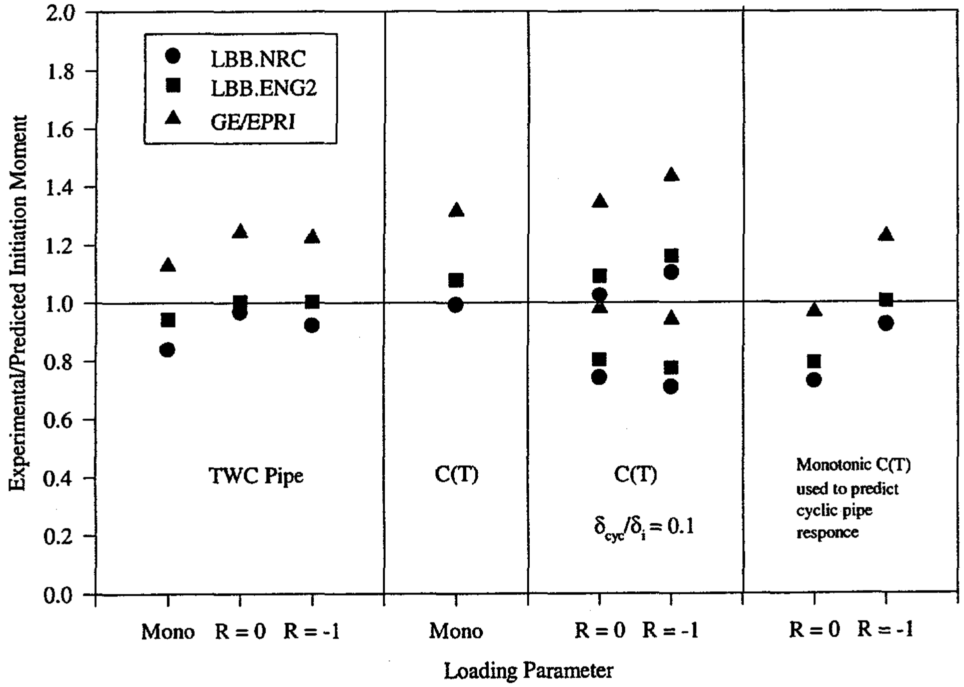

Figure 4.17 Carbon steel experimental/predicted initiation moments using a variety of cyclic-load C(T) and TWC pipe J-R curves

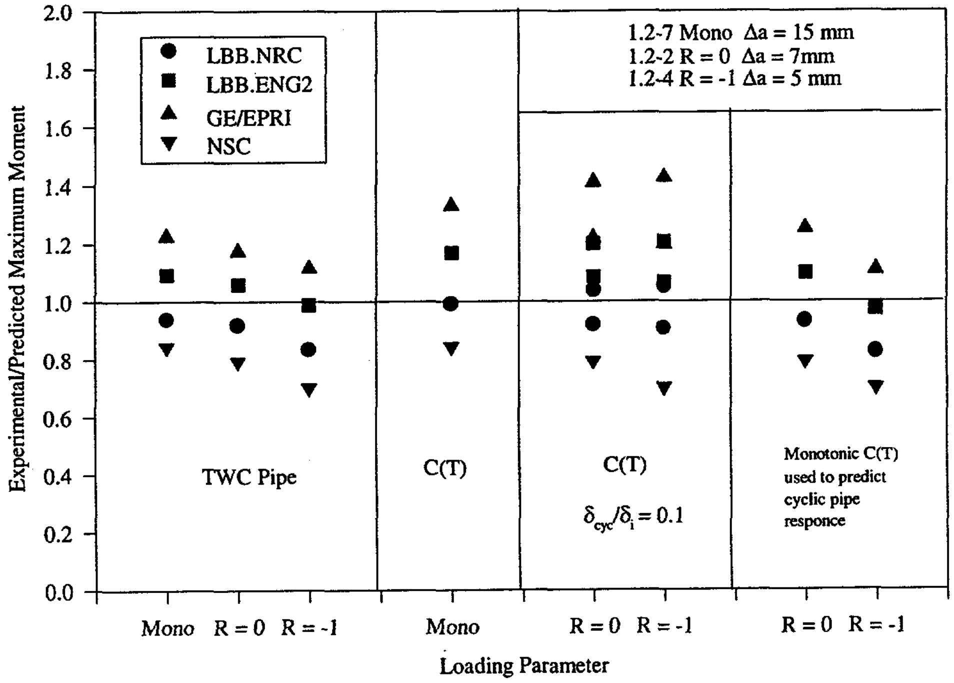

Figure 4.18 Carbon steel experimental/predicted maximum moments using a variety of cyclic-load C(T) and TWC pipe J-R curves

extension values at maximum moment for the carbon steel TWC experiments. In all cases, the NSC analysis overpredicted the maximum moment in the experiments. This trend is expected since this material has a lower toughness and fracture mechanics will govern over collapse. In this case, the LBB.ENG2 analysis yielded the most accurate predictions. As for the stainless steel, the accuracy of the predictions was not sensitive to the J-R curve used. Whether the monotonic-load C(T) J-R curve or the TWC cyclic-load pipe J-R curve was used, the analysis results were similar. Clearly, the differences in the analysis predictions of maximum load using different J-R curves fall within the scatter caused by the inaccuracies of the estimation schemes.

4.1.3.4 Cyclic Moment Prediction Results

The general conclusion that can be made from the carbon steel and stainless steel cyclic moment predictions is that these predictions appear to be insensitive to the J-R curve used. Even when the monotonic-load J-R curve was used, the predictions were approximately equal to the predictions made using the cyclic-load pipe J-R curve. Even though this may seem surprising at first, a closer look at the load-displacement records of these tests reveals that these results are expected. In Section 2.1.4.1, the load-displacement records of these tests were discussed. Figure 2.12 shows those results. As previously discussed, the decrease in maximum load for the cyclic experiments was small compared with the decrease in load-line displacement at maximum load. The maximum decrease in maximum load was approximately 20 percent. This trend is expected in the stainless steel since for this pipe and crack geometry, the experimental results were very close to limit load. A pipe that is close to limit load will be insensitive to maximum load changes due to loading history. Therefore, the prediction of experimental load will also be insensitive to the different load history J-R curves used. It is appropriate to state that the monotonic C(T) J-R curve can be used in predicting cyclic-load pipe moment response for the pipe tests examined. Note, however, that the monotonic-load J-R curve will probably not be able to predict the pipe displacement at maximum load, since the largest difference between the cyclic- and monotonic-load tests lies in the displacements. Figure 2.12 shows that the decrease in displacement at maximum load in a cyclic-load test could be as large as 80 percent of the displacement in a monotonic-load test. Clearly, this large difference will cause large differences in the displacement predictions. Studying this effect was beyond the scope of this investigation. More importantly, for larger diameter pipes, the initiation and maximum loads should be further from the limit load. Hence, the cyclic-load effect on toughness reduction may result in lower initiation and maximum loads for larger diameter pipe. This effect is explored in the following section.

4.1.4 Cyclic-Load Sensitivity Analysis

To assess the effect of pipe diameter on the maximum moments for cyclically loaded pipe, a series of J-estimation scheme analyses was conducted. For these analyses, the LBB.ENG2 method was chosen since it is typically more accurate than the other analysis schemes in predicting the maximum moment results of quasi-static, monotonic pipe experiments (Ref. 4.14). The same stress-strain curve fits that were used for the pipe predictions in Section 4.1.3 were also used in these analyses. The predictions were made for both the stainless steel and carbon steel base metals.

4.1.4.1 Stainless Steel Results

Table 4.7 shows the constant values used in these analyses. The quasi-static stress-strain properties were derived from an average of Specimens A23-1 and A23-2 from Reference 4.1. The maximum loads were

Table 4.7 Constant values used in stainless steel cyclic-load sensitivity analyses

TWC, Percent	R_M/t	σ_f, MPa	α	n	σ_o, MPa	ϵ_o
38	5.51	290	9.58	3.2145	131	0.000716

normalized by the Net-Section-Collapse analysis, using the average of the yield and ultimate strengths as the flow stress. The effect of pipe diameter on the normalized maximum moment at various stress ratios can be seen in Figure 4.19. These calculations show that as the pipe diameter is increased the normalized maximum moment at all stress ratios is decreased. Interestingly, the amount of decrease among the various stress ratios seems to be constant. Whether the pipe diameter is 0.1 m or 1 m, the R = -1 case shows a 20 percent decrease as compared to the R = 0 case.

The effect of displacement increment on the normalized maximum moment for pipes of various diameters can be seen in Figure 4.20. All of the analyses used J-R curves from the R = -1 experiments. The maximum load predictions using the J-R curve from the C(T) experiments with $\delta_{cyc}/\delta_i = 0.1$ were nearly identical to predictions using the cyclic-load pipe J-R curve. However, the predictions using the J-R curve from the C(T) experiment with $\delta_{cyc}/\delta_i = 0.2$ gave results similar to the case with $\delta_{cyc}/\delta_i = 0.1$ at small pipe diameters but about 10 percent lower at larger pipe diameters. This finding is due to the extrapolation of the J-R curve instead of an actual effect on the moments due to the cyclic displacement increment. The results for the $\delta_{cyc}/\delta_i = 0.025$ case show that this case is the most detrimental for all ranges of pipe diameters considered.

4.1.4.2 Carbon Steel Results

The same analysis procedures were used for the carbon steel analyses as were used for the stainless steel analyses. Table 4.8 shows the constant values used in these analyses. The quasi-static stress-strain properties were derived from Specimen F30-104. The effect of stress ratio on the normalized maximum moment as a function of the pipe diameter is shown in Figure 4.21. This figure shows that the load-carrying capacity of the carbon steel is more affected by intermediate stress ratios than is the stainless steel. It also shows that the decrease in load-carrying capacity in the carbon steel is greater at large diameters than at small diameters. For the R = -1, case there is a 20 percent decrease in maximum load for a 0.17m (6.69 inch) diameter pipe, while there is a 27 percent decrease in maximum load for a 1.3m (51.2 inch) pipe.

Table 4.8 Constant values used in carbon steel cyclic-load sensitivity analyses

TWC, Percent	R_M/t	σ_f, MPa	α	n	σ_o, MPa	ϵ_o
36.6	5.68	446.5	1.97	5.366	294	0.00152

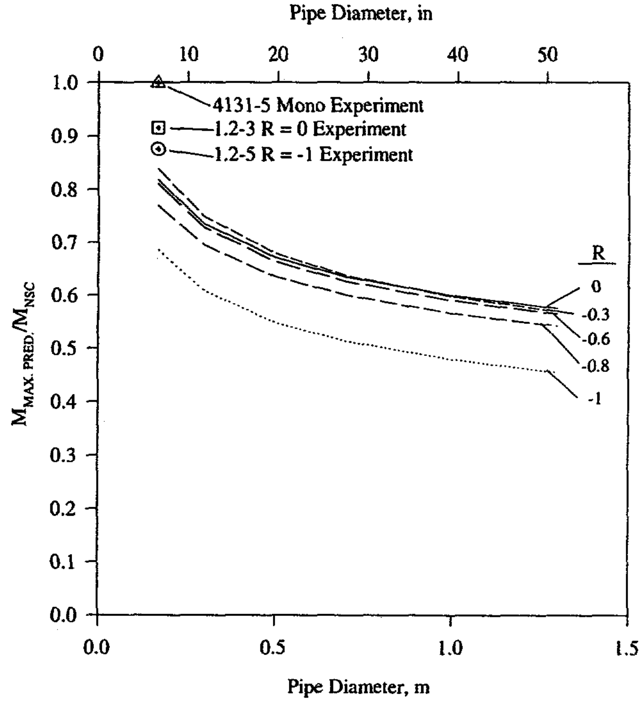

Figure 4.19 Normalized maximum moment predictions versus pipe diameter for stainless steel TWC pipe

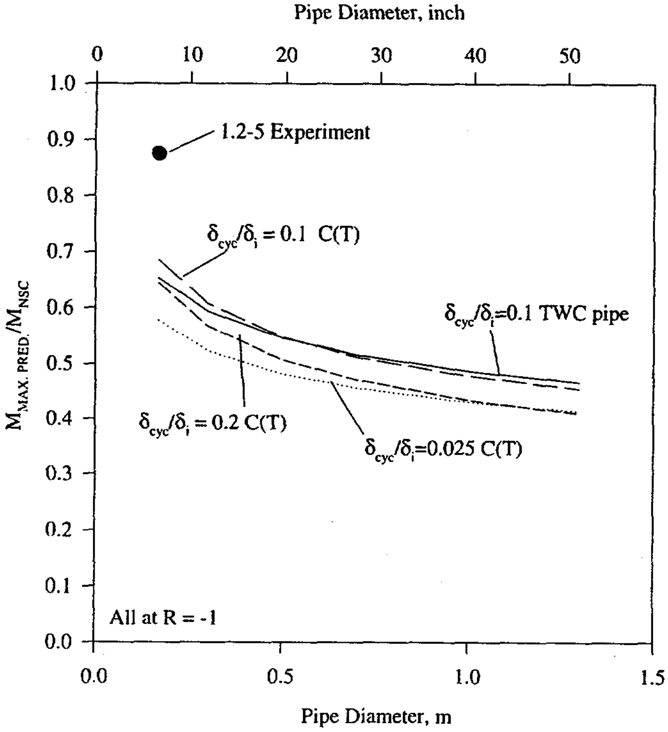

Figure 4.20 Normalized maximum moment predictions versus pipe diameter for a variety of plastic displacement increments in stainless steel TWC pipe

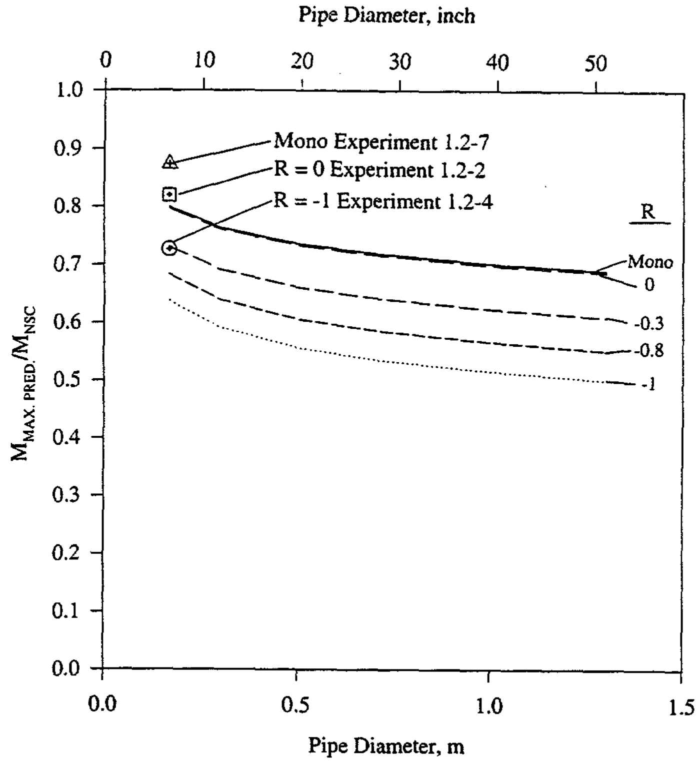

Figure 4.21 Normalized maximum moment predictions versus pipe diameter for carbon steel TWC pipe

An important question arising from these sensitivity analyses is how relevant are these results when considering a seismic event? If these tests are estimating that, for larger pipe diameters, the number of cycles to reach maximum moment is large, i.e., greater than 100, then the effects of cyclic loads are small since the typical seismic event ranges from 5 to 30 cycles. Figure 4.22 shows the predicted number of cycles to maximum moment as a function of pipe diameter for both materials. When the stress ratio is -1, the number of cycles to maximum moment for both materials falls in the band for a typical seismic event. This result indicates that a seismic event with a stress ratio of -1 is likely to take a TWC pipe beyond its maximum load-carrying capacity for all pipe sizes considered.

4.2 Dynamic-Loading Effects

In nuclear piping, dynamic loads can occur with cyclic loading, as in a seismic event or as large monotonic loads, as in water-hammer or pressure relief valve blowdown events. In order to make accurate dynamic-loading pipe predictions, both the appropriate stress-strain curve and J-R curve need to be used in the analyses. In this section, first the aspect of what stress-strain curve should be used in the J-estimation schemes for making dynamic pipe fracture predictions is addressed. Secondly, moment predictions are compared to pipe fracture data. Finally, sensitivity calculations that are aimed at examining the effects of pipe diameter on the maximum loads for dynamically loaded pipe are discussed.

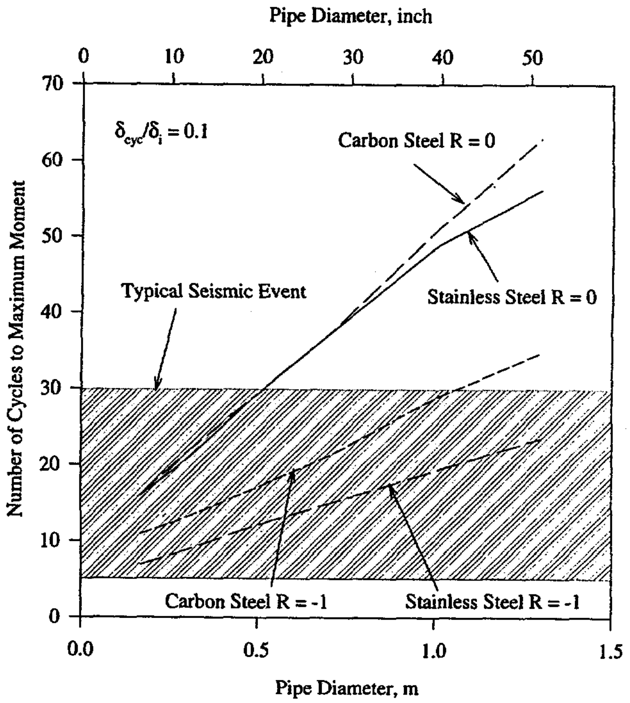

Figure 4.22 Number of cycles to maximum moment versus pipe diameter for both carbon and stainless steel TWC pipe

4.2.1 Determination of Appropriate Material Properties to Use in Dynamic-Load Pipe Test Predictions

The current practice in dynamic pipe fracture analyses is to determine the peak uncracked pipe dynamic loads, and use them in a fracture analysis. Usually, quasi-static material properties are used in the fracture analyses. As shown in this report, loading rates typical of seismic events can cause the strength and toughness of nuclear piping materials to change. Consequently, it was desired to determine if the dynamic material properties give significantly different load predictions than the quasi-static properties.

In making a dynamic pipe fracture prediction, one can conduct either a finite element analysis or use a simple closed-form pipe fracture solution. In finite element analyses, it is possible to perform visco-plastic analyses where the stress-strain curve is a function of the strain rate. For ferritic pipe steels at LWR temperatures, dynamic strain aging frequently causes a decrease of the stress-strain curve with increasing loading rate. This type of visco-plastic behavior is not common, that is, typical materials have a stress-strain curve that increases with increasing loading rate. Hence, special material constitutive laws need to be used in the FEM analysis to model a dynamic strain aging sensitive material. This detailed analysis is beyond the scope of this investigation.

Closed-form fracture solutions consist of either limit-load analyses, simple fracture analyses, or more detailed J-estimation schemes. For the limit-load analyses, one is required to know the yield and ultimate strength values (Ref. 4.10). For the simple fracture analyses like the Battelle DPZP (Ref. 4.16) or R6 Option 1 approach (Ref. 4.17), the yield, ultimate, and J-R curves are needed. For the J-estimation schemes, the appropriate stress-strain and J-R curves are needed.

The determination of the loading rate for the J-R curve is relatively simple. This is because large amplitude dynamic loads will occur near the first natural frequency of the pipe system of interest. Hence, the J-R curve specimen should be tested so that the time to reach crack initiation corresponds to one quarter of the period of the first natural frequency.

The determination of what strain-rate should be used in the tensile test is more complicated. The strain rates in a cracked structure differ throughout the structure. Hence, in a pipe fracture analysis, an effective strain rate for the cracked pipe must be determined. Because of the difficulty in incorporating dynamic strain aging into constitutive laws for FEM analyses, it was easier, and perhaps more convincing to determine this point experimentally.

This experimental investigation involved two aspects. First, a particular carbon steel pipe was found that had the same toughness in quasi-static and dynamic C(T) tests, but the quasi-static and dynamic stress-strain curves were different. A dynamic pipe test on this material (Japanese carbon steel, STS410) was available through Reference 4.18. Consequently, an identical quasi-static pipe experiment was conducted for relative comparisons. This pipe experiment and its results are presented.

The second aspect of this investigation was to compare existing quasi-static and dynamic C(T) specimen results. If identical specimens are compared, then the shapes of the load-displacement curves up to crack initiation will show if there are differences in the strain-hardening exponent, and hence confirm if there are differences in the stress-strain behavior in these specimens between quasi-static and dynamic loading. One could conceivably use the Key-Curve Approach (Ref. 4.19) or the GE/EPRI h_3-function (Ref. 4.20) to calculate the strain-hardening exponents. Since a larger percentage of a C(T) specimen experiences plasticity than a cracked pipe (unless there is a very small crack in the pipe), the C(T) specimen results may show larger effects of loading rate on the effective strain-hardening exponent than a pipe experiment.

The rate for the dynamic-load C(T) experiments (0.2 seconds to crack initiation) was determined in the IPIRG-1 program by a finite element analysis of an inertially loaded pipe experiment (Ref. 4.21). From this analysis it was concluded that a C(T) test run with crack initiation in 0.2 seconds was representative of these pipe tests. All of the IPIRG-1 and IPIRG-2 dynamic C(T) tests were conducted at rates that produced crack initiation in 0.2 seconds. It was not until more recently in the IPIRG-2 program that the criterion was developed for the maximum time to initiation being about one-quarter of the first natural period. This criterion would give a time of 0.0625 seconds to crack initiation for a pipe system with a natural frequency of 4 Hz.

The rates for the dynamic tensile tests are more difficult to quantify, hence rates of 1/s and 10/s were chosen as approximations of the effective strain rate for a cracked pipe. However, a calculation, based on the STS410 6-inch nominal diameter pipe tests (Ref. 4.18), showed that the strain rate in the uncracked pipe was on the order of 10^{-3}/s which is much closer to the quasi-static rate than to the dynamic-loading rate.

In order to help understand this problem, a quasi-static-load companion pipe test (IPIRG-2 Experiment 3.3-1) to the 6-inch nominal diameter dynamic-load pipe test on STS410 material (IPIRG-2 Experiment 4.2-1) was conducted in this program. This quasi-static test was conducted using conditions identical to those of the dynamic test except that the loading rate was decreased several orders of magnitude.

The test specimen for this experiment was fabricated from a 6-inch nominal diameter, Schedule 120, STS410 carbon steel pipe; that contained a circumferential through-wall crack. The pertinent experimental parameters and test results are listed in Table 4.9.

Table 4.9 Parameters and results for Experiment 3.3-1

Experimental Parameters	
Test material	STS410 carbon steel
Material identification	IP-F13
Crack location	Base metal
Average outside pipe diameter	166.0 mm (6.535 inch)
Average pipe wall thickness	14.5 mm (0.569 inch)
θ/π	0.166
Loading conditions	Quasi-static, monotonic
Outer span for four-point bending	1.524 m (60 inches)
Inner span for four-point bending	0.610 m (24 inches)
Test temperature	300 C (572 F)
Experimental Results	
Moment at crack initiation (based on initiation at Tip A)	71.32 kN-m (631 x 10^3 lb-in)
Maximum moment	92.76 kN-m (821 x 10^3 lb-in)

Figure 4.23 shows the experimental load-displacement curve; also shown in this figure is the load-displacement record from the dynamic, monotonic-loading experiment (Experiment 4.2-1). Since these pipe tests had cracks that grew at different angles from the circumferential plane (48 degrees for Experiment 3.3-1 and 38 degrees for Experiment 4.2-1), the data only up to crack initiation should be considered. As shown in Figure 4.23, the quasi-static-load and the dynamic-load experiments had approximately the same load-displacement record up to the point of crack initiation. The dynamic-load experiment showed a slightly higher yield point, which is typical of dynamic tests.

After some crack growth, the quasi-static test had a higher load-displacement record than the dynamic test. This is attributed to angled crack growth. As discussed earlier, previous work on this phenomenon (Ref. 4.5) suggests that as the crack growth becomes more axial, the area under the moment-rotation curve increases, thus increasing the apparent resistance. Since the crack in the quasi-static experiment grew at an angle about 10 degrees more than the dynamic experiment, it would be expected to have a higher load-displacement record. However, these differences may be due to material property variations.

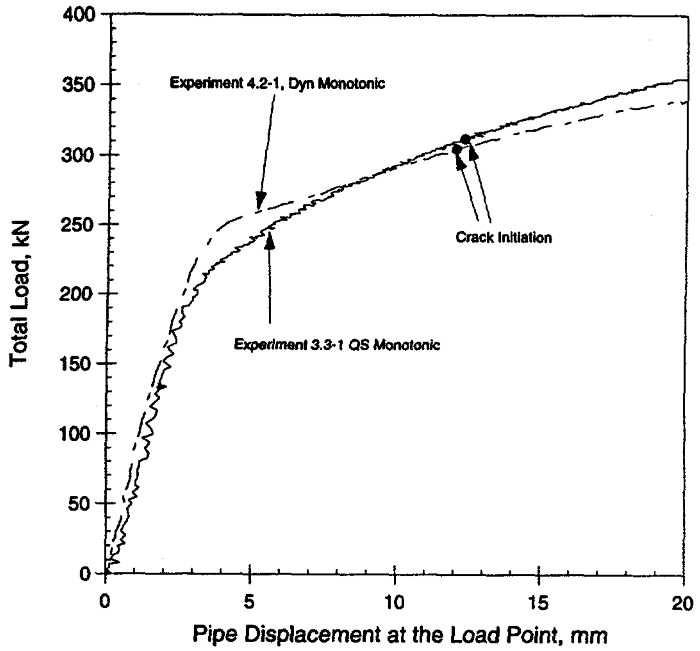

Figure 4.23 Load versus pipe displacement at the load point for Experiments 4.2-1 and 3.3-1

Figure 4.24 shows the calculated J-R curves for Experiment 3.3-1, as well as for other pipe tests on the STS410 material. The J-R curves for these pipe tests were calculated using the ETAFACTR code, which was discussed in Section 4.1.1. As shown in Figure 4.24, the J-R curve for the quasi-static, monotonic-loading experiment was nearly identical to the dynamic, monotonic-loading experiment until about 4 mm of crack extension. After this point the quasi-static test had a higher apparent resistance due to the angular crack growth. These results are similar to the C(T) results for this material indicating that this material's resistance is not affected by increasing strain rate.

4.2.1.2 Dynamic and Quasi-static Effects in C(T) Specimen Load-Displacement Records

Figure 4.25 shows the load-displacement record for the quasi-static- and dynamic-load C(T) experiments from the same pipe material. Interestingly, the quasi-static test and the dynamic test with crack initiation in 0.2 seconds show the same trend as was seen in the pipe test comparisons This result indicates that even though the strain rate at the crack tip in both a C(T) and pipe experiment may be high, the effective strain rate is similar to quasi-static strain rates. As discussed in Section 3.0 of this report, intermediate stress-strain curves were developed for the STS410 carbon steel pipe. These tests indicated that at a strain rate of 10^{-2}/s, the ultimate strength was reduced by about 10 percent as compared to a test whose strain rate was 10^{-4}/s, see Figure 3.6. However, Figure 4.23 indicates that the load-displacement behavior of these pipe experiments are very similar up to the point of crack initiation whether the loading rate is quasi-static or dynamic. Therefore, it is appropriate to use quasi-static stress-strain properties in making dynamic moment predictions. Note, however, that this conclusion is applicable only to this material. Hence, available data from C(T) tests for other ferritic pipe materials were also examined.

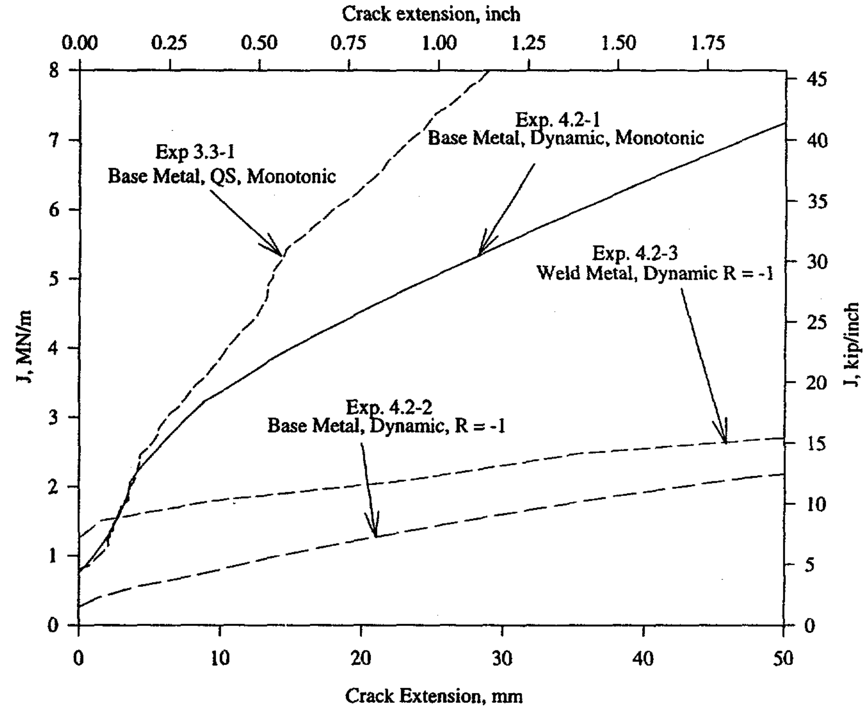

Figure 4.24 J-R curves for a variety of carbon steel TWC pipe experiments

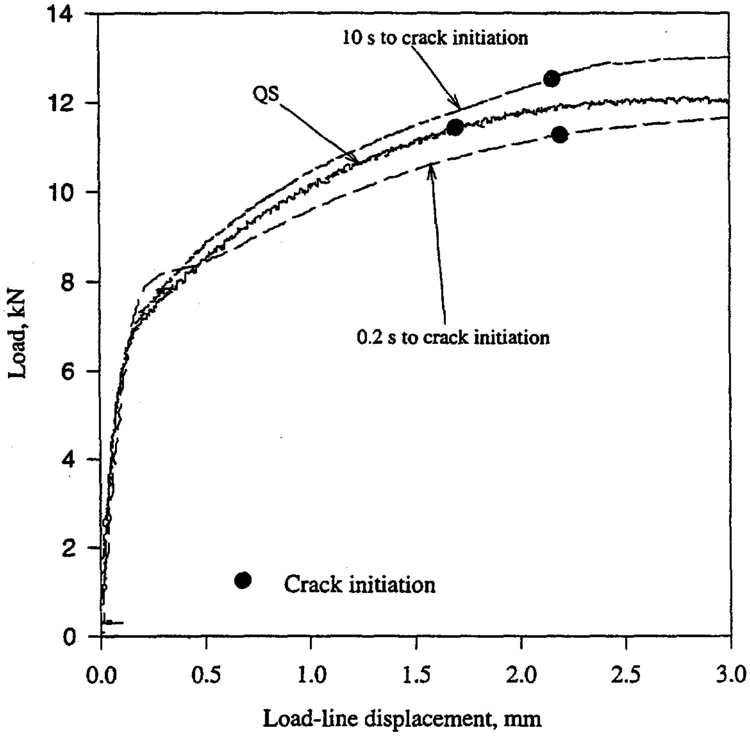

Figure 4.25 Load versus load-line displacement for STS410 C(T) experiments

Existing C(T) specimen data were examined for Pipes DP2-F30 and DP2-F29. Both of these pipes were highly susceptible to dynamic strain aging as evident by stress-strain curve and J-R curve differences from quasi-static to dynamic rates. Figure 4.26 shows the load-displacement records for the quasi-static and dynamic C(T) tests. Even though the initiation toughness values are different at the different loading rates, the load-displacement records are virtually identical up to the point of crack initiation. From this it can be concluded that the quasi-static stress-strain curve appears to be sufficient for fracture predictions at rates investigated in this program.

4.2.2 Dynamic Moment Prediction Results

In this section, a series of analyses was conducted to assess which J-estimation scheme gave the best predictions when compared to existing dynamic pipe fracture data. The best method is then used in the subsequent sensitivity analyses. The analyses will revolve around the carbon steel pipes described in Section 3.0 of this report. The following pipe tests were chosen for these analyses:

1. IPIRG-1 Experiment 1.2-8 on pipe DP2-F30 which is an A106 Grade B carbon steel pipe containing a through-wall crack that was tested under dynamic 4-point bending. The material showed a decrease in strength and toughness with increasing strain rate. Also several crack jumps occurred in both the pipe test and the quasi-static-loading C(T) tests.

2. IPIRG-2 Experiment 4.2-1 on pipe IP-F13 which is an STS410 Japanese carbon steel pipe containing a through-wall crack and tested under dynamic 4-point bending. The material showed a decrease in strength but no significant change in toughness with increasing strain rate.

3. IPIRG-2 Experiment 1-9 on pipe DP2-F22 which is an A106 Grade B carbon steel pipe containing a through-wall crack and tested under dynamic 4-point bending and internal pipe pressure. The material showed a decrease in both strength and toughness with increasing strain rate.

4. IPIRG-1 Experiment 1.3-2 on pipe DP2-F29 which is an A106 Grade B carbon steel pipe containing a surface crack and tested in a pipe system experiment with internal pressure and using a single-frequency forcing function. In this experiment, the crack initiated and fracture instability occurred during the first cycle where plasticity occurred, so the load history was effectively monotonic, dynamic loading.

Each of the pipe tests was analyzed using the pipe, quasi-static-load C(T), and dynamic-load C(T) J-R curves as well as the quasi-static, 1/s and 10/s stress-strain curves when available (see Table 4.10), however, only results using the quasi-static stress-strain curve are presented based on the results of Section 4.2.1.

These analyses were conducted using the NRCPIPE code Version 1.4g and the NRCPIPES code Version 2.0. The through-wall-crack pipe analyses were conducted using the J-estimation schemes described in Section 4.1.3.1, while the surface-crack pipe analyses were conducted with the following J-estimation schemes:

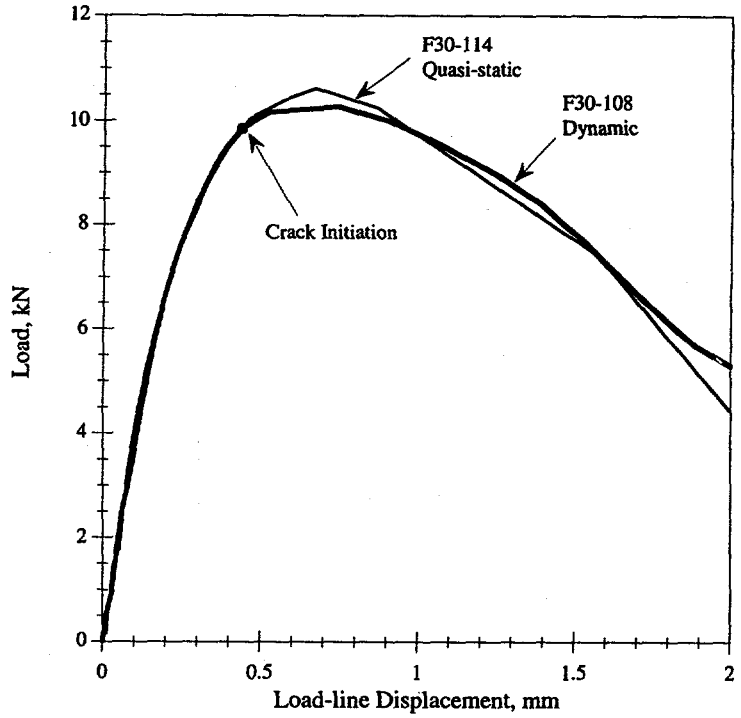

(a) DP2-F30

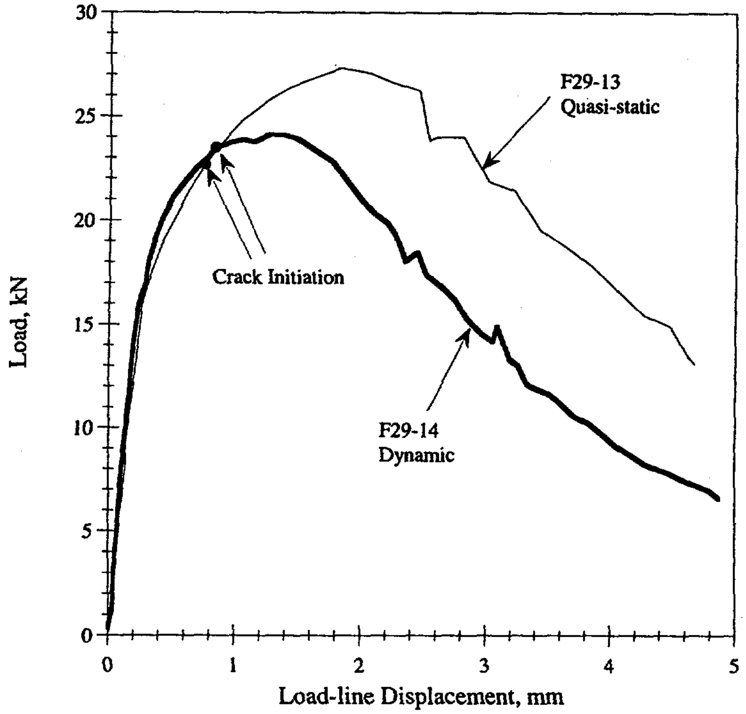

(b) DP2-F29

Figure 4.26 Load versus displacement for carbon steel C(T) specimens

Table 4.10 Constants used in predicting dynamic-load carbon steel TWC experiments

Material Properties			**Experiment, Pipe ID**			
			1.2-8, DP2-F30	**4.2-1, IP-F13**	**1-9, DP2-F22**	**1.3-2, DP2-F29**
Stress- Strain	QS	Spec. #	F30-104	IP-F13-T1	F22-T1	F29-5
		σ_o, MPa	294	215.8	258.6	241
		ϵ_o	0.001551	0.001138	0.001364	0.00127
		α	2.134	3.201	2.758	2.19
		n	5.318	3.717	3.556	3.39
J-R Curve	Pipe	Spec. #	1.2-8	4.2-1	1.9	n/a
		J_i, kN/m	103.8	750.1	423.5	n/a
		C	89.7	400.3	102942	n/a
		m	0.6743	0.7333	1.228	n/a
	QS C(T)	Spec. #	F30-112	IP-F13-1	F22-3	F29-11
		J_i, kN/m	69.0	389.4	77.1	122.3
		C	92.2	276.1	8.815	143.2
		m	0.5571	0.6306	0.6253	0.4561
	Dyn C(T)	Spec. #	F30-110	IP-F13-5	F22-2	F29-14
		J_i, kN/m	50.0	507.4	43.7	88.5
		C	73.9	225.2	4.380	59.2
		m	0.6336	0.6749	0.6324	0.7776

• SC.TNP	Reference 4.22
• SC.TKP	Reference 4.22
• SC.ENG2	Reference 4.23
• R6 Revision 3 Opt 1 - bending only	Reference 4.17.

The R6 method was also used in the TWC pipe analyses. The procedures used in preparing the data for these analyses were identical to the ones described in Section 4.1.3.1.

4.2.2.1 Initiation Moment

The initiation moments were predicted for all of the cases except for the surface-cracked pipe system test (Experiment 1.3-2). During that experiment, all of the d-c electric potential data were lost, therefore, the moment values at crack initiation could not be determined. Figures 4.27, 4.28, and 4.29 show the

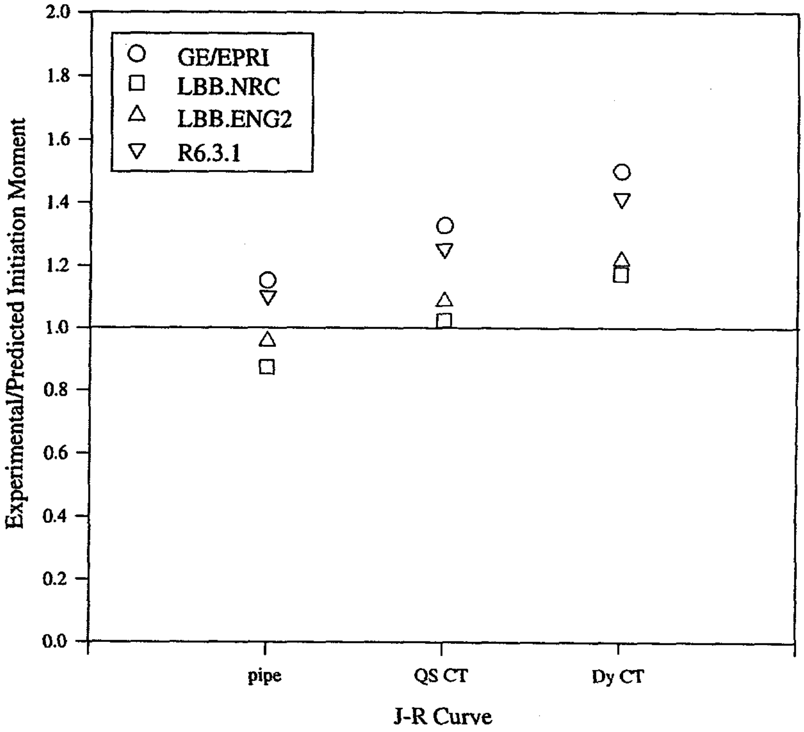

Figure 4.27 Experimental/predicted initiation moments for Experiment 1.2-8

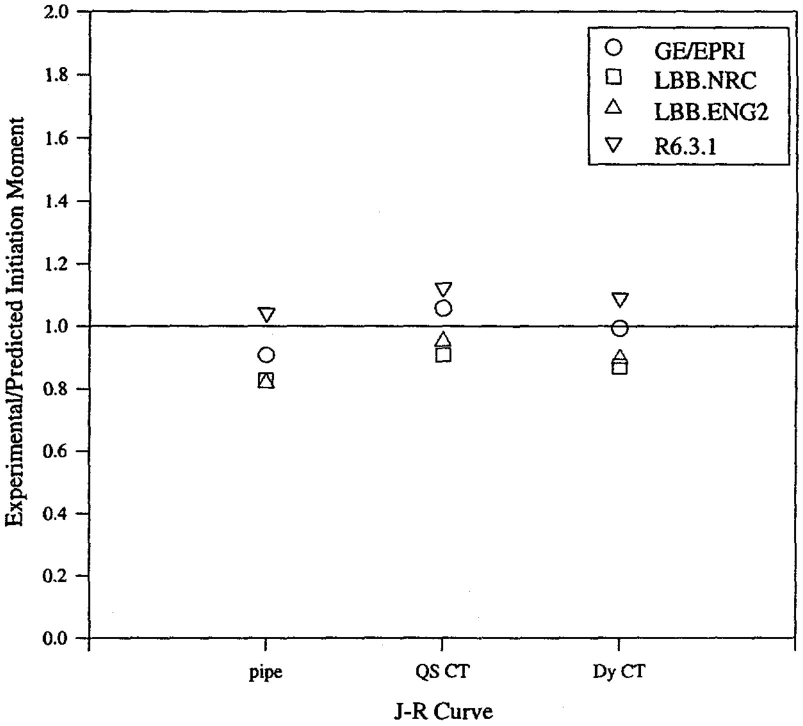

Figure 4.28 Experimental/predicted initiation moments for Experiment 4.2-1

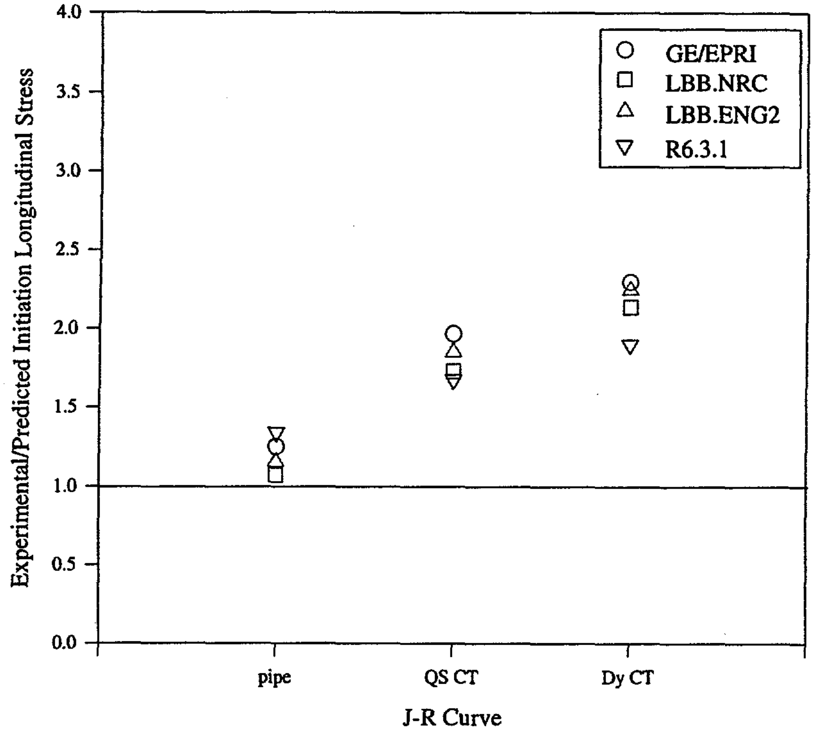

Figure 4.29 Experimental/predicted initiation longitudinal stress for Experiment 1-9

predicted versus experimental initiation moment values for Experiments 1.2-8, 4.2-1, and 1-9, respectively. Since Experiment 1-9 was loaded in bending and pressure, the moment values were converted to longitudinal stress in order to take into account the axial loading due to pressure. Since the version of the J-estimation scheme computer code did not account for the effects of pressure on the moment, the moment was adjusted using the following equations which have been found to give reasonable predictions in other past pressure and bend experiments (Refs. 4.14 and 4.22),

$$\begin{aligned} M_{Pred}^{B+T} &= M_{Pred}^{B} - \Delta M \\ \Delta M &= M_{NSC}^{B} - M_{NSC}^{B+T} \end{aligned} \tag{4-2}$$

The effect of the different J-R curves on the initiation moment predictions is questionable. For Experiment 4.2-1 (Figure 4.28), the dynamic-load C(T) J-R curve and the pipe J-R curve give about the same predictions, while the quasi-static J-R curve underpredicted the moments slightly more than using the other J-R curves. For Experiments 1.2-8 and 1-9 (Figures 4.27 and 4.29) the dynamic-load C(T) J-R curve produced the largest under prediction of moments, while the pipe J-R curve produced the best predictions. Logically, the pipe J-R curve should produce the best predictions, followed by the dynamic-load C(T) J-R curves.

Maximum Moment Figures 4.30 through 4.33 show the maximum moment predictions for Experiments 1.2-8, 4.2-1, 1-9 and 1.3-2, respectively. Tables 4.11, 4.12, 4.13, and 4.14 show the initiation and maximum moment ratios for Experiments 1.2-8, 4.2-1, 1-9 and 1.3-2, respectively. Since Experiments 1-9 and 1.3-2 were bend and pressure tests, the moment values were converted to longitudinal stress in order to take into account the axial loading due to pressure. Since the version of the J-estimation scheme computer codes did not account for the effects of pressure on the moment, the maximum moments were adjusted the same way as were the initiation moments (see Equation 4-2).

Using the J_M curve in the analysis tends to reduce the scatter between the estimation schemes. This finding is apparent if Figures 4.28 and 4.31 for Experiment 4.2-1 are compared. When used for predicting maximum moments, the J-estimation schemes performed better for the case of pure bending then they did for pressure and bending. In general, for the case of pressure-plus-bending, the estimation schemes produced stress ratios about 20 percent higher than for the case of pure bending. This result may be linked to inherent limitations of the estimation scheme.

The difference in predictions when using J-R curves from the pipe experiments, the quasi-static-load C(T) experiments, or the dynamic-load C(T) experiments was small. This result is surprising since, for carbon steel materials, the failure is driven more by fracture toughness than it is by collapse. However, the scatter between the estimation schemes may mask the effect of the different J-R curves. If one particular estimation scheme is studied, the effect of varying the J-R curve becomes more apparent. In almost all

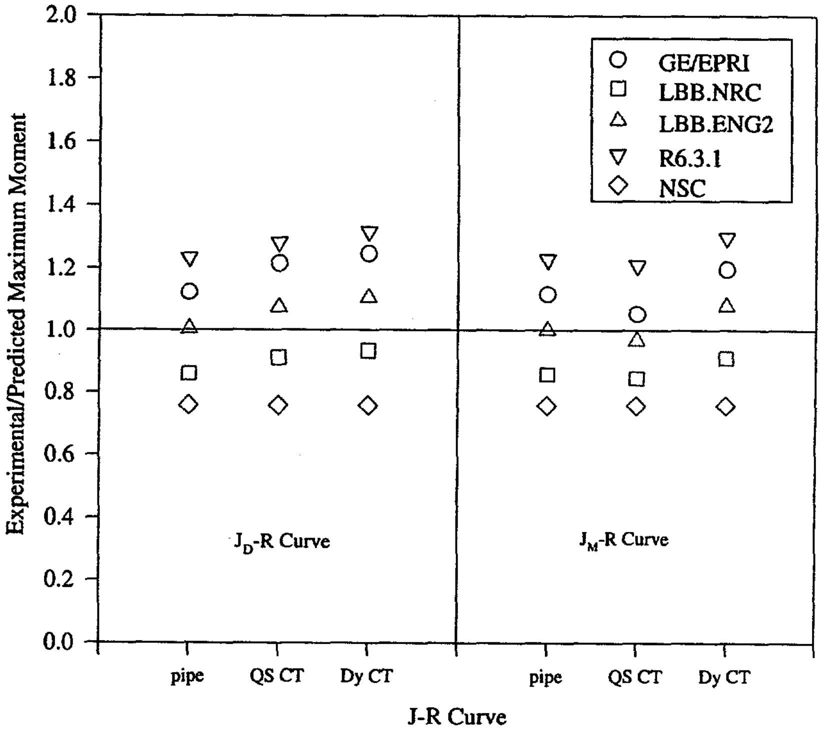

Figure 4.30 Experimental/predicted maximum moments for Experiment 1.2-8

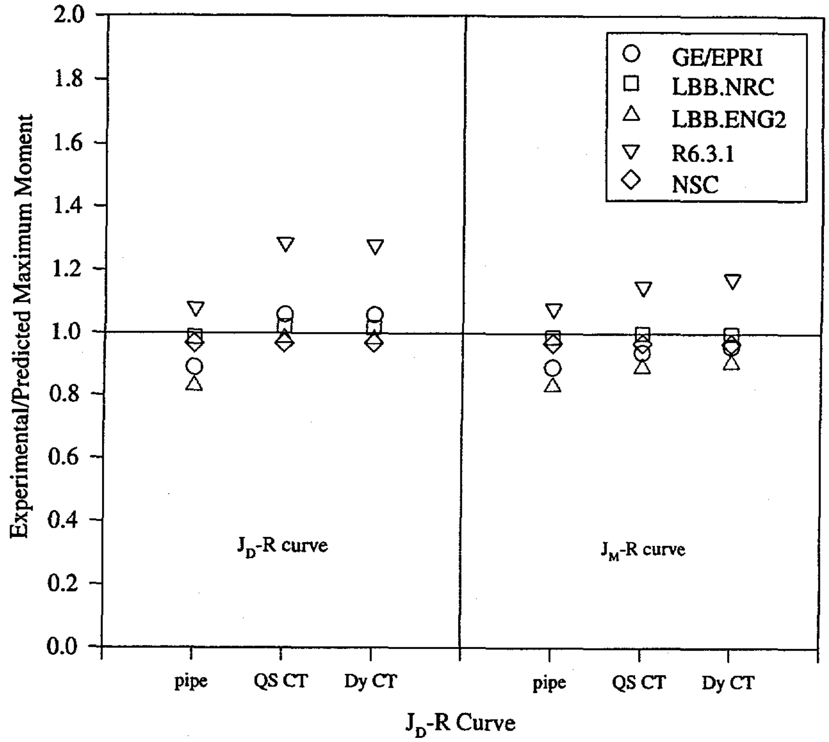

Figure 4.31 Experimental/predicted maximum moment for Experiment 4.2-1

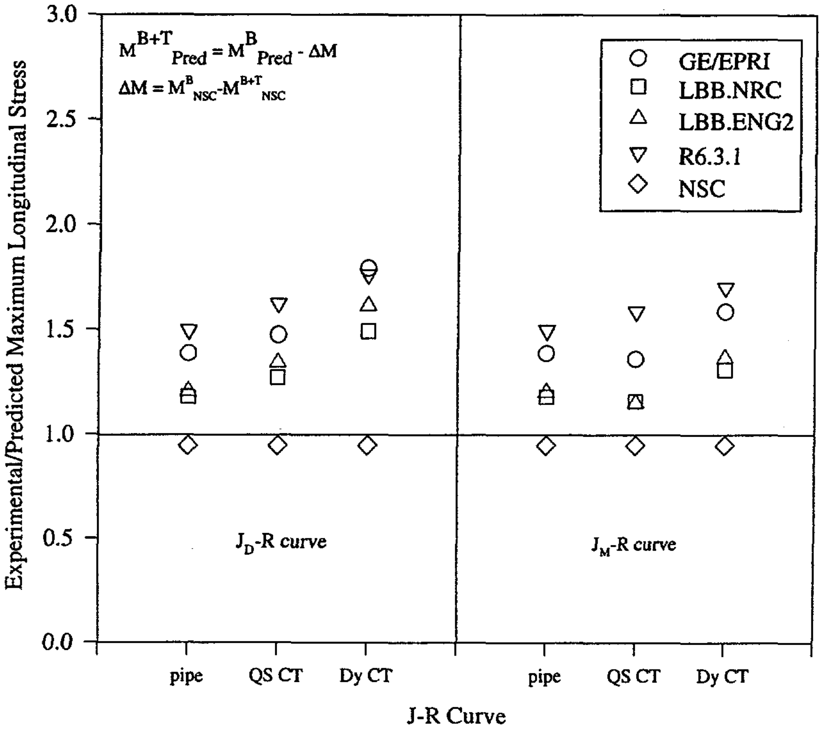

Figure 4.32 Experimental/predicted maximum longitudinal stress for Experiment 1-9

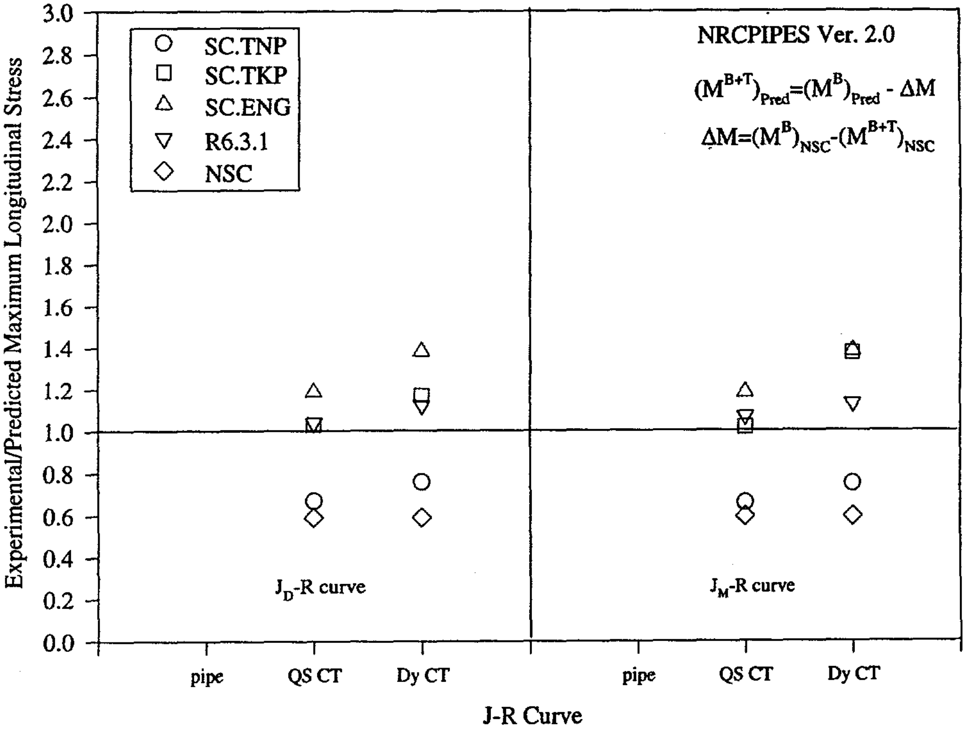

Figure 4.33 Experimental/predicted maximum longitudinal stress for Experiment 1.3-2

Table 4.11 Dynamic initiation moment and maximum moment predictions for Experiment 1.2-8

		Experimental-to-Predicted Moment Ratios								
	J-R curve	GE/EPRI		LBB.NRC		LBB.ENG2		R6		NSC
J-R Curve	Type	Initiation	Maximum	Initiation	Maximum	Initiation	Maximum	Initiation	Maximum	Maximum
Pipe Exp 1.2-8	JD	1.153	1.123	0.873	0.860	0.957	1.005	1.104	1.233	0.759
Pipe Exp 1.2-8	JM	1.153	1.118	0.873	0.859	0.957	1.002	1.104	1.230	0.759
QS C(T) F30-112	JD	1.329	1.215	1.025	0.912	1.087	1.075	1.255	1.282	0.759
QS C(T) F30-112	JM	1.329	1.055	1.025	0.846	1.087	0.969	1.255	1.212	0.759
Dyn C(T) F30-110	JD	1.501	1.246	1.176	0.935	1.220	1.107	1.417	1.316	0.759
Dyn C(T) F30-110	JM	1.501	1.199	1.176	0.913	1.220	1.081	1.417	1.300	0.759

Table 4.12 Dynamic initiation moment and maximum moment predictions for Experiment 4.2-1

		Experimental-to-Predicted Moment Ratios								
	J-R curve	GE/EPRI		LBB.NRC		LBB.ENG2		R6		NSC
J-R Curve	Type	Initiation	Maximum	Initiation	Maximum	Initiation	Maximum	Initiation	Maximum	Maximum
Pipe Exp 4.2-1	JD	0.906	0.889	0.826	0.986	0.819	0.829	1.042	1.081	0.966
Pipe Exp 4.2-1	JM	0.906	0.888	0.826	0.986	0.819	0.828	1.042	1.080	0.966
QS C(T) IPF13-1	JD	1.057	1.058	0.907	1.020	0.953	0.982	1.123	1.287	0.966
QS C(T) IPF13-1	JM	1.057	0.936	0.907	0.999	0.953	0.888	1.123	1.151	0.966
Dyn C(T) IPF13-5	JD	0.993	1.057	0.870	1.016	0.895	0.979	1.090	1.280	0.966
Dyn C(T) IPF13-5	JM	0.993	0.955	0.870	0.997	0.895	0.903	1.090	1.175	0.966

Table 4.13 Dynamic initiation longitudinal stress and maximum longitudinal stress predictions for Experiment 1-9

		Experimental-to-Predicted Longitudinal Stress Ratios								
	J-R Curve	GE/EPRI		LBB.NRC		LBB.ENG2		R6		NSC
J-R Curve	Type	Initiation	Maximum	Initiation	Maximum	Initiation	Maximum	Initiation	Maximum	Maximum
Pipe Exp 1-9	JD	1.246	1.387	1.069	1.181	1.153	1.207	1.338	1.496	0.945
Pipe Exp 1-9	JM	1.246	1.386	1.069	1.180	1.153	1.203	1.338	1.496	0.945
QS C(T) F22-3	JD	1.964	1.473	1.727	1.271	1.850	1.342	1.675	1.622	0.945
QS C(T) F22-3	JM	1.964	1.360	1.727	1.159	1.849	1.150	1.675	1.587	0.945
Dyn C(T) F22-2	JD	2.298	1.791	2.136	1.491	2.246	1.613	1.900	1.760	0.945
Dyn C(T) F22-2	JM	2.298	1.585	2.136	1.308	2.246	1.366	1.900	1.702	0.945

Table 4.14 Dynamic maximum longitudinal stress predictions for Experiment 1.3-2

	J-R	Experimental-to-Predicted Longitudinal Stress Ratios				
	J-R Curve	SC.TNP	SC.TKP	SC.ENG	R6	NSC
J-R Curve	Type	Maximum	Maximum	Maximum	Maximum	Maximum
QS C(T) F29-11	JD	0.668	1.029	1.186	1.037	0.590
QS C(T) F29-11	JM	0.659	1.017	1.181	1.067	0.590
Dyn C(T) F29-14	JD	0.758	1.170	1.380	1.121	0.590
Dyn C(T) F29-14	JM	0.750	1.372	1.380	1.129	0.590

cases, using the dynamic-load C(T) J-R curve produced higher predictions than the quasi-static-load J-R curve. For example, in Figure 4.30, which shows predictions for Experiment 1.2-8, the LBB.ENG2 method most accurately predicted the experimental moments, with only a slight variation in results when substituting quasi-static- and dynamic-load J-R curves. In this case, using the dynamic C(T) J_M-R curve gave a slight underprediction and the quasi-static C(T) J_M-R curve gave a slight overprediction of the maximum moments. Clearly, differences due to the uncertainties in the prediction schemes outweigh the differences in predictions due to material property variations.

4.2.3 Sensitivity Analyses for Dynamic Loading

To assess the effect of pipe diameter on the maximum moment for dynamically loaded pipe, a series of J-estimation scheme analyses was conducted. For these analyses, the LBB.ENG2 method was chosen since it was more accurate in predicting maximum loads than the other analysis methods. The carbon steel materials tested in this investigation fall into two categories:

1. Stress-strain curve and J-R curve lowered by increasing the strain rate (DP2-F30, DP2-F22, DP2-F29).

2. Stress-strain curve lowered but J-R curve unaffected by increasing the strain rate (IPF13).

In order to fully assess the effect of pipe diameter, an analysis using each of the material types is required. However, for the IP-F13 material, since the J-R curve is not affected by an increasing strain rate, and it is appropriate to use the quasi-static stress-strain properties to predict the dynamic pipe response, the effect of diameter on the maximum moment of a dynamically loaded pipe would be the same as the effect of diameter on a quasi-statically loaded pipe. Therefore, only an analysis using a material whose stress-strain curve and J-R curve are lowered by increasing the strain rate was performed. Table 4.15 shows the constants used in this analysis. All of the analyses were conducted using the quasi-static stress-strain properties and the dynamic-load C(T) J-R curve (F30-110) extrapolated as discussed in Section 4.1.3.1.

Table 4.15 Constant values used in dynamic-load sensitivity analyses

Stress-Strain Curve	TWC, Percent	R_M/t	σ_f, MPa	σ_o, MPa	ϵ_o	α	n
F30-104, QS	36.6	5.68	446.5	294	0.00152	1.97	5.366

Figures 4.34 and 4.35 show the results of these sensitivity analyses. Figure 4.34 shows the normalized initiation moment prediction versus pipe diameter for the 6-inch nominal diameter A106 Grade B (DP2-F30) pipe. Also included in this figure are the normalized initiation moments for each of the pipe experiments. Note that all moment values on this figure have been normalized with respect to the Net-Section Collapse analysis predicted moment. This figure shows a large decrease in initiation moment prediction with increasing pipe diameter. For a pipe whose diameter is 1.25 m (49.2 inches), the normalized predicted initiation moment was approximately 40 percent of the normalized initiation moment for 0.152 m (6 inch) diameter pipe. Figure 4.35 shows the normalized maximum moment predictions versus pipe diameter for the 6-inch nominal diameter A106 Grade B (DP2-F30) pipe. Also included on this figure are the normalized maximum moments for each of the pipe experiments. Again, all moment

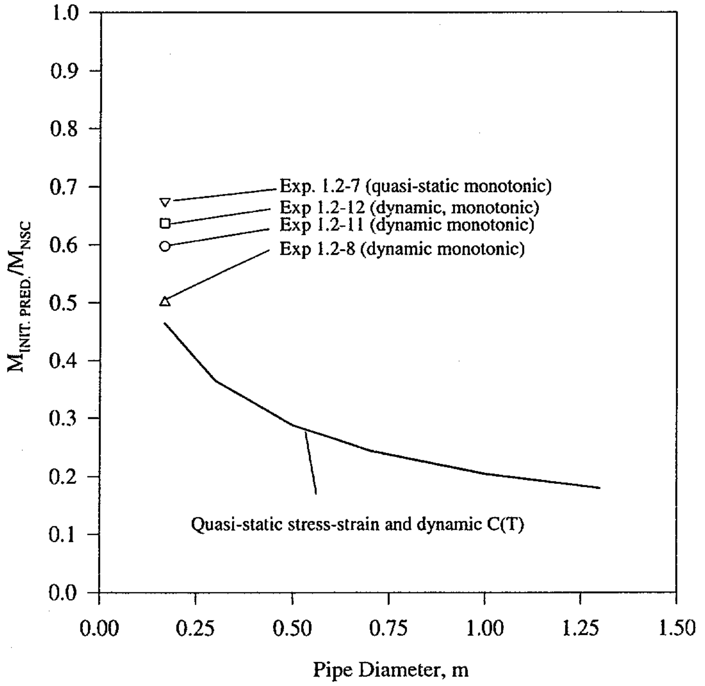

Figure 4.34 Normalized dynamic-initiation-moment prediction versus pipe diameter for TWC carbon steel pipe

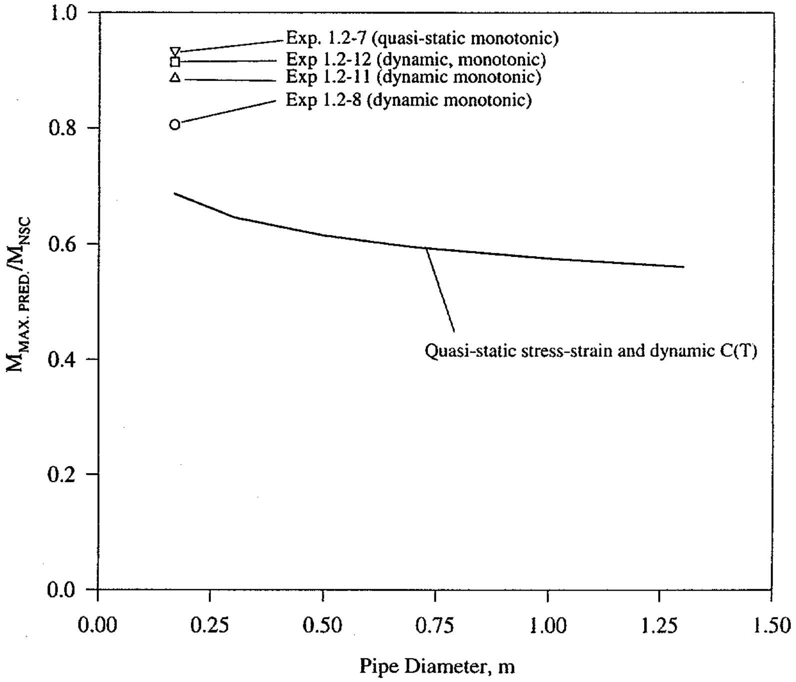

Figure 4.35 Normalized dynamic-maximum-moment predictions versus pipe diameter for carbon steel TWC pipe

values on this figure have been normalized with respect to the moments the Net-Section Collapse analysis predicted. The trends shown for the initiation moment are also present in the maximum moment predictions, but are less severe in the latter. For a pipe whose diameter is 1.25 m (49.2 inches), the normalized maximum moment predicted is approximately 80 percent of the normalized maximum moment for the 0.152 m (6 inch) diameter pipe.

4.3 References

4.1 Scott, P., Olson, R., and Wilkowski, G., "The IPIRG-1 Pipe System Fracture Tests -- Analytical Results," ASME PVP, Vol. 280, pp 153-165, June 1994.

4.2 Zahoor, A., and Kanninen, M. F., "A Plastic Fracture Mechanics Prediction of Fracture Instability in a Circumferentially Cracked Pipe in Bending - Part I: J-Integral Analysis," *ASME Journal of Pressure Vessel Technology*, Vol. 103, pp 352-358, 1981.

4.3 Pan, J., Ahmad, J. A., Kanninen, M. F., and Popelar, C. H., "Applications of a Tearing Instability Analysis for Strain Hardening Materials to a Circumferentially Cracked Pipe in Bending," ASTM STP 833, pp 721-748, 1984.

4.4 Miura, N., and Wilkowski, G., "J-R Curves from Through-Wall-Cracked Pipe Tests - Combined Loading and Short-Crack Considerations," ASME PVP, Vol. 304, pp 171-179, 1995.

4.5 Mohan, R., Marschall, C., Krishnaswamy, P., Brust, F., Ghadiali, N., and Wilkowski, G., "Effects of Toughness Anisotropy and Combined Loading on Fracture Behavior of Ferritic Nuclear Pipe," NUREG/CR-6299, April 1995.

4.6 Scott, P., Wilson, M., Olson, R., Marschall, C., Schmidt, R., and Wilkowski, G., "Stability of Cracked Pipe Under Inertial Stresses," NUREG/CR-6233, BMI-2177, Vol. 1, August, 1994.

4.7 Olson, R., Scott, P., Marschall, C., and Wilkowski, G., "Comparison of Fracture Toughness Values from an IPIRG-1 Large-Scale Pipe System Test and C(T)-Specimens on Wrought TP304 Stainless Steel," ASME PVP, Vol. 280, pp 241-254, June 1994.

4.8 Rudland, D. L., Brust, F., and Wilkowski, G., "Fracture Toughness Evaluation of a 16-inch Nominal Diameter TP304 Stainless Steel Pipe Used in Pipe Fracture Experiments," NUREG/CR-6446, BMI-2194, December 1996.

4.9 Marschall, C. W., Mohan, R., Krishnaswamy, P., Wilkowski, G. M., "Effect of Dynamic Strain Aging on the Strength and Toughness of Nuclear Ferritic Piping at LWR Temperatures," NUREG/CR-6226, BMI-2176, October 1994.

4.10 Kanninen, M. F., and others, "Mechanical Fracture Predictions for Sensitized Stainless Steel Piping with Circumferential Cracks," Battelle Final Report to EPRI, Report NP-192, September 1976.

4.11 Klecker, R. and others, "NRC Leak-Before-Break (LBB.NRC) Analysis Method for Circumferential Through-Wall-Cracked Pipes Under Axial Plus Bending Loads," NUREG/CR-4572, May 1986.

4.12 Brust, F. W., "Approximate Methods for Fracture Analyses of Through-Wall-Cracked Pipes," NUREG/CR-4853, February 1987.

4.13 Kumar, V. and others, "Advances in Elastic-Plastic Fracture Analysis," EPRI Report NP-3607, August 1984.

4.14 Brust, F.W., and others, "Assessment of Short Through-Wall Circumferential Cracks in Pipes," NUREG/CR-6235, BMI-2179, April 1995.

4.15 Wilkowski, G. M., Marschall, C. W., and Landow, M., "Extrapolation of C(T) Specimen J-R Curves for Use in Pipe Flaw Evaluations," ASTM STP 1074, pp 56-84, 1990.

4.16 Wilkowski, G.M., and Scott, P.M., "A Statistical Based Circumferentially Cracked Pipe Fracture Mechanics Analysis for Design or Code Implementation," *Nuclear Engineering and Design*, Vol. 111, pp 173-187, 1989.

4.17 Milne, I., Ainsworth, R. A., Dowling, A. R., and Steward, A. T., "Assessment of the Integrity of Structures Containing Defects," R/H/R6-Rev. 3, published by Central Electric Generating Board, England, May 1986.

4.18 Rudland, D.L., Scott, P.M., and Wilkowski, G.M., "The Effect of Cyclic and Dynamic Loads on Carbon Steel Pipe," NUREG/CR-6438, BMI-2188, February 1996.

4.19 Ernst, Hugo, Paris, P.C., Rossow, Mark, and Hutchinson, J.W., "Analysis of Load-Displacement Relationship to Determine J-R Curve and Tearing Instability Material Properties," Fracture Mechanics, ASTM STP 677, pp 581-599, 1979.

4.20 Kumar, V. and others, "An Engineering Approach for Elastic-Plastic Fracture Analysis," EPRI Report NP-1931, 1981.

4.21 Marschall, C. W., Landow, M., and Wilkowski, G. M., "Loading Rate Effects on Strength and Fracture Toughness of Pipe Steels Used in Task 1 of the IPIRG Program," NUREG/CR-6098, October 1993.

4.22 Scott, P. M., and Ahmad, J., "Experimental and Analytical Assessment of Circumferentially Surface-Cracked Pipe under Bending," NUREG/CR-4872, April 1978.

4.23 Krishnaswamy, P., Scott, P., Mohan, R., Rahman, S., Choi, Y. H., Brust, F., Kilinski, T., Ghadiali, N., Marschall, C., and Wilkowski, G., "Fracture Behavior of Circumferential Short-Surface-Cracked Pipe," NUREG/CR-6298, November 1995.

5.0 SUMMARY AND DISCUSSION OF TECHNICAL RESULTS

The results from the cyclic- and dynamic-load study carried out in Task 3 of the IPIRG-2 program are summarized below in Section 5.1. Section 5.6 then discusses the application of these results to LBB and in-service flaw evaluations.

5.1 Results From Cyclic-Load C(T) Experiments

This section discusses the results of the cyclic-load C(T) experiments. First, the effects of cyclic loads on the load-displacement behavior of the C(T) specimens are discussed. A comparison of maximum load and displacements in the C(T) tests, although not directly useful themselves, provide insight into the effects of the different load histories evaluated. Since the crack lengths of the specimens tested are similar, the trends shown should be consistent with the J values calculated. Also, the mechanisms of crack tip degradation present during the cyclic event are discussed. This discussion aids in the understanding of the documented toughness degradation due to cyclic loading.

5.1.1 Load History Effects

In this investigation, a series of quasi-static, cyclic-load C(T) experiments was conducted on four materials: stainless steel base metal, stainless steel SAW, carbon steel base metal, and carbon steel SAW. Dynamic, cyclic-load C(T) experiments were conducted on the stainless steel and carbon steel SAWs. These experiments were run in displacement control at various R-ratios and plastic cyclic displacement increments (the plastic cyclic displacement divided by the displacement at crack initiation under monotonic loading, δ_{cyc}/δ_i) using a BASIC control program that was used in past IPIRG-1 TWC pipe experiments. This plastic cyclic displacement is synonymous with ratcheting in uncracked pipe. Note that the inverse of the δ_{cyc}/δ_i value is the number of cycles to crack initiation if there was no degradation from the cyclic loading, however, if cyclic degradation occurs, the number of cycles to initiation might actually be much less.

5.1.1.1 Stainless Steel and Carbon Steel Base Metal

For the base metal C(T) experiments, the reduction in maximum load due to the cyclic loading was a maximum of 20 percent in several of the $R = -1$ cases. However, the load-line displacement at maximum load decreased significantly. For the stainless steel tested with a normalized cyclic displacement increment of 0.025 (i.e., 40 cycles to crack initiation), the load-line displacement decreased by about 80 percent of the monotonic-loading value. Also for the stainless steel, there was a minimal decrease in the load-line displacement at the maximum load between the R-ratios of 0 and -0.6, and then a steep decrease between -0.6 and -1. However, this observation is dependent on the normalized cyclic displacement increment. For the case with δ_{cyc}/δ_i of 0.2 (i.e., 5 cycles to crack initiation), no significant load-displacement differences were seen at R-ratios up to -0.6, but at δ_{cyc}/δ_i of 0.025, a 10 percent decrease in the maximum load was observed at an R-ratio of -0.6 as compared to the quasi-static monotonic experiment. This indicates that at smaller cyclic displacement increments, either there is a greater loss in the apparent toughness due to the crack growing in highly damaged material or contributions to the crack growth from fatigue have become substantial.

Since only one normalized cyclic displacement increment was run for the carbon steel base metal material, only conclusions about the effect of different R-ratios can be made. In comparing the carbon steel results with the stainless steel results at the same displacement increment, the carbon steel seems to be more affected by cyclic loading at each R-ratio investigated, except at R = -1. For example, at an R-ratio of -0.3, where no decrease in the C(T) specimen load and only a slight decrease in displacement was observed in the stainless steel material, a significant drop in the load-displacement record is shown for the carbon steel material as compared to the monotonic results. Also, there seems to be a threshold in the effect of R-ratio in the carbon steel. At an R-ratio of -0.8 and -1, the percentage decrease, as compared with the monotonic experiment, in both the maximum load and the displacement at maximum load were nearly identical, which was not true for the stainless steel where the effects of cyclic loading tended to be greater at R = -1 than at R = -0.8.

5.1.1.2 Stainless Steel and Carbon Steel Submerged-Arc Weld

Dynamic, monotonic loading increased the maximum load as compared to quasi-static, monotonic loading for both the austenitic and ferritic welds. For the stainless steel SAW (A8W4), that increase was 20 percent, while for the carbon steel SAW (F40W) that increase was 13 percent. In terms of the change in displacements at maximum load from quasi-static to dynamic loading, the stainless steel SAW experienced a larger decrease in this displacement than the carbon steel SAW; on average about 35 percent for the stainless steel SAW and 20 percent for the carbon steel SAW.

All cyclic-load weld specimens were tested with $\delta_{cyc}/\delta_i = 0.1$ (i.e., 10 cycles to crack initiation). For the quasi-static cyclic experiments, the reduction in maximum load was minimal for both SAWs as compared to the quasi-static monotonic experiments. The greatest reduction in maximum load was 10 percent, observed in the stainless steel SAW tested at R = -1. Interestingly, the reduction in maximum load for the dynamic-cyclic experiments was greater than the reduction for the quasi-static cyclic experiments. In all of the quasi-static, cyclic-load weld C(T) cases, the maximum reductions in maximum load, as compared to the quasi-static, monotonic experiment was 10 percent. For the dynamic, cyclic-load weld C(T) cases, the maximum reduction in maximum load, as compared to the dynamic, monotonic experiment was 20 percent.

5.1.2 Crack-Tip Degradation from Cyclic Loading

There appear to be two main physical mechanisms present in the cyclic degradation process - crack-tip sharpening and void sharpening. Both the stainless and the carbon steel base metals investigated showed evidence of crack-tip sharpening. Because of the more ductile nature of stainless steel, the larger crack-tip-opening displacement in this material caused the sharpening to be less severe than in the carbon steel specimens. This sharpening acts to increase the crack-tip stress intensity and promote crack extension, thus lowering the apparent fracture resistance. From the load-displacement record, the carbon steel specimens were strongly affected by the intermediate R-ratios. Since the carbon steel has a lower toughness than the stainless steel, it has less crack-tip blunting. Hence, it may take less compressive load to sharpen the crack tip. Therefore, intermediate R-ratios could decrease the load-carrying capacity in the carbon steel, but have little effect on the stainless steel. Since the crack will close until the initial crack faces transmit compressive loads, it appears logical that there should be a limit to the amount the load and displacement are decreased by the cyclic loading. In the carbon steel base metal tested in this investigation, that limit seems to occur at an R-ratio of -0.8. For this material, decreasing the R-ratio from

-0.8 to -1 did not decrease the load-displacement curve any further. Theoretically, the same effect should be observed in the stainless steel base metal; however, tests at R-ratios with more compression than the R = -1 case were not conducted in this study.

With respect to void sharpening, the metallographic studies showed that only the carbon steel experienced this phenomenon. Sharp voids tend to enhance void coalescence and lower the apparent fracture toughness. The argument for this mechanism is similar to the one just made for the crack-tip sharpening, the higher the materials toughness, the larger the compressive load needed to promote void sharpening. Perhaps for compressive loading larger than that used in this study, void sharpening might occur in the stainless steel specimens. The crack tip and void sharpening mechanisms work together in degrading the material's fracture resistance under cyclic loading.

5.2 Results from Analytical and Numerical Evaluations of Cyclic-Loading Effects on Fracture

In this section, the analytical and numerical evaluations of the cyclic-load C(T) specimens are discussed. First, the J-R curves calculated from the "upper envelope" of the load-displacement curve approach and the ASTM E813/1152 standard are discussed and compared to the η-factor J-R curves calculated for the cyclic TWC pipe experiments. Second, the results from a series of finite element analyses of a cyclic-load C(T) specimen are discussed. These analyses were conducted to verify the J-R curves calculated from the ASTM procedure. Next, the results from a series of TWC moment predictions using the cyclic-load C(T) J-R curves are discussed. These predictions were performed to determine if these cyclic J-R curves can be used to predict cyclic TWC pipe response. Finally, the results from a series of analyses are discussed that were used to determine the effect of pipe diameter on the maximum-moment predictions.

5.2.1 J-R Curves Calculated from C(T) Experiments

For both the carbon steel and stainless steel base metal tested, the cyclic-load C(T) experiments produced J at crack initiation values, J_i, that were in reasonable agreement with the cyclic-load pipe J_i values with similar load histories. Hence, using the pipe δ_{cyc}/δ_i in the C(T) tests gave good similitude at crack initiation. This is an important finding.

The agreement between the C(T) and TWC pipe tests, however, was not very good after some crack growth. The relative decrease in J ($J_{QS,cyc}/J_{QS,mono}$) after crack growth equal to 30 percent of the original ligament due to cyclic loading between the C(T) and TWC pipe specimens was comparable even if the absolute comparisons of J were poor.

For the stainless steel tested in this study, it was found that doubling δ_{cyc}/δ_i after crack initiation in the C(T) tests gave a more reasonable estimate of the crack growth per cycle in the TWC pipe tests. However, the problem in using δ_{cyc}/δ_i as the control parameter in the tests may be attributed to the differences in specimen size. In all cases examined in this investigation, the C(T) specimens, tested with a constant δ_{cyc}/δ_i, underpredicted the J response after some crack growth in the TWC pipe experiments, indicating that moment predictions using these J-R curves will underpredict the moment response. A discussion of the similitude between the TWC pipe and the C(T) specimen and how to circumvent this problem is found in Section 5.6.

The decrease in resistance due to cyclic loading may be related to the materials' yield-to-ultimate strength ratio. The trends shown suggest that a linear relationship may exist between the relative decrease in resistance due to cyclic loading and the material strength. This relationship may aid in the creation of a criterion that could be used to predict a material's response to cyclic loading; however, the confidence level of such a criterion is not high due to the limited experimental data available.

It appears from this work that there is a material dependency on the degradation due to cyclic loading. Figure 5.1 is a schematic illustrating the effect of R-ratio and initial material toughness on the cyclic J-R curve of materials. The trends are such that lower toughness materials are more affected by cyclic loading, and more negative R-ratios will increase the amount of degradation. These findings indicate that dynamically cycling a specimen may increase the cyclic degradation as compared to cycling at quasi-static rates.

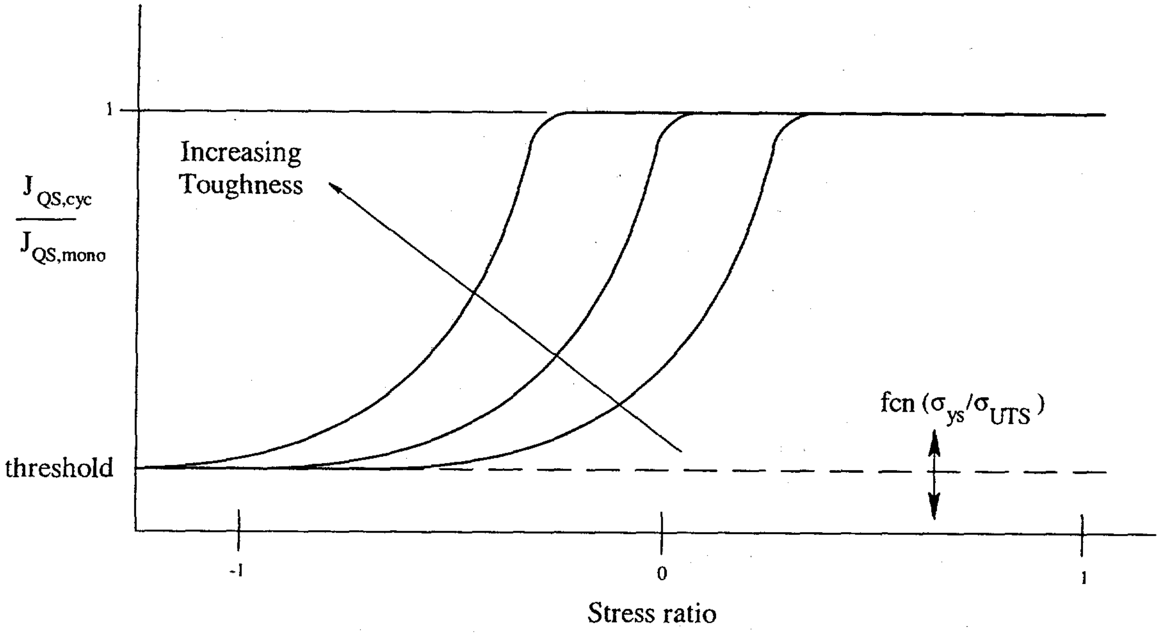

Figure 5.1 Schematic of relationship between cyclic toughness degradation and stress ratio

5.2.2 Verification of Experimental Cyclic J-R Curve Calculations Using the Finite Element Method

In order to verify the analysis procedure to calculate the J-R curves from the cyclic C(T) experiments, a series of two-dimensional finite element analyses was conducted. The point being addressed was the validity of using the upper envelope of the cyclic load-displacement curve with the ASTM E813/1152 J-R calculation procedure to get the cyclic J-R curve. These analyses were conducted under plane stress and generalized plane strain using the classical isotropic and kinematic hardening laws. The ABAQUS finite element code was used in these analyses. From these analyses, the kinematic hardening law produced results that closely matched the tensile portion of the cyclic loading history but severely underpredicted the compressive portion. On the other hand, using the isotropic-hardening law (using both a linear fit and a Ramberg-Osgood fit of the stress-strain behavior) overpredicted both the tensile and compressive loads. A combined isotropic/kinematic hardening law may capture the cyclic load history trends better; however, these types of combined laws are not presently available in the ABAQUS code. A further limitation in the ABAQUS code is that only bilinear stress-strain curves are allowed when using kinematic hardening, whereas multi-linear stress-strain curves are allowed when using isotropic hardening.

The J-integral value during the cyclic-loading event was calculated from the FEM plane stress analyses. The FEM predicted value of J at crack initiation for both the kinematic and isotropic analyses compared well with the ASTM J value calculated from the experimental results. After the first unloading, J became very path dependent in these analyses. The path dependence is due to the global unloadings that occur at each cycle. For a monotonic-load case with crack growth, the J values evaluated along the far field paths do not deviate greatly from each other because the unloadings are localized at the crack tip. After an unload, the far-field crack reinitiation value of J was smaller than that before unloading on the prior cycle. Moreover, the difference between the load and reload value of J appeared to increase with the number of cycles, which was a direct consequence of the path-dependent behavior of J during the cyclic event.

After crack growth, the kinematic analysis, which predicted the experimental tensile loads accurately, produced J values that were lower than the ASTM J values calculated from the experimental test record. The isotropic analysis produced J values that were slightly higher than the experimental ASTM J values. Since the kinematic hardening analysis underpredicted the experimental compressive loads, and the isotropic analysis overpredicted the experimental tensile and compressive loads, it would seem likely that an analysis that accurately predicted the experimental load-displacement response would also produce J values similar to the ASTM J values. When the ASTM procedure for calculating J was used with the upper envelope of the finite element predicted load-displacement response, the resulting J-R curve agreed very well with the far-field J-R curve calculated directly from the finite element analysis. Therefore, these results suggest that the upper envelope approach to calculating the cyclic J-R curve produces an accurate representation of the material's fracture behavior.

5.2.3 Predictions of TWC Pipe Response

Several analyses were conducted to determine if the cyclic-load J-R curves should be used in predicting the crack initiation and maximum loads of cyclically loaded 6-inch nominal diameter TWC pipe experiments. The general conclusion is that the moment predictions were insensitive to the J-R curve used. Even when the monotonic-loading J-R curve was used, the moment predictions were approximately equal to the predictions made using the cyclic-load pipe J-R curve. For the 6-inch nominal diameter TWC pipes investigated, the moments at crack initiation and maximum load were very close to limit load and therefore not very sensitive to changes in toughness, which is especially true for the very tough stainless steel pipe. The particular A106 Grade B pipe used had a low enough toughness so that the moments were in the EPFM region, but there were not large effects on the moments due to the cyclic loads. Since the experimental scatter in maximum load from replicate pipe experiments could be as much as 10 percent, the difference between using a monotonic- or cyclic-load J-R curve will be insignificant. Therefore, it is appropriate to state that for these 6-inch nominal diameter carbon steel and stainless steel pipe materials, the monotonic-load C(T) J-R curve can be used in predicting cyclic-load pipe moments at crack initiation and maximum load. However, for larger diameter pipes, initiation and maximum loads should be further from limit load. Hence, the cyclic-load effect on toughness reduction will result in lower initiation and maximum loads for larger diameter pipe.

5.2.4 Effect of Pipe Diameter on Maximum Moment Predictions

To investigate the effect of pipe diameter on the maximum moment for cyclically loaded pipe, a series of sensitivity studies was performed. For these analyses, the LBB.ENG2 method was chosen since it has been found to be reasonablely accurate in predicting loads from past quasi-static pipe experiments. The predictions were made for the circumferential TWC in the base metal of both stainless steel and carbon steel pipe. These calculations showed that as the pipe diameter is increased, the maximum moment at all R-ratios is decreased. Interestingly, for the stainless steel base metal, the percent decrease in load-carrying capacity between J-R curves at different R-ratios is constant. Whether the pipe diameter is 0.1 m (3.94 inches) or 1 m (39.4 inches), the R = -1 case shows a 20 percent decrease as compared to the R = 0 case. The decrease in load-carrying capacity in the carbon steel is slightly greater at large diameters than at small diameters. For the R = -1 case, there is a 16 percent decrease in maximum load for a 6-inch nominal diameter pipe, while there is a 20 percent decrease in maximum load for a 1.3 m (51.2 inch) diameter pipe, indicating that the cyclic degradation effect of the maximum load is slightly greater for larger diameter pipes.

These analyses have shown that when the R-ratio is -1, the number of cycles to maximum moment for both materials falls in the band for a typical seismic event, i.e., 5-30 large amplitude cycles. This result indicates that a seismic event with an R-ratio of -1 is likely to produce enough crack growth to take a TWC pipe beyond its maximum load-carrying capacity for all typical nuclear pipe sizes. However, surpassing maximum moment does not constitute a double-ended-guillotine break; instability of the crack would depend on many factors, for example, the ratio of the primary to secondary stresses.

5.3 Results of Tests at Dynamic Rates of Loading

In this section, the results from a series of dynamic tensile and fracture toughness tests are discussed. The purpose of these experiments was to expand on the dynamic material property database. In past programs, dynamic loading decreased the ultimate strength and fracture toughness of carbon steel base metals tested as compared with quasi-static experiments. Dynamic loading either had no effect or increased the ultimate strength and fracture toughness of the stainless steel base metals tested in past programs. This investigation only studied the dynamic effects on carbon steel materials.

5.3.1 Dynamic Tensile Experiments

All of the carbon steel materials tested showed a decrease in ultimate strength with an increase in strain rate. As the strain rate is increased, the interstitial atoms have less time to diffuse to the moving dislocations; thus, the plastic strains are greater and the limit load is less. Interestingly, even though the ultimate strength decreased in all cases, the yield strengths increased slightly or were unchanged. At a strain rate of 1/s, the ultimate strength decreased for the six ferritic base metals and two ferritic SAWs tested in this program and the IPIRG-1 program by 7 to 25 percent.

5.3.2 Dynamic Fracture Toughness Experiments

Even though the dynamic-loading effect on the stress-strain response was similar for the materials tested, the effects of dynamic loading on the fracture resistance were variable. While some base metal specimens showed a decrease in both J_i and the J-R curve with increasing loading rate, others showed no change in resistance with the same increase in loading rate. The submerged-arc welds tested, on the other hand, showed a significant increase in both J_i and the J-R curve with increasing strain rate. However, the Japanese carbon steel (STS410) TIG weld showed no change in the J-R curve with increasing strain rate.

Two factors that may affect the dynamic toughness behavior were explored. These two factors were the yield-to-ultimate strength ratio of the material, and the high temperature-to-room temperature Brinell hardness ratio. The trends presented suggest that dynamically loaded carbon steel materials whose yield-to-ultimate ratio is greater than 0.5 will have toughness values that are equal to or higher than those tested at quasi-static loading rates. This apparent dependency on yield-to-ultimate ratio may aid in the creation of a criterion that would characterize a material's fracture toughness response to dynamic loading; however, the data in this correlation show a larger amount of scatter than desired.

Another measure that was examined for dynamic toughness is the change in Brinell hardness from test temperature to room temperature, which was used as a dynamic strain aging screening criterion (Ref. 5.1). Correlations with this parameter were generally good, but again there was more scatter in the data than desired. It may be that both these parameters are needed to describe the change in toughness of ferritic steels at LWR temperatures and dynamic loading rates.

It should also be noted that from the IPIRG-1 results and other efforts in IPIRG-2, generally for austenitic materials the dynamic toughness was the same or higher than at quasi-static rates.

5.4 Predictions of Pipe Response to Dynamic Loading

In industry, quasi-static material properties are used in making predictions of the dynamic response of a piping system. If dynamic loading has a detrimental effect on the material properties, as described in the preceding section, then the quasi-static properties may give results that mispredict the actual behavior. In order to make accurate dynamic moment predictions, both the appropriate stress-strain and J-R curve need to be used. In this section, the results of the determination of the appropriate material properties to use in dynamic moment predictions are discussed. Also, the results from a series of initiation and maximum moment predictions using the dynamic material properties are discussed. The purpose of these analyses was to determine if dynamic material properties are needed to accurately predict the dynamic TWC and SC pipe response. Finally, the results from a series of maximum moment predictions are discussed that are aimed at determining the effect of pipe diameter on maximum moment predictions of dynamically loaded TWC pipe. In this section, the term "fracture ratio" refers to the ratio of the experimental-to-predicted moments for the unpressurized experiments and the ratio of the experimental-to-predicted longitudinal stress for the pressurized experiments. Fracture ratios greater than 1.0 show the inherent margin in the analysis procedure.

5.4.1 Determination of Appropriate Material Properties to Use in Dynamic Moment Predictions

The loading rate for the dynamic-load C(T) experiments was determined in the IPIRG-1 program from a finite element analysis of an inertially loaded pipe experiment. It was determined that a C(T) specimen that had a crack which initiated in 0.2 seconds would be representative of the dynamic, cyclic pipe tests conducted at 4 Hz. All of the IPIRG-1 and IPIRG-2 C(T) specimens were conducted at this rate. It is appropriate to use these data in predicting moments for a cracked pipe which has the same time to crack initiation.

Choosing the correct stress-strain curve to use in a J-estimation scheme is more difficult than determining the loading rate for a fracture test. The rates for the dynamic tensile tests are more difficult to quantify, hence rates of 10^{-5}/s to 10/s were chosen as bounds of the effective strain rate for a cracked pipe. Calculations based on the STS410 6-inch nominal diameter pipe tests, showed that the strain rate in the uncracked pipe was on the order of 10^{-3}/s, which is much closer to the quasi-static rate than to the dynamic rate.

A comparison between the load-displacement responses of the quasi-static and dynamic, monotonic-load TWC pipe and C(T) experiments for both the STS410 and several A106 Grade B pipe materials showed no differences up to crack initiation. Even for the carbon steels whose initiation toughnesses were different under quasi-static and dynamic loading, the load-displacement response was identical up to crack initiation. Therefore, the quasi-static stress-strain curve is sufficient for fracture predictions at the rates investigated in this program.

5.4.2 Predictions of Dynamic, Monotonic-Loading Pipe Test Loads Using Quasi-static and Dynamic Material Properties

Several J-estimation-scheme moment predictions were made in order to determine if the dynamic properties were necessary in predicting dynamic pipe response. It was found that using the J_M curve in the analysis tended to reduce the scatter among the estimation schemes. When predicting maximum moments, the J-estimation schemes performed better for the case of pure bending than they did for pressure and bending. In general, for the case of pressure plus bending the estimation schemes produced fracture ratios about 20 percent greater than for the case of pure bending. This is consistent with experience from the NRC's Short Cracks in Piping and Piping Welds research program, Refs. 5.2 and 5.3. This result may be linked to inherent limitations of the estimation schemes, as was also noted in References 5.2 and 5.3.

The difference in maximum load predictions when using J-R curves from the 6-inch nominal diameter pipe experiments, the quasi-static-loading C(T) experiments, or the dynamic-loading C(T) experiments was small. This observation was expected in the stainless steel material since the maximum moments for the pipes investigated were very close to limit load, which would cause an apparent insensitivity to toughness. However, the scatter between the J-estimation schemes may mask the effect of the different J-R curves. If one particular estimation scheme is studied, the effect of varying the J-R curve becomes more apparent. In almost all cases, using the dynamic-load, C(T), J-R curve produced lower moment predictions than did the quasi-static-load, C(T), J-R curve. For example, when making maximum-moment predictions for IPIRG-1 Experiment 1.2-8, the LBB.ENG2 method most accurately predicted the experimental loads using quasi-static stress-strain properties, with only a slight variation in results when substituting quasi-static- and dynamic-load J-R curves. For IPIRG-1 Experiment 1.2-8, using the dynamic C(T) J_M-R curve gave a slight underprediction and the quasi-static C(T) J_M-R curve gave a slight overprediction of the maximum moments. Clearly, differences due to the uncertainties in the prediction schemes outweigh the differences in moment predictions due to material property variations for the relatively small diameter pipe experiments analyzed.

5.4.3 Effect of Diameter on Pipe Response to Dynamic Loading

To assess the effect of different pipe diameters on the maximum moments for dynamically loaded pipe, a series of J-estimation scheme analyses was conducted. For these analyses, the LBB.ENG2 method was chosen since it is reasonably accurate in predicting quasi-static TWC pipe moments. Also, the quasi-static stress-strain curves were used in these analyses since they were found to be most appropriate to use in predicting loads in dynamic pipe experiments. An analysis using a material whose J-R curve was lowered by increasing the strain rate was performed. Since some of the TWC pipe materials had toughness values that were not affected by increasing strain rate, it would be pointless to analyze these materials since these analyses would add nothing to the discussion about the effects of dynamic loading. The comparisons showed that increasing the pipe diameter increased the amount of load-carrying capacity reductions as compared to the quasi-static experiments; for a pipe whose diameter is 1.25 m (49.2 inch), the calculated maximum moment (normalized by the limit load) was 80 percent of the normalized maximum moment for a 0.152 m (6 inch) diameter pipe.

5.5 Cyclic and Dynamic Effects in Fracture

The trends from this investigation suggest that both the dynamic and cyclic effect on toughness may be linearly related to the materials' yield-to-ultimate strength ratio. If this is the case, then all that is required to make an estimate of the toughness of a structure subjected to dynamic, cyclic loads are the quasi-static, monotonic J-R curve and the stress-strain curve. A method for estimating the dynamic, cyclic resistance may be used that multiplies the quasi-static, monotonic resistance to the relative decrease in resistance due to both cyclic and dynamic effects producing an estimate of the dynamic, cyclic resistance. Dynamic, cyclic ($J_{dyn,cyc}$) quasi-static, monotonic (J_{QS}), dynamic, monotonic, (J_{dyn}) and quasi-static, cyclic (J_{cyc}) J-R curves were developed for two base metals and two weld metals. The $J_{dyn,cyc}$ term for the base metal experiments was taken from Reference 5.4, but the other J terms described were developed from the C(T) specimens tested in this investigation. The weld metal experiments were the dynamic, cyclic C(T) specimens tested in this study. Figure 5.2 shows the experimental J values at some crack growth for the dynamic, cyclic experiments versus a calculated J using the quasi-static, monotonic resistance and the relative decrease in J due to cyclic and dynamic loading. In Figure 5.2, F_{dyn} is defined as $J_{dyn,mono}/J_{QS,mono}$ which is the ordinate in Figure 3.12 and F_{cyc} is defined as $J_{QS,cyc}/J_{QS,mono}$, which is the ordinate in Figure 2.48. Note that all J values shown in Figure 5.2 are taken at a crack extension of 30 percent of the original ligament, i.e., at the maximum limit of valid crack growth in the tests.

The open symbols in Figure 5.2 represent the results taken directly from the experimental data, i.e., the values of F_{dyn} and F_{cyc} were taken directly from Figures 2.48 and 3.12 and not the best fit trend curve. The solid symbols represent results calculated from the best fit of the data in Figures 2.48 and 3.12. The trend

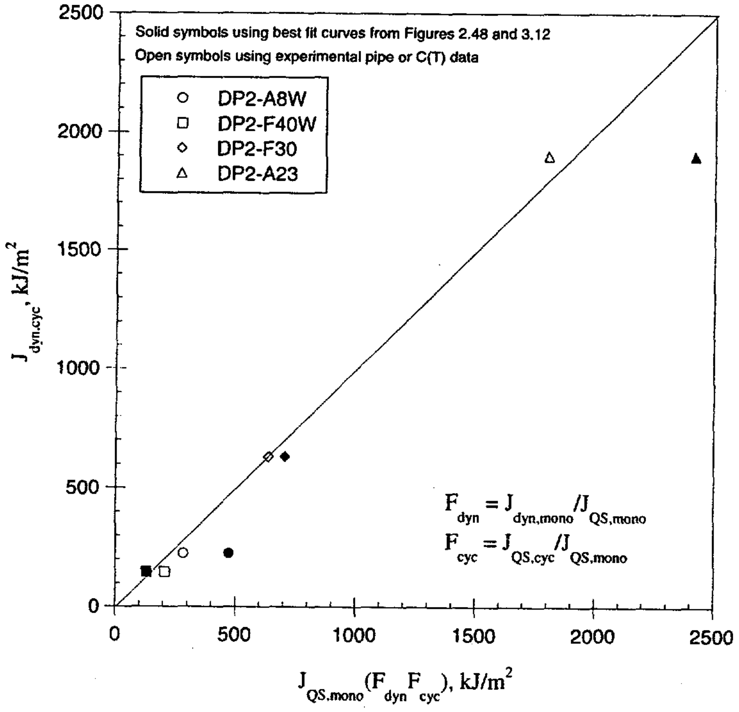

Figure 5.2 Experimental versus calculated J for dynamic, cyclic loading

in Figure 5.2 suggests that by multiplying the percent change in the monotonic resistance due to the cyclic and dynamic loading to the quasi-static, monotonic resistance produces a good approximation of the actual resistance due to dynamic, cyclic loading. However, when the linear relationship between the materials' yield-to-ultimate ratio and the relative decrease in quasi-static monotonic resistance due to cyclic and dynamic loading was used, the estimates of the dynamic, cyclic resistance were higher than the experimental values. This trend suggests that with some refinement, a suitable criterion can be developed to predict the resistance under dynamic, cyclic loading using the quasi-static, monotonic properties.

5.6 Application to Cracked-Pipe System Behavior and Similitude

In this concluding section, several comments need to be made on how the cyclic and dynamic loading data generated in this task can be used in LBB and in-service flaw evaluations. Particular attention needs to be paid to the facts that:

(a) In all of the experiments conducted in this investigation, the stress ratio and δ_{cyc}/δ_i values were held constant during each experiment. However, in a typical seismic event, these parameters are not constant.

(b) There is the question of toughness similitude for cyclic loading between the geometry of a test specimens , i.e., a C(T) specimen, and a TWC pipe that undergoes loads from an actual seismic event.

Alternative approaches to account for cyclic effects on toughness are either the use of a bounding assumption, or the use of an iterative scheme like the one suggested below. This iterative scheme is an evolving technology approach to identify the appropriate cyclic history for a cracked pipe undergoing seismic loading. At the same time, this iterative scheme would also capture plasticity effects on the seismic loads that will tend to truncate inertial loads.

The laboratory specimen investigations on cyclic loading effects throughout this report dealt with constant R-ratio and plastic-cyclic-displacement-increment (δ_{cyc}/δ_i) loading conditions. Real plant piping under seismic loading will have variable R-ratios and δ_{cyc}/δ_i. One option is to pick a bounding condition and use it for all cases. As an example, the R-ratios for uncracked pipe might be bounded as -0.5 from a large number of pipe elastic-stress analysis reports and using the following simple definition. (This definition assumes the bending planes are the same for normal (N) and safe-shutdown earthquake (SSE) loading.)

$$R = (N\text{-}SSE)/(N+SSE) \tag{5-1}$$

Cracked pipe will, however, have a more negative R-ratio than uncracked pipe as was discussed in Reference 5.5. Hence, one option is to use the R = -1, J-R curve as a bounding case for cracked pipe. For operational-basis earthquake (OBE) loads, the R-ratios may be much more positive, and perhaps only the dynamic effect on the toughness needs to be accounted for.

Another option is to try to make a more detailed time-history evaluation of the cracked pipe, which would automatically include plasticity effects on the seismic loads. Since cyclic loading during ductile tearing would reduce the load-carrying capacity, and plasticity will lower the seismic stresses, these two factors will counteract each other. Determining the appropriate cyclic-load history for a cracked-pipe system undergoing seismic loads is a difficult problem. The following procedure could be used in an iterative analytical/experimental analysis to solve this problem, and develop more realistic pipe flaw evaluations.

> The first step in this iterative procedure is to estimate what the load history might be on the pipe at the crack location during a seismic event. To assist in making such an assessment, the nonlinear cracked-pipe element developed during the course of the IPIRG and other NRC programs (Refs. 5.6 - 5.8) can be used. With such an element, the nonlinear aspects of the crack and of the piping system can be used to estimate the dynamic loads, as well as the load history at the crack location. Much as in the same way that the IPIRG-2 seismic forcing function was developed (Ref. 5.9), a plant pipe system could be analyzed with any appropriate seismic forcing function. The nonlinear response of the cracked-pipe system could be analyzed initially using the pipe material's dynamic, monotonic J-R curve to determine the cracked pipe moment-rotation curve. From this analysis, the cyclic load history on the cracked-pipe could be determined.
>
> The second step is to develop a cyclic J-R curve using the loading history determined in the first step by taking the pipe load history and applying it to a C(T) specimen. This, however, brings in the question of similitude between pipe and C(T) specimens during cyclic loading. From the results in this report, it was shown that up to crack initiation, a constant δ_{cyc}/δ_i parameter works well in obtaining similitude between C(T) and TWC pipe specimens. However, once the crack initiates, there are geometry effects between the pipe and C(T) specimen that require a change in the test δ_{cyc}/δ_i control parameter. In this report, it was shown earlier that for the 6-inch nominal diameter TWC pipe experiments conducted in the IPIRG-1 program, the crack growth per cycle was approximately twice that in the C(T) tests for the same δ_{cyc}/δ_i parameter. The existing

through-wall-cracked pipe J-estimation schemes can predict experimental load-displacement-crack growth relationships reasonably well, so this difference in crack growth per cycle between a pipe and C(T) specimen was examined. Figure 5.3 shows that for the same amount of crack growth per cycle to occur, δ_{cyc}/δ_i would have to be increased by a factor of 2. Since crack growth and displacement are linearly related (see Figure 5.3), this prediction is in agreement with the experimental observations. Consequently, the problem of similitude can be overcome by using a pipe analysis with the appropriate dynamic loading history to determine the δ_{cyc}/δ_i parameter for control of the C(T) test. This δ_{cyc}/δ_i parameter would change after crack initiation occurs, and would probably be much different for a through-wall-cracked pipe than for a surface-cracked pipe. A cyclic J-R curve can then be calculated from the experimental cyclic C(T) data.

The third step is to use the load-history J-R curve from the second step to redefine the cracked-pipe element moment-rotation curve and rerun the cracked-pipe FEM analysis. The cyclic history on the cracked pipe in this iterative step is then used to assess the cyclic loads on the C(T) specimen. If the new cracked-pipe history is close to that used for the C(T) test in the second step, then a solution is obtained with consistent load histories in the cracked-pipe analysis and the C(T) specimen J-R curve. If not, then a second C(T) specimen may have to be run using the load-history from the second FEM cracked-pipe run.

It is expected that this iterative experimental/analytical process should converge quickly since the seismic forcing function is constant, and it is a matter of determining at what time crack initiation might occur. Additionally, from the general trends observed in this program with R-ratios, material toughness, and δ_{cyc}/δ_i parameter values, engineering judgement can be used to minimize the error in the first iteration step.

In this process, consistency in load-history effects on material properties will be obtained, and plasticity effects in the pipe system can be accounted for in a more realistic pipe system fracture evaluation. In Reference 5.5, for instance, it was found that when accounting for the nonlinear dynamic behavior, the dynamic loads in a cracked-pipe system were a factor of five lower than the load calculated when using typical LBB analysis procedure with elastic uncracked pipe stress analyses. However, in Reference 5.5, the detrimental effects of cyclic loads on the toughness were not investigated, so there may be less margin due to these effects.

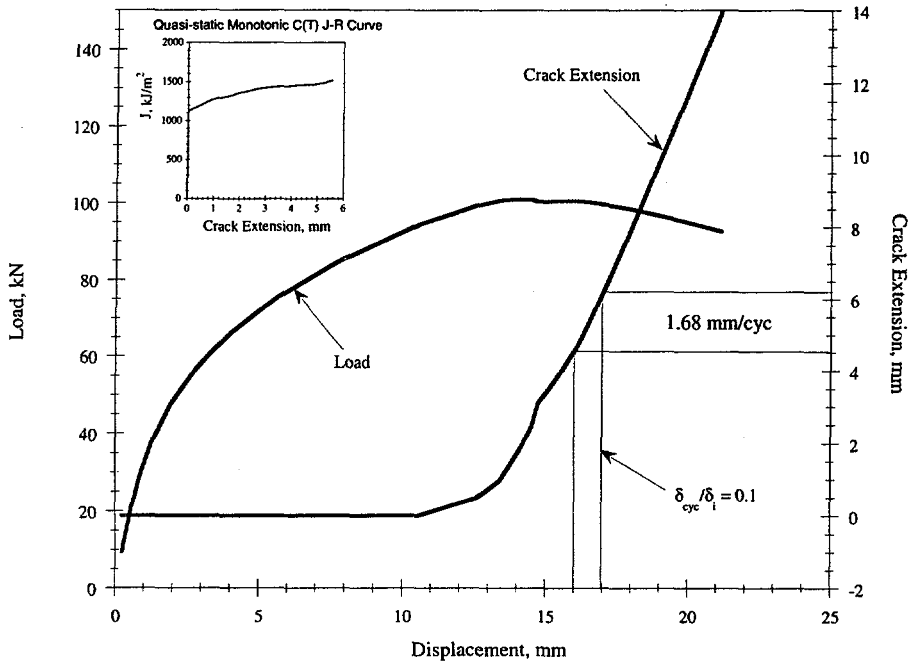

(a) GE/EPRI J-estimation scheme prediction of TWC pipe Experiment 4131-5 (Pipe DP2-A23) (J-R curve used in the calculation is inserted figure)

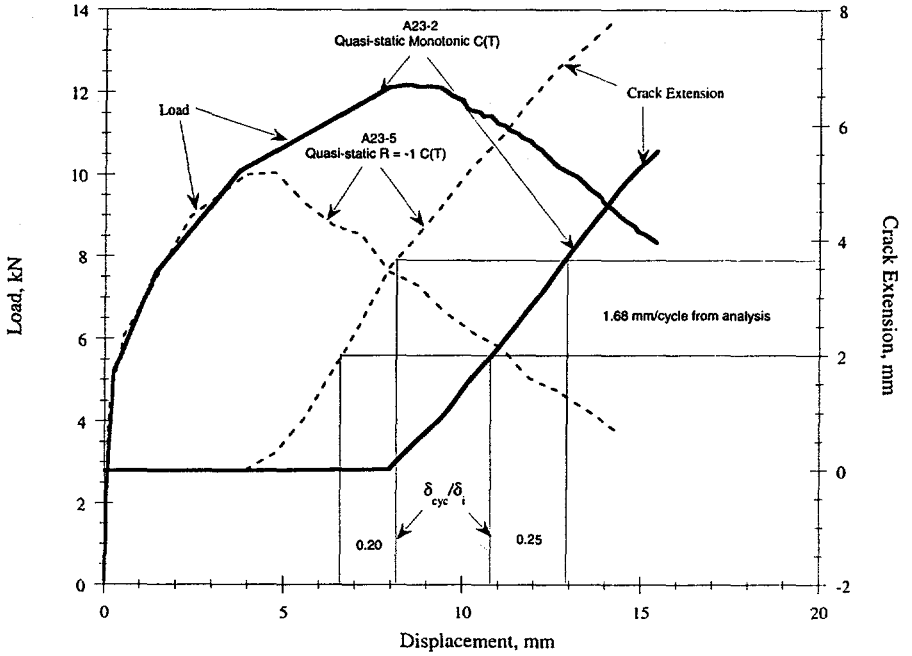

(b) C(T) specimen results

Figure 5.3 Load-displacement-crack growth records from a GE/EPRI TWC pipe prediction and C(T) specimens illustrating the need to change δ_{cyc}/δ_i after crack initiation to produce comparable cyclic crack growth between the two specimen types

5.7 References

5.1 Marschall, C. W., Mohan, R., Krishnaswamy, P., and Wilkowski, G. M., "Effect of Dynamic Strain Aging on the Strength and Toughness of Nuclear Ferritic Piping at LWR Temperatures," NUREG/CR-6226, October 1994.

5.2 Krishnaswamy, P., Scott, P., Mohan, R., Rahman, S., Choi, Y. H., Brust F., Kilinski, T., Ghadiali, N., Marschall, C., and Wilkowski, G., "Fracture Behavior of Circumferential Short-Surface-Cracked Pipe," NUREG/CR-6298, November 1995.

5.3 Brust, F., Scott, P., Rahman, S., Ghadiali, N., Kilinski, T., Francini, R., Marschall, C., Muira, N., Krishnaswamy, P., and Wilkowski, G., "Assessment of Short Through-Wall Circumferential Cracks in Pipes - Experiments and Analyses," NUREG/CR-6235, April 1995.

5.4 Wilkowski, G., Kramer, G., Vieth, P., Francini, R., and Scott, P., "The Effect of Cyclic Loading During Ductile Tearing on Circumferentially Cracked Pipe -- Analytical Results," ASME PVP Vol. 280, pp 221-240, June 1994.

5.5 Olson, R., Wolterman, R., and Wilkowski, G., "Margins for Dynamic FEM Analysis of Cracked Pipe Under Seismic Loading for the DOE New Production Reactor," ASME PVP Vol. 280, pp 119-134, June 1994.

5.6 R. Olson, P. Scott, and G. Wilkowski, "Application of a Nonlinear Spring Element to Analysis of Circumferentially Cracked Pipe under Dynamic Loading," *Pressure Vessel Fracture, Fatigue and Life Management*, ASME PVP Vol. 233, pp 279-292, June 1992.

5.7 Olson, R., Wolterman, R., Scott, P., Krishnaswamy, P., and Wilkowski, G., "The Next Generation Methodology for Cracked Pipe System Subjected to Dynamic Loads," ASME PVP Vol. 275-1, pp 159-172, June 1994.

5.8 Olson, R. J., Wolterman, R. L., Wilkowski, G. M., and Kot, C. A. "Validation of Analysis Methods for Assessing Flawed Piping Subjected to Dynamic Loading," NUREG/CR-6234, August 1994.

5.9 Olson, R., Scott, P., and Wilkowski, G., "Design of the IPIRG-2 Simulated Seismic Forcing Function," NUREG/CR-6439, February 1996.

Table A.1 - Specimen Dimensions for Stainless Steel Base Metal Cyclic C(T) Specimens

Specimen ID	w, mm	B, mm	B_N, mm	a_i, mm
A23-2c	25.27	12.68	12.68	13.56
A23-4c	25.38	12.68	12.68	13.47
A23-5c	25.35	12.62	12.62	13.37
A23-6c	25.43	12.68	12.68	13.77
A23-7c	25.91	12.70	12.70	13.39
A23-11c	25.32	12.62	12.62	13.67
A23-12c	25.50	12.70	12.70	13.69
A23-13c	25.81	12.70	12.70	13.69
A23-14c	25.45	12.70	12.70	13.51
A23-15c	25.20	12.71	12.71	13.46
A23-16c	25.50	12.72	12.72	13.56
A23-17c	25.32	12.69	12.69	13.22
A23-18c	25.25	12.69	12.69	13.16
A23-19c	25.35	12.68	12.68	13.15
A23-20c	25.20	12.68	12.68	13.23
A23-21c	25.40	12.68	12.68	13.03
A23-22c	25.40	12.73	12.73	13.28

Table A.2 - Specimen Dimensions for Carbon Steel Base Metal Cyclic C(T) Specimens

Specimen ID	w, mm	B, mm	B_N, mm	a_i, mm
F30-1c	25.60	11.19	11.19	13.69
F30-2c	25.43	11.17	11.17	13.31
F30-3c	25.53	11.18	11.18	12.98
F30-4c	25.54	11.19	11.19	13.44
F30-5c	25.46	11.18	11.18	13.23
F30-6c	25.29	11.19	11.19	13.23
F30-7c	25.36	11.18	11.18	13.28
F30-12c	25.49	11.18	11.18	13.18

Table A.3 - Specimen Dimensions for Stainless Steel SAW Cyclic C(T) Specimens

Specimen ID	w,mm	B, mm	B_n, mm	a_i, mm
A8W-101c	50.876	19.177	15.461	26.985
A8W-102c	50.800	19.177	15.392	27.003
A8W-103c	50.876	19.177	15.418	26.551
A8W-104c	50.800	19.152	15.723	26.883
A8W-106c	50.902	19.177	15.476	26.314
A8W-107c	50.902	19.152	15.464	26.949
A8W-108c	50.902	19.177	15.428	26.467

Table A.4 - Specimen Dimensions for Carbon Steel SAW Cyclic C(T) Specimens

Specimen ID	w,mm	B, mm	B_n, mm	a_i, mm
F40W-1c	25.502	12.583	11.326	13.602
F40W-3c	25.375	12.654	10.160	13.421
F40W-4c	25.425	12.649	10.033	13.411
F40W-5c	25.400	12.624	10.185	13.485
F40W-7c	25.400	12.598	10.033	13.632
F40W-8c	25.400	12.624	9.901	13.310
F40W-10c	25.400	12.344	9.830	13.754
F40W-11c	25.476	12.637	10.490	13.023
F40W-12c	25.400	12.637	10.338	13.305
F40W-13c	23.419	12.624	10.556	13.492

Table A.5 - Specimen Dimensions for Carbon Steel C(T) Specimens

Specimen ID	Approximate Time to Crack Initiation, sec	Specimen Dimensions mm			
		w	B	B_N	a_i
F22-2	0.2	25.40	9.14	7.75	13.14
F22-3	600	25.48	9.14	7.32	13.59
IPF1-1d	0.2	76.20	35.23	28.12	40.60
IPF1-2d	0.2	76.20	35.28	28.17	40.23
IPF1-8	600	76.15	35.38	28.60	41.22
DP2-F9-1d	0.2	50.80	13.87	11.10	27.61
DP2-F9-2d	0.2	50.80	13.87	11.10	27.53
DP2-F9-19	600	50.80	14.00	11.20	25.91

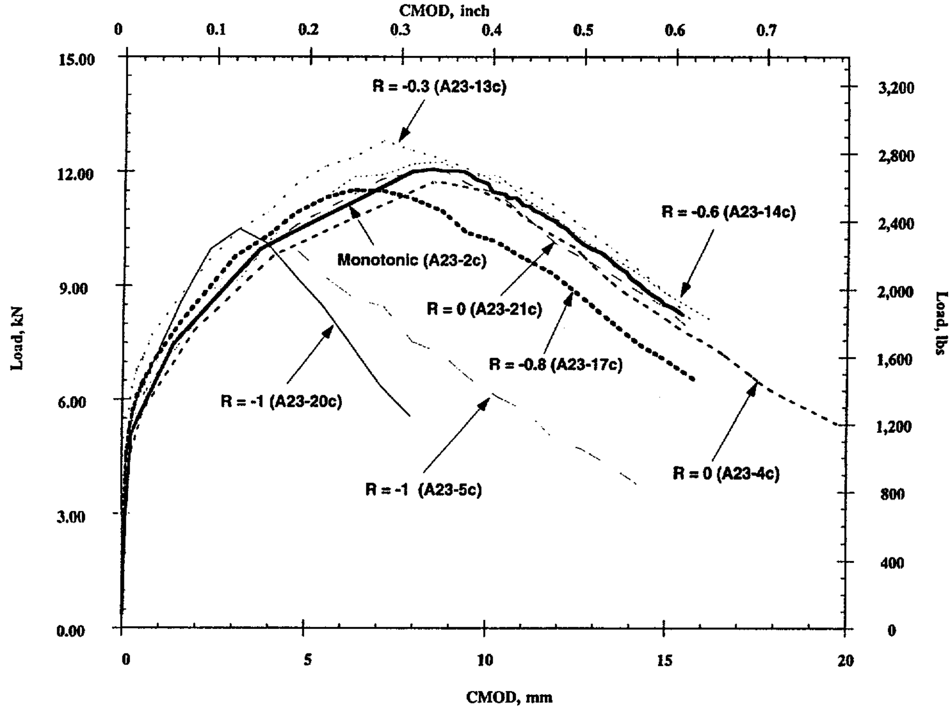

Figure B-1 Load-CMOD curves for stainless steel base metal C(T) specimen with $\delta_{cyc}/\delta_i = 0.1$

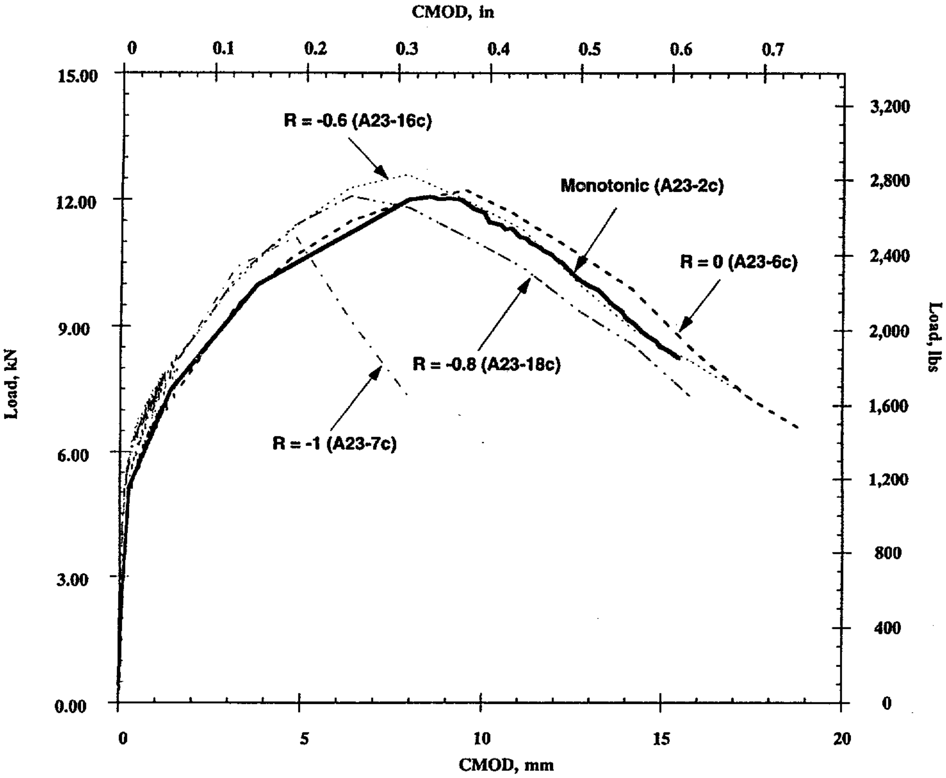

Figure B-2 Load-CMOD curves for stainless steel base metal C(T) specimens with $\delta_{cyc}/\delta_i = 0.2$

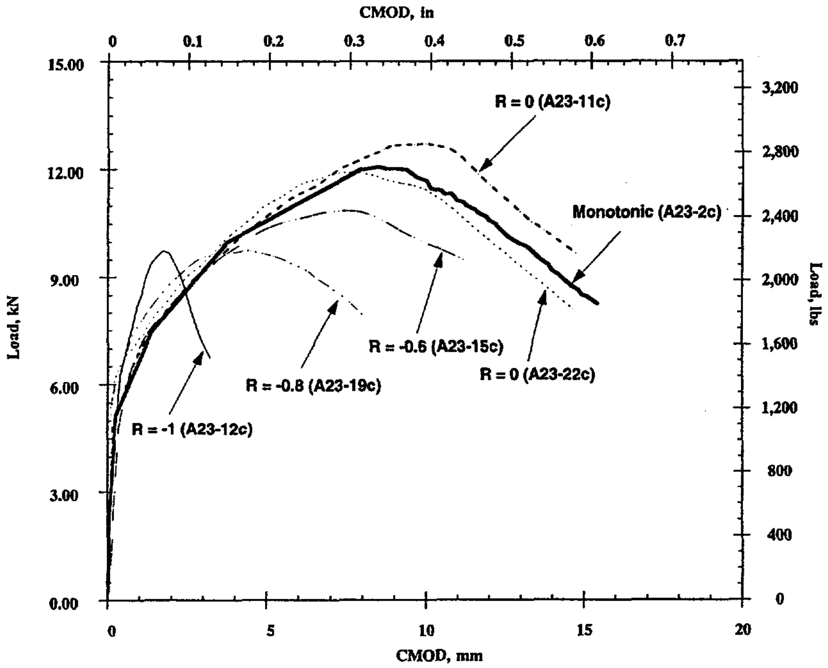

Figure B-3 Load-CMOD curves for stainless steel base metal C(T) specimen with $\delta_{cyc}/\delta_i = 0.025$

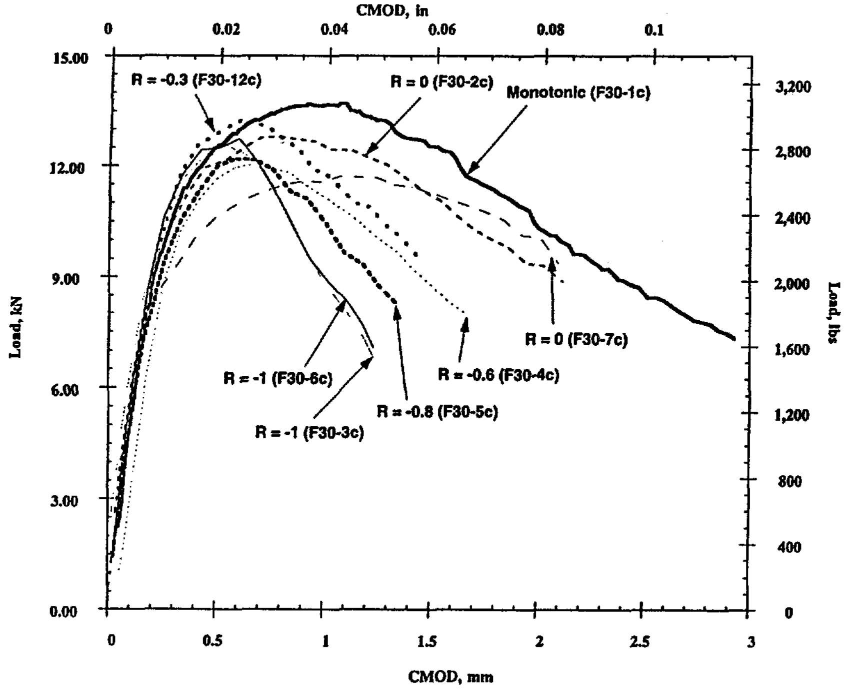

Figure B-4 Load-CMOD curves for carbon steel base metal with $\delta_{cyc}/\delta_i = 0.1$

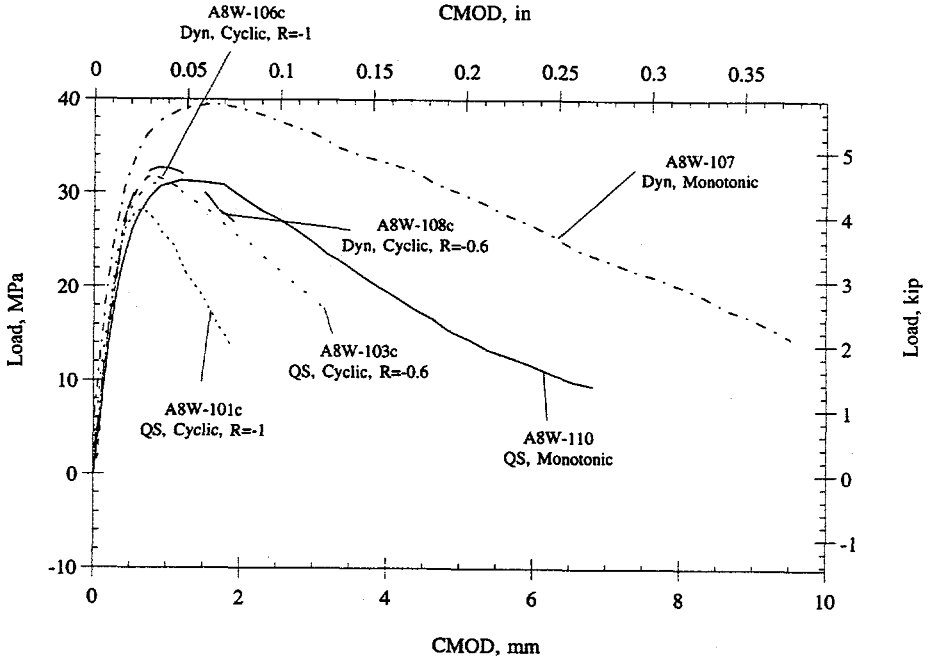

Figure B-5 Load-CMOD curves for stainless steel SAW C(T) specimens with $\delta_{cyc}/\delta_i = 0.1$

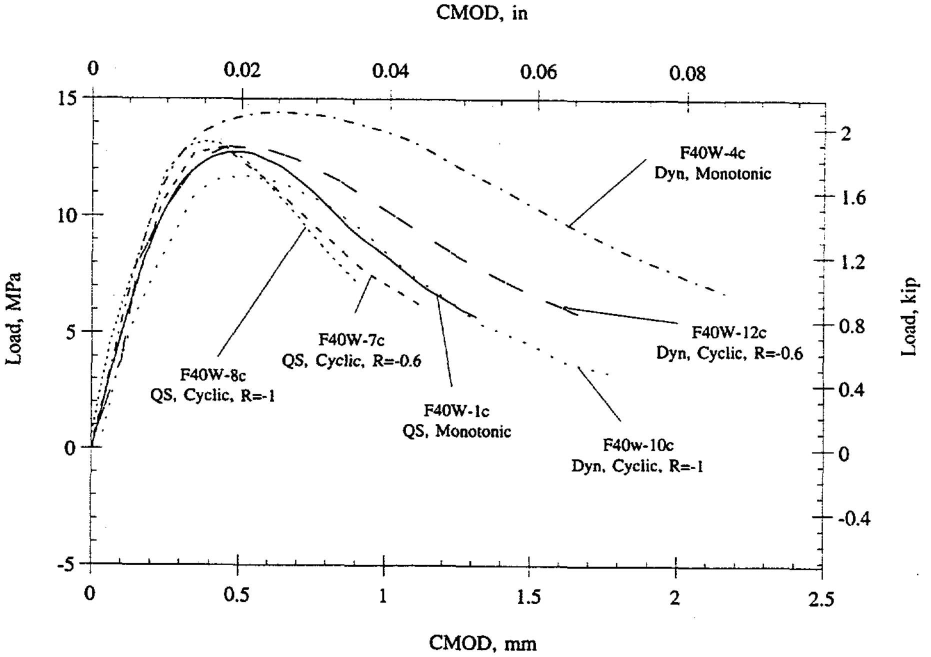

Figure B-6 Load-CMOD curves for carbon steel SAW C(T) specimens with $\delta_{cyc}/\delta_i = 0.1$

NRC FORM 335
(2-89)
NRCM 1102,
3201, 3202

U.S. NUCLEAR REGULATORY COMMISSION

BIBLIOGRAPHIC DATA SHEET

(See instructions on the reverse)

1. REPORT NUMBER *(Assigned by NRC, Add Vol., Supp., Rev., and Addendum Numbers, if any.)*
NUREG/CR-6440
BMI-2190

2. TITLE AND SUBTITLE
The Effects of Cyclic and Dynamic Loading on the Fracture Resistance of Nuclear Piping Steels
Technical Report: October 1992 - April 1996

3. DATE REPORT PUBLISHED
MONTH: December
YEAR: 1996

4. FIN OR GRANT NUMBER
D2060

5. AUTHOR(S)
D. L. Rudland, F. Brust, and G. M. Wilkowski

6. TYPE OF REPORT
Technical

7. PERIOD COVERED *(Inclusive Dates)*

8. PERFORMING ORGANIZATION – NAME AND ADDRESS *(If NRC, provide Division, Office or Region, U.S. Nuclear Regulatory Commission, and mailing address; if contractor, provide name and mailing address.)*

Battelle
505 King Avenue
Columbus, OH 43201-2693

9. SPONSORING ORGANIZATION – NAME AND ADDRESS *(If NRC, type "Same as above"; if contractor, provide NRC Division, Office or Region, U.S. Nuclear Regulatory Commission, and mailing address.)*

Division of Engineering Technology
Office of Nuclear Regulatory Research
U.S. Nuclear Regulatory Commission
Washington, D.C. 20555- 0001

10. SUPPLEMENTARY NOTES
M.E.Mayfield, NRC Project Manager

11. ABSTRACT *(200 words or less)*

This report presents the results of the material property evaluation efforts performed within Task 3 of the IPIRG-2 Program. Several related investigations were conducted. (1) Quasi-static, cyclic-load compact tension specimen experiments were conducted using parameters similar to those used in IPIRG-1 experiments on 6-inch nominal diameter through-wall-cracked pipes. These experiments were conducted on a TP304 base metal, an A106 Grade B base metal, and their respective submerged-arc welds. The results showed that when using a constant cyclic displacement increment, the compact tension experiments could predict the through-wall-cracked pipe crack initiation toughness, but a different control procedure is needed to reproduce the pipe cyclic crack growth in the compact tension tests. (2) Analyses conducted showed that for 6-inch diameter pipe, the quasi-static, monotonic J-R curve can be used in making cyclic pipe moment predictions; however, sensitivity analyses suggest that the maximum moments decrease slightly from cyclic toughness degradation as the pipe diameter increases. (3) Dynamic stress-strain and compact tension tests were conducted to expand on the existing dynamic database. Results from dynamic moment predictions suggest that the dynamic compact tension J-R and the quasi-static stress-strain curves are the appropriate material properties to use in making dynamic pipe moment predictions.

12. KEY WORDS/DESCRIPTORS *(List words or phrases that will assist researchers in locating the report.)*

cyclic loading, dynamic loading, nuclear pipe, fracture, J-integral, J-R curve, fracture toughness, carbon steel, stainless steel, welds, dynamic strain aging, elastic-plastic fracture, compact tension specimen

13. AVAILABILITY STATEMENT
Unlimited

14. SECURITY CLASSIFICATION
(This Page) Unclassified
(This Report) Unclassified

15. NUMBER OF PAGES

16. PRICE